Properties and Behavior of UHPC-Class Materials

Publication FHWA-HRT-18-036

March 2018

Research, Development, and Technology
Turner-Fairbank Highway Research Center
6300 Georgetown Pike
McLean, VA 22101-2296

U.S. Department of Transportation
Federal Highway Administration

FOREWORD

Ultra-high performance concrete (UHPC) is an advanced construction material that can positively influence the future of the highway infrastructure. Since 2001, the Federal Highway Administration has been at the forefront of developing UHPC-based solutions for pressing challenges. The growing usage of UHPC across the U.S. highway infrastructure has focused attention on the need for common assessment of the basic performance measures often associated with UHPCs. This study provides significantly enhanced breadth of knowledge relative to FHWA's early work on this topic, as published in FHWA-HRT-06-103. By assessing properties for multiple UHPCs, FHWA is providing needed answers while also delivering a framework for future UHPC property assessments.

Cheryl Allen Richter, P.E., Ph.D.
Director, Office of Infrastructure
Research and Development

TECHNICAL REPORT DOCUMENTATION PAGE

1. Report No. FHWA-HRT-18-036	2. Government Accession No.	3. Recipient's Catalog No.
4. Title and Subtitle Properties and Behavior of UHPC-Class Materials		5. Report Date March 2018
		6. Performing Organization Code:
7. Author(s) Zachary B. Haber, Igor De la Varga, Benjamin A. Graybeal, Brian Nakashoji, and Rafic El-Helou		8. Performing Organization Report No.
9. Performing Organization Name and Address Office of Infrastructure Research & Development Federal Highway Administration 6300 Georgetown Pike McLean, VA 22101-2296		10. Work Unit No. 11. Contract or Grant No.
12. Sponsoring Agency Name and Address Office of Infrastructure Research & Development Federal Highway Administration 6300 Georgetown Pike McLean, VA 22101-2296		13. Type of Report and Period Covered Final Report: 2014-2017 14. Sponsoring Agency Code HRDI-40

15. Supplementary Notes
The document content was prepared by Zachary Haber of FHWA, Igor De la Varga of SES Group and Associates, LLC under laboratory support contract DTFH61-13-D-00007, Brian Nakashoji of PSI, Inc., under laboratory support contract DTFH61-10-D-00017. Content was also prepared by Benjamin Graybeal of FHWA who leads the FHWA Structural Concrete Research Program. Portions of this report were prepared under laboratory support contract DTFH61-16-D-00033 Finally, Rafic El-Helou, a National Research Council Post-Doctoral Fellow, assisted with the research effort.

16. Abstract
Ultra-high performance concrete (UHPC) is being adopted for a variety of different bridge construction and rehabilitation applications. In North America, the most popular application of UHPC in bridge construction is for field-cast closure pours between adjacent prefabricated bridge elements, which are employed in many accelerated bridge construction (ABC) projects; this application has proven to be a common entry point for many bridge owners. As the demand for this innovative class of materials increases, so will the need for knowledge regarding the material properties and material characteristics. To fill this knowledge gap, researchers at Federal Highway Administration's (FHWA's) Turner-Fairbank Highway Research Center (TFHRC) executed an experimental study on six different commercially-available materials being marketed as "UHPC-class". The goal of the research was to provide the bridge engineering community with a more comprehensive set of properties for this class of materials, which in turn could facilitate broader use within the sector. The UHPC-class materials were evaluated using 14 different ASTM, AASHTO, or FHWA-TFHRC-developed test methods. Results indicate that these materials behave similarly with respect to some performance measures such as compressive strength, tensile strength, and durability, but vary with respect to others such as dimensional stability, bond to precast concrete, and compressive creep.

17. Key Words UHPC, Ultra-high performance fiber-reinforced concrete, cementitious composite, bridge engineering, accelerated bridge construction, durability, mechanical properties, bond.		18. Distribution Statement No restrictions	
19. Security Classif. (of this report) Unclassified	20. Security Classif. (of this page) Unclassified	21. No. of Pages 153	22. Price N/A

Form DOT F 1700.7 (8-72) Reproduction of completed page authorized

SI* (MODERN METRIC) CONVERSION FACTORS

APPROXIMATE CONVERSIONS TO SI UNITS

Symbol	When You Know	Multiply By	To Find	Symbol
		LENGTH		
in	inches	25.4	millimeters	mm
ft	feet	0.305	meters	m
yd	yards	0.914	meters	m
mi	miles	1.61	kilometers	km
		AREA		
in^2	square inches	645.2	square millimeters	mm^2
ft^2	square feet	0.093	square meters	m^2
yd^2	square yard	0.836	square meters	m^2
ac	acres	0.405	hectares	ha
mi^2	square miles	2.59	square kilometers	km^2
		VOLUME		
fl oz	fluid ounces	29.57	milliliters	mL
gal	gallons	3.785	liters	L
ft^3	cubic feet	0.028	cubic meters	m^3
yd^3	cubic yards	0.765	cubic meters	m^3
	NOTE: volumes greater than 1000 L shall be shown in m^3			
		MASS		
oz	ounces	28.35	grams	g
lb	pounds	0.454	kilograms	kg
T	short tons (2000 lb)	0.907	megagrams (or "metric ton")	Mg (or "t")
		TEMPERATURE (exact degrees)		
°F	Fahrenheit	5 (F-32)/9 or (F-32)/1.8	Celsius	°C
		ILLUMINATION		
fc	foot-candles	10.76	lux	lx
fl	foot-Lamberts	3.426	candela/m^2	cd/m^2
		FORCE and PRESSURE or STRESS		
lbf	poundforce	4.45	newtons	N
lbf/in^2	poundforce per square inch	6.89	kilopascals	kPa

APPROXIMATE CONVERSIONS FROM SI UNITS

Symbol	When You Know	Multiply By	To Find	Symbol
		LENGTH		
mm	millimeters	0.039	inches	in
m	meters	3.28	feet	ft
m	meters	1.09	yards	yd
km	kilometers	0.621	miles	mi
		AREA		
mm^2	square millimeters	0.0016	square inches	in^2
m^2	square meters	10.764	square feet	ft^2
m^2	square meters	1.195	square yards	yd^2
ha	hectares	2.47	acres	ac
km^2	square kilometers	0.386	square miles	mi^2
		VOLUME		
mL	milliliters	0.034	fluid ounces	fl oz
L	liters	0.264	gallons	gal
m^3	cubic meters	35.314	cubic feet	ft^3
m^3	cubic meters	1.307	cubic yards	yd^3
		MASS		
g	grams	0.035	ounces	oz
kg	kilograms	2.202	pounds	lb
Mg (or "t")	megagrams (or "metric ton")	1.103	short tons (2000 lb)	T
		TEMPERATURE (exact degrees)		
°C	Celsius	1.8C+32	Fahrenheit	°F
		ILLUMINATION		
lx	lux	0.0929	foot-candles	fc
cd/m^2	candela/m^2	0.2919	foot-Lamberts	fl
		FORCE and PRESSURE or STRESS		
N	newtons	0.225	poundforce	lbf
kPa	kilopascals	0.145	poundforce per square inch	lbf/in^2

*SI is the symbol for the International System of Units. Appropriate rounding should be made to comply with Section 4 of ASTM E380.
(Revised March 2003)

TABLE OF CONTENTS

LIST OF FIGURE

LIST OF TABLES

LIST OF ABBREVIATIONS

AASHTO	American Association of State Highway and Transportation Officials
ABC	Accelerated bridge construction
ACI	American Concrete Institute
ADT	Average daily traffic
ASR	Alkali-silica reaction
CSH	calcium-silicate-hydrate
DEF	Delayed ettringite formation
DEMEC	detachable mechanical strain gauge
DTT	Direct tension test
FHWA	Federal Highway Administration
FRC	Fiber-reinforced concrete
HSC	High-strength concrete
IC	Internal curing
LWA	Lightweight aggregate
LVDT	linear variable differential transducers
MOR	Modulus of rupture
NSC	Normal strength concrete
PBE	Prefabricated bridge element
PBES	Prefabricated bridge elements and systems
RCPT	Rapid chloride ion penetration test
RDME	Relative dynamic modulus of elasticity
RH	Relative humidity
SAP	Superabsorbent polymer
SCTT	Split cylinder tension test
SEM	Scanning electron microscope
SP	Pseudo stress plateau
TFHRC	Turner-Fairbank Highway Research Center
TH	Tension hardening
UHPC	Ultra-high performance concrete
w/b	Water-to-binder ratio
w/c	Water-to-cement ratio
w/s	Water-to-solids ratio

LIST OF NOTATION

b = beam or flexural element width

$C(t)$ = creep coefficient defined as a function of time, t

c_{si} = clear half spacing between adjacent reinforcing bars

c_{so} = clear side cover

C_u = long-term creep coefficient

D = specimen diameter

d_b = reinforcing bar diameter

E = elastic modulus

E_c = compressive elastic modulus of UHPC

f_c = compressive stress of UHPC

f'_c = compressive strength of concrete or UHPC

f_{cr} = first cracking strength of UHPC in tension

f_e = elastic tension strength of UHPC

f_{ft} = flexural tensile strength

f_p = fiber-bridging strength of UHPC

f_r = modulus of rupture of concrete

f_s = tension stress in a reinforcing bar

$f_{s,\,max}$ = maximum tension stress in a reinforcing bar

$f_{s,\,min}$ = minimum tension stress in a reinforcing bar

f_{st} = splitting tensile stress

f_y = specified yield strength of steel reinforcement

h = beam or flexural element depth

I_{cr} = moment of inertia of a cracked section

I_g = gross moment of inertia

l = specimen length

l_d = embedment length of reinforcing steel

l_f = length of fiber reinforcement

l_s = reinforcing bar lap splice length

L = simply-supported length of a flexural element

M_{cr} = cracking moment

M_y = yielding moment

M_u = ultimate moment

P = applied load

t = Time

V_f = volumetric fiber reinforcement content of UHPC; otherwise referred to as the percent of fiber reinforcement by volume

y_t = distance between the neutral axis of bending and the extreme tension fiber of a flexural element

α = linearity deviation parameter

$\Delta\varepsilon$ = change in tensile strain in a reinforcing bar

Δf_s = reinforcing bar stress range

$(\Delta F)_{TH}$ = constant amplitude fatigue threshold

$\Delta\phi$ = change in interface curvature

Δ_y = yield displacement of a flexural member

Δ_u = ultimate displacement of a flexural member

$\varepsilon_{axial,\ 10}$ = axial strain at 10 percent of peak load

$\varepsilon_{axial,\ 30}$ = axial strain at 30 percent of peak load

ε_c = compressive strain of UHPC

$\varepsilon_{circ,\ 10}$ = circumferential strain at 10 percent of peak load

$\varepsilon_{circ,\ 30}$ = circumferential strain at 30 percent of peak load

ε_{cr} = strain corresponding to the first cracking strength of UHPC in tension, f_{cr}

ε_{cp} = strain due to compressive creep

$\varepsilon_{cp}(t)$ = strain due to compressive creep as a function of time, t

ε_e = strain corresponding to the elastic tension strength, f_e, of UHPC

ε_n = normalized compressive strain of UHPC

ε_p = strain corresponding to the fiber-bridge strength, f_p, of UHPC

ε_{sh} = shrinkage strain measured during creep testing

$\varepsilon_{t,max}$ = measured strain at peak load for a given cycle

$\varepsilon_{t,min}$ = measured strain at minimum load for a given cycle

ε_{total} = strain measured during creep testing; $\varepsilon_{total} = \varepsilon_{cp} + \varepsilon_{sh}$

ϕ_{max} = measured curvature at peak load for a given cycle

ϕ_{min} = measured curvature at minimum load for a given cycle

CHAPTER 1. INTRODUCTION AND BACKGROUND

INTRODUCTION

Advances in concrete technology such as high-strength steel micro-fiber reinforcement, superplasticizers, gradation optimization, and supplementary cementitious materials, began to be packaged together into a new generation of cementitious composite materials in the 1970s and 1980s. In the 1990s, this new class of materials was brought to market and has become known as ultra-high performance concrete (UHPC). UHPC-class materials can be differentiated from conventional concrete-like materials by their exceptional mechanical and durability properties. Most notably, UHPC is composed of a very dense cementitious matrix with a discontinuous pore structure that results in very low permeability and high compressive strength. Furthermore, the matrix is reinforced with high volumes (typically equal to or greater than 2 percent fiber by volume) of high-strength steel microfiber reinforcement which allows for post-cracking tensile ductility.

Currently, there is not a universally-accepted definition of what constitutes an ultra-high performance concrete. Thus, the definition developed by the United States Federal Highway Administration (FHWA) is adopted for the purposes of this publication, which is as follows:

> *UHPC is a cementitious composite material composed of an optimized gradation of granular constituents, a water-to-cementitious materials ratio less than 0.25, and a high percentage of discontinuous internal fiber reinforcement. The mechanical properties of UHPC include compressive strength greater than 21.7 ksi (150 MPa) and sustained post-cracking tensile strength greater than 0.72 ksi (5 MPa). UHPC has a discontinuous pore structure that reduces liquid ingress, significantly enhancing durability compared to conventional concrete.* (Graybeal 2014a)

Although UHPC has been commercially available for more than a decade in the United States and Canada, the associated knowledge base required for effective design and deployment is just beginning to become more widely-available. Bridge designers and bridge owners are increasingly starting to see some of the advantages of using UHPC-class materials in bridge design and construction. As the interest in UHPC-class materials grows, interested bridge designers and owners will look to better understand the mechanical and durability properties of this advanced material along with how UHPC behaves in structural elements. To meet this growing need, the structural concrete research group at the FHWA Turner-Fairbank Highway Research Center executed an extensive study on the properties and performance of six different, commercial-available UHPC-class materials that may be suitable for highway bridge applications. This report presents the details and finding of that extensive study.

APPLICATIONS OF UHPC IN NORTH-AMERICAN HIGHWAY BRIDGES

Background

UHPC in its present form started to become commercially available in North America by the late 1990s; first in Canada in the late 1990s followed by the US in the early 2000s. The first North

American bridge to use UHPC was constructed in Sherbrooke, Quebec, Canada in 1997 (Blais and Couture 1999). This was a precast, prestressed open-web space truss pedestrian bridge that contained nonprestressed (passive) steel reinforcement. FHWA began investigating the use of UHPC for highway infrastructure in 2001 and has been working with State transportation departments to deploy the technology since 2002. The first US bridge to employ UHPC was constructed in Wapello County, Iowa in 2006; this bridge is known as the Mars Hill Bridge. The bridge features three precast, prestressed UHPC girders. The cross-sectional geometry of the girders was optimized to take advantage of the mechanical properties of UHPC. Since these initial deployments, the interest in UHPC as a material for bridge construction has increased significantly. Not only has there been a significant amount of research conducted by FHWA, academic research groups, and state transportation agencies, but the number of bridge constructed using UHPC has increased significantly since 2006. This trend is shown in figure 1 and figure 2 which depict the cumulative number of bridge constructed with UHPC since 2006 in the US and Canada, respectively. By the conclusion of 2016, there have been more than 180 bridges built in the US and Canada that employ UHPC. The location of each of these bridges is accessible through the FHWA UHPC Deployments web page (FHWA 2017a) and Interactive UHPC Bridge Map (FHWA 2017b).

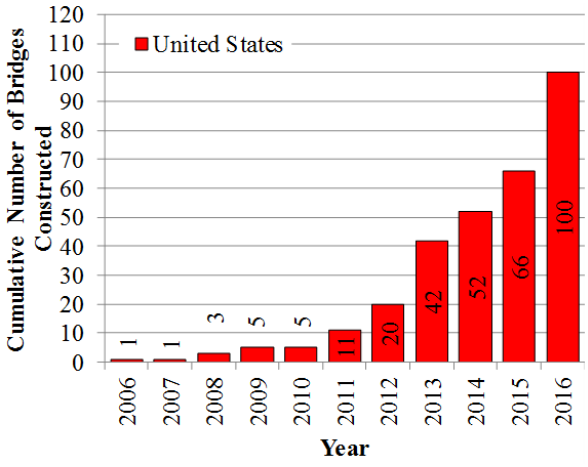

Figure 1. Graph. Timeline of UHPC in bridge construction in the United States.

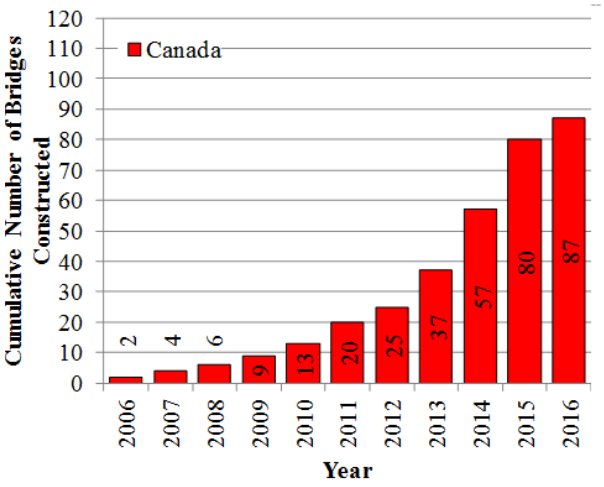

Figure 2. Graph. Timeline of UHPC in bridge construction in Canada.

Applications

The following sections provide some context as to how UHPC is currently being deployed in highway bridge applications. Figure 3 through figure 6 illustrates some specific applications of UHPC in bridge construction in North America.

Field-Cast Connection Between Prefabricated Bridge Elements

Currently, the most popular North American application of UHPC in bridge construction is for connections between prefabricated bridge elements and systems (PBES). Furthermore, this is also

the most common entry point for bridge owners interested in adding UHPC to their design and construction toolbox.

Prefabricated elements offer advantages in terms of component quality, construction site safety, and construction timeline; however, their use presents challenges in terms of field assembly of elements and performance of field-installed connections. Connections between prefabricated bridge decks and adjacent bridge elements are commonly created using interlaced reinforcing bars, connectors, or protruding studs that are contained within a pocket-like void or a long connection seam; herein, these are otherwise referred to as "connection regions" or simply "connections." These connection regions are formed and filled with field-cast grout materials. These connections provide structural continuity and are critical for development of load paths between structural elements. Using field-cast UHPC in place of conventional cementitious grout-like materials for closure pours can simultaneously address multiple concerns with the use of prefabricated elements. The advanced mechanical properties of UHPC allow field-cast connections to be smaller, to contain less expensive connectors, and to outperform the connected elements thus eliminating the connections as a weak link in the structure. The fresh properties of UHPC allow tight and potentially hidden connection spaces to be filled with little concern of honeycombing or unintended voids. The durability properties of UHPC allow the field-cast connections to withstand the aggressive environments that have in the past caused field-cast grouts and conventional concretes to prematurely degrade. Figure 3-a, -b, and -c illustrates a few common methods by which UHPC is used to connect adjacent precast bridge decks and modular superstructure elements.

Two additional applications of UHPC connections are shown in figure 4 and figure 5. Figure 4 illustrates how UHPC have been use to connect adjacent precast, prestressed box girders. This application was previously studied by researchers at TFHRC and has since been deployed on a bridge in Fayette County, Ohio. (Yuan and Graybeal 2016; Steinberg, Semendary, and Walsh 2016; Graybeal 2017) The use of UHPC in this application eliminates the need for transverse post-tensioning or for a structural concrete overlay. In effect, this detail creates a continuously reinforced concrete slab at the top flange level of the boxes capable of transferring shear, moment, axial tension, and axial compressive forces across the connection. This greatly simplifies the design and construction of such systems.

Figure 5 illustrates the use of UHPC for creating connections between bridge columns and pier caps (or footings). Reinforced concrete columns typically employ larger diameter reinforcing bars compared with other elements such as bridge decks. Thus, the lap splice length required to develop such bars can be very large. This can be especially challenging when trying to use prefabricated systems. Using UHPC, precast column-to-cap or column-to-footing connection details can be greatly simplified. Using a lap spliced connection, what would require several feet of development length with conventional closure materials, can be achieved with inches of development length using UHPC.

Completed in 2014, the Hooper Road Bridge used UHPC to connect existing reinforced concrete columns to precast bent caps; the details shown in figure 5 are from the Hooper Road Project. The superstructure reconstruction also employed the use of precast concrete deck panels. Using conventional connection grout materials, the lap splice length would have been greater than 40 inches (1 m). Using UHPC the column-cap connection details were greatly simplified. The

connection was reduced to 12 inches (305 mm) in length with a required lap splice length of 11.5 inches (292 mm). Furthermore, the use of UHPC reduced the need for secondary reinforcement within the connection region.

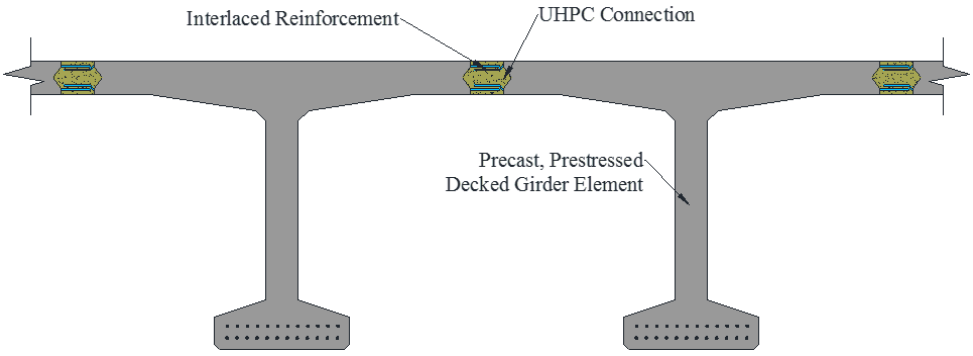

A. UHPC connections between precast, prestressed decked girder elements.

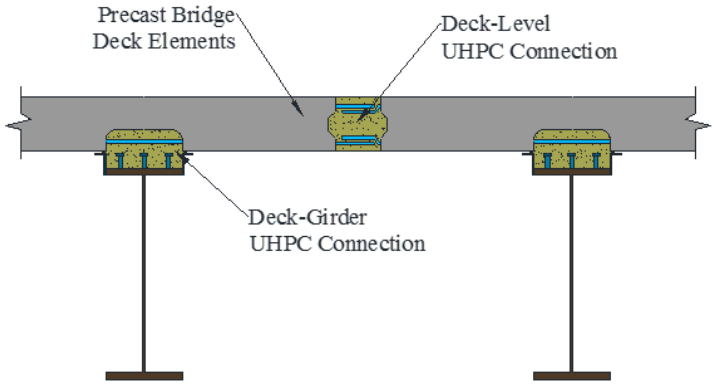

B. UHPC connections between precast bridge deck elements and supporting girders.

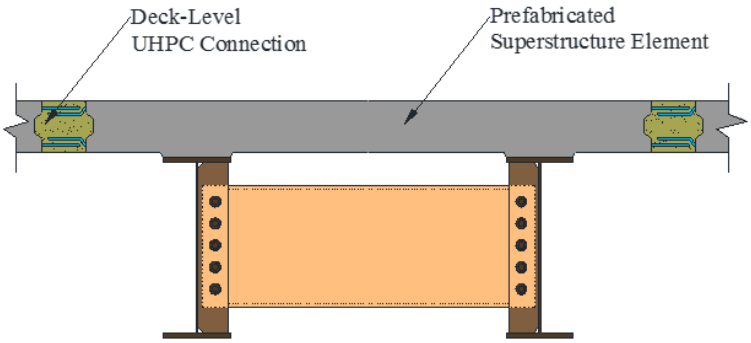

C. UHPC connections between modular superstructure element.

Figure 3. Illustrations. Applications of UHPC connections between prefabricated bridge deck and modular superstructure elements.

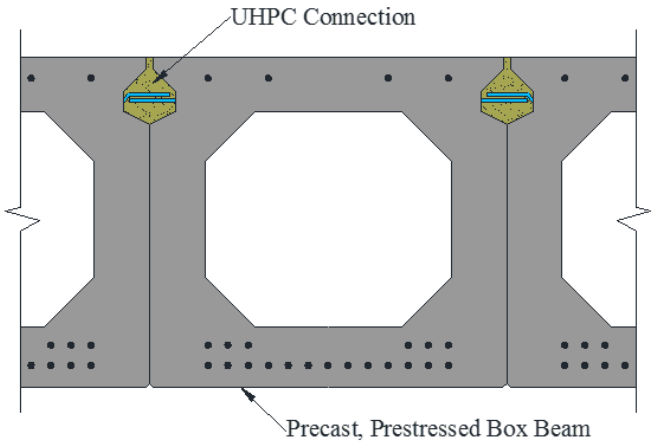

Figure 4. Illustration. UHPC connections between adjacent precast, prestressed box beams.

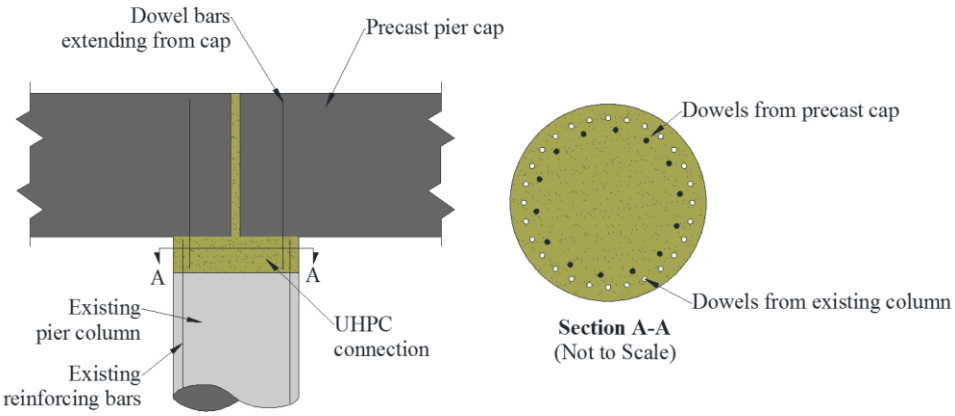

Figure 5. Illustration. UHPC connections between an existing bridge column and a new precast pier cap element.

UHPC-Based Rehabilitation Solutions

Bridge owners spend a significant portion of their budget each year on rehabilitating deteriorated bridges. Bridge decks, which inherently exist in an aggressive environment and serve as the roof of the underlying structure, are recognized to deteriorate more rapidly than other elements in the structure. This action constricts the use of the facility and exposes the underlying structure to accelerated degradation. Some of the UHPC-based bridge rehabilitation solutions being considered in North America include UHPC overlays, UHPC link slabs to rehabilitate deteriorated expansion joints, UHPC encasement to rehabilitate deteriorated steel beams at leaking joints, and pile/column jacketing.

The use of UHPC as a field-applied overlay to rehabilitate a deteriorated reinforced concrete bridge deck is an emerging solution that can potentially afford decades of renewed bridge service without the expense of a full bridge deck replacement (concept illustrated in figure 6). As an overlay material, UHPC can provide both structural strengthening and protection from ingress of

contaminates using a 1 inch (25 mm) to 2 inch (51 mm) layer of material. This minimizes required material volume and can minimize additional dead load on the bridge structure compared with some traditional overlay solutions. The research and development behind this concept was pioneered in Switzerland, and has been deployed on a number of Swiss highway bridges. (Habel, Denarié, and Brühwiler 2007; Noshiravani and Bruhwiler 2013; Brühwiler and Denarié 2013) A notable deployment of this concept was on the 2.1 km-long Chillon viaduct which boarders the shores of Lake Geneva. (Brühwiler et al. 2015)

This concept saw its first deployment in the United States in May 2016 on a three-span reinforced concrete slab bridge location in Brandon, Iowa. This bridge was designed and constructed in the 1960s, and although it has a low average daily traffic (ADT), it carries large trucks with agricultural loads. The bridge deck was beginning to exhibit delamination and spalling along the curbline nearest the deck drains and at each end at the expansion joints. It is likely that the deterioration was related to chloride laden water ingress into the concrete and past the strip seal expansion joints, leading to reinforcement corrosion and freeze-thaw cycle-related distress. Deterioration had progressed to the point that maintenance actions were necessary. A UHPC overlay solution was selected to repair the deteriorated deck. This project was considered a demonstration project for UHPC overlays.

Six months after the overlay was installed, a research team from FHWA TFHRC conducted a field study to assess the bond between the UHPC over and underlying concrete deck. Prior to placing the UHPC overlay, the existing concrete deck was milled to remove poor-quality concrete and provide a roughed surface to enhance bonding. Bond was assessed using the direct tension pull-off test method. (ASTM C1583 / C1583M-13 2013) This test method entails gluing a steel disc on the test surface, and partially coring the deck to create a test sample. A direct tensile load is then applied to the steel disc. If the bond between the overlay material and the substrate is sound, then failure will occur by fracture of the substrate or bonded material. Good bond between the UHPC overlay and the underlying concrete deck was found at all tested locations; additional details from this study can be found in Haber, Munoz, and Graybeal (2017)

In the past, it was not uncommon to construct multi-span bridges with numerous expansion joints located over intermediate piers. These expansion joints often fail to redirect chloride-laden water from the deck, resulting in leakage and the need for continual maintenance of both the joint and the underlying structure. One emerging remediation solution is to eliminate the leaking joint and replace with a field-cast UHPC link slab designed to provide a durable seal without attracting significant structural loads. This solution has been deployed on numerous bridges in the State of New York.

The Connecticut Department of Transportation has been leading efforts to develop a UHPC-based repair solution for deteriorated steel girders through work at the University of Connecticut. (Zmetra 2015) Concepts similar to that shown in figure 7 have been studied through large-scale experimental testing and detailed analytically modelling. Corroded steel is removed from the beams and then short studs are welded to intact steel. A form is then placed around the beam and the UHPC is cast. The UHPC allows for both increased shear resistance of the beam as well as increased bearing resistance at the support. Experimental studies showed that beams end repaired using this concept could meet or exceed their intended capacity at the ultimate limit state.

Lastly, field-cast UHPC has been identified as an emerging solution for upgrading the strength and ductility of superstructure-supporting elements such as driven piles and bridge columns. This concept is illustrated in figure 8, which shows a concrete pile or bridge column employing a UHPC jacket. Traditionally, piles and columns are retrofitted using pre-formed steel jackets, fiber-reinforced polymer sheets, or bulky concrete jackets. Canadian researchers demonstrated that the seismic performance of a bridge column with deficient lap splices in the plastic hinge zone could be significantly improved by UHPC jacketing. (Massicotte, Dagenais, and Garneau 2014) Furthermore, this solution has been deployed in British Columbia on the ON-11 bridge over the Fraser River.

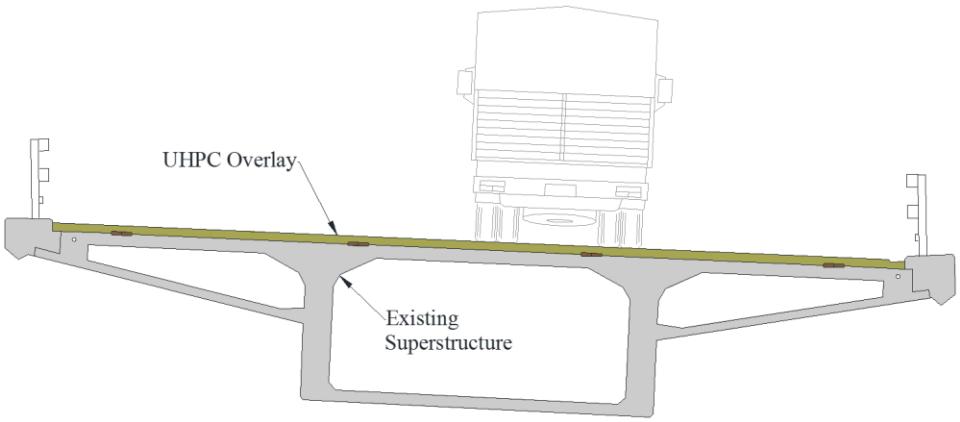

Figure 6. Illustration. Bridge deck overlay using UHPC.

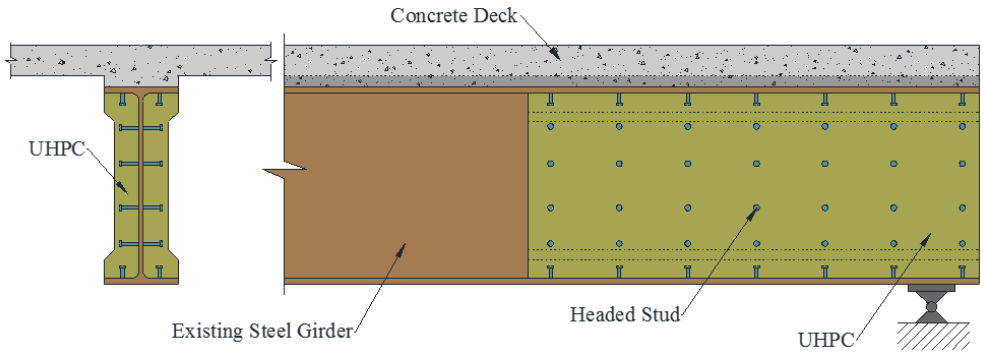

Figure 7. Illustration. Strengthening of an existing steel girder using UHPC encasement.

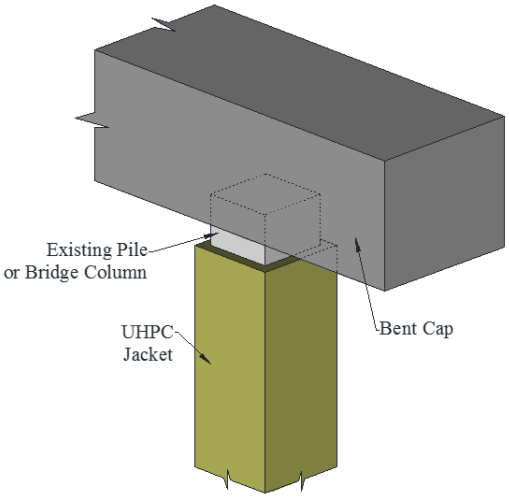

Figure 8. Illustration. Retrofit of an existing pile or bridge column using a UHPC jacket.

100 Percent UHPC Structural Bridge Elements

UHPC's mechanical and durability properties allow for beneficial modifications to conventional concrete bridge component solutions. They also allows for the development of structural components, previously deemed impractical. Using UHPC, prestressed girders and decked girder systems can be developed with an emphasis on addressing important transportation infrastructure issues such as creating longer lasting bridges through enhanced durability or allowing for longer spans with shallower, lighter weight superstructures.

In all the cases where 100 percent UHPC structural bridge elements have been used in North America, UHPC elements have been precast. Opening in 2006, the Mars Hill Bridge was the first vehicular bridge in the United States to use UHPC. This 110 foot (33.5 m) span bridge was originally designed using conventional concrete prestressed girders, and was planned to be a 3-span structure with two intermediate piers. Using the enhanced material properties of UHPC, the bridge could be constructed as a single span with 3 supporting girders at a 9.5-foot (2.7-meter) spacing. The original girder, an Iowa 45 inch (1143 mm) deep bulb tee, was optimized to more efficiently make use of UHPC's enhanced properties. The resulting girder was shallower and was 25 percent lighter than the original Iowa bulb tee. A comparison of the original and optimized girders is shown in figure 9.

Shown in figure 10, researchers at Iowa State University (ISU) developed a novel precast UHPC H-pile for deep foundations. (Vande Voort, Suleiman, and Sritharan 2008) Using UHPC's high compressive strength, a reduced cross-section could be developed compared with standard prestressed conventional concrete piles without compromising pile strength. The reduced cross-section also improved drivability. Having approximately the same weight as a similarly sized steel pile, the UHPC pile was lighter and easier to handle and transport than traditional concrete piles. The enhanced durability characteristics of UHPC could potentially reduce maintenance costs and help extend the lives of some bridges, particularly those in harsh environments.

Researchers at TFHRC developed and tested a series of innovative 100 percent UHPC pi-shaped girders; herein referred to as "pi-girders." An illustration of these girders is shown in figure 11.

Two generation of girders were tested experimentally and a family of these girders was created through an extensive analytical study using finite-element analysis. (Graybeal 2009b, 2009a; Zhang, Graybeal, and Chen 2013) The pi-girders were developed to specifically leverage the advanced mechanical properties of UHPC. The girders were developed to be light weight and low profile.

In 2008, pi-girders were used to construct the middle span of the Jakway Park Bridge location in Buchanan County, Iowa. (Keierlebar et al. 2010) The bridge was 115 feet, 4 inches (35.2 meters) long and 24 feet, 9 inches (7.5 meters) wide, and serviced two lane of traffic. The middle span of the bridge measured 51 feet, 2 inches (15.6 meters) long and was constructed using three 33-inch (838-mm) deep pi-girders. As of 2016, the bridge is still in service and has exhibited good performance.

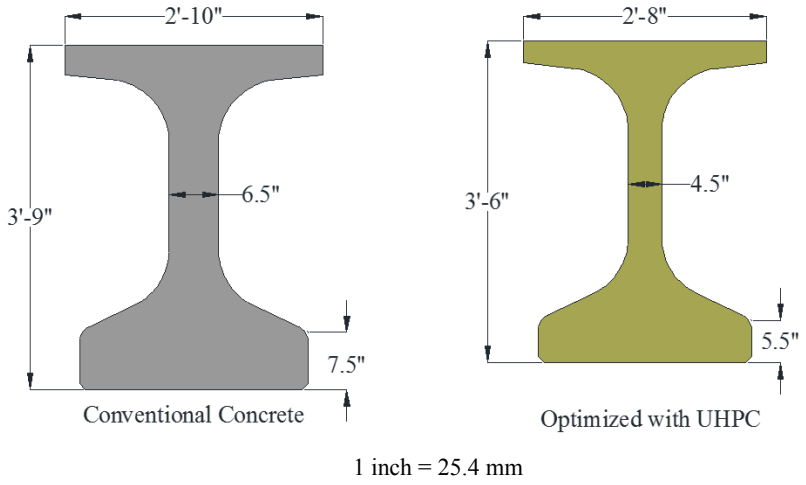

Figure 9. Illustration. Comparison of prestressed bridge girders for the Mars Hill Bridge composed of conventional concrete and optimized with UHPC.

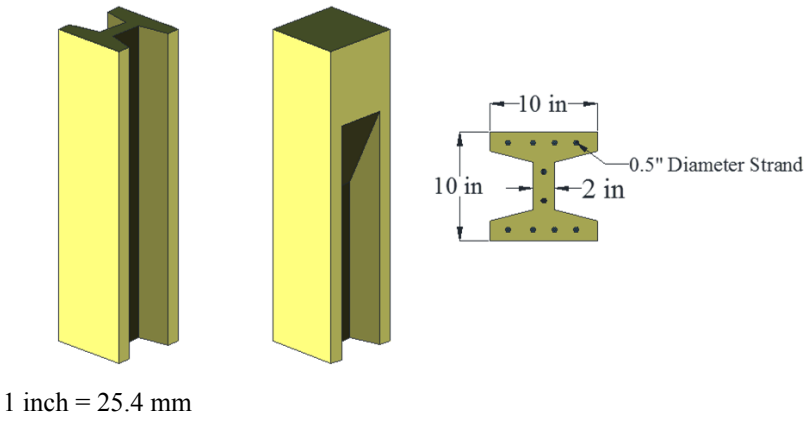

Figure 10. Illustration. Precast, prestressed UHPC H-piles.

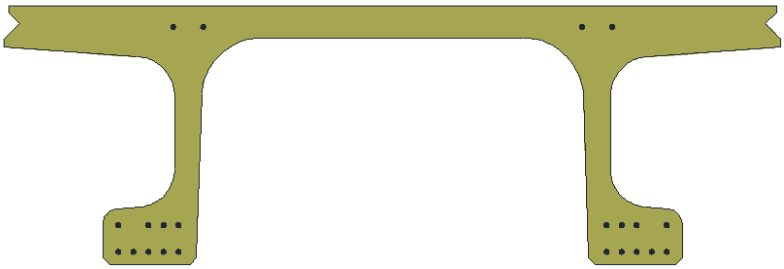

Figure 11. Illustration. Precast, prestressed UHPC pi-girder element.

OBJECTIVE AND REPORT OUTLINE

The objective of this research was to evaluate the materials properties and behavior of different commercially available UHPC-class materials. Emphasis was placed on properties relevant to the bridge engineering and design community. Tests were conducted on both material- and component levels. Material-level focused on mechanical and durability properties, and were conducted using standard or slightly modified versions of ASTM test methods, or test methods developed at the FHWA TFHRC. Many of these material-level tests were conducted according to the methods discussed in ASTM C1856 *Standard Practice for Fabricating and Testing Specimens of Ultra-High Performance Concrete. (*ASTM C1856/C1586-17 2017) It should be noted that ASTM C1856 refers to existing practices and test methods and includes modifications to these referenced standards for application to UHPC. Tests at the component-level focused on bond to reinforcing bars and performance in precast bridge deck connections. The report outline presented below lists the focus and contents of each chapter is presented below:

1. ***Chapter 2 – Materials:*** This chapter describes the materials tested in this study and includes the following:
    - Material mix design.
    - Fiber reinforcement geometry and properties.
    - Chemical admixtures.
2. ***Chapter 3 – Batching and Placement:*** This chapter describes the batching, mixing, and placement procedures and reports some fresh properties of each material. The chapter includes the following for each material:
    - Batching procedures.
    - Description of the mixers used.
    - Mixing procedures and mixing timeline.
    - Placement and curing procedures per specimen type.

- Workability as determined by ASTM C1437 using the modifications described in ASTM C1856. (ASTM C1437-15 2015; ASTM C1856/C1586-17 2017)

- Setting time as determined by ASTM C403. (ASTM C403 / C403M-08 2008, 403)

3. ***Chapter 4 – Mechanical Properties:*** This chapter presents the mechanical properties of the different UHPC-class materials. It has three different focal areas: behavior under compressive loading, behavior under tensile loading, and bond strength between UHPC and precast concrete. The chapter discusses specimen preparation, test methods and test results for the following properties tests:

    - Compressive Strength per ASTM C39 using the modifications described in ASTM C1856. (ASTM C39 / C39M-16b 2016, 39; ASTM C1856/C1586-17 2017, 18)

    - Modulus of elasticity and Poisson's ratio per ASTM C469 using the modifications described in ASTM C1856. (ASTM C469 / C469M-14 2014, 469; ASTM C1856/C1586-17 2017)

    - Compressive Stress-Strain Response.

    - Direct tension behavior according to the methods described by Graybeal and Baby (2013).

    - Indirect tensile behavior per ASTM C496. (ASTM C496 / C496M-11 2004, 4)

    - Interface bond strength between UHPC and precast concrete tested per ASTM C1583 and a modified test based on ASTM 78. (ASTM C1583 / C1583M-13 2013; ASTM C78 / C78M-16 2016)

4. ***Chapter 5 – Creep and Shrinkage:*** This chapter covers compressive creep, drying and autogenous shrinkage, and fresh volume deformations of the different UHPCs. The following tests are included:

    - Compressive creep determined using ASTM C512; however, the loads applied to specimens were modified slightly. (ASTM C512-15 2015, 5)

    - Autogenous and drying shrinkage determined by ASTM C157 using the modifications described in ASTM C1856. (ASTM C157-08 2008; ASTM C1856/C1586-17 2017)

    - Fresh volume deformation per ASTM C827. (ASTM C827-16 2016)

5. ***Chapter 6 – Durability:*** This chapter discusses tests and test results associated with durability and includes the following:

    - Rapid chloride ion penetration tested (RCPT) according to ASTM C1202 using the modifications described in ASTM C1856. (ASTM C1202-12 2012; ASTM C1856/C1586-17 2017)

- Surface resistivity tested according to AASHTO TP 95. (AASHTO TP 95 2014)

- Freeze-thaw resistance tested according to ASTM C666 using the modifications described in ASTM C1856. (ASTM C666-15 2015; ASTM C1856/C1586-17 2017)

6. ***Chapter 7 – Structural Performance:*** This chapter focuses on how the different UHPC-class materials perform at the structural- or component-level. Two sets of tests are included:

    - Bond of reinforcing steel to UHPC tested using the methods described by Yuan and Graybeal (2014).

    - Performance of UHPC in prefabricated bridge deck connections.

7. ***Chapter 8 – Summary and Conclusions:*** This chapter summarizes the research presented and provides some overarching conclusions to the work.

CHAPTER 2. MATERIALS

INTRODUCTION

This chapter introduces the six different commercially-available UHPC-class materials investigated in this study. The nomenclature, which is used throughout the document, is presented first. The subsequent sections provide a detailed description of each UHPC material, and the associated mix designs, respectively. The final section in this chapter presents a concise summary of the six materials.

NOMENCLATURE

Table 1 presents the nomenclature used throughout the report. Each UHPC was given a text, color, and geometric identifier; color and geometric identifiers are primarily employed in the presentation results.

Table 1. Nomenclature used to identify the six UHPC-class materials.

Text Identification	Color Identification	Geometric Identification
U-A	Black	●
U-B	Purple	■
U-C	Green	▲
U-D	Red	◆
U-E	Blue	✖
U-F	Orange	○

MATERIAL DESCRIPTIONS

The mix proportions presented in the following subsections are those recommended by the UHPC suppliers. The research team also investigated UHPC mixtures with fiber volume fractions that differed from those recommended by the suppliers. Of specific interest were mixtures with 2 percent fiber by volume, which is the fiber volume fraction commonly used in UHPC mixtures deployed on highway bridge projects in the United States. The Summary section at the end of the chapter presents the mix proportions for different fiber volume fractions.

Material U-A

Material U-A is a UHPC-class material that was laboratory developed in the United States and has seven material constituents. Specifically, it contains Class H oil well cement, fine silica sand,

finely ground quartz flour, amorphous micro-silica (silica fume), a polycarboxylate-type superplasticizer, steel fiber reinforcement, and water. Unlike the other UHPC-class materials tested in this study, the powder constituents of U-A were not pre-blended. That is, each powder solid was individually packaged and was not necessarily supplied by the same manufacturer. These materials had to be batched, and blended on-site at TFHRC; batching and blending was carried out prior to mixing individual batches of U-A, and is described in greater detail in Chapter 3.

The steel fiber reinforcement used in U-A is pictured in figure 12. These fibers were delivered in 44-lb (20 kg) bags. As shown in figure 12, the fibers came in soluble adhesive-bonded fiber bundles. During the mixing process, this adhesive dissolves and the fibers are allowed to individually disburse. The fibers had a nominal length of 1.18 inches (30 mm), a nominal diameter of approximately 0.022 inches (0.55 mm), and were deformed at each end. The tensile strength for the steel fibers was reported by the manufacturer to be 160 ksi (1,100 MPa).

Table 2 lists the developer recommended mix proportions for U-A. The developer recommended a 3 percent fiber volume fraction be used.

Figure 12. Photo. Photo of the steel fiber reinforcement used in U-A.

Table 2. Recommended mix proportions for U-A.

Constituent	lb / yd^3	kg / m^3	Percentage by Weight
Cement	1,328	788	31.5
Silica Sand	1,288	764	30.5
Ground Quartz	367	218	8.7
Silica Fume	518	307	12.3
Superplasticizer	23	14	0.5
Water	278	165	6.6
Steel Fibers*	416	247	9.9

* 3 percent fibers by volume

Material U-B

Material U-B is proprietary UHPC-class material obtained from a European supplier. This product had three primary constituents that were supplied by the manufacturer: a pre-blended, pre-bagged powder mix containing all of the solids (with the exception of fibers); a commercially-available superplasticizer, and steel fiber reinforcement. The dry powder constituents were delivered in 55-lb (25-kg) bags, and the steel fiber reinforcement was delivered in 44-lb (20-kg) cardboard boxes. The steel fiber reinforcement used in U-B is pictured in figure 13. U-B employed fibers with two different lengths, but similar mechanical properties. The "long" fibers had a nominal length of 0.79 inches (20 mm) and a nominal diameter of 0.012 inches (0.3 mm). The "short" fibers had a nominal length of 0.5 inches (13 mm) and a nominal diameter of 0.012 inches (0.3 mm). The tensile strength of the fibers, as reported by the manufacturer, was greater than 305 ksi (2,100 MPa).

Table 3 lists the supplier recommended mix proportions for U-B. The supplier recommended a 2 percent fiber volume fraction.

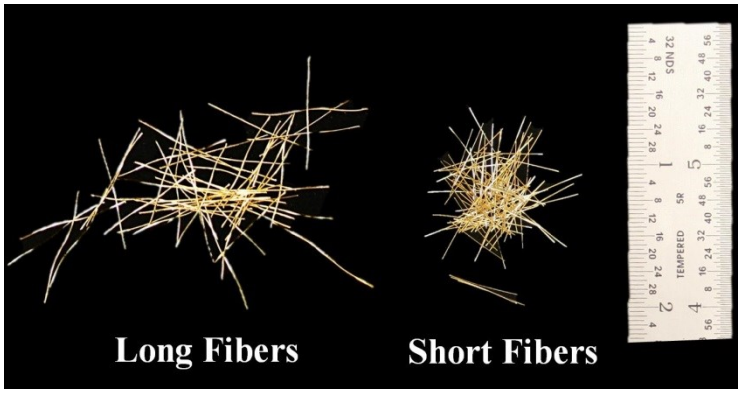

Figure 13. Photo. of the steel fiber reinforcement used in U-B.

Table 3. Recommended mix proportions for U-B.

Constituent	lb / yd^3	kg / m^3	Percentage by Weight
Pre-Blended, Pre-Bagged Powder	3,516	2,086	84.0
Liquid Admixtures	48	28	1.1
Short, Steel Fibers*	88	52	2.1
Long, Steel Fibers*	179	106	4.3
Water	354	210	8.5

* 2 percent combined fibers by volume

Material U-C

Material U-C is proprietary UHPC-class material obtained from a second European-based supplier. This product had two primary constituents that were supplied by the manufacturer: a pre-blended, pre-bagged powder mix containing all of the solids (with the exception of fibers) and the chemical admixtures such as superplasticizer; and steel fiber reinforcement. The dry powder

constituents were delivered in 52-lb (23.5-kg) bags, and the steel fiber reinforcement was delivered in 44-lb (20-kg) cardboard boxes. The steel fiber reinforcement used in U-C is pictured in figure 14. U-C employed a single type of fiber that had a nominal length of 0.5 inches (13 mm) and a nominal diameter of 0.012 inches (0.3 mm). The minimum tensile strength of the fibers, as reported by the manufacturer, was 348 ksi (2,400 MPa).

Table 4 lists the supplier recommended mix proportions for U-C. The supplier recommended a 4.5 percent fiber volume fraction.

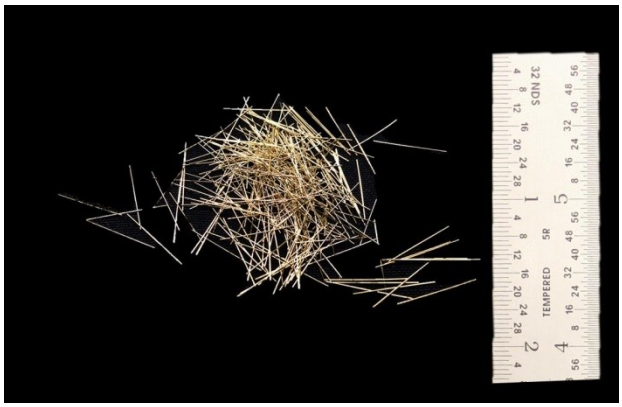

Figure 14. Photo. of the steel fiber reinforcement used in U-C.

Table 4. Recommended mix proportions for U-C.

Constituent	lb / yd^3	kg / m^3	Percentage by Weight
Pre-Blended, Pre-Bagged Powder	3,600	2,136	80.4
Steel Fibers	612	363	13.7
Water	268	159	6.0

* 4.5 percent fibers by volume

Material U-D

Material U-D is proprietary UHPC-class material supplied by the U.S.-based subsidiary of a multinational corporation. This product had five primary constituents that were supplied by the manufacturer: a pre-blended, pre-bagged powder mix containing all of the solids (with the exception of fibers); a modified phosphonate plasticizer; a modified polycarboxylate high-range water-reducing admixture; a non-chloride accelerator; and steel fiber reinforcement. The dry powder constituents were delivered in 50-lb (23-kg) bags, and the steel fiber reinforcement was delivered in 44-lb (20-kg) bags. The steel fiber reinforcement used in U-D is pictured in figure 15. U-D employed a single type of fiber that had a nominal length of 0.5 inches (13 mm) and a nominal diameter of 0.008 inches (0.2 mm). The tensile strength of the fibers, as reported by the manufacturer, was 399 ksi (3,750 MPa).

Table 5 lists the supplier recommended mix proportions for U-D. The supplier recommended a 2 percent fiber volume fraction.

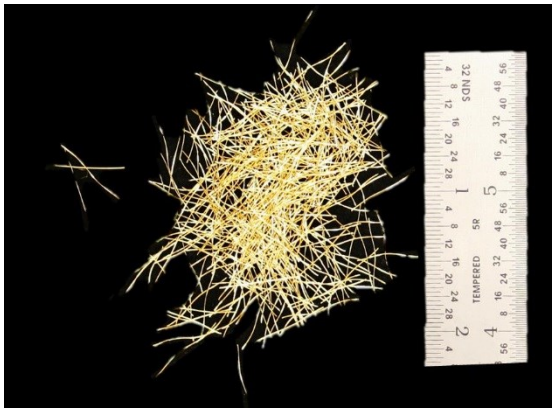

Figure 15. Photo. of the steel fiber reinforcement used in U-D.

Table 5. Recommended mix proportions for U-D.

Constituent	lb / yd^3	kg / m^3	Percentage by Weight
Pre-Blended, Pre-Bagged Powder	3,700	2,195	86.6
Plasticizer	20	12	0.5
Superplasticizer	30	18	0.7
Accelerator	39	23	0.9
Steel Fibers	263	156	6.2
Water	219	130	5.1

* 2 percent fibers by volume

Material U-E

Material U-E is proprietary UHPC-class material originating from Canada and supplied by a U.S.-based subsidiary of a multinational corporation. This product had three primary constituents that were supplied by the manufacturer: a pre-blended, pre-bagged powder mix containing all of the solids (with the exception of fibers); a commercially-available superplasticizer; and steel fiber reinforcement. The dry powder constituents were delivered in 55-lb (25-kg) bags, and the steel fiber reinforcement was delivered in 33-lb (15-kg) bags. The steel fiber reinforcement used in U-E is pictured in figure 16. U-E employed a single type of fiber that had a nominal length of 0.5 inches (13 mm) and a nominal diameter of 0.008 inches (0.2 mm). The tensile strength of the fibers, as reported by the manufacturer, was 399 ksi (3,750 MPa).

Table 6 lists the supplier recommended mix proportions for U-E. The supplier recommended a 2 percent fiber volume fraction.

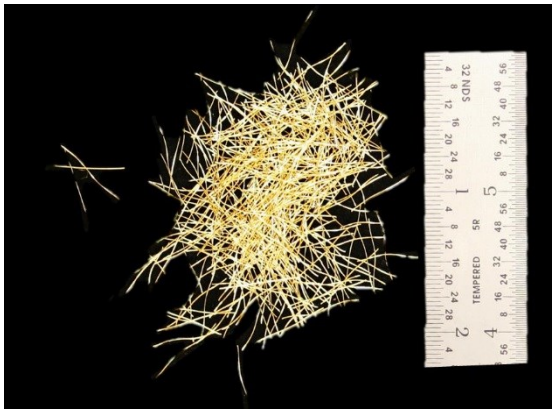

Figure 16. Photo. of the steel fiber reinforcement used in U-E.

Table 6. Recommended mix proportions for U-E.

Constituent	lb / yd^3	kg / m^3	Percentage by Weight
Pre-Blended, Pre-Bagged Powder	3,236	1,920	75.8
Liquid Admixtures	73	43	1.7
Steel Fibers	263	156	6.2
Water	379	225	8.9

* 2 percent fibers by volume

Material U-F

Material U-F is proprietary UHPC-class material originating from Europe. This product was formulated specifically as a structural overlay for highway bridges. The product had four primary constituents that were supplied by the manufacturer: a pre-blended, pre-bagged powder mix containing all of the solids (with the exception of fibers and a powder-based admixture); a modified polycarboxylate high-range water-reducing admixture; a powder-based thickening agent; and steel fiber reinforcement. The dry powder constituents (excluding the thickening agent) were delivered in a single 2-ton (907-kg) supersack, and the steel fiber reinforcement was delivered in 44-lb (20-kg) bags. The steel fiber reinforcement used in U-F is pictured in figure 17. U-F employed a single type of fiber that had a nominal length of 0.5 inches (13 mm) and a nominal diameter of 0.008 inches (0.2 mm). The tensile strength of the fibers, as reported by the manufacturer, was 399 ksi (3,750 MPa).

Table 7 lists the supplier recommended mix proportions for U-F. The supplier recommended a 3.25 percent fiber volume fraction.

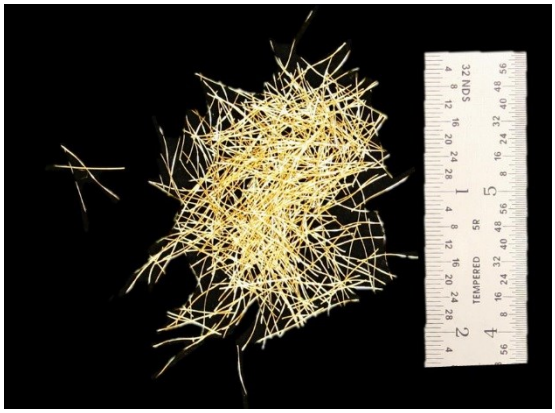

Figure 17. Photo. of the steel fiber reinforcement used in U-F.

Table 7. Recommended mix proportions for U-F.

Constituent	lb / yd^3	kg / m^3	Percentage by Weight
Pre-Blended, Pre-Bagged Powder	3,725	2,210	87.2
Superplasticizer	66	39	1.5
Viscosity Modifying Agent	1.5	0.89	0.035
Steel Fibers	426	253	10.0*
Water	241	143	5.6

* 3.25 percent fibers by volume

SUMMARY

Table 8 provides a comprehensive summary of the different UHPC-class materials, and their respective mix proportions and fiber properties. As mentioned previously, this table shows the fiber quantities required for different fiber volume fractions. The supplier-recommended fiber volume fraction quantities are shown in bold.

Table 8. Summary of mix proportions, and fiber reinforcement properties.

ID		U-A		U-B		U-C		U-D		U-E		U-F	
Mix Design		lb/yd^3	(kg/m^3)	lb/yd^3	(kg/m^3)	lb/yd^3	(kg/m^3)	lb/yd^3	(kg/m^3)	lb/yd^3	(kg/m^3)	lb/yd^3	(kg/m^3)
Pre-blended dry powders		3503[†]	(2078)[†]	3516	(2086)	3600	(2136)	3700	(2195)	3236	(1920)	3725	(2210)
Water		278	(165)	354	(210)	268	(159)	219	(130)	379	(225)	241	(143)
Chemical admixtures	Liquid	23	(13.7)	48	(28.7)	na		89[††]	(53)[††]	73	(44)	65.7	(39)
	Solid	na		na		preblended[*]		na		na		1.5	(0.89)
		Short / Long Fibers											
Steel fiber content (Percent)	2	277	(126)	**88 / 179**	**(52 / 106)**	272	(123.6)	**263**	**(156)**	**263**	**(156)**	284	(168)
	3	**416**	**(247)**	132 / 269	(78 / 159)	408	(242)	395	(234)	395	(234)	**-**	**-**
	3.25	-	-	-	-	-	-	-	-	-	-	**426**	**(253)**
	4	554	(329)	176 / 358	(104 / 212)	544	(323)	526	(312)	526	(312)	568	(337)
	4.50	623	(370)	198 / 403	(117 / 239)	**612**	**(363)**	592	(351)	592	(351)	639	(379)
Steel Fiber		Short / Long Fibers											
Tensile strength, ksi (MPa)		160 (1100)[‡]		≥305 (2100)		348 (2400)		399 (3750)		399 (3750)		399 (3750)	
Length, in (mm)		1.18 (30)[‡]		0.5 (13) / 0.79 (20)		0.5 (13)		0.5 (13)		0.5 (13)		0.5 (13)	
Diameter, in (mm)		0.022 (0.55)[‡]		0.012 (0.3)		0.012 (0.3)		0.008 (0.2)		0.008 (0.2)		0.008 (0.2)	

[†] = Not pre-blended but come in as separate ingredients, which include fine silica sand, finely ground quartz flour, portland cement, and amorphous micro-silica

[*] = The chemical admixtures were dry powders and pre-blended with other powder ingredients

[††] = It includes three chemicals, a modified phosphonate plasticizer, a modified polycarboxylate high-range water-reducing admixture, and a non-chloride accelerator

[‡] = Fibers were straight with hooked ends and did not have a brass coating

na = Not applicable

CHAPTER 3. MIXING, PLACEMENT, AND FRESH PROPERTIES

INTRODUCTION

This chapter covers batching, mixing, placement and curing of the UHPC materials used in this study. The flow of each UHPC batch was measured prior to placing the material in molds or forms and average results from those measurements are presented. Also, the initial and final setting times for the UHPC materials were measured and are presented.

BATCHING

Batching of the UHPC constituents either took place in the FHWA TFHRC concrete laboratory or the FHWA TFHRC large-scale structural testing laboratory. Batch sizes ranged from 0.5 ft^3 – 4 ft^3 (0.014 m^3 – 0.11 m^3) depending on the type and quantity of specimens being cast. Although there were some subtle differences, the general batching procedure for each UHPC-class material was the same. All UHPC constituents were proportioned by weight using a digital scale according to the proportions discussed in Chapter 2.

During the batching process, the powder-based materials were proportioned first. The powder constituents of U-B, U-C, U-D, and U-E were pre-blended and delivered in approximately 55-lb (25-kg) bags. The powder constituents of these materials would typically be proportioned by bag count. However, it was found that nominal bag (printed) weight, and the measured weight differed slightly. Thus, prior to batching, the bag weight was validated using a digital scale. The powder-based constituents of U-A were not pre-blended or pre-bagged. Thus, each powder-based material (cement, sand, silica fume, etc.) was batched individually using 5-gallon (19-liter) buckets and a digital scale; these constituents were not combined until the mixing procedure commenced. The powder constituents of U-F, with the exception of the powder-based admixture, were pre-blended and were delivered in a supersack. During batching, the pre-blended U-F powder was transferred to 5-gallon (19-liter) buckets and weighed. The fibers for each UHPC-class material were delivered in sturdy, plastic-lined paper bags or cardboard boxes, and were batched using 5-gallon (19-liter) buckets. The chemical admixtures were also batched in 5-gallon (19-liter) buckets, unless the quantities were small. Smaller quantities would be batched in a small plastic cup. The required water was the last constituent to be batched, and was batched no more than 30 minutes prior to commencing the mixing operations. This was completed last to reduced potential evaporation of mix water.

MIXING

UHPC was mixed in one of three different mixers depending on batch size. UHPC requires more mixing energy than conventional concrete. Thus, the maximum volume of UHPC mixed in each mixer was significantly reduced compared with the printed or recommended capacity used for mixing conventional concrete. For smaller batches, less than 0.75 ft^3 (0.021 m^3), a bowl and paddle mixer with planetary action was used (figure 18). For median-sized batches, between 0.75 ft^3 (0.021 m^3) and 1.0 ft^3 (0.028 m^3), a 1934 vintage pan mixer was used (figure 19). This mixer is somewhat underpowered for mixing UHPC, resulting in extended mix times compared with the other two mixers. Regardless, this mixer was able to impart enough energy into the mix to obtain sufficient rheology for the casting of laboratory specimens. For larger batches, between 1.1 ft^3

(0.031 m^3) and 4 ft^3 (0.11 m^3), a large pan-style mixer with orbital mixing action was used (figure 20). This mixer is similar, although much smaller, than those commonly used for field-cast UHPC projects.

Figure 18. Photo. Planetary bowl and paddle mixer for UHPC batches up to 0.75 ft^3 (0.02 m^3).

Figure 19. Photo. Small pan-style mixer for UHPC batches up to 1.0 ft^3 (0.028 m^3).

Figure 20. Photo. Large pan-style mixer with orbital mixing action for UHPC batches up to 4.0 ft^3 (0.11 m^3).

Each manufacturer had unique mixing procedure for UHPC. Although each mixing procedure was unique, in general, there were a number of key steps common to each mixing procedure. First, most suppliers recommend that the powder constituents be added to the mixer, and pre-mixed for a short period of time prior to the addition of any liquid constituents such as water or admixtures. A short period of pre-mixing allows for any potential segregated solids to be re-incorporated homogeneously throughout the powder-based materials. Second, it is usually recommended that water and a portion (if not all) of the liquid admixtures be slowly introduced into the mixer while the mixer blades are turning. This is to allow a better initial distribution of water throughout the mix. Third, after addition of liquids, there is an extended mixing-only period between 4 and 8 minutes (minimum) in length, but in practice can be as long at 10 to 15 minutes. During this time, water and chemical admixtures are being thoroughly incorporated, and the mixture should slowly change into a thick (i.e., viscous), fluid-like paste. Once the mixture has "turned over" to a fluid-like paste, fibers are slowly added over the course of 1 to 2 minutes. Once the fibers are added, it is suggested that the mixer turns for a short, additional time period to ensure that the fibers are uniformly distributed.

The mixing procedures provided by the UHPC suppliers were reviewed by the research team, and may have been modified slightly to facilitate mixing at TFHRC. Table 9 through table 14 list the mixing procedures used by the research team for materials U-A through U-F, respectively. Each table provides the minimum time required to complete a given step in the mixing process and minimum cumulative time elapsed. It is noted that the time required to complete a given mixing step could vary depending on the mixer, laboratory temperature, and a number of other factors.

Figure 21 compares the mixing procedures of the six different UHPC-class materials; the steps have been somewhat generalized. This figure illustrates the similarity between the different mixing procedures, and the suggested time frames for each step.

Table 9. Mixing procedure for U-A.

Step	Description	Time per Step (min)	Cumulative Time (min)
1	Place powder constituents into mixer	0	0
2	Turn on mixer, and mix powder constituents for 2 minutes	2	2
3	Add water and liquid admixtures over the course of 1.5 minutes	1.5	3.5
4	Mix for a minimum of 6 minutes, once paste-like mix for an additional 2 minutes	8	11.5
5	Add fibers into the mixture over the course of 1.5 minute	1.5	13
6	Continue mixing for an additional 4 minutes after addition of fibers	4	17

Table 10. Mixing procedure for U-B.

Step	Description	Time per Step (min)	Cumulative Time (min)
1	Place powder constituents into mixer	0	0
2	Turn on mixer, and mix powder constituents for 1 minute	1	1
3	Add water and liquid admixtures over the course of 1.5 minutes	1.5	2.5
4	Mix for a minimum of 4 minutes, once paste-like mix for an additional 2 minutes	6	8.5
5	Add short fibers into the mixture over the course of 1 minute	1	9.5
6	Add long fibers into the mixture over the course of 1.5 minutes	1.5	11
7	Continue mixing for an additional 5.5 minutes after addition of fibers	5.5	16.5

Table 11. Mixing procedure for U-C.

Step	Description	Time per Step (min)	Cumulative Time (min)
1	Place powder constituents into mixers	0	0
2	Turn on mixer, and mix powder constituents for 1 minute	1	1
3	Add water over the course of 1.5 minutes	1.5	2.5
4	Mix for a minimum of 4 minutes, once paste-like mix for an additional 2 minutes	6	8.5
5	Add fibers into the mixture over the course of 1.5 minute	1.5	10
6	Continue mixing for an additional 2.5 minutes after addition of fibers	2.5	12.5

Table 12. Mixing procedure for U-D.

Step	Description	Time per Step (min)	Cumulative Time (min)
1	Place powder constituents into mixer	0	0
2	Turn on mixer and add water and superplasticizer over the course of 2 minutes	2	2
3	Mix for an additional 5 minutes	5	7
4	Add additional liquid admixture over the course of 1 minute	1	8
5	Mix for an additional 2.5 minutes	2.5	10.5
6	Add fibers into the mixture over the course of 2 minute	2	12.5
7	Continue mixing for an additional 1 minute after addition of fibers	1	13.5

Table 13. Mixing procedure for U-E.

Step	Description	Time per Step (min)	Cumulative Time (min)
1	Place powder constituents into mixer	0	0
2	Turn on mixer, and mix powder constituents for 1 minute	1	1
3	Add 50 percent of the required water over the course of 1 minute	1	2
4	Add the remaining water and superplasticizer over the course of 1 minute	1	3
5	Mix for a minimum of 6 minutes until paste-like	6	9
6	Add fibers into the mixture over the course of 2 minute	2	11
7	Continue mixing for an additional 3 minutes (minimum) after addition of fibers	3	14

Table 14. Mixing procedure for U-F.

Step	Description	Time per Step (min)	Cumulative Time (min)
1	Place powder constituents into mixer	0	0
2	Turn on mixer, and mix powder constituents for 2 minute	2	2
3	Add water and 50 percent of the required liquid admixtures over the course of 1 minute	1	3
4	Mix for an additional 4 minutes	4	7
5	Add the remaining liquid admixture over the course of 1 minute	1	8
6	Mix for an additional 2 minutes	2	10
7	Add fibers into the mixture over the course of 2 minutes	2	12
8	Mix for an additional 2 minutes	1	13
9	Add powder-based admixture over the course of 2 minutes	2	15
10	Mix for an additional 2 minutes	2	17

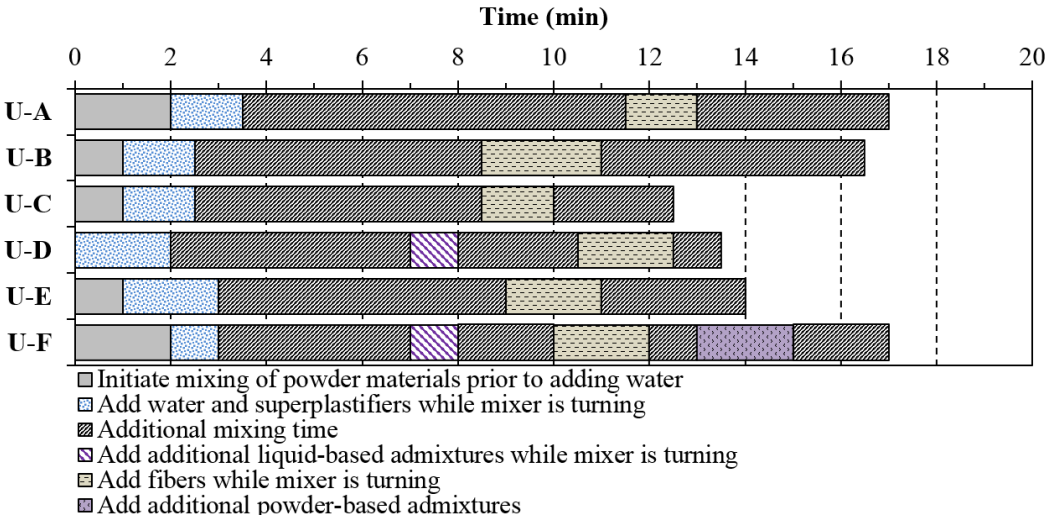

Figure 21. Graph. Comparison of mixing time amongst the six UHPC-class materials.

PLACEMENT AND CURING

A number of different specimen types were used over the course of this research. Unless specifically stated otherwise in a subsequent section or chapter, the following placement and curing procedures were employed. In all cases, UHPC was placed using either a hand-held scoop or a 5-gallon (19-liter) bucket depending on the size of the specimens, and unless noted otherwise, specimens were cured in ambient laboratory conditions at a temperature of 73 ± 3.6 ºF (23 ± 2 ºC) and a relative humidity (RH) of 50 ± 5 percent.

Figure 22 through figure 24 depict UHPC being placed in a series of relatively small specimens. For cylindrical specimens (figure 22), UHPC was placed in a single lift. For smaller, prismatic, beam- or bar-shaped specimens (figure 23), UHPC was poured into the mold at one end and allowed to flow toward the other end. Once filled, cylinders and beam- or bar-like specimens were placed on a concrete vibrating table for 5 to 15 seconds to remove entrapped air. Specimens were subsequently screeded to remove excess material, and sealed using plastic caps or sheet plastic to reduce evaporation. For slab-like specimens (figure 24), such as those used for direct-tension bond testing, UHPC was poured in the center of the specimen and allowed to flow radially until of the form was full.

In deck-level connections regions, which are discussed in Chapter 7, UHPC was placed into one end of the connection and allowed to flow toward the other end until full; shown in figure 25. Lastly, placement of UHPC in rebar bond tests was first poured from one end of the specimen and allowed to flow to the other end until the form was mostly filled. Thereafter, UHPC was poured from various locations to top-off the form. Once filled, the exposed UHPC surfaces in these specimens were then loosely covered with sheet plastic; this is shown in figure 26.

Figure 22. Photo. Placement of UHPC in a cylindrical specimen.

Figure 23. Photo. Placement of UHPC in a prismatic specimen.

Figure 24. Photo. Placement of UHPC topping on interface bond test specimens.

Figure 25. Photo. Placement of UHPC in the connection region of a deck-level connection specimen.

Figure 26. Photo. Curing of UHPC in deck-level connection specimen.

WORKABILITY

Immediately after mixing, the workability properties of fresh UHPC were assessed using ASTM C1437 using the modifications described in ASTM C1856. (ASTM C1437-15 2015; ASTM C1856/C1586-17 2017) This method is otherwise referred to as a flow table test. A photo of the flow table test apparatus is shown in figure 27. Fresh UHPC was poured into the cone-shaped mold, atop a standard 10-in (254-mm) diameter flow table. UHPC was placed in a single lift, and excess material was removed using a small rubber screed bar. With the exception of materials U-C and U-F, which were consolidated using a rubber tamping rod, the UHPC was allowed to self-consolidate. Once filled and screeded, the cone-shaped mold was slowly lifted, and the UHPC material was allowed to flow until no more movement was detected. The diameter of UHPC was then measured along the four lines marked on the table. The average of these initial measurements is referred to as the "static" flow. Subsequently, 20 drops were applied to the table, and the average diameter of UHPC was determined again; this is referred to as the "dynamic" flow.

Figure 28 depicts the average flow table measurements for UHPC with 2-percent fiber by volume with the exception of U-F which had 3-percent fiber by volume. Materials U-B, U-D, and U-E were very flowable, all exhibiting static flows greater than 7 inches (178 mm). Materials U-A, U-C, and U-F exhibited much lower static flows. Given the thixotropic formulation of U-F, this result is not surprising. It should be mentioned that the flow of a UHPC can be adjusted by changing the water content, adjusting the chemical admixtures and mix water temperature, or by adjusting the fiber content. However, these types of modifications to mix proportions or procedure should be carefully considered as they can also affect other properties.

Figure 27. Photo. Flow table apparatus.

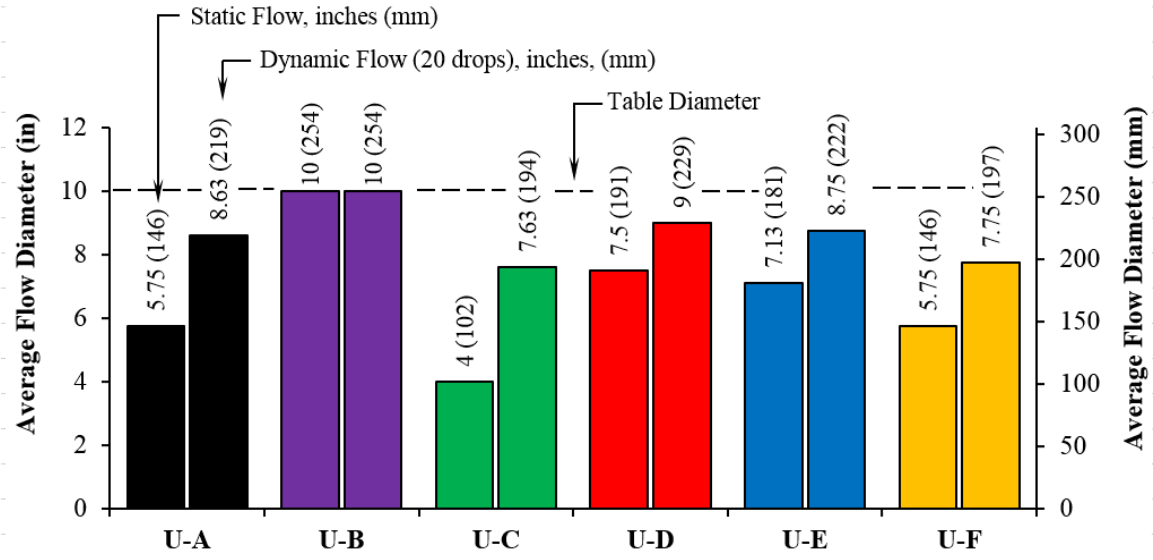

Figure 28. Graph. Average measurements from flow table testing of fresh UHPC.

SET TIME

The setting time of the mixtures was measured according to ASTM C403 (ASTM C403 / C403M-08 2008). The test is based on measuring the pressure force needed to cause a set of standard flat-headed needles to penetrate 1 inch (25.4 cm) into the material being tested, as shown in figure 29. The material is placed in a 6-inch- (152-cm-) diameter by 6-inch- (152-cm-) height cylinder and the top surface is finished with a trowel and covered with a plastic lid to avoid evaporation. The specimens are stored in a controlled environmental room at 73.4 °F ± 1.8 °F (23 °C ± 1 °C) and a RH of 50 ± 5 percent. Readings are taken periodically after placing the material. The initial and

final set tests are determined when pressures of 500 psi (3.45 MPa) and 4,000 psi (27.6 MPa) are reached, respectively.

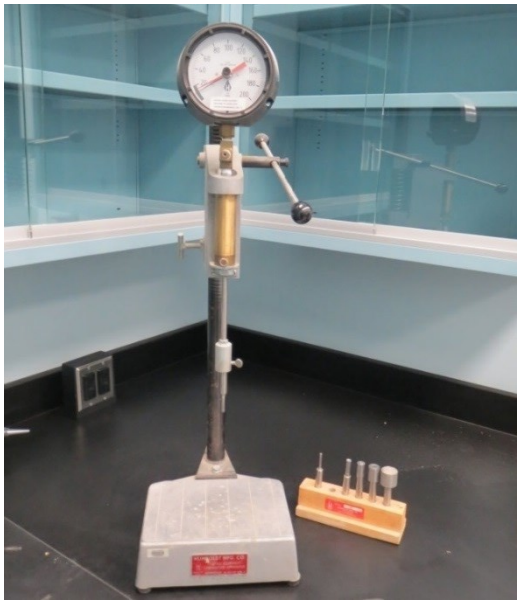

Figure 29. Photo. Setting time loading apparatus and penetration needles.

Figure 30 presents the observed initial and final set times for the six different UHPCs. The setting times for U-F were not determined due to the thixotropic properties of the material; in the fresh state, this material exhibited significant resistance to needle penetration. The setting time values for U-A and U-E could not be accurately measured as they occurred during out of normal operational laboratory hours (i.e., 7am through 4pm). Initial set times ranged from 4.3 to over 9 hours, and final set times ranged from 7 to just under 24 hours.

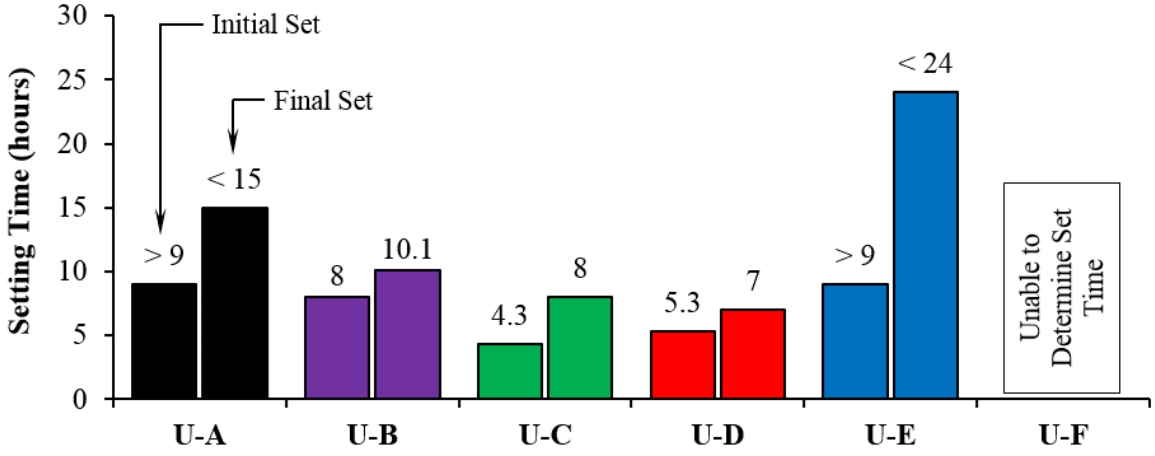

Figure 30. Graph. Observed setting times.

CHAPTER 4. MECHANICAL PROPERTIES

INTRODUCTION

This chapter presents the mechanical properties of the different UHPC-class materials. There were three different focal areas: behavior under compressive loading, behavior under tensile loading, and bond strength between UHPC and precast concrete. The UHPCs were evaluated using two different types of tensile tests: the direct tensile test (DTT) and an indirect split cylinder-type tensile test (SCTT). The subsequent sections describe specimen fabrication, preparation, test methods, instrumentation, and findings.

BEHAVIOR IN COMPRESSION

Test Methods and Specimens Preparation

Compressions tests were conducted using cylinders with a 3-inch (76-mm) nominal diameter and nominal length of 6-inches (152-mm). During casting, each cylinder mold was filled with a single lift of UHPC. Once filled, cylinders were placed on a concrete vibrating table for 5 to 15 seconds to remove entrapped air. The consolidated cylinders were subsequently capped and allowed to cure for 24 hours prior to being stored in the laboratory.

The cylinders were prepared for testing by grinding both ends to create parallel surfaces through the use of a fixed end grinder. After preparation, the cylinders exhibited length to diameter ratios of approximately 1.9. Prior to testing, each cylinder was measured and weighed. Diameter and length measurements were taken at three different locations in order to determine the average geometry of the sample. Average dimensions and the recorded weight were used to calculate each sample's density.

Two tests were carried out on the cylinders: compressive strength, and modulus of elasticity. The compressive strength of UHPC was evaluated according to ASTM C39 using the modifications described in ASTM C1856 (ASTM C39 / C39M-16b 2016), and the modulus of elasticity tests were completed according to and ASTM C469 (ASTM C469 / C469M-14 2014). Both tests used the modifications described in ASTM C1856 which specifies an increased load rate of 150 psi/sec (1 MPa/sec) in order to reduce the required testing time. (ASTM C1856/C1586-17 2017) It was shown by Graybeal 2014c that the loading rate of UHPC in compression could be increased without affecting the compressive strength or elastic modulus test method.

Some of the cylinders were only tested for compressive strength, while others were tested for modulus of elasticity and then immediately thereafter for compressive strength. During modulus of elasticity tests and the subsequent compressive strength tests, the strain readings were electronically captured continuously from the initiation of loading through the application of the peak compressive load. Axial strains were measured using a trio of linear variable displacement transducers (LVDTs) attached to a pair of parallel rings mounted on the cylinder (shown in figure 31); the parallel ring gauge length was 3 inches (76 mm). Circumferential strain was recorded using a chain-type extensometer mounted at the mid-height of the sample (also shown in figure 31).

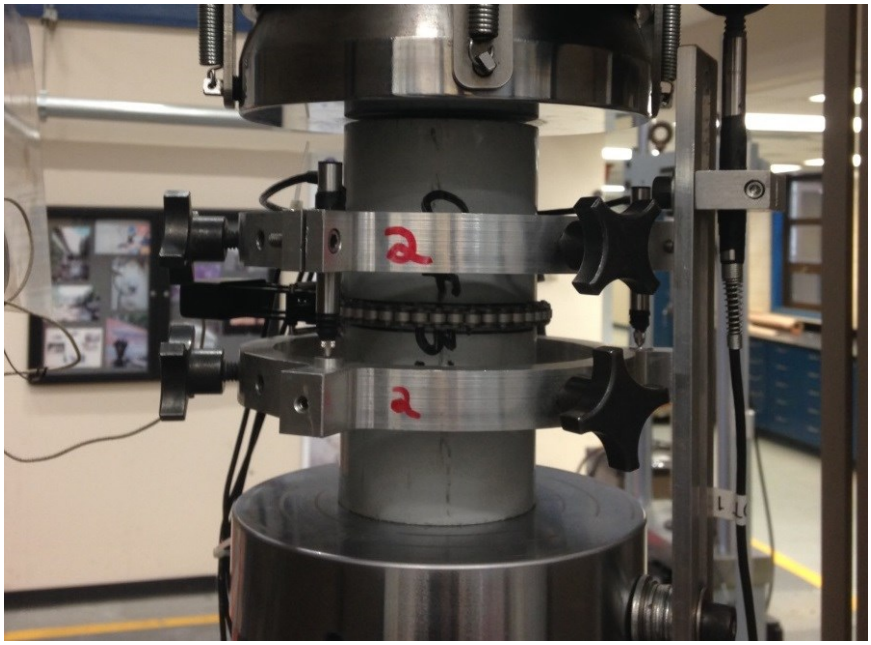

Figure 31. Photo. Test configuration for elastic modulus and Poisson's ratio tests.

Results

Compressive Strength Gain

The compressive strength gain as a function of time is presented in figure 32, figure 33, figure 34, figure 35, and figure 36 for U-A, U-B, U-C, U-D, and U-E, respectively. Compressive strength was determined as the peak compressive stress achieved prior to loss of load bearing capacity. For each UHPC, a series of cylinders were tested with 2-percent fibers by volume, and in some cases additional fiber volume contents were tested. Each data point represents the average of two to five tested samples, and vertical error bars represent ± one standard deviation. Also, each graph shows a curve representing a best-fit natural logarithm trend line.

Figure 37 compares the strength gain behavior of the UHPCs using the trend lines developed for UHPCs with 2.0 percent fiber by volume, which were shown in figure 32 through figure 36. These curves are only presented to provide a comparison between the different UHPCs, and should not be used for strength-gain prediction. In some cases, the best-fit strength gain behavior was forecasted. In general, U-D exhibited the most rapid strength gain which is not unexpected given that this material employs an accelerating admixture. Of the other materials, U-C tended to gain strength the most rapidly, followed by U-B and U-A which both exhibited similar strength gain rates. Lastly of the five UHPCs, U-E exhibited the slowest strength gain rate. Further comparison is provided in table 15, which shows the average compressive strength of the five UHPCs at select ages. For structural applications, it has been suggested that the minimum strength of UHPC should be 14 ksi (96.5 MPa). (Graybeal 2014a) Each of the five UHPC reached 14 ksi (96.5 MPa) within 7 days of casting.

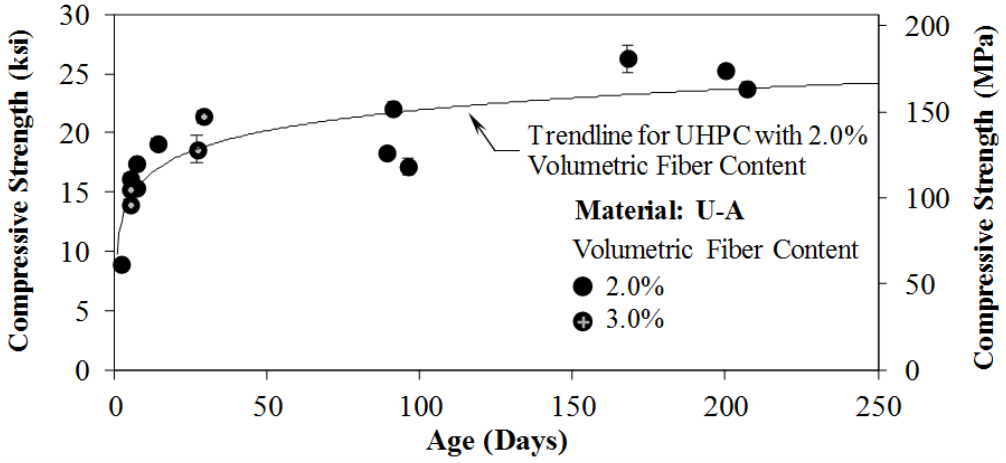

Figure 32. Graph. Compressive strength gain as a function of time for U-A.

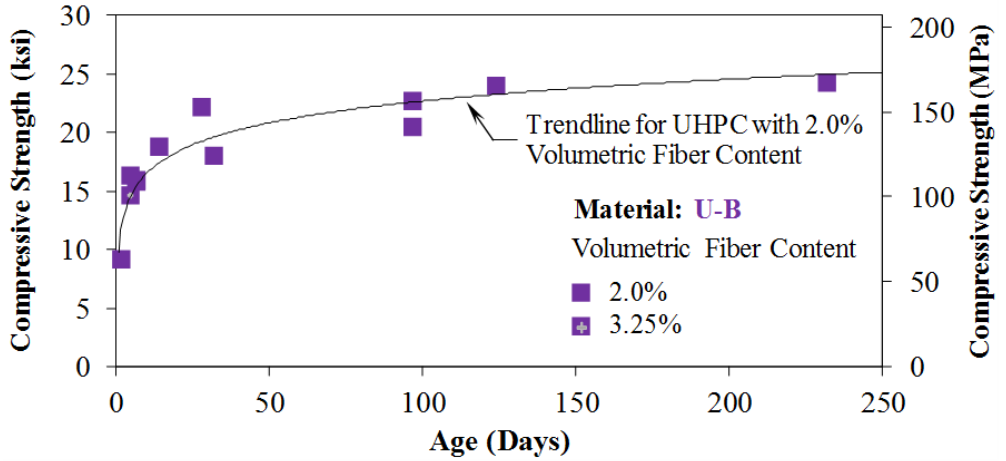

Figure 33. Graph. Compressive strength gain as a function of time for U-B.

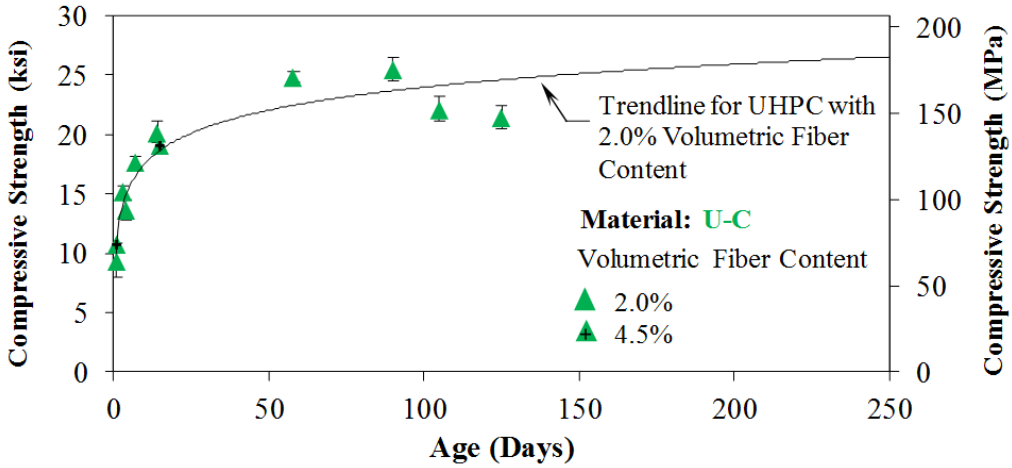

Figure 34. Graph. Compressive strength gain as a function of time for U-C.

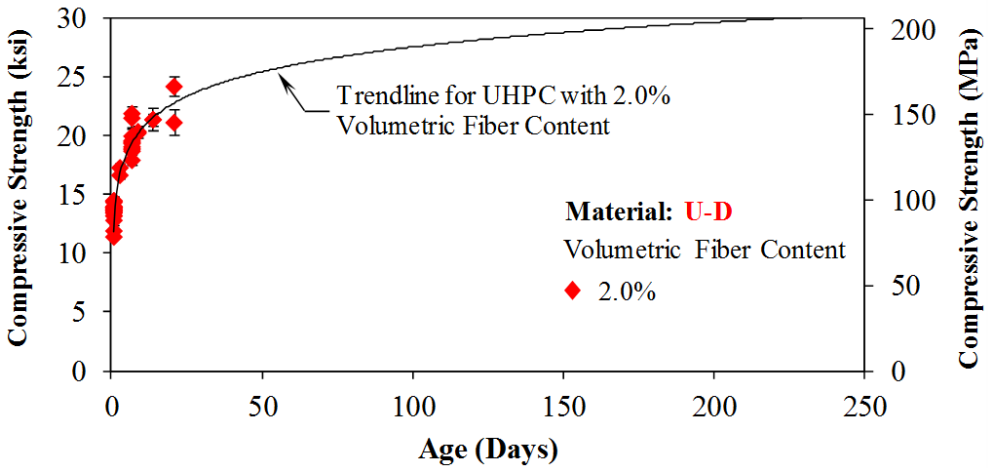

Figure 35. Graph. Compressive strength gain as a function of time for U-D.

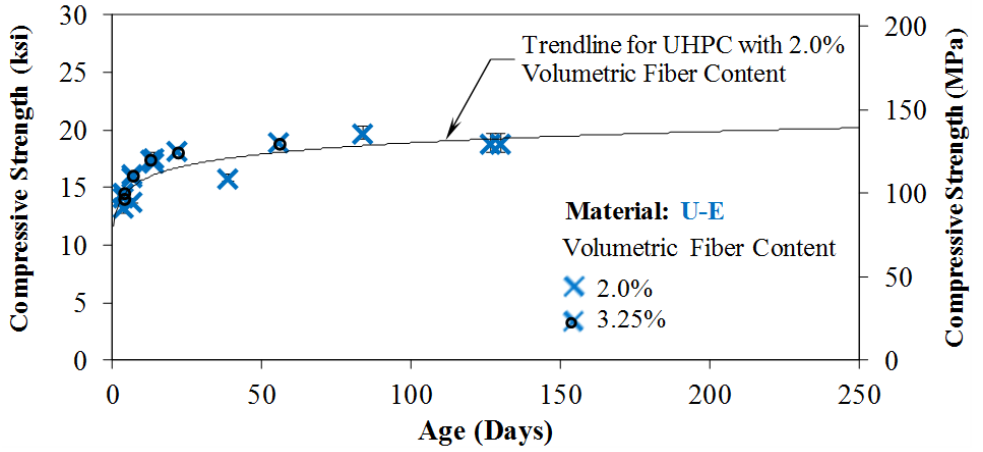

Figure 36. Graph. Compressive strength gain as a function of time for U-E.

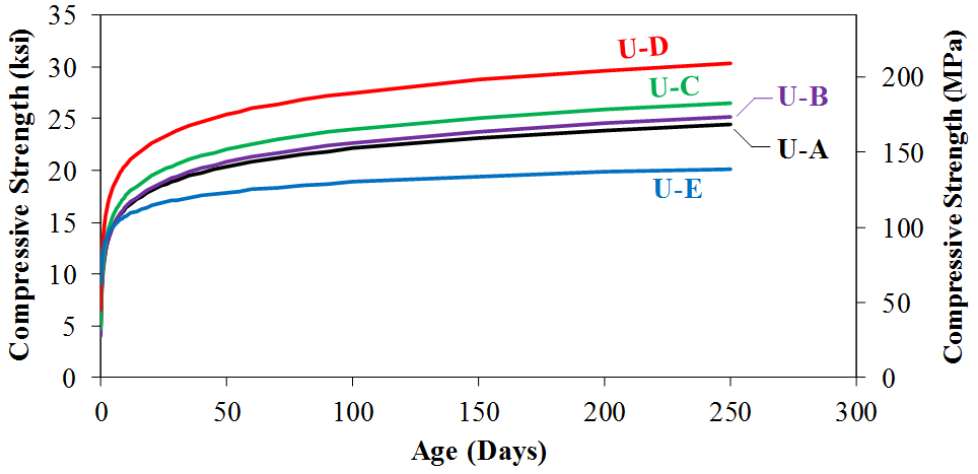

Figure 37. Graph. Compressive strength gain trendlines for UHPCs with 2 percent fiber.

Table 15. Select data from compressive strength gain tests.

Age (days)	Compressive Strength	U-A		U-B		U-C		U-D		U-E	
		ksi	(MPa)	ksi	(MPa)	ksi	(MPa)	ksi	(MPa)	ksi	(MPa)
2	Average	8.95	(61.7)	9.16	(63.1)	-		-		-	
	Standard Deviation	0.21	(1.45)	0.16	(1.10)	-		-		-	
	No. of Samples	3		3		-		-		-	
3	Average	-		-		15.2	(105)	16.9	(117)	-	
	Standard Deviation	-		-		0.51	(3.49)	0.29	(2.00)	-	
	No. of Samples	-		-		3		6		-	
7	Average	17.4	(120)	15.8	(109)	17.7	(122)	19.5	(135)	14.9	(102)
	Standard Deviation	0.20	(1.36)	0.48	(3.33)	0.41	(2.83)	0.44	(3.05)	0.20	(1.35)
	No. of Samples	3		6		3		36		6	
14	Average	19.1	(131)	18.8	(130)	20.2	(139)	21.3	(147)	17.4	(120)
	Standard Deviation	0.44	(3.00)	0.41	(2.85)	0.91	(6.30)	0.72	(4.98)	0.24	(1.68)
	No. of Samples	3		3		3		6		5	

Stress-Strain Behavior

The compressive stress-strain behavior of U-A, U-B, U-C, U-D, and U-E are shown in figure 38 through figure 42, respectively. For each UHPC, a family of curves is shown for UHPC mixtures with a 2 percent fiber volume fraction. Each curve represents the average stress-strain response determined from a set of three cylinder samples tested at a given age; data was truncated at the point of peak compressive stress. As would be expected, as the age of the UHPC increases so does the strength and stiffness of the material. Furthermore, as strength and stiffness increase, the nonlinearity prior to failure tends to decrease. This observation was previously noted by Graybeal (2007), and can also be observed in the data collected by Graybeal and Stone (2012).

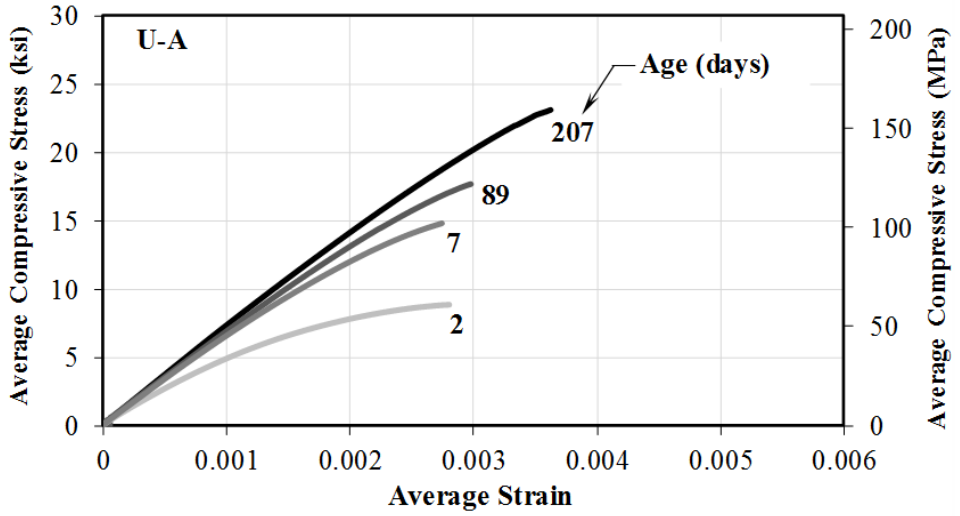

Figure 38. Graph. Compressive stress-strain response of material U-A.

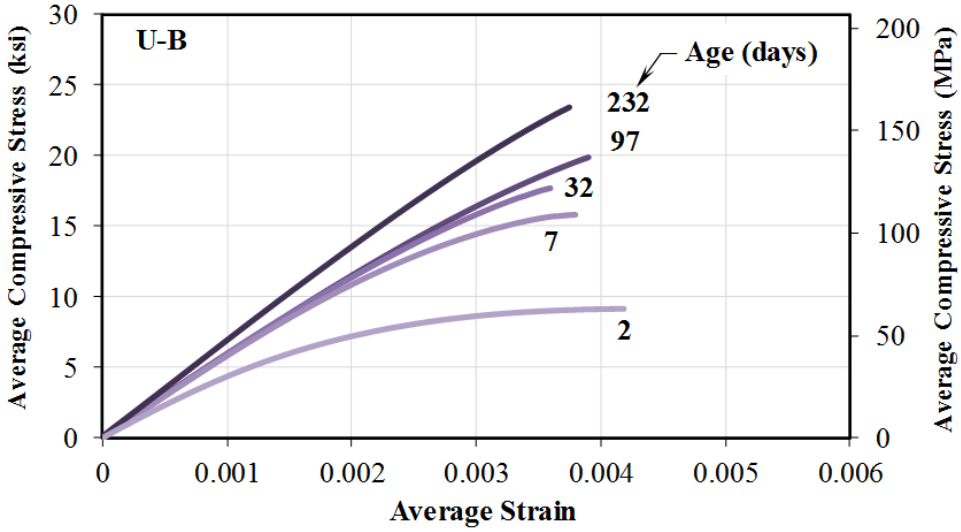

Figure 39. Graph. Compressive stress-strain response of material U-B.

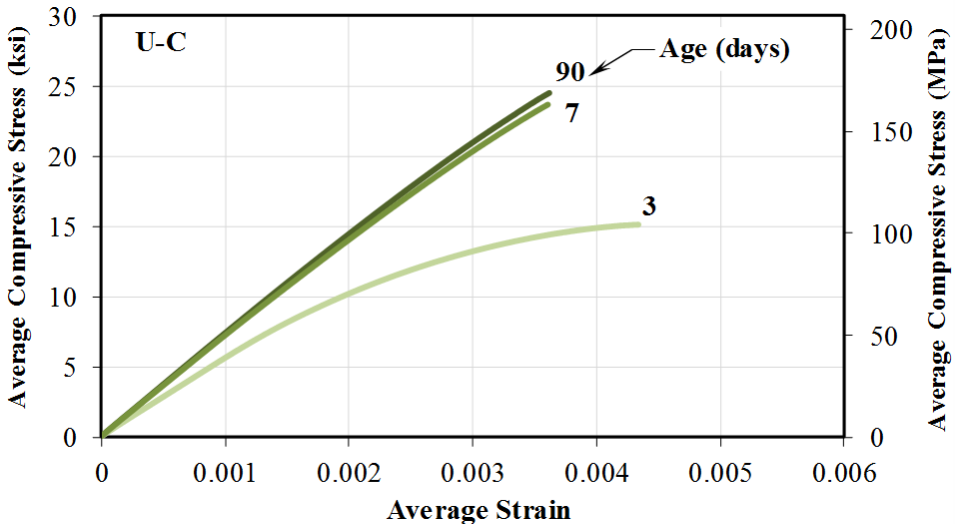

Figure 40. Graph. Compressive stress-strain response of material U-C.

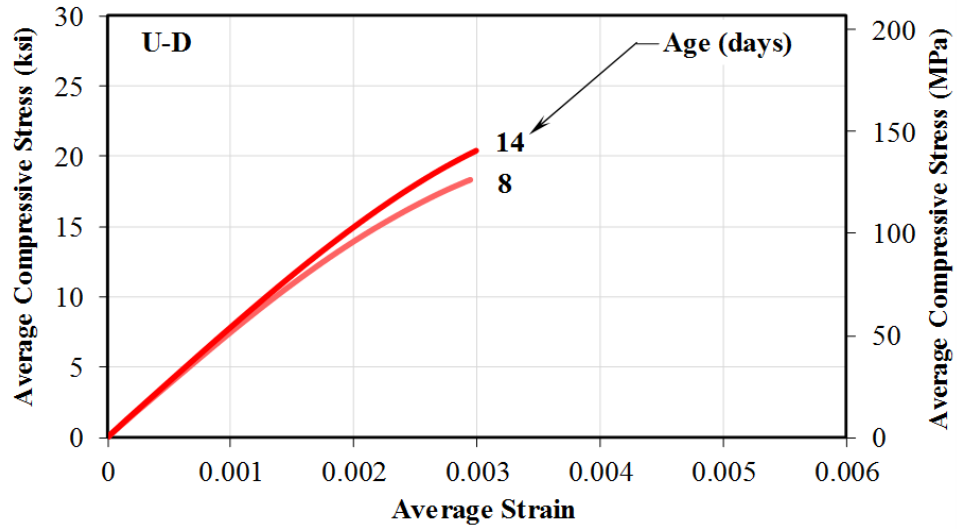

Figure 41. Graph. Compressive stress-strain response of material U-D.

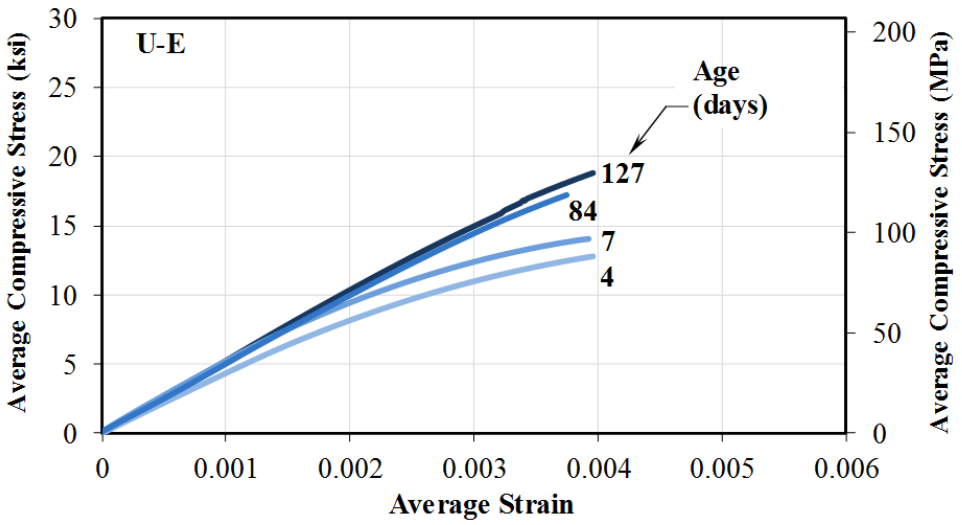

Figure 42. Graph. Compressive stress-strain response of material U-E.

In engineering design, constitutive material models are used to compute stresses and strains within element cross sections. These stresses and strains are subsequently used to determine the moment capacity of the section. As discussed by Graybeal (2007), the stress-strain behavior of UHPC prior to reaching peak compressive stress, f'_c, is approximately linear up to about 50 percent of f'_c. Thereafter, the compressive stress-strain response begins to exhibit softening and thus a non-linear response. The following section examines the linearity of the UHPC compressive stress strain response using the procedure described by Graybeal (2007).

Figure 43 represents the constitutive stress-strain equation for UHPC defined as a function of deviation from the linear elastic response. This expression was first proposed by Graybeal (2007), and has been used in subsequent studies to describe the pre-peak stress-strain response of UHPC. Here the compressive stress, f_c, is defined by the product of the compressive strain, ε_c, the elastic modulus of UHPC, E_c, and one minus the linearity deviation parameter, α. The term α represents the magnitude of how much the actual stress-strain curve deviates from the linear-elastic curve. This concept is illustrated in figure 44, which shows the actual compressive stress-strain behavior of UHPC compared with the linear-elastic response.

The linearity was accessed for $\alpha = 0.01$, 0.03, 0.05, 0.1, and 0.15. Furthermore, an additional point data point was defined for each specimen at the peak stress and corresponding strain or at the final reliable data point prior to reaching the peak compressive stress. For each material, a best-fit curve was used to approximate the relation between α and the normalized compressive strains, which is defined by figure 45. It was found that power function of the form shown in had the best goodness of fit.

$$f_c = \varepsilon_c E_c (1\text{-}\alpha)$$

Figure 43. Equation. Constitutive equation for UHPC in compression defined as a function of deviation from the linear-elastic behavior.

Where

f_c = compressive stress of UHPC

ε_c = compressive strain of UHPC

E_c = compressive elastic modulus of UHPC

α = linearity deviation parameter

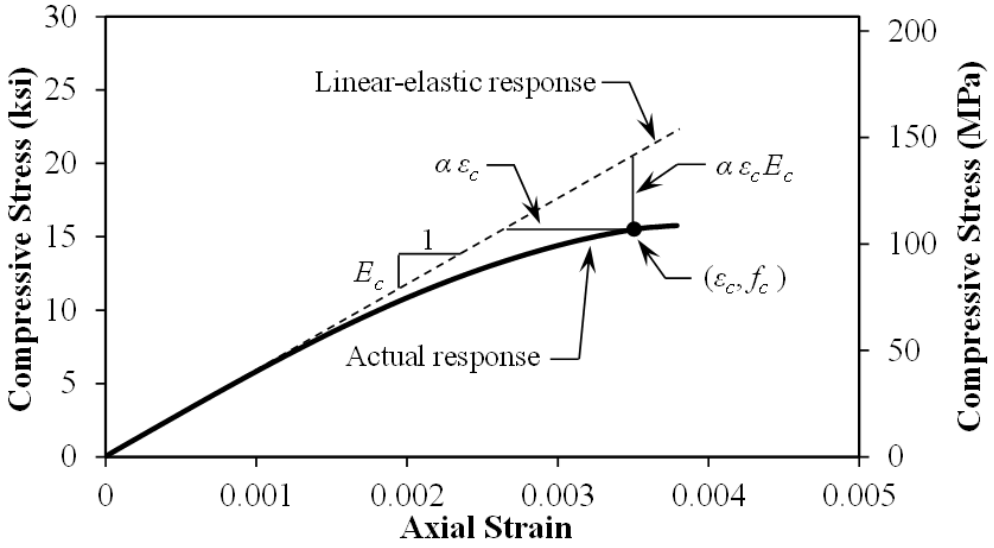

Figure 44. Illustration. Actual compressive stress-strain response of UHPC compared with the linear-elastic behavior.

$$\varepsilon_n = \frac{\varepsilon_c E_c}{f'_c}$$

Figure 45. Equation. Normalized compressive strain.

Where

f'_c = compressive strength of UHPC

ε_c = compressive strain of UHPC

E_c = compressive elastic modulus of UHPC

$$\alpha = a\, x^{b}$$

Figure 46. Equation. General form of the power function used for best-fit curves.

Where

x = the normalized compressive strain as defined by figure 45. Shown as "x" to be consistent with figure 47 through figure 52

a = fit parameter

b = fit parameter

The results from this analysis are presented in figure 47 through figure 52 for materials U-A through U-E, respectively. Figure 52 presents results when the data from all five materials is considered as a single set. The fit parameters for each UHPC are listed in table 16, along with the fit parameters considering all the data collected. By examining the fit coefficients, it can be concluded that the different UHPC exhibited very similar behavior regarding stress-strain linearity.

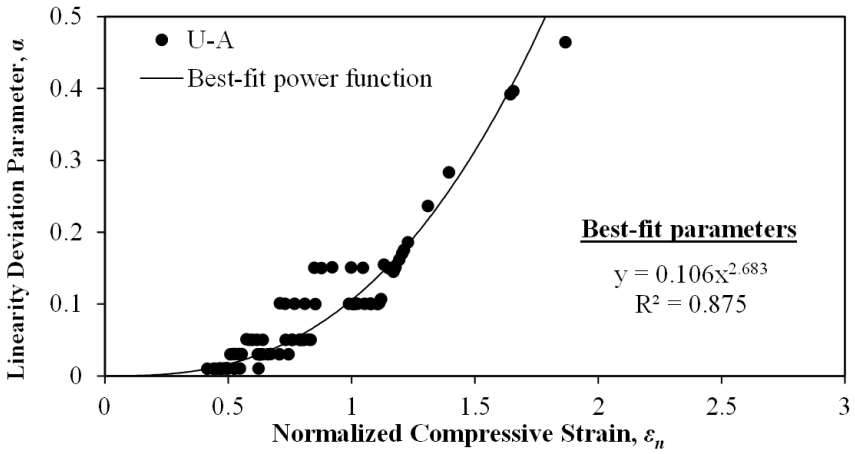

Figure 47. Graph. Deviation from the linear elastic compressive behavior for U-A.

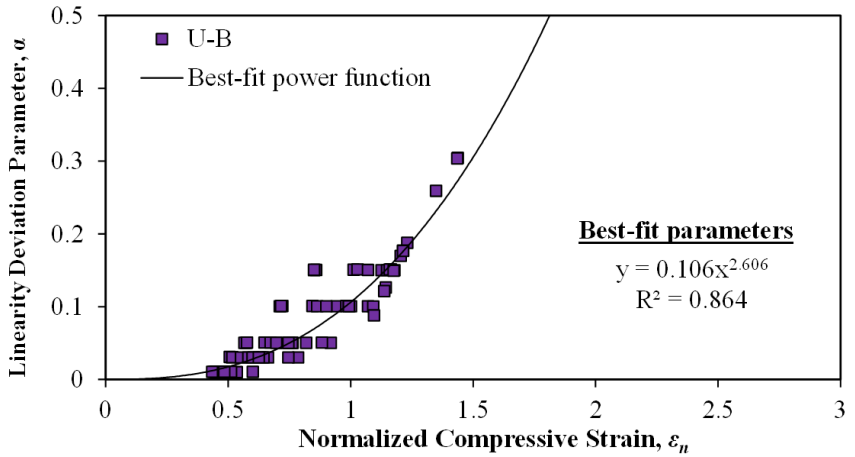

Figure 48. Graph. Deviation from the linear elastic compressive behavior for U-B.

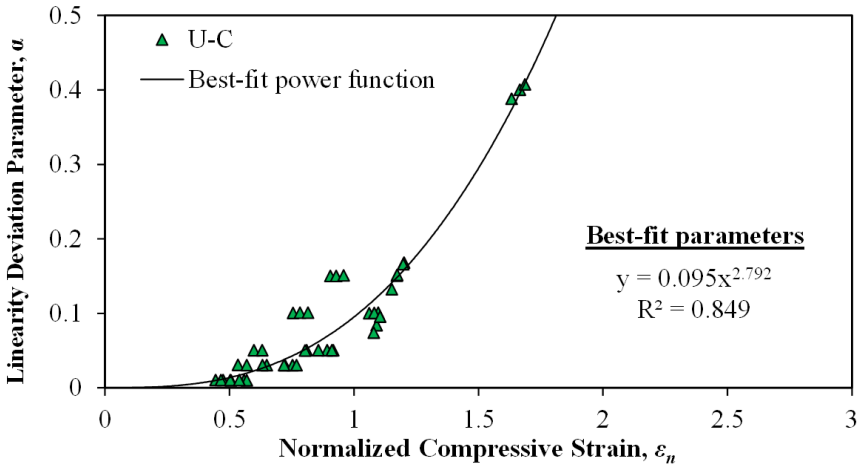

Figure 49. Graph. Deviation from the linear elastic compressive behavior for U-C.

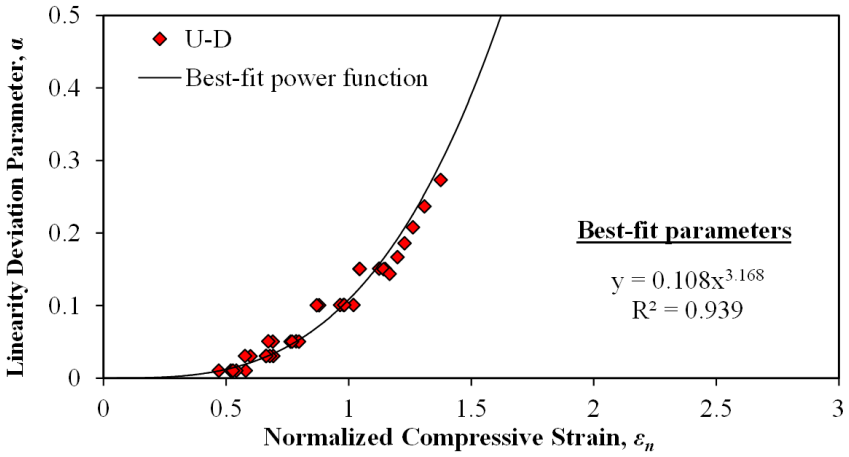

Figure 50. Graph. Deviation from the linear elastic compressive behavior for U-D.

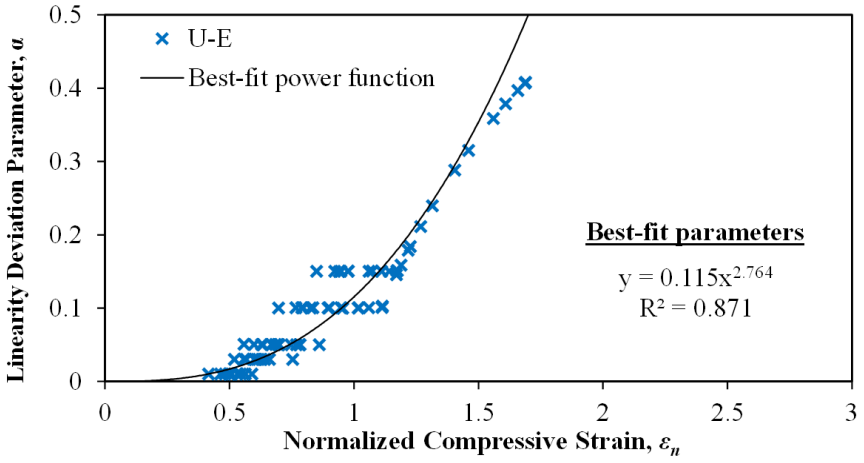

Figure 51. Graph. Deviation from the linear elastic compressive behavior for U-E.

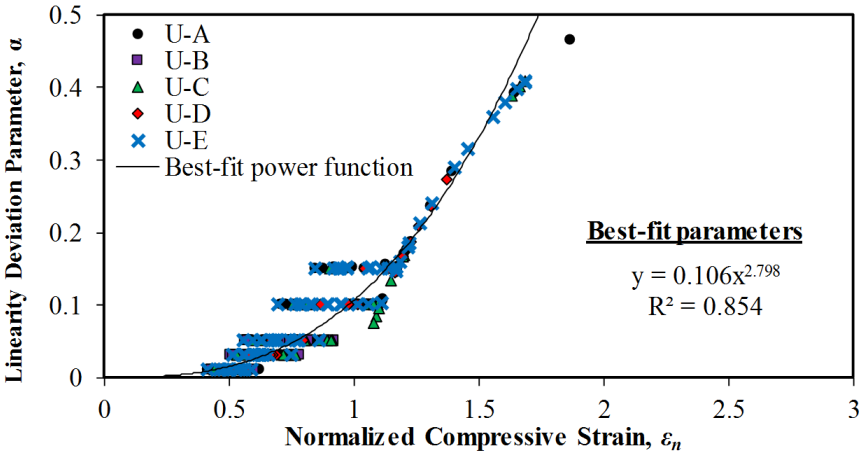

Figure 52. Graph. Deviation from the linear elastic compressive behavior for all five UHPCs.

Table 16. Best-fit curve parameters from linearity analysis.

Material	Fit Parameters		
	A	*b*	R^2
U-A	0.106	2.683	0.875
U-B	0.106	2.606	0.864
U-C	0.095	2.792	0.849
U-D	0.108	3.168	0.939
U-E	0.115	2.764	0.871
Average	0.106	2.754	0.841

Figure 53 and figure 54 compare measured stress-strain curves with those calculated using the expressions shown in figure 43 and the fit parameters listed in table 16 under "Average." Figure 53 a shows the comparison between average measured and calculated stress-strain curves for three different UHPC at early age with peak compressive strength around 15 ksi (103.4 MPa), and figure 54 a shows a similar set curves when the compressive strengths are greater than 18 ksi (122 MPa). In general, at lower compressive strengths the calculated stress-strain response tends to slightly under-estimate the strain corresponding to the peak compressive stress, and the converse is true when the peak compressive stress of UHPC is higher.

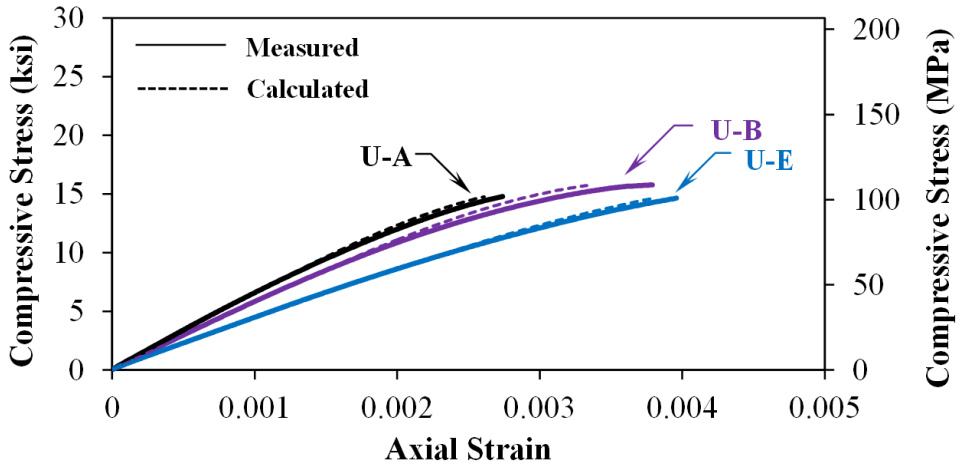

Figure 53. Graph. Comparison between measured and calculated stress-strain curves with UHPC compressive strength near 15 ksi (103 MPa).

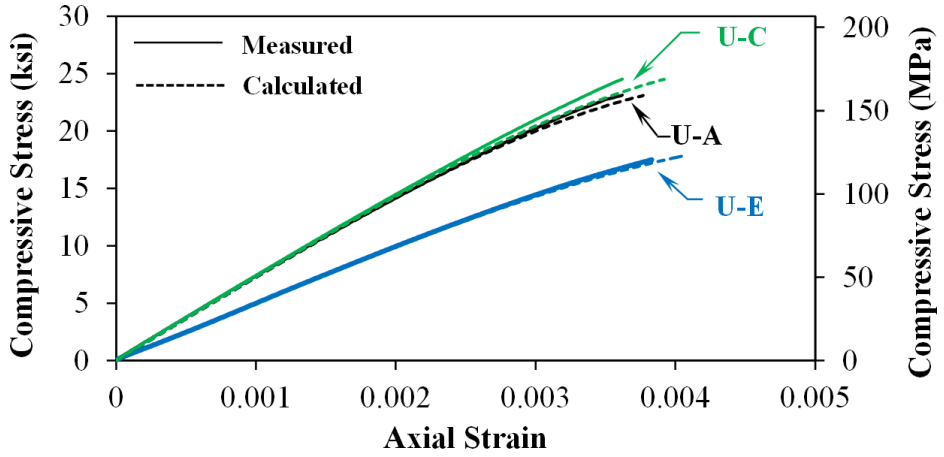

Figure 54. Graph. Comparison between measured and calculated stress-strain curves with UHPC compressive strength above 18 ksi (122 MPa).

Measured Strains

Figure 55 and figure 56 depict the measured and average compressive strains at peak compressive stress, respectively. In figure 55, each data point represents data from individual tested samples. It can be observed that there is little correlation between peak compressive strength and the associated measured strains, which is not unexpected for the compressive strength range shown. Strains at peak compressive stress ranged between 0.00274 (U-A) and 0.00524 (U-E). The average peak compressive strain at peak compressive stress for each material is presented in figure 56. The error bars shown represent ± one standard deviation.

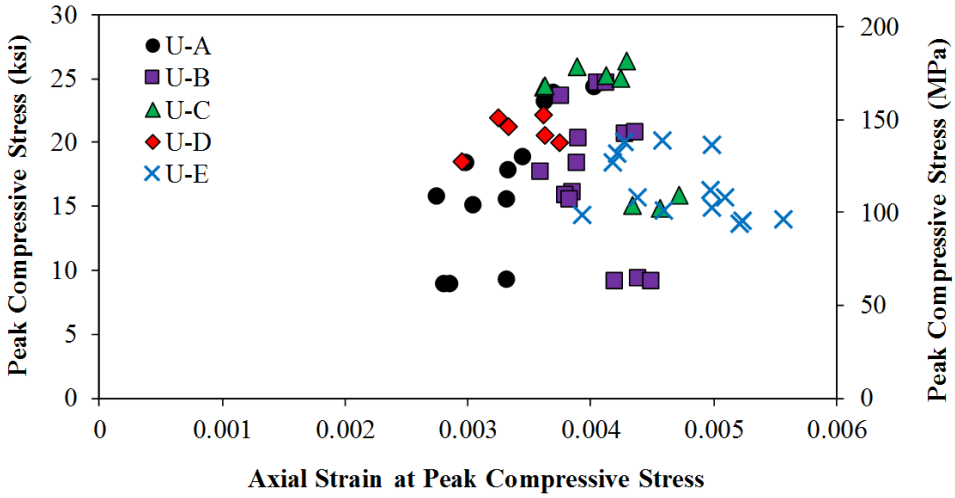

Figure 55. Graph. Axial compressive strains measured at peak compressive stress.

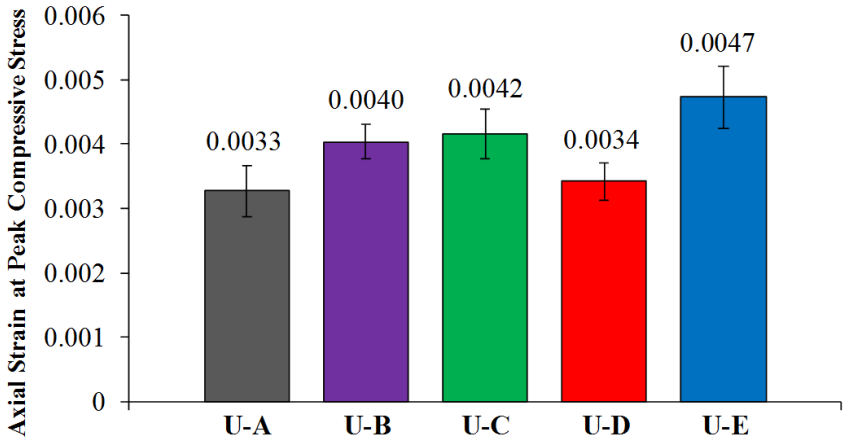

Figure 56. Graph. Average axial compressive strains measured at peak compressive stress.

Figure 57 depicts the measured circumferential strains at peak compressive stress, respectively; these measurements were not taken for U-D specimens. In figure 57, each data point represents data from individual tested samples. It can be observed that there is little correlation between peak compressive strength and the associated circumferential strain. Circumferential strains at peak compressive stress ranged between 0.0064 and 0.00297; both of these strains occurred in U-E specimens. The average peak circumferential strain at peak compressive stress for each material is presented in figure 58. The error bars shown represent ± one standard deviation.

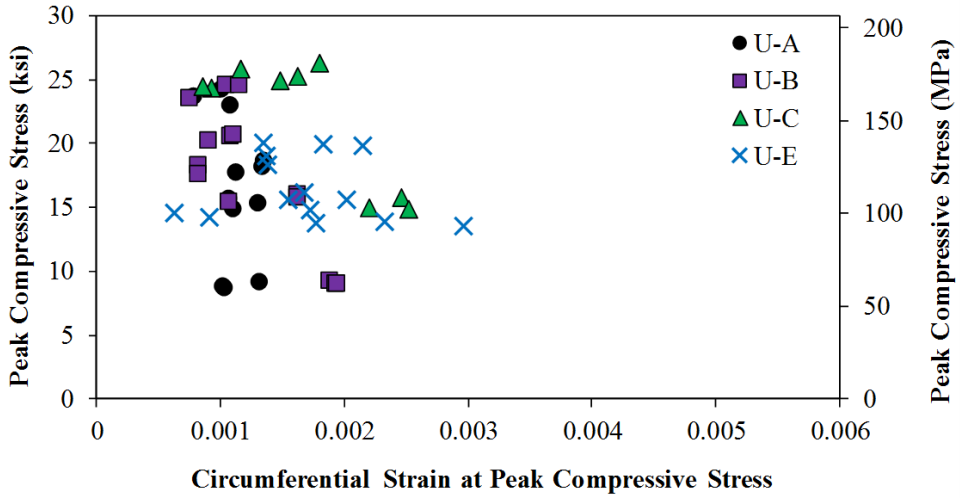

Figure 57. Graph. Circumferential strains measured at peak compressive stress.

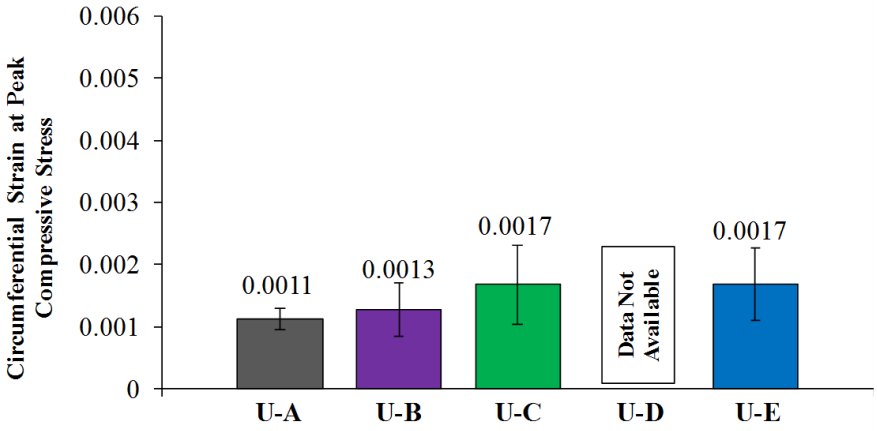

Figure 58. Graph. Average circumferential strains measured at peak compressive stress.

Elastic Modulus and Poisson Ratio

The modulus of elasticity was calculated based on a best fit approximation of the stress-strain response between ten and thirty percent of the peak compressive stress for each cylinder sample. The elastic moduli of the different UHPC are presented in figure 59 as a function of the peak compressive strength. There is a clear relationship between the elastic modulus of UHPC and the compressive strength, which has been previously shown in a number of different research studies focused on materials properties of UHPC. (Ma and Orgass 2004; Graybeal 2006c, 2007; Graybeal and Stone 2012) Traditionally, the elastic modulus of concrete has been expressed as a function of $\sqrt{f'_c}$. Similar approaches have been used for UHPC.

Herein, a trendline was fit to the data shown in figure 59, the resulting best-fit equation is shown in figure 60. This trendline, along with that developed by Graybeal (2007) which is shown in figure 61, are shown in figure 59. Both equations are very similar, and thus the UHPCs tested in this study exhibited elastic moduli similar to those reported previously.

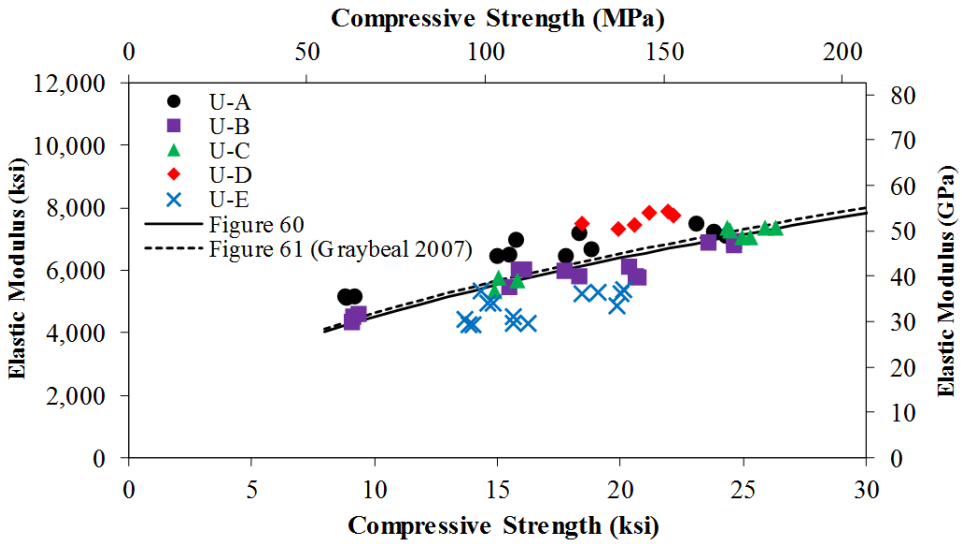

Figure 59. Graph. Elastic modulus of UHPC as a function of compressive strength.

$$E_c = 1{,}430\sqrt{f'_c} \quad \text{(ksi)}$$

Figure 60. Equation. Best-fit relationship for the data shown in figure 59.

$$E_c = 1{,}460\sqrt{f'_c} \quad \text{(ksi)}$$

Figure 61. Equation. Relationship proposed by Graybeal (2007) for the elastic modulus of UHPC.

The Poisson's ratio was determined using the expression shown in figure 62. The individual Poisson's ratio measurements are presented as a function of compressive strength in figure 63. The average Poisson's ratios, which are shown in figure 64, varied between 0.145 and 0.175, which are similar to those reported by previous studies. (Ahlborn, Peuse, and Misson 2008) The error bars shown represent ± one standard deviation.

$$\nu = -\frac{\varepsilon_{circ,30} - \varepsilon_{circ,10}}{\varepsilon_{axial,30} - \varepsilon_{axial,10}}$$

Figure 62. Equation. Expression for determination of Poisson's ratio.

Where

$\varepsilon_{circ,\ 30}$ = circumferential strain at 30 percent of peak load

$\varepsilon_{circ,\ 10}$ = circumferential strain at 10 percent of peak load

$\varepsilon_{axial,\ 30}$ = axial strain at 30 percent of peak load

$\varepsilon_{axial,\ 10}$ = axial strain at 10 percent of peak load

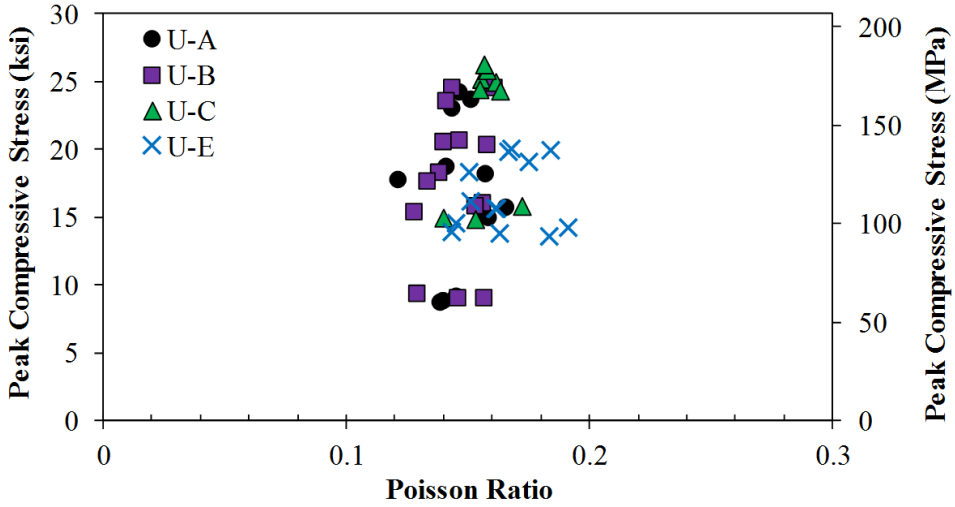

Figure 63. Graph. Measured Poisson's ratios vs. peak compressive stress.

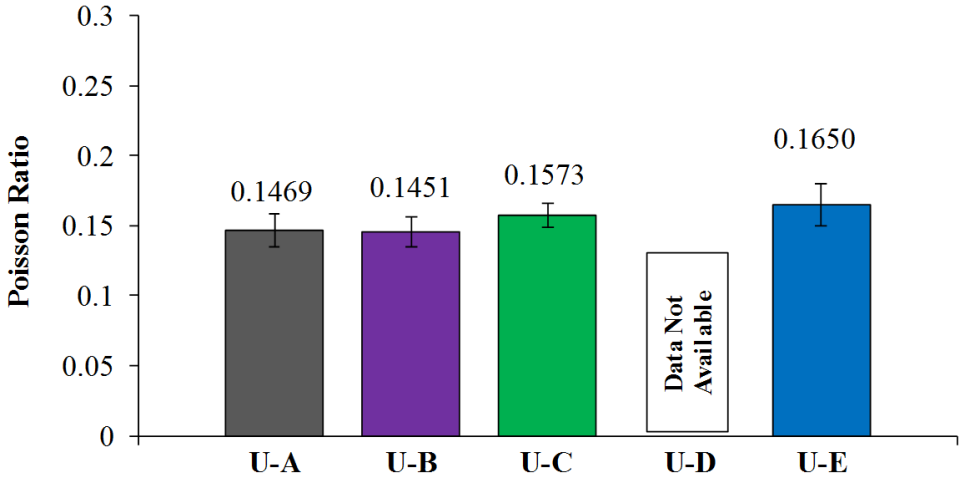

Figure 64. Graph. Average Poisson's ratios.

BEHAVIOR IN DIRECT TENSION

Test Methods and Specimens Preparation

Direct tension tests were conducted using the method developed by Graybeal and Baby (2013). DTT specimens were constructed using 2 inch x 2 inch x 17 inch (50.8 mm x 50.8 mm x 431.8 mm) prismatic specimen molds. The prismatic specimens were cast horizontally in open-top rigid steel molds. The UHPC was poured into the mold at one end and allowed to flow toward the other end. Once filled, DTT molds were placed on a concrete vibrating table for 5 to 15 seconds to help release entrapped air. After vibration, the exposed surface of each specimen was screeded then loosely covered with sheet plastic to minimize evaporation. The specimens were allowed to cure for at least 24 hours prior to being demolded and being stored in the laboratory.

Figure 65 depicts the DTT set-up. Prior to testing, aluminum grips were fabricated and installed on either end of the prismatic specimen. The ends of the specimen, where grips were to be installed,

were lightly roughened and degreased. Furthermore, the corners of prismatic specimen were dressed to remove stray fibers or excess UHPC that might interfere with bonding the grip plates. The grip plates were bonded using a thin layer of high-strength, high-stiffness structural epoxy, which was allowed to cure for at least 12 hours prior to testing.

Direct tension tests were executed on a 225-kip (1000-kN) capacity uniaxial testing frame with a computer controlled, closed-loop hydraulic actuator (shown in figure 66). Prior to installing the specimen, the hydraulic grips of the test machine were aligned using a specially-design alignment fixture. Misaligned grips can cause eccentric loading in the prismatic specimen resulting in premature cracking. The test frame gripped specimens using two sets of diamond-faced, hydraulic-actuated wedge grips that applied lateral pressure onto opposing surfaces on each end of the specimen. During testing, axial strain was measured using a parallel ring extensometer which contained four LVDTs; shown in figure 65 and figure 66. For the tests discussed herein, the extensometer had a 4-inch (102-mm) gauge length. Load was measured via the on-board load cell attached to the load frame, and data was recorded using a digital data logger.

Specimens were subjected to a loading protocol that had three primary load steps. First, the specimen was loaded in displacement control at a rate of -0.0001 in./sec (-0.00254 mm/sec) until a compressive load of -4000 lbs (-17.8 kN) was reached. At which point, loading was paused momentarily to re-configure the loading parameters. Load was then reversed, in displacement control, at a rate of 0.0001 in./sec (0.00254 mm/sec) until the average extensometer strain reached 25,000 microstrain or strain localization occurred. At which point, the loading rate was increased to 0.001 in./sec (0.0254 mm/sec). Loading continued until the average displacement along the gauge length reached 0.2 inches (5.1 mm) or strain localization occurred. Upon completion of the test, specimens were assessed for cracking and failure location.

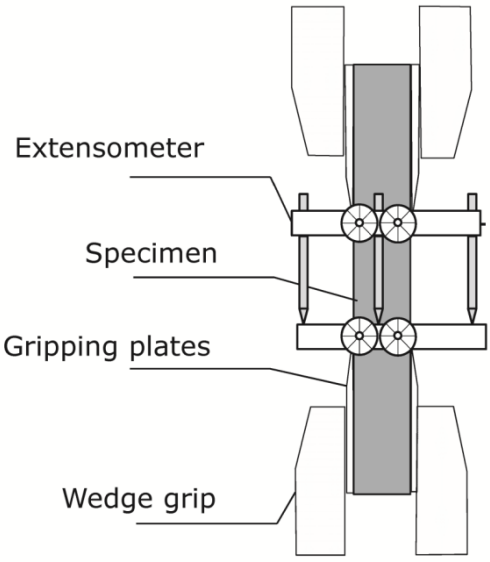

Figure 65. Illustration. Direct tensile test (DTT) schematic.

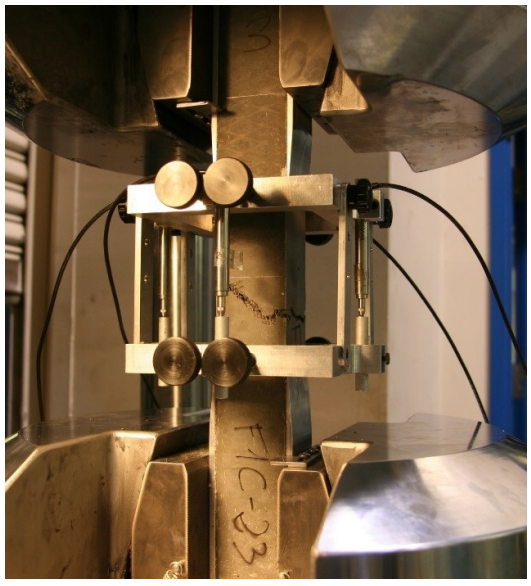

Figure 66. Photo. Photo taken during direct tension testing.

For each set of DTT specimens tested, a corresponding set of companion compression strength specimens were also fabricated and tested. These specimens were constructed and tested as described in the previous section entitled "Compression Tests."

Results

The direct tension test procedure described in the previous section gives a thorough understanding and quantification of the tensile mechanical behavior of UHPC. Since matrix formulation, fiber type, orientation, and amount are not unique, several characteristic tensile responses are typically observed with UHPC materials. Figure 67 depicts an idealized uniaxial tension stress-strain response observed with UHPC materials. The idealized response can be broken down into three distinct phases which are described below:

Phase I: The elastic phase refers to the global elastic straining of the material before the formation of any discrete cracks. It is characterized by an initial linearly elastic response, described by the modulus of elasticity, E, until the elastic tension strength, f_e, is reached as shown in figure 68. The elastic tension strength can be thought of as the cracking stress of the cementitious matrix (UHPC without fibers) but its value could be impacted by the fiber content, geometry, and orientation. As the material is strained beyond its elastic strain, $\varepsilon_e = f_e / E$, micro-cracks start to form engaging the fibers and resulting in further increases in strength, at a gradual loss of stiffness (non-linear behavior), until the first cracking strength, f_{cr}, is reached. The first cracking strength, f_{cr}, and its corresponding strain, ε_{cr}, mark the formation of the first discrete crack and are generally represented by a clear stress discontinuity or a significant change in the shape of the stress-strain response as shown in figure 69.

Phase II: The multi-cracking phase, refers to the portion of the behavior where the material exhibit the formation of multiple cracks until the strain localizes in a single discrete crack. Due to the post-cracking strength of UHPC provided by the fiber reinforcement, the material in this phase accumulates strain in both the uncracked matrix between cracks and within the crack-bridging fibers, resulting in the formation of simultaneous cracks without significant widening of the individual cracks. (Graybeal and Baby 2013) Depending on the material formulation, fiber content, and casting method, the multi-cracking response can be characterized by a pseudo stress plateau (SP) where the stress is nearly constant as the strain increases, tension hardening (TH) where the load continues to increase as new cracks form, or a combination of both as shown in figure 69. The multi-cracking phase ends when either when the stress or strain reaches the fiber-bridging strength, f_p, or its corresponding strain, ε_p. Some fiber-reinforced materials do not exhibit a multi-cracking phase and the load starts to drop at the onset of the first crack. Materials that exhibit this behavior, such as conventional fiber-reinforced concretes (FRC), are not considered UHPC class materials per FHWA definition since it does not show a sustained post-cracking tension capacity.

Phase III: The localized deformation phase, refers to the portion of the behavior where the deformation is localized into an individual crack, which continues to widen as the

fibers bridging the cracks debond and pull out of the matrix as shown in figure 70. During this phase, the remainder of the material unloads elastically, and therefore the response is based on deformation not strain. (Graybeal and Baby 2013) The decrease in load relative to the increase in crack opening, or the rate at which the material loses capacity, can be gradual or steep, as shown in figure 70, depending on multiple factors controlling the efficiency of the fibers including type, content, orientation, and frictional bond.

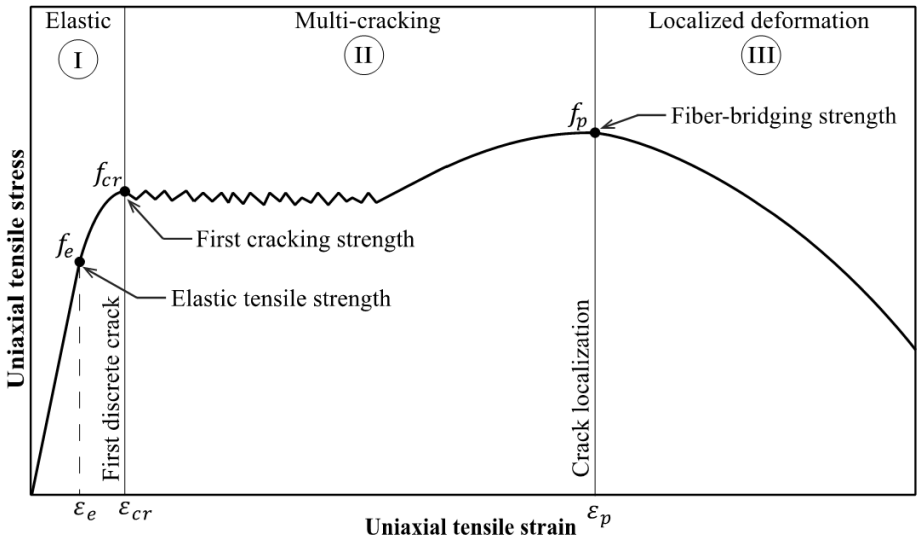

Figure 67. Illustration. Idealized uniaxial tensile response for UHPC.

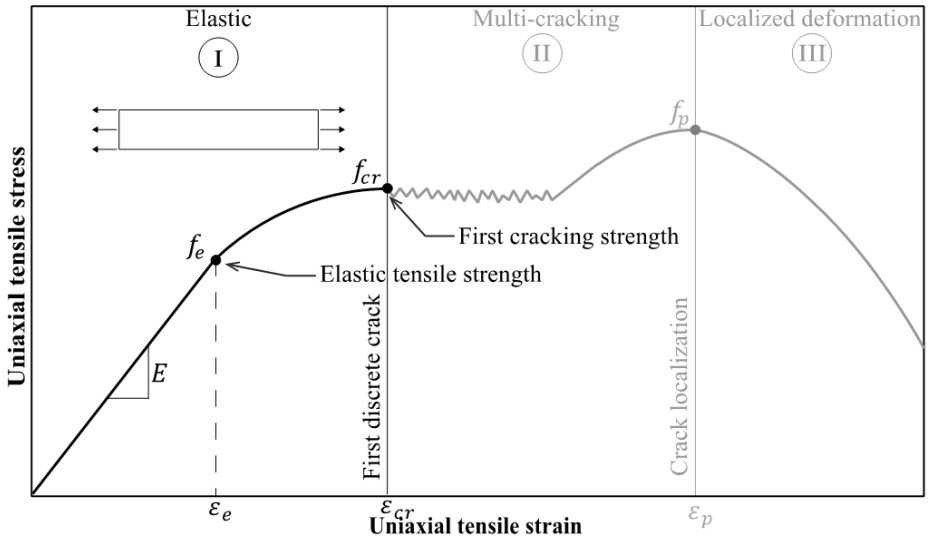

Figure 68. Illustration. Idealized uniaxial tensile response showing the behavior in the elastic phase.

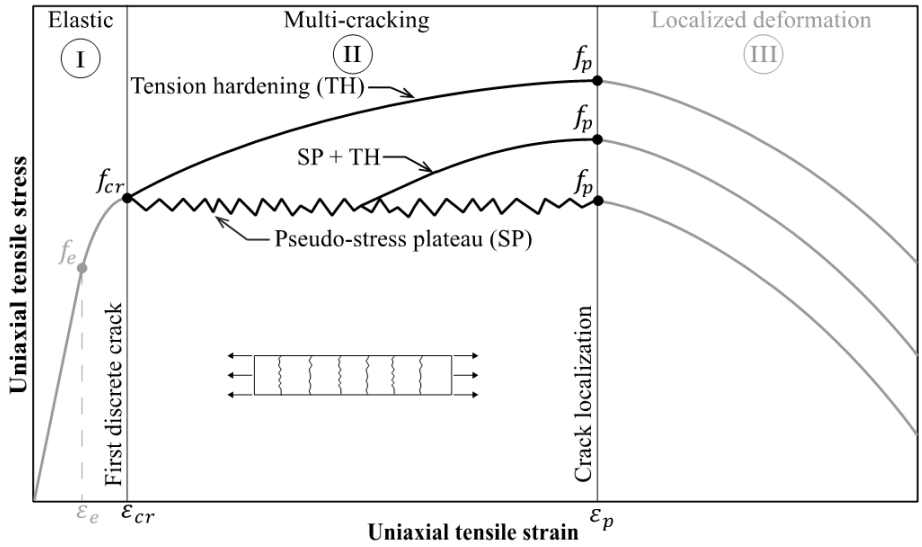

Figure 69. Illustration. Idealized uniaxial tensile response showing the behavior in the multi-cracking phase.

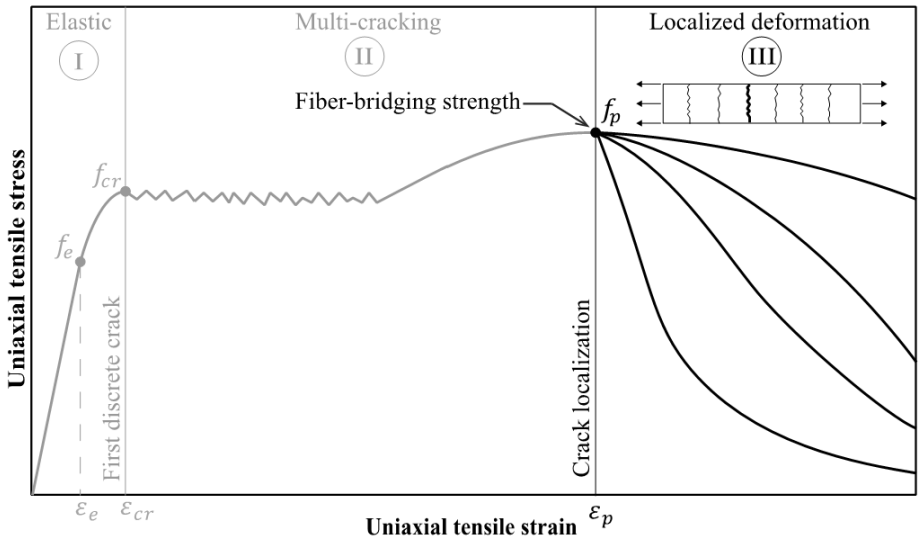

Figure 70. Illustration. Idealized uniaxial tensile response showing the behavior in the localized deformation phase.

The modulus of elasticity exhibited by the tested tension specimens is directly determined from the individual tensile responses by calculating the best linear fit to the data collected during the compressive portion of the specimen's stress-strain response, recorded during the first loading step when the specimen is assumed to be uncracked. The average results of the modulus of elasticity values are presented in table 17 for each test group.

The first cracking stress is visually evident for tensile characteristic trends exhibiting pseudo stress plateau where a clear stress discontinuity is manifested by an abrupt decrease in stress. For these cases, the first cracking stress is taken as the value of stress at the peak of the first drop in load as shown in figure 71. In a number of cases, low local peak stresses or early stress discontinuities were observed within the elastic region of the response as shown in figure 72. This discontinuity is either the result of the residual bending stresses generated during specimen's installation into the grips of the testing machine, or the outcome of the specimen's geometric imperfection and material heterogeneity, an effect that is more pronounced in small size specimens. Since the material response after this low value of peak stress remains elastic, it does not represent a change in the material behavior and is therefore not representative of the real tensile behavior of the composite. The first cracking stress for such cases is taken as the value of stress at the peak preceding the second drop in load. For strain hardening characteristic curves, the first cracking is chosen at the midpoint of the non-linear transitional zone between the elastic and strain hardening regimes as shown in figure 73. However, visually selecting the first cracking of UHPC is subject to user error and bias, thus standard procedures are required to evaluate this parameter objectively and systematically. Since this issue is similar in nature to determining the yield strength of high strength steel, whose behavior does not necessarily show a clear transition between the elastic and hardening regimes, an offset method is adopted herein to determine the first cracking strength of UHPC. A linear line having a slope equal to the elastic modulus is drawn at an offset strain of 0.02 percent for each of the individual tensile trends as shown in figure 71 through figure 73. The first cracking stress and strain corresponds to the intersection of the offset line with the stress-strain curve. The average first cracking results for both the visual and offset methods for each testing

group are reported in table 18. The first cracking stress obtained by the both methods is similar for each testing group proving the robustness and effectiveness of the offset method in capturing the first cracking stress for the UHPCs examined in this report. A 0.02 percent offset method is recommended to obtain the UHPC first cracking stress for use in material models for the design of UHPC members.

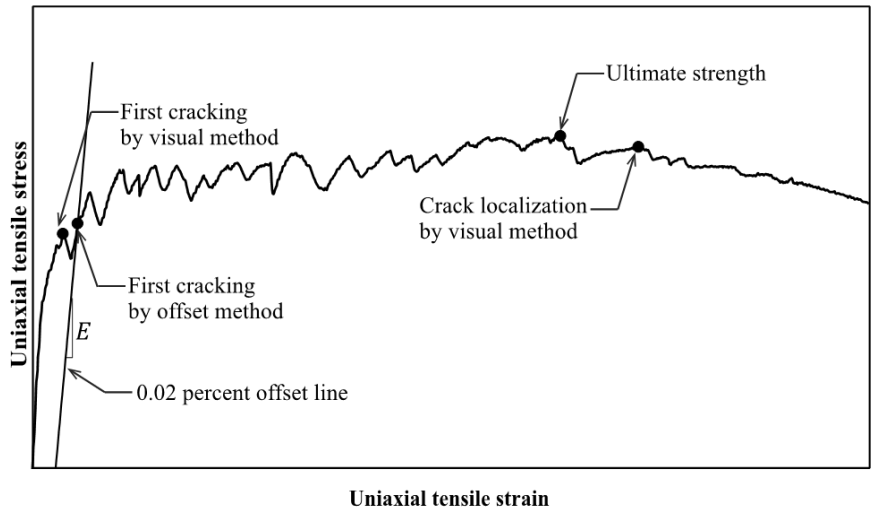

Figure 71. Illustration. Typical stress-strain relationships of a tensile test specimen exhibiting pseudo stress plateau.

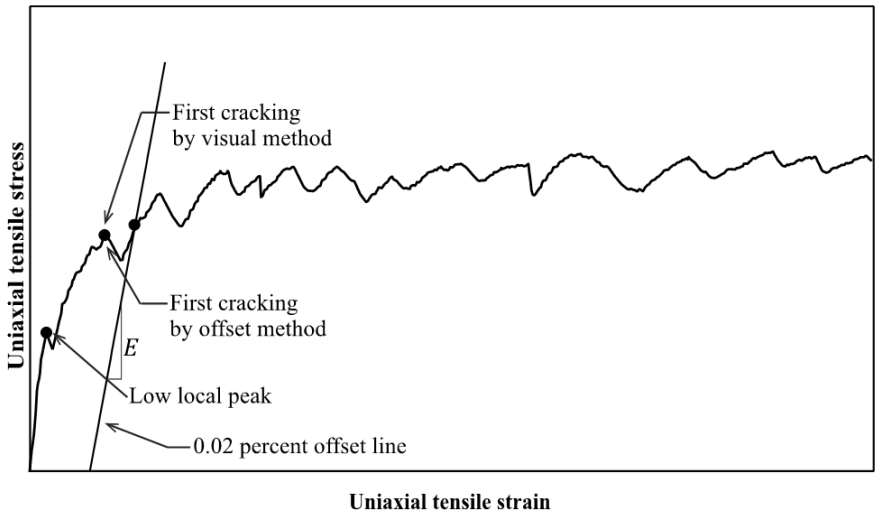

Figure 72: Illustration. Example stress-strain relationship of a tensile test specimen exhibiting low local peak stress.

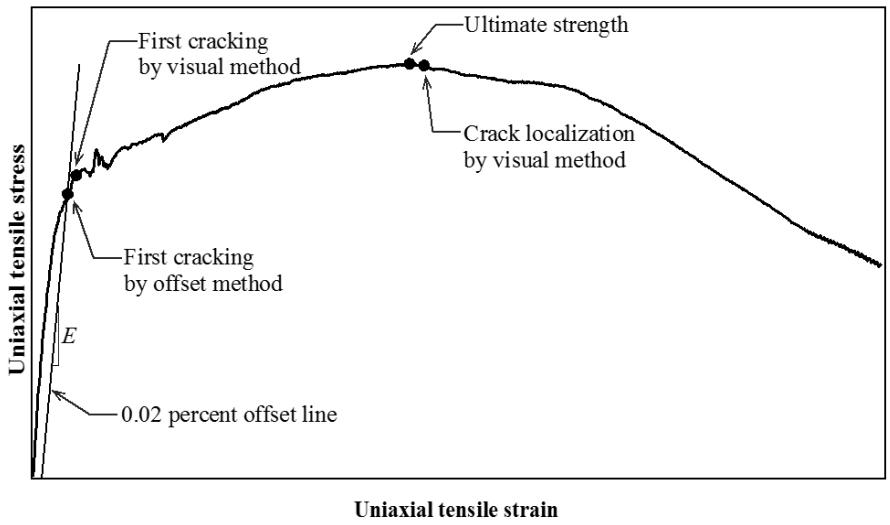

Figure 73: Illustration. Typical stress-strain relationships of a tensile test specimen exhibiting tension hardening behavior.

After the first crack is formed, the tensile response varies significantly depending on the material composition and fiber content. The multi-cracking domain can be defined based on the first cracking stress and localization strain, in case of pseudo stress plateau characteristic behavior, or based on the first cracking stress and the ultimate stress and its corresponding strain in case of tension hardening. The localization strain is defined as the strain at which the cracks are localized into a single discrete crack; it is visually chosen on the stress-strain trends when the stress starts to decrease in a continuous manner (figure 71 and figure 73). The ultimate stress is defined as the maximum stress registered during a tension test. The average results of the localization and ultimate stress and strains are shown in table 19 for each test group. As a general rule, when the UHPC exhibits strain hardening behavior, the localization and ultimate stress and strains are approximately equal but greater than the cracking stress and strain. In case of a pseudo stress plateau behavior, the cracking, localization, and ultimate stresses are approximately equal but the localization strain is greater than the cracking strain and the strain at ultimate stress.

The individual stress-strain trends obtained from the direct tension specimens are presented figure 74 through figure 87; the average result is shown with a bold line. The average curve of a test group was calculated from individual stress values at one value of strain. The axial stress was calculated by dividing the axial load by the cross-sectional area of the specimen and the strain value is calculated by averaging the displacement readings of the four attached LVDTs divided by the gauge length. The average curves pertaining to each of the tested UHPCs are compared in figure 88 through figure 92. The effect of fiber content on the tension response of UHPC is shown in figure 93 and figure 94.

By examining figure 88 through figure 94, it can be concluded that fiber content has a significant effect on the characteristic tensile response of UHPC. Increasing the fiber content improved the overall resistance against tensile load by increasing the cracking and ultimate stresses of the composite. For example, the cracking and ultimate stresses of U-A increased by approximately 57 percent and 44 percent when the fiber volume was increased from 2 percent to 3 percent,

respectively. In a number of cases, adding fibers has also changed the response from pseudo stress plateau to strain hardening (see figure 88, figure 91, and figure 92 for U-A, U-D, and U-E, respectively). All the UHPCs examined in this study showed a pseudo stress or strain hardening characteristic responses. However, U-C showed a significantly smaller crack straining domain with the cracks localizing shortly after the end of the elastic regime, at which the material started to soften resulting in a continuous drop in loads as shown in figure 90.

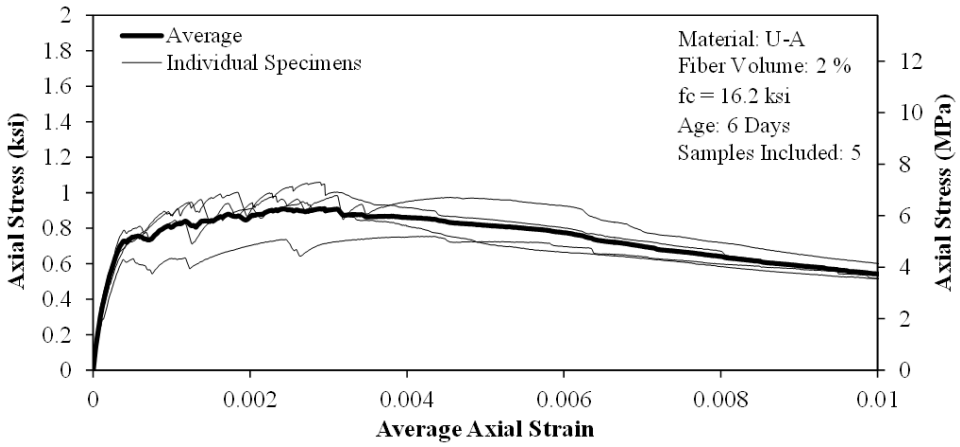

Figure 74. Graph. Tensile stress-strain response of U-A samples with 2 percent fiber volume.

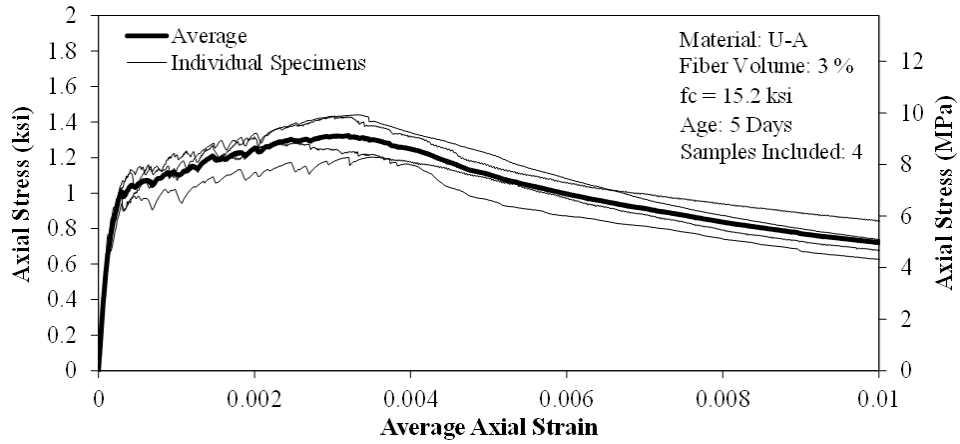

Figure 75. Graph. Tensile stress-strain response of U-A samples with 3 percent fiber volume.

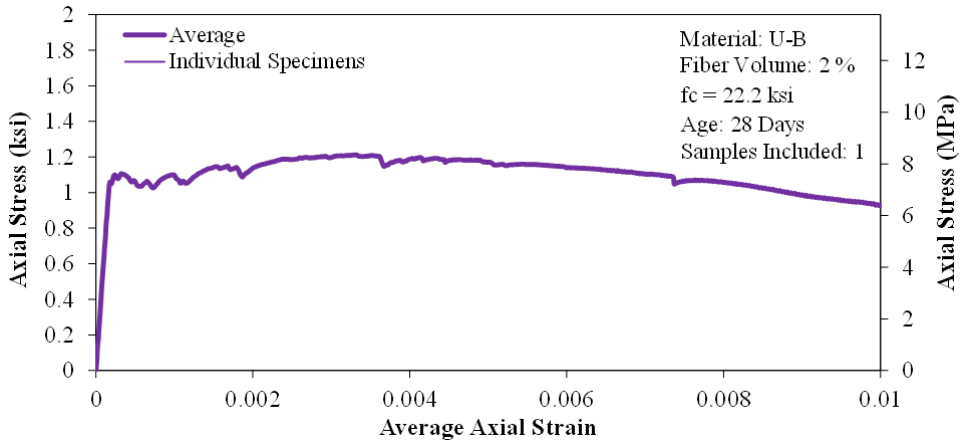

Figure 76. Graph. Tensile stress-strain response of U-B samples with 2 percent fiber volume.

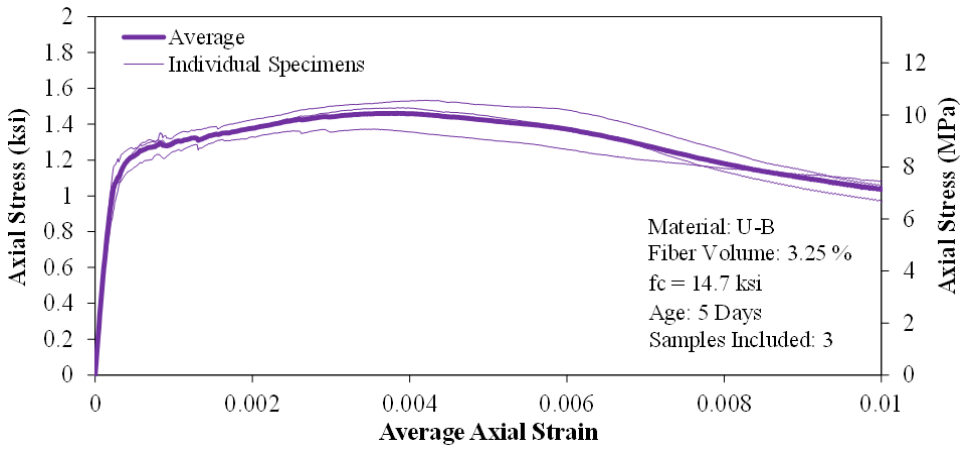

Figure 77. Graph. Tensile stress-strain response of U-B samples with 3.25 percent fiber volume.

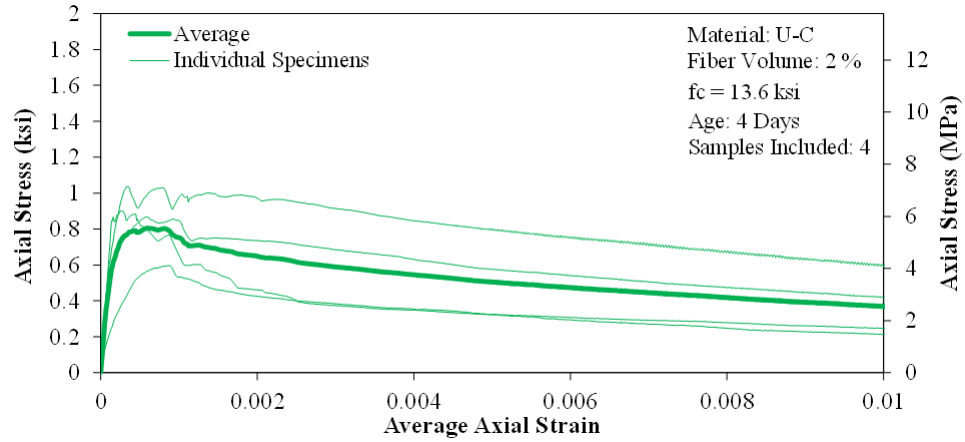

Figure 78. Graph. Tensile stress-strain response of U-C samples with 2 percent fiber volume.

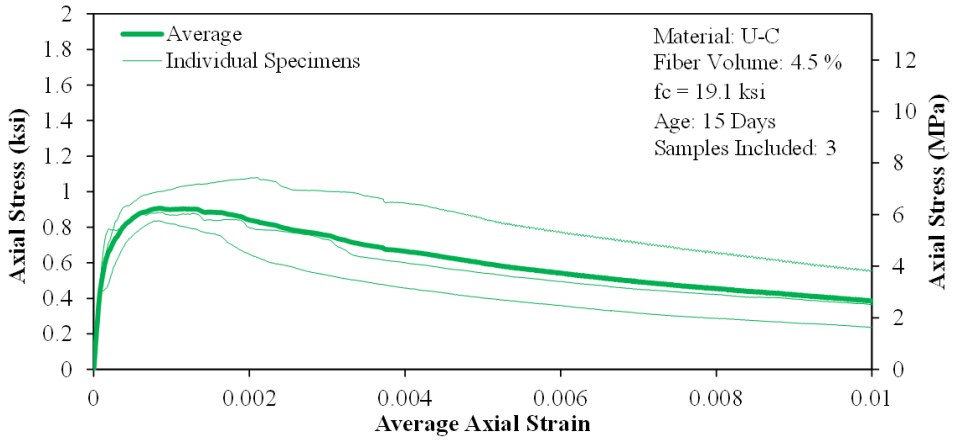

Figure 79. Graph. Tensile stress-strain response of U-C samples with 4.5 percent fiber volume.

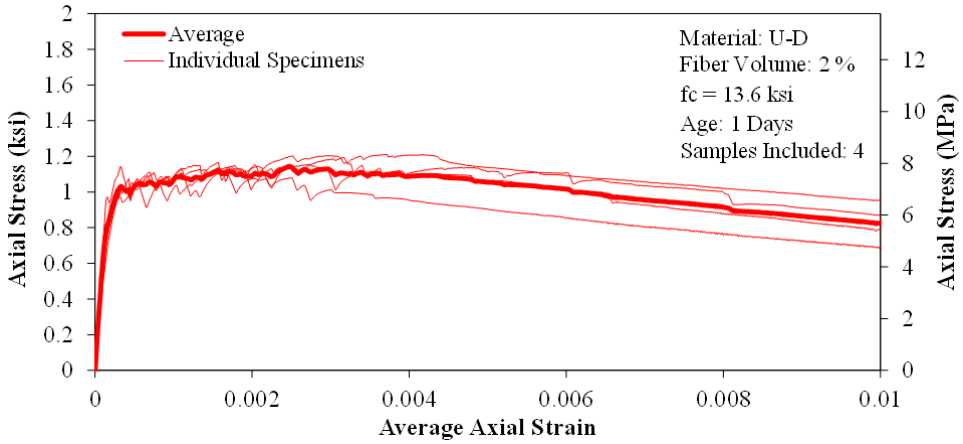

Figure 80. Graph. Tensile stress-strain response of U-D samples with 2 percent fiber volume after 1 day of curing.

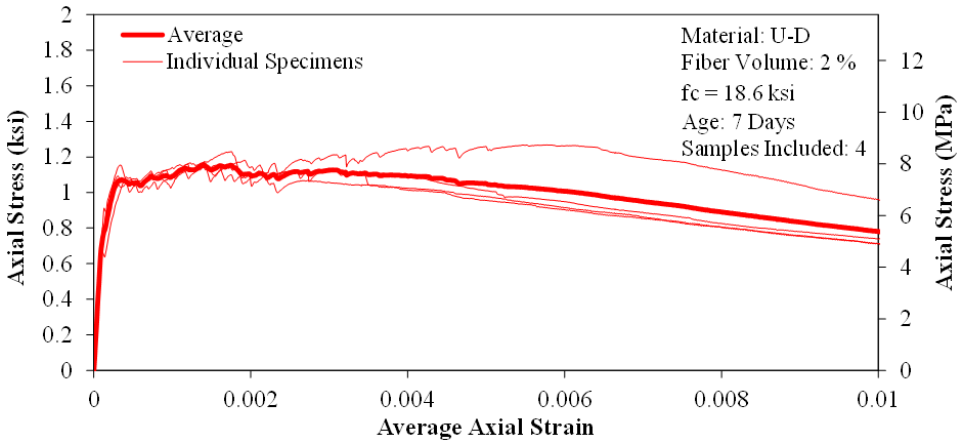

Figure 81. Graph. Tensile stress-strain response of U-D samples with 2 percent fiber volume after 7 days of curing.

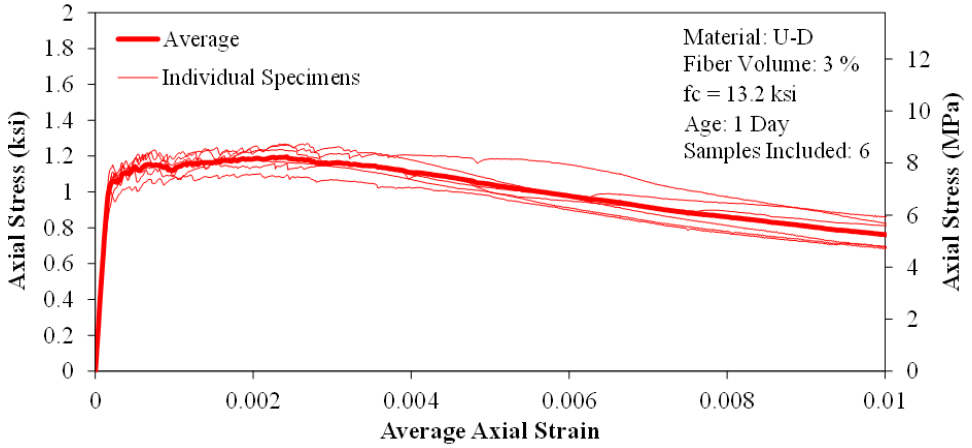

Figure 82. Graph. Tensile stress-strain response of U-D samples with 3 percent fiber volume after 1 day of curing.

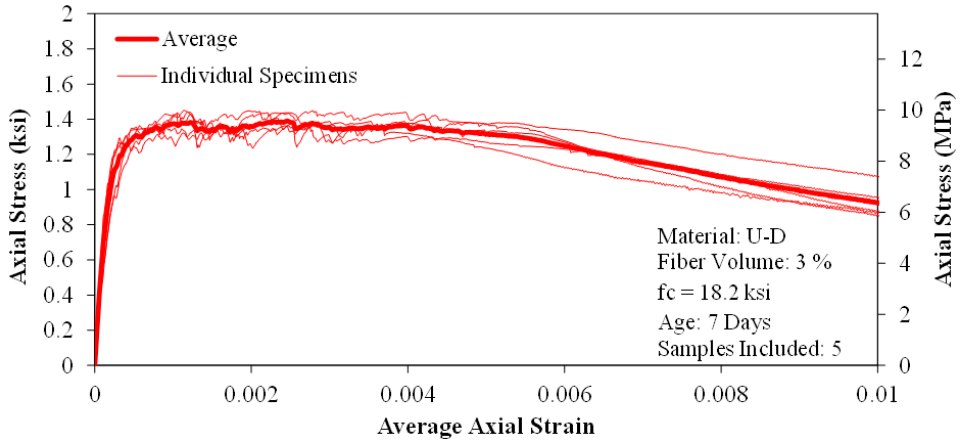

Figure 83. Graph. Tensile stress-strain response of U-D samples with 3 percent fiber volume after 7 day of curing.

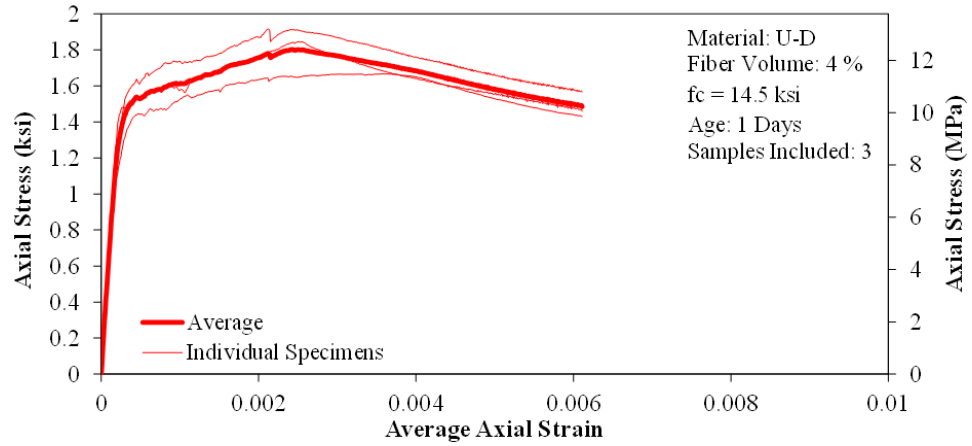

Figure 84. Graph. Tensile stress-strain response of U-D samples with 4 percent fiber volume after 1 day of curing.

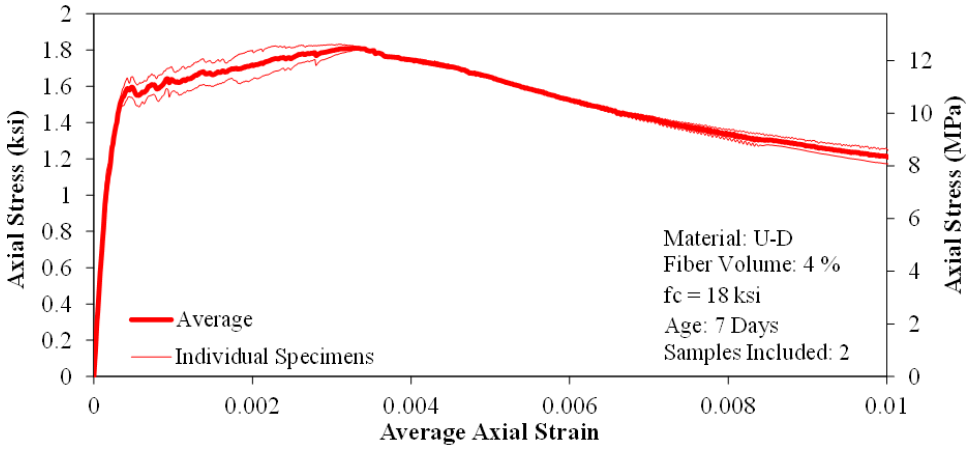

Figure 85. Graph. Tensile stress-strain response of U-D samples with 4 percent fiber volume after 7 day of curing.

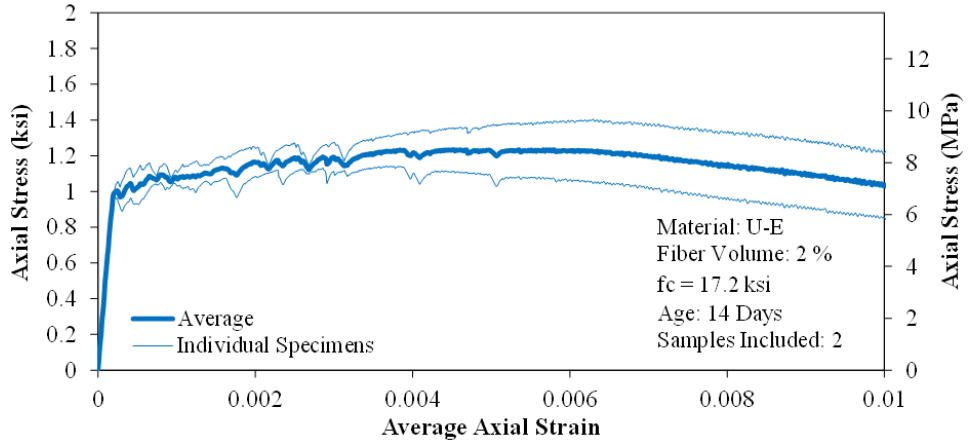

Figure 86. Graph. Tensile stress-strain response of U-E samples with 2 percent fiber volume.

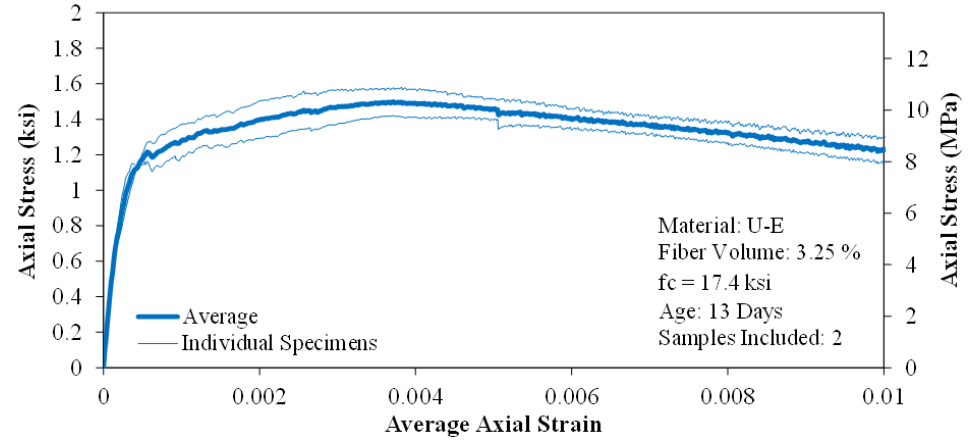

Figure 87. Graph. Tensile stress-strain response of U-E samples with 3.25 percent fiber volume.

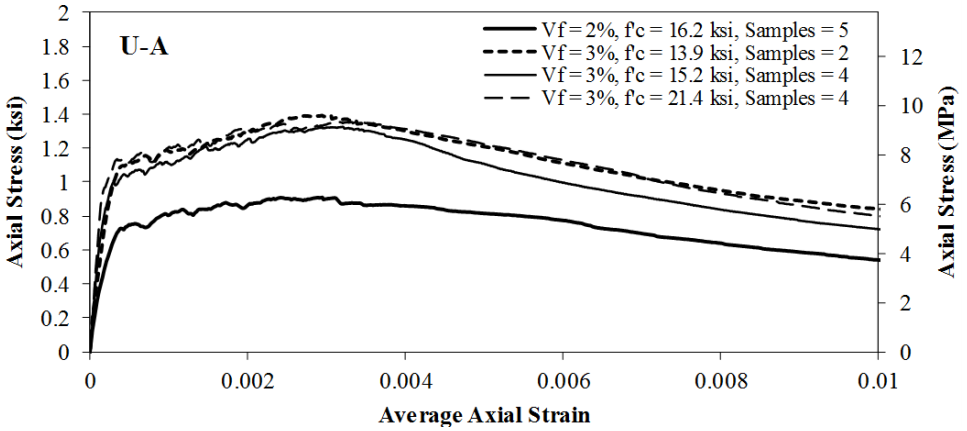

Figure 88. Graph. Average tensile stress-strain behavior from U-A specimens.

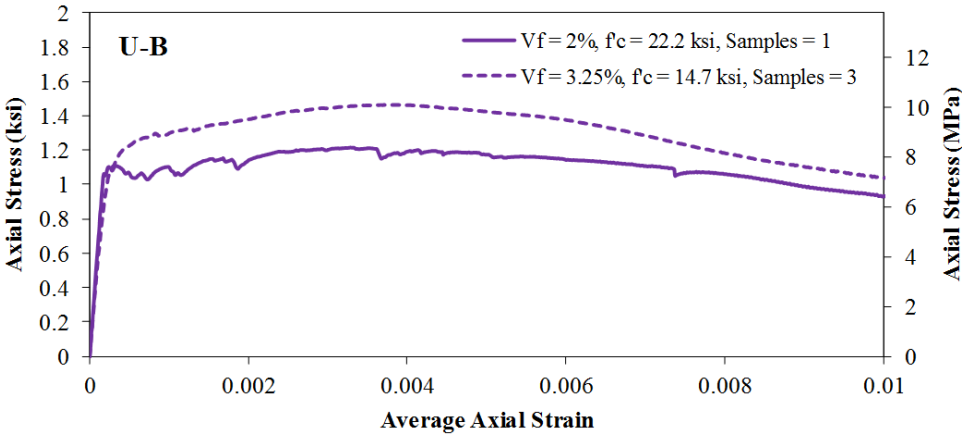

Figure 89. Graph. Average tensile stress-strain behavior from U-B specimens.

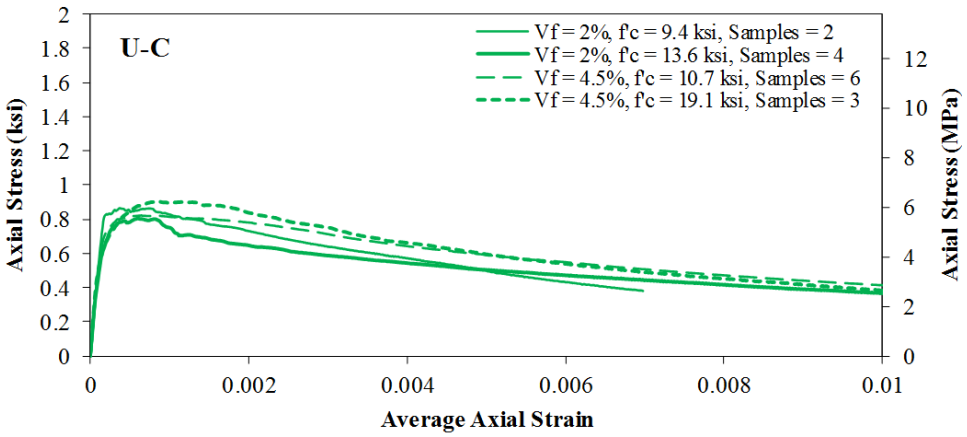

Figure 90. Graph. Average tensile stress-strain behavior from U-C specimens.

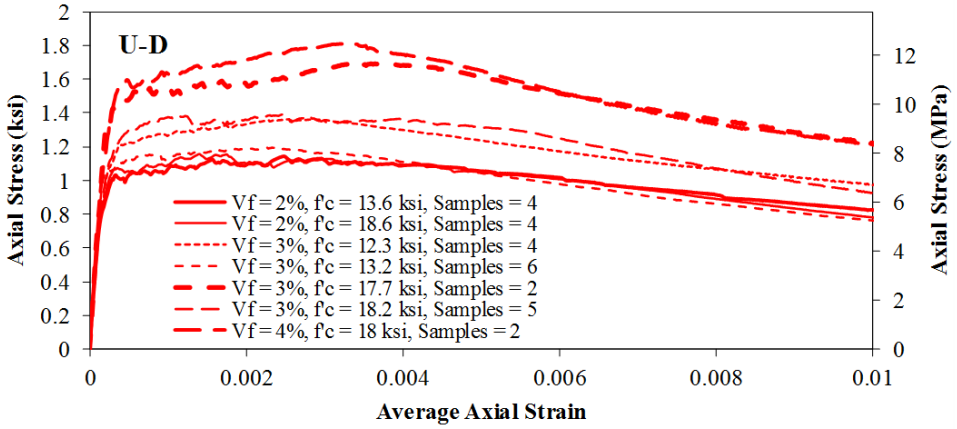

Figure 91. Graph. Average tensile stress-strain behavior from U-D specimens.

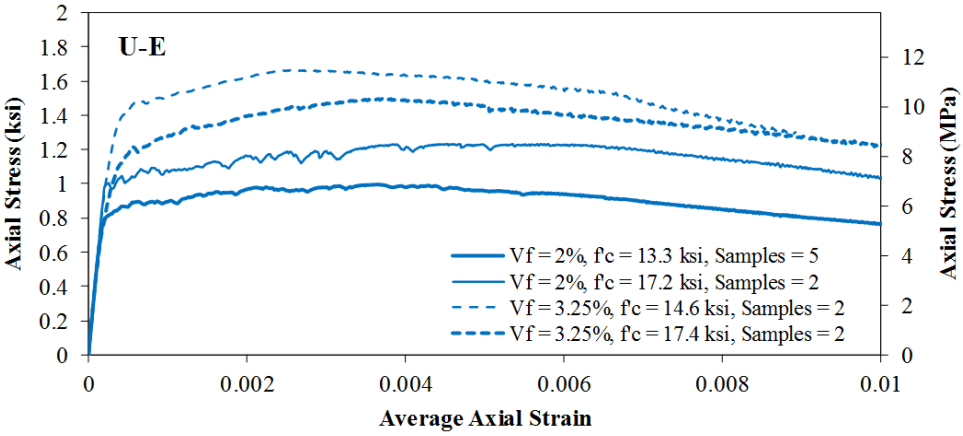

Figure 92. Graph. Average tensile stress-strain behavior from U-E specimens.

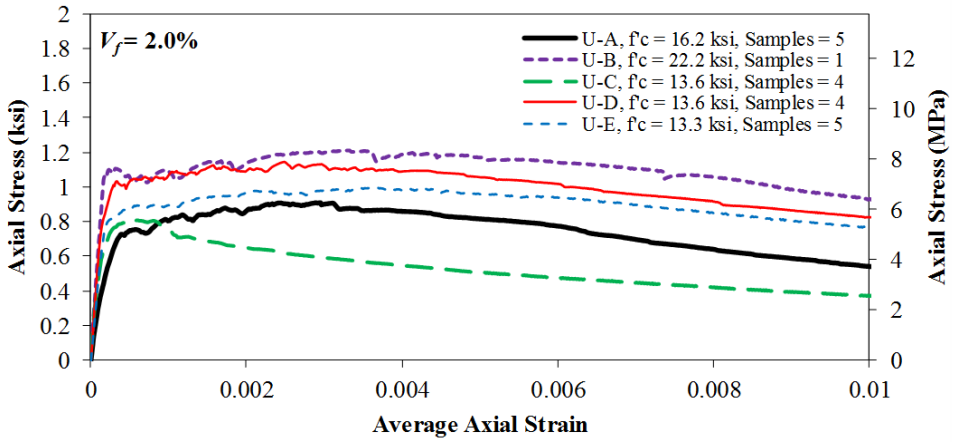

Figure 93. Graph. Comparison of average tensile stress-strain response for 2.0 percent fiber volume.

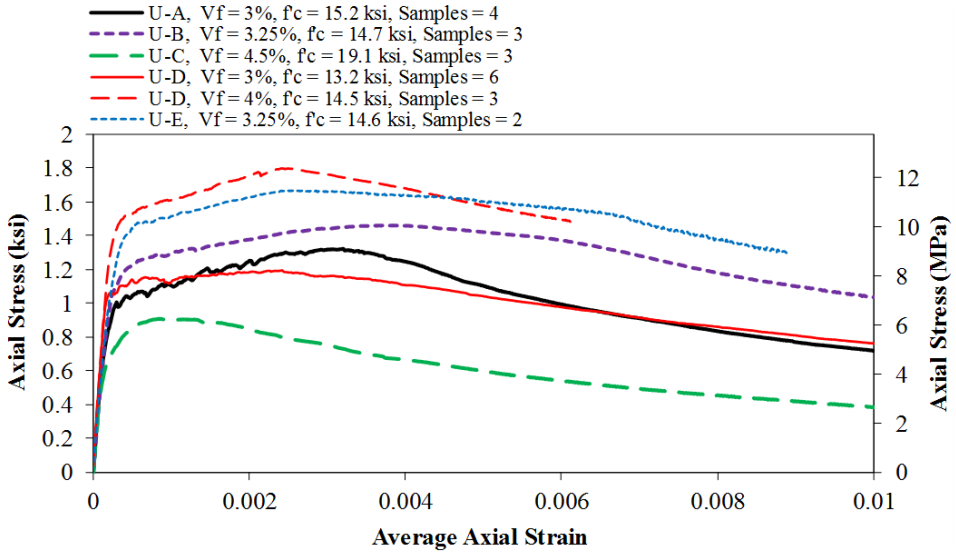

Figure 94. Graph. Comparison of average tensile stress-strain response for fiber volume contents between 3.0 percent and 4.5 percent.

Table 17: Summary of modulus of elasticity results from direct tensile testing.

ID	V_f (Percent)	Age (days)	Average Compressive Strength		Modulus of Elasticity			
					Average		Standard Deviation	
			ksi	(MPa)	ksi	(GPa)	ksi	(GPa)
U-A	2.00	6	16.2	(112)	5,661	(39.0)	1,184	(8.16)
U-A	3.00	5	13.9	(95.8)	6,767	(46.7)	148.1	(1.02)
U-A	3.00	5	15.2	(105)	6,972	(48.1)	253.0	(1.74)
U-A	3.00	27	18.6	(128)	7,541	(52.0)	314.5	(2.17)
U-A	3.00	29	21.4	(148)	7,555	(52.1)	174.0	(1.20)
U-B	2.00	6	16.3	(112)	5,630	(38.8)	415.8	(2.87)
U-B	2.00	28	22.2	(153)	6,268	(43.2)	*	*
U-B	3.25	5	14.7	(101)	5,891	(40.6)	137.2	(0.95)
U-C	2.00	1	9.4	(64.8)	6,127	(42.2)	88.4	(0.61)
U-C	2.00	4	13.6	(93.8)	5,981	(41.2)	1,294	(8.92)
U-C	4.50	1	10.7	(73.8)	5,955	(41.1)	181.0	(1.25)
U-C	4.50	15	19.1	(132)	6,340	(43.7)	214.9	(1.48)
U-D	1.00	1	13.7	(94.5)	5,424	(37.4)	*	*
U-D	1.00	7	19.8	(137)	7,173	(49.5)	7.4	(0.05)
U-D	2.00	1	13.6	(93.8)	6,943	(47.9)	238.5	(1.64)
U-D	2.00	7	18.6	(128)	8,137	(56.1)	1,066	(7.35)
U-D	2.50	1	14.0	(96.5)	7,063	(48.7)	547.1	(3.77)
U-D	3.00	1	13.2	(91.0)	6,823	(47.0)	108.7	(0.75)
U-D	3.00	1	12.3	(84.8)	6,744	(46.5)	492.9	(3.40)
U-D	3.00	7	18.2	(126)	7,400	(51.0)	136.2	(0.94)
U-D	3.00	7	17.7	(122)	7,500	(51.7)	98.0	(0.68)
U-D	4.00	1	14.5	(100)	6,933	(47.8)	215.3	(1.48)
U-D	4.00	7	18.0	(124)	7,394	(51.0)	158.2	(1.09)
U-E	2.00	4	13.3	(91.7)	4,947	(34.1)	147.3	(1.02)
U-E	2.00	14	17.2	(119)	5,365	(37.0)	75.1	(0.52)
U-E	3.25	5	14.6	(101)	5,685	(39.2)	169.5	(1.17)
U-E	3.25	13	17.4	(120)	5,778	(39.8)	236.5	(1.63)

* Data set only included a single, satisfactory sample

Table 18: Summary of first cracking results from direct tensile testing.

ID	V_f (percent)	Age (days)	Average Compressive Strength		Visual Pick Method						0.02 percent Offset Method					
					Cracking Stress				Cracking Strain		Cracking Stress				Cracking Strain	
					Average		Standard Deviation		Average	Standard Deviation	Average		Standard Deviation		Average	Standard Deviation
			ksi	(MPa)	ksi	(MPa)	ksi	(MPa)			ksi	(MPa)	ksi	(MPa)		
U-A	2.00	6	16.2	(112)	0.80	(5.50)	0.08	(0.58)	0.00052	0.00023	0.70	(4.83)	0.09	(0.59)	0.00033	0.00002
U-A	3.00	5	13.9	(95.8)	1.11	(7.63)	0.02	(0.15)	0.00037	0.00006	1.09	(7.49)	0.02	(0.16)	0.00036	0.00001
U-A	3.00	5	15.2	(105)	1.03	(7.12)	0.07	(0.47)	0.00034	0.00005	1.00	(6.87)	0.08	(0.58)	0.00034	0.00001
U-A	3.00	27	18.6	(128)	1.17	(8.03)	0.10	(0.72)	0.00044	0.00009	1.06	(7.31)	0.10	(0.72)	0.00034	0.00001
U-A	3.00	29	21.4	(148)	1.05	(7.25)	0.07	(0.51)	0.00020	0.00008	1.12	(7.75)	0.06	(0.43)	0.00035	0.00001
U-B	2.00	6	16.3	(112)	1.05	(7.22)	0.18	(1.25)	0.00044	0.00018	1.01	(6.98)	0.22	(1.51)	0.00038	0.00004
U-B	2.00	28	22.2	(153)	1.06	(7.32)	*	*	0.00018	*	1.10	(7.56)	*	*	0.00038	*
U-B	3.25	5	14.7	(101)	1.22	(8.38)	0.09	(0.61)	0.00040	0.00012	1.21	(8.35)	0.06	(0.44)	0.00041	0.00002
U-C	2.00	1	9.40	(64.8)	0.84	(5.79)	0.00	(0.00)	0.00020	0.00004	0.86	(5.91)	0.01	(0.04)	0.00034	0.00000
U-C	2.00	4	13.6	(93.8)	0.84	(5.79)	0.18	(1.25)	0.00048	0.00031	0.76	(5.22)	0.27	(1.83)	0.00032	0.00003
U-C	4.50	1	10.7	(73.8)	0.83	(5.72)	0.09	(0.59)	0.00031	0.00012	0.80	(5.51)	0.09	(0.65)	0.00033	0.00002
U-C	4.50	15	19.1	(132)	0.72	(4.98)	0.25	(1.70)	0.00027	0.00018	0.76	(5.27)	0.14	(0.95)	0.00032	0.00003
U-D	1.00	1	13.7	(94.5)	0.49	(3.37)	*	*	0.00018	*	0.45	(3.07)	*	*	0.00028	*
U-D	1.00	7	19.8	(137)	0.43	(2.94)	0.04	(0.25)	0.00021	0.00021	0.36	(2.49)	0.03	(0.23)	0.00025	0.00000
U-D	2.00	1	13.6	(93.8)	1.02	(7.03)	0.04	(0.29)	0.00032	0.00010	1.00	(6.92)	0.06	(0.42)	0.00034	0.00001
U-D	2.00	7	18.6	(128)	1.08	(7.45)	0.12	(0.83)	0.00026	0.00011	1.08	(7.44)	0.07	(0.45)	0.00033	0.00002
U-D	2.50	1	14.0	(96.5)	1.28	(8.83)	0.12	(0.83)	0.00033	0.00021	1.25	(8.61)	0.03	(0.23)	0.00038	0.00002
U-D	3.00	1	13.2	(91.0)	1.12	(7.70)	0.05	(0.33)	0.00027	0.00012	1.10	(7.61)	0.05	(0.33)	0.00036	0.00001
U-D	3.00	1	12.3	(84.8)	1.26	(8.68)	0.21	(1.46)	0.00036	0.00015	1.25	(8.58)	0.21	(1.42)	0.00038	0.00003
U-D	3.00	7	18.2	(126)	1.31	(9.01)	0.04	(0.25)	0.00042	0.00012	1.23	(8.50)	0.08	(0.54)	0.00037	0.00001
U-D	3.00	7	17.7	(122)	1.40	(9.64)	0.12	(0.80)	0.00029	0.00001	1.41	(9.70)	0.10	(0.72)	0.00039	0.00001
U-D	4.00	1	14.5	(100)	1.48	(10.2)	0.19	(1.29)	0.00042	0.00007	1.46	(10.1)	0.22	(1.51)	0.00041	0.00003
U-D	4.00	7	18.0	(124)	1.67	(11.5)	0.10	(0.71)	0.00042	0.00002	1.66	(11.5)	0.11	(0.79)	0.00043	0.00001
U-E	2.00	4	13.3	(91.7)	0.94	(6.51)	0.13	(0.88)	0.00030	0.00010	0.89	(6.15)	0.17	(1.20)	0.00038	0.00003
U-E	2.00	14	17.2	(112)	1.03	(7.08)	0.12	(0.83)	0.00026	0.00010	1.01	(6.98)	0.15	(1.05)	0.00039	0.00003
U-E	3.25	5	14.6	(95.8)	1.41	(9.75)	0.06	(0.43)	0.00048	0.00007	1.38	(9.53)	0.09	(0.64)	0.00044	0.00001
U-E	3.25	13	17.4	(105)	1.24	(8.54)	0.14	(0.97)	0.00046	0.00014	1.17	(8.09)	0.11	(0.75)	0.00040	0.00001

* Data set only included a single, satisfactory sample

Table 19: Summary of localization point and ultimate tensile strength from direct tensile testing.

ID	V_f (percent)	Age (days)	Average Compressive Strength		Localization Point (Visual Method)						Ultimate Point					
					Localization Stress				Localization Strain		Ultimate Stress				Strain at Ultimate	
					Average		Standard Deviation		Average	Standard Deviation	Average		Standard Deviation		Average	Standard Deviation
			ksi	(MPa)	ksi	(MPa)	ksi	(MPa)			ksi	(MPa)	ksi	(MPa)		
U-A	2.00	6	16.2	(112)	0.93	(6.42)	0.11	(0.77)	0.00347	0.00093	0.94	(6.47)	0.11	(0.78)	0.00287	0.00096
U-A	3.00	5	13.9	(95.8)	1.42	(9.76)	0.19	(1.30)	0.00279	0.00036	1.42	(9.76)	0.19	(1.30)	0.00280	0.00035
U-A	3.00	5	15.2	(105)	1.34	(9.22)	0.12	(0.80)	0.00321	0.00045	1.34	(9.25)	0.12	(0.81)	0.00311	0.00041
U-A	3.00	29	21.4	(128)	1.38	(9.48)	0.14	(0.94)	0.00291	0.00074	1.38	(9.51)	0.14	(0.94)	0.00280	0.00076
U-B	2.00	28	22.2	(148)	1.21	(8.32)	*	*	0.00356	*	1.21	(8.36)	*	*	0.00328	*
U-B	3.25	5	14.7	(112)	1.47	(10.1)	0.08	(0.57)	0.00392	0.00042	1.47	(10.1)	0.08	(0.58)	0.00388	0.00030
U-C	2.00	1	9.40	(153)	0.88	(6.07)	0.02	(0.11)	0.00060	0.00019	0.88	(6.10)	0.01	(0.07)	0.00038	0.00012
U-C	2.00	4	13.6	(101)	0.83	(5.73)	0.17	(1.15)	0.00102	0.00058	0.85	(5.87)	0.18	(1.27)	0.00051	0.00027
U-C	4.50	1	10.7	(64.8)	0.86	(5.95)	0.12	(0.82)	0.00136	0.00077	0.87	(6.00)	0.11	(0.78)	0.00096	0.00080
U-C	4.50	15	19.1	(93.8)	0.93	(6.42)	0.13	(0.89)	0.00141	0.00065	0.93	(6.44)	0.13	(0.88)	0.00125	0.00073
U-D	1.00	7	19.8	(73.8)	0.52	(3.58)	*	*	0.00085	*	0.52	(3.59)	*	*	0.00082	*
U-D	2.00	1	13.6	(132)	1.13	(7.76)	0.07	(0.50)	0.00392	0.00159	1.17	(8.09)	0.03	(0.21)	0.00247	0.00149
U-D	2.00	7	18.6	(94.5)	1.15	(7.90)	0.07	(0.51)	0.00385	0.00175	1.21	(8.31)	0.05	(0.37)	0.00262	0.00211
U-D	2.50	1	14.0	(137)	1.32	(9.12)	*	*	0.00446	*	1.37	(9.43)	*	*	0.00251	*
U-D	3.00	1	13.2	(93.8)	1.18	(8.16)	0.07	(0.46)	0.00297	0.00070	1.21	(8.32)	0.07	(0.45)	0.00201	0.00068
U-D	3.00	1	12.3	(128)	1.37	(9.45)	0.28	(1.91)	0.00271	0.00048	1.38	(9.50)	0.27	(1.87)	0.00214	0.00081
U-D	3.00	7	18.2	(96.5)	1.36	(9.36)	0.05	(0.33)	0.00457	0.00072	1.42	(9.81)	0.04	(0.26)	0.00198	0.00076
U-D	3.00	7	17.7	(91.0)	1.69	(11.7)	0.19	(1.30)	0.00432	0.00080	1.70	(11.7)	0.18	(1.25)	0.00402	0.00052
U-D	4.00	1	14.5	(84.8)	1.81	(12.5)	0.13	(0.88)	0.00288	0.00071	1.81	(12.5)	0.13	(0.89)	0.00274	0.00076
U-D	4.00	7	18.0	(126)	1.82	(12.5)	0.02	(0.13)	0.00328	0.00024	1.82	(12.5)	0.02	(0.13)	0.00326	0.00024
U-E	2.00	4	13.3	(122)	1.01	(6.96)	0.16	(1.10)	0.00404	0.00107	1.02	(7.06)	0.15	(1.00)	0.00321	0.00172
U-E	2.00	14	17.2	(100)	1.27	(8.76)	0.18	(1.27)	0.00506	0.00173	1.27	(8.78)	0.19	(1.28)	0.00498	0.00186
U-E	3.25	5	14.6	(124)	1.71	(11.8)	0.14	(0.95)	0.00392	0.00206	1.71	(11.8)	0.13	(0.93)	0.00375	0.00181
U-E	3.25	13	17.4	(91.7)	1.50	(10.4)	0.11	(0.77)	0.00376	0.00008	1.50	(10.4)	0.11	(0.77)	0.00377	0.00008

* Data set only included a single, satisfactory sample

BEHAVIOR IN INDIRECT TENSION (SPLIT CYLINDER TENSION TESTING)

Test Methods and Specimens Preparation

Split cylinder-type tensile test specimens were constructed using 4-inch (102-mm) nominal diameter cylinders with an 8-inch (203-mm) nominal length. During casting, each cylinder mold was filled with a single lift of UHPC. Once filled, cylinders were placed on a concrete vibrating table for 5 to 15 seconds to remove entrapped air. The consolidated cylinders were subsequently capped and allowed to cure for 24 hours prior to being stored in the laboratory. SCTT specimens were cast from the same batch of UHPC as DTT specimens and their corresponding compression test cylinders.

The cylinders were prepared for testing by grinding both ends to create parallel surfaces through the use of a fixed end grinder. After preparation, the cylinders exhibited length to diameter ratios of approximately 1.9. Prior to testing, each cylinder was measured; diameter and length measurements were taken at three different locations in order to determine the average geometry of the sample.

Cylinder specimens were tested using a modified version of ASTM C496 (ASTM C496 / C496M-11 2004), which was originally proposed by Nanni (1988), and later modified by Graybeal (2006). The set-up for SCTT specimens is shown in figure 95. A pair of LVDTs were used to capture the total lateral deformation across the middle of the cylindrical specimen. LVDTs were attached to a spring-loaded clamp fixture that was mounted on the outside of the cylinder which transferred the deformation to the transducers. The splitting tension test was performed by applying compressive line loads along two opposing lengths on the side of the cylinder. Tensile stresses and lateral expansion are generated perpendicular to the direction of the compressive forces. Load was applied in displacement control such that splitting tensile stress loading rate was 508 psi/min (3.5 MPa/min); this rate was increased from 145 psi/min (1.0 MPa/min), which is specified in the original ASTM C496 standard, to reduce the time required to complete a single test. During testing, data was logged digitally using a data acquisition system that captured load from the test frame load cell, actuator displacement, and displacements from the LVDTs.

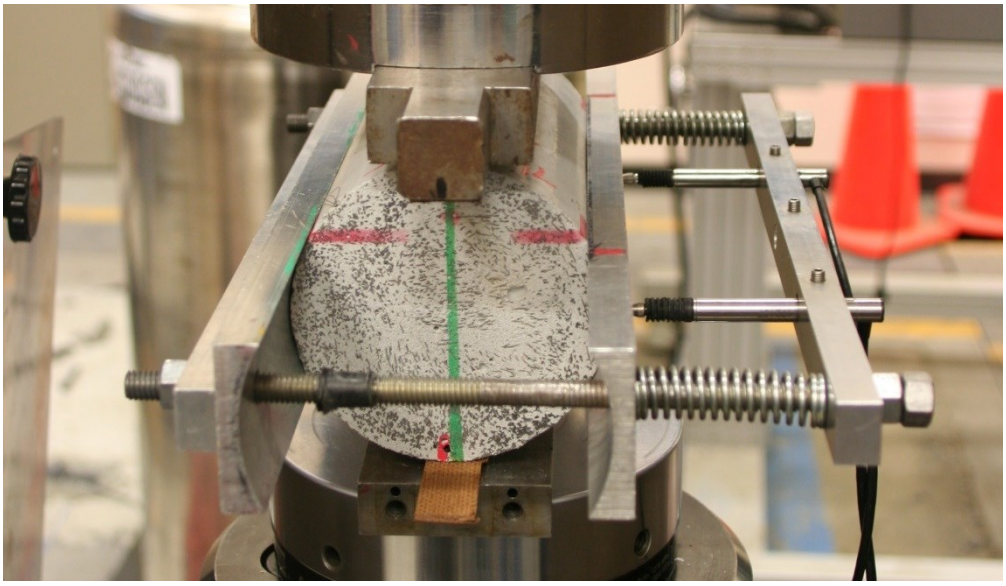

Figure 95. Photo. Split cylinder tension test (SCTT).

Results

The primary results determined from splitting cylinder tensile tests were the splitting tensile stress at first cracking and the peak splitting tensile stress. Both results were determined using the equation shown in figure 96. Figure 97 illustrates the splitting tensile stress versus lateral deformation behavior that was observed during most tests. The curve is initially linear until the first cracking stress is reached. At which point, an abrupt discontinuity in the stress-deformation curve occurs. This is a result of a slight, instantaneous lateral deformation due to crack formation. Figure 98 shows a photo of a specimen shortly after first cracking occurs. After this point, the splitting tensile stress typically continues to increase until the peak splitting tensile strength is reached. After the peak splitting tensile strength is reached the stress slowly begins to decline as the specimen undergoes significant lateral deformation. This post-peak deformation is a result of fiber bridging and crack localization. This can be observed in figure 99 which shows a specimen after the completion of the test. A wide, vertical crack can be observed where a number of fibers cross the cracking plane.

$$f_{st} = \frac{2P}{\pi l D}$$

Figure 96. Equation. Splitting tensile stress as defined by ASTM C496.

Where

P = applied load

l = specimen length

D = Specimen diameter

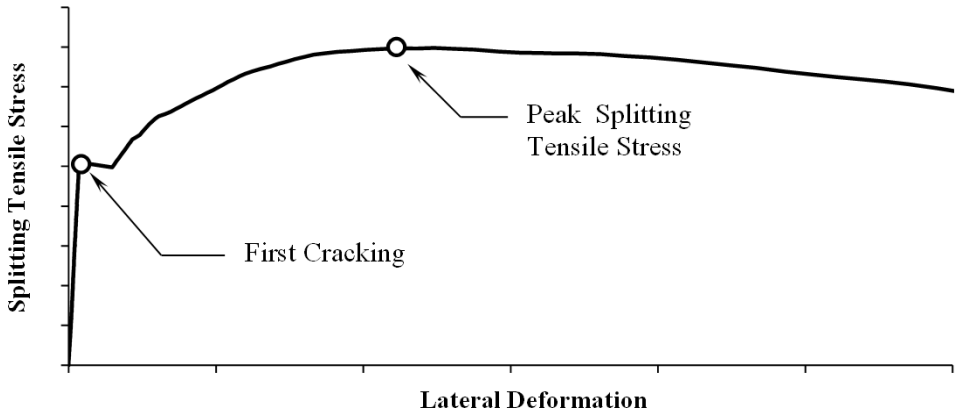

Figure 97. Illustration. Typical stress-deformation behavior of a splitting tensile test specimen.

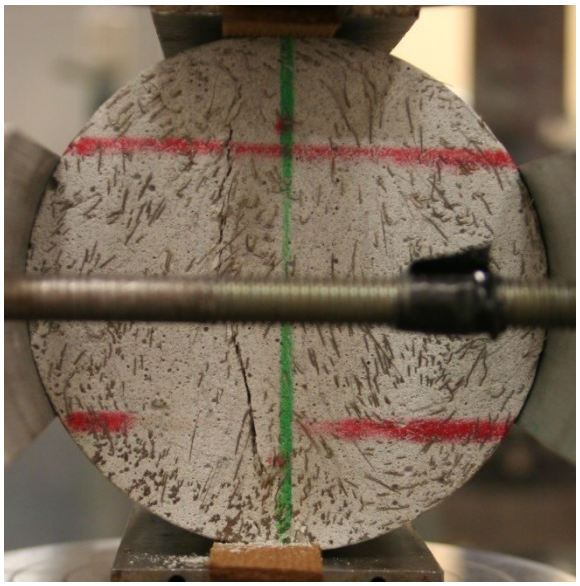

Figure 98. Photo. Splitting cylinder tensile test specimen shortly after first cracking.

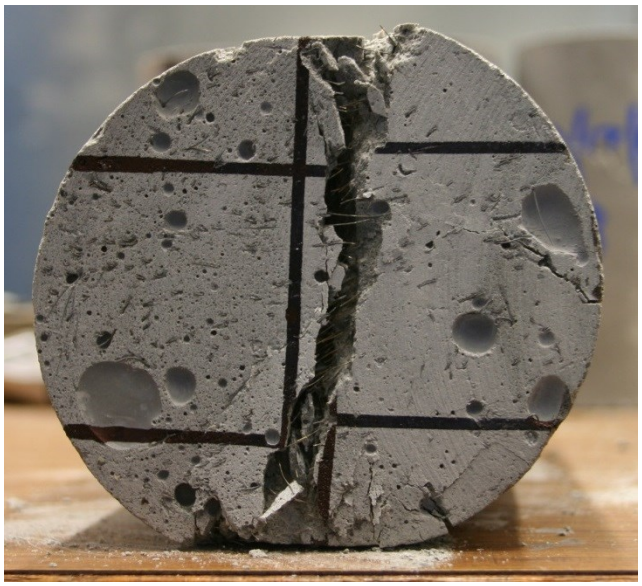

Figure 99. Photo. Splitting cylinder tensile test specimen shortly after failure.

A total of 85 splitting tensile tests were conducted with different fiber volume fractions, which is denoted V_f, and at different ages. Table 20 provides a summary of the results and the variables associated with each specimen set. A comparison of select splitting tensile test results are shown in figure 100. The data shown in this figure represents UHPCs with compressive strength between 13.2 ksi (91 MPa) and 16.3 ksi (112 MPa) at the time of testing. The data is presented in two groups: specimens containing 2.0 percent fiber by volume and those containing volume fractions other than 2.0 percent. Error bars represent ± one standard deviation. Each UHPC, regardless of

type and fiber volume fraction, exhibited approximately the same first cracking strength; the first cracking strength was approximately 1.0 ksi (6.9 MPa). The peak splitting tensile stress, in each case, was significantly greater than the first cracking strength. Lastly, there appeared to be little correlation between fiber volume fraction and the peak splitting tensile strength. Figure 101 presents the relationship between fiber volume fraction and the first cracking and peak splitting tensile strength. Aside from the apparent decrease is key stress values when U-D with 1.0 percent fiber volume was tested, there seems to be little correlation between the two strength values and the fiber volume fraction.

Table 20. Summary of results from splitting tensile testing.

ID	V_f (percent)	Age (days)	Average Compressive Strength		First Cracking Strength				Peak Splitting Tensile Strength			
					Average		Standard Deviation		Average		Standard Deviation	
			ksi	(MPa)	ksi	(MPa)	ksi	(MPa)	ksi	(MPa)	ksi	(MPa)
U-A	3	5	13.9	(95.8)	1.04	7.20)	0.18	(1.24)	2.57	(17.7)	0.25	(1.70)
U-A	3	5	15.2	(105)	1.12	(7.72)	0.16	(1.11)	2.56	(17.6)	0.21	(1.44)
U-A	3	29	21.4	(148)	1.00	(6.86)	0.06	(0.42)	2.57	(17.7)	0.16	(1.10)
U-B	2	5	16.3	(112)	1.05	(7.21)	0.11	(0.75)	1.88	(13.0)	0.29	(1.99)
U-B	3.25	5	14.7	(101)	0.91	(6.27)	0.08	(0.55)	1.95	(13.4)	0.15	(1.04)
U-C	2	1	9.40	(64.7)	1.00	(6.90)	0.04	(0.25)	1.93	(13.3)	0.19	(1.34)
U-C	2	4	13.6	(93.9)	0.98	(6.72)	0.07	(0.49)	2.33	(16.1)	0.11	(0.74)
U-C	4.5	1	10.8	(74.2)	0.92	(6.35)	0.07	(0.47)	2.08	(14.3)	0.09	(0.65)
U-C	4.5	15	19.1	(131)	1.09	(7.53)	0.04	(0.30)	3.04	(20.9)	0.26	(1.80)
U-D	1	1	13.7	(94.6)	0.90	(6.20)	0.12	(0.82)	1.44	(9.92)	0.11	(0.76)
U-D	1	7	19.8	(137)	0.77	(5.34)	0.10	(0.66)	1.74	(12.0)	0.09	(0.62)
U-D	3	1	12.3	(84.9)	1.07	(7.34)	0.18	(1.27)	2.62	(18.1)	0.27	(1.85)
U-D	3	7	17.7	(122)	1.01	(6.96)	0.07	(0.51)	2.54	(17.5)	0.25	(1.70)
U-D	3	1	13.2	(90.6)	0.92	(6.32)	0.07	(0.47)	2.08	(14.4)	0.20	(1.35)
U-D	3	7	18.2	(125)	1.00	(6.89)	0.07	(0.50)	2.56	(17.7)	0.28	(1.90)
U-D	4	1	14.5	(99.6)	0.95	(6.56)	0.09	(0.60)	2.16	(14.9)	0.20	(1.40)
U-E	2	4	13.3	(91.3)	1.09	(7.49)	0.19	(1.32)	2.67	(18.4)	0.26	(1.80)
U-E	2	21	17.3	(119)	1.02	(7.03)	0.08	(0.53)	2.57	(17.7)	0.25	(1.71)
U-E	3.25	5	14.6	(100)	0.94	(6.47)	0.07	(0.51)	2.10	(14.4)	0.23	(1.62)
U-E	3.25	13	17.4	(120)	1.01	(6.99)	0.08	(0.52)	2.73	(18.8)	0.18	(1.26)

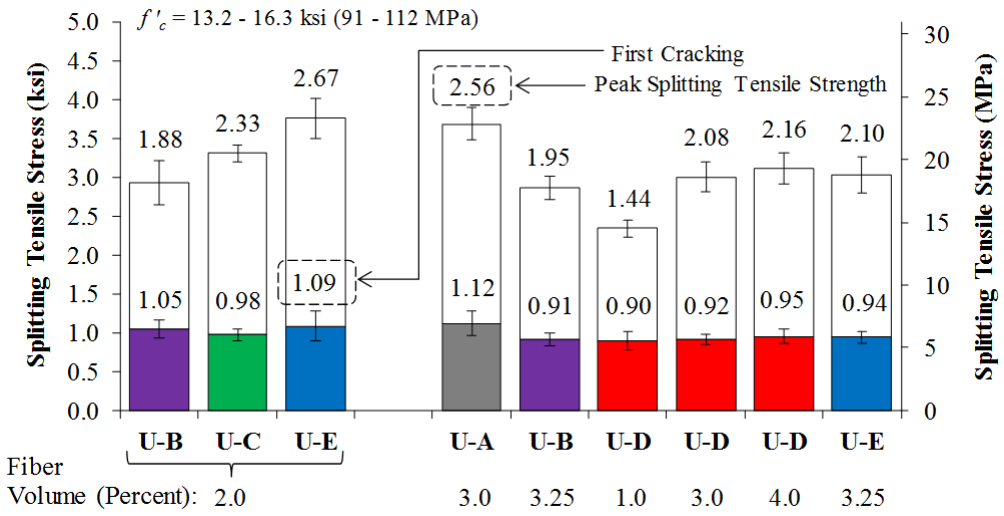

Figure 100. Graph. Comparison of select splitting tensile test results.

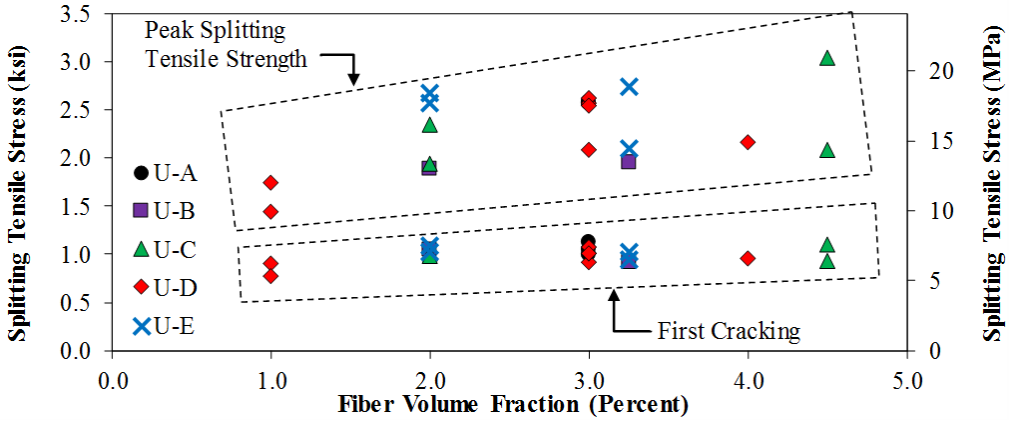

Figure 101. Graph. Comparison of splitting tensile behavior as a function of fiber volume fraction.

UHPC-TO-CONCRETE BOND BEHAVIOR

Test Methods and Specimens Preparation

The interface bond strength between precast concrete and UHPC was assessed using two different methods based on current ASTM standards. Figure 102 and figure 103 show illustrations of the two test methods used to evaluate bond strength. The flexural beam bond test (shown in figure 102) was based on ASTM C78 (ASTM C78 / C78M-16 2016), which is originally intended for measuring the modulus of rupture of concrete using a 6 inch x 6 inch x 21 inch (152 x 152 x 534 mm) prism specimen. The direct tension bond pull-off test (shown in figure 103) was based on ASTM C1583 (ASTM C1583 / C1583M-13 2013), which is typically used to evaluate the bond between concrete and repair materials.

Previous studies conducted by the authors have shown that the flexural beam bond test method is a viable option for testing bond strength between two materials provided that the bond strength is not especially low (De la Varga, Haber, and Graybeal 2016); bond strengths should be greater than 100 psi (0.69 MPa). Specimens were created by first casting a precast concrete beam half, 10.5 inches (267 mm) in length, with an exposed aggregate finish on one end. The exposed aggregate finish was created using an in-form paint-on retarding agent on one face of the beam mold, which was subsequently pressure washed after concrete was cast and allowed to cure for 24 hours. A representative photo of the exposed aggregate surface is shown in figure 104. The precast concrete half was allowed to cure for at least 28 days before casting UHPC against the exposed aggregate face. Prior to casting UHPC, the exposed aggregate surface was cleaned using pressurized air to remove dirt and grit, and was left dry prior to casting UHPC; thus, interface pre-wetting was not employed. Specimens were left in their molds until the predetermined test dates, which occurred once the UHPC had cured for 7 and 14 days; in some cases a third set of specimens were tested well after 14 days. The test configuration and loading rates were taken directly from the ASTM C78 standard. Specimens were loaded in third-point bending with a shear span of 6 inches (153 mm). Load was applied such that the stress at the extreme tension fiber consistently increased at a rate between 125 and 175 psi/min (0.86 and 1.21 MPa/min) until rupture occurred. After failure, the maximum load and failure location were recorded. Three beam specimens were tested for each UHPC age.

The test specimens for the direct tension pull-off test were created by first casting a concrete base slab measuring 36 inches x 36 inches (914 mm x 914 mm) square by 4 inches (102 mm) thick. Similar to beam specimens, the precast concrete had an exposed aggregate finish and was allowed to cure at 28 days prior to casting a 2-in. (51-mm) thick UHPC topping upon the exposed aggregate surface of the concrete base slab. In preparation for testing, 2-inch (51-mm) diameter pull-off discs were glued to the UHPC surface, and a partial core was drilled at each disc location. The partial core passed through the UHPC layer and 1 inch into the concrete base slab. A specialized pull-off test fixture was used to apply the load according to the ASTM C1583 standard and to record data. Tensile load is applied to the steel disc at a constant rate of 5 ± 2 psi/sec (34.5 ± 13.8 kPa/sec) until failure occurred. The failure load and the failure mode were recorded, and the nominal tensile stress could be calculated. If failure occurred at the grout-concrete interface, then the true bond strength could be assessed. If failure occurs in either the concrete substrate or UHPC material, then the tensile strength of the failing material could be assessed and the interface bond strength could be recognized to be higher than the value achieved. Finally, the test was rejected if failure occurred at the epoxy-UHPC interface. At least three valid tests should be completed and the results averaged for any particular failure mode.

Both series of tests used ready-mix concrete from the same truck, which was delivered to TFHRC. The concrete had a specified 28-day compressive strength of 6 ksi (41.3 MPa). Table 21 lists the constituents of the ready-mix concrete, and the average 28 day mechanical properties are reported in table 22.

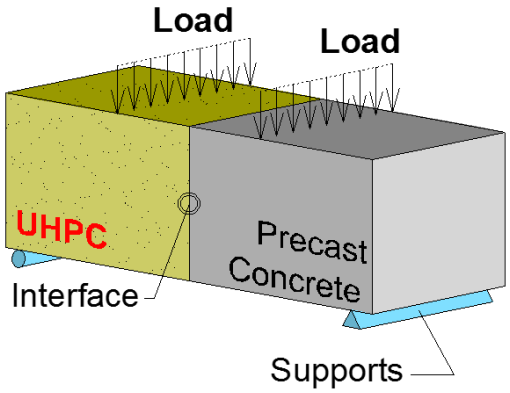

Figure 102. Illustration. Flexural beam bond test based on ASTM C78.

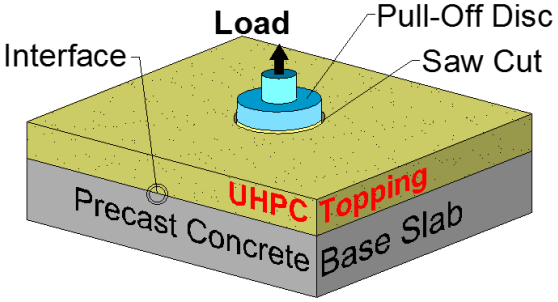

Figure 103. Illustration. Direct tension bond pull-off test based on ASTM C1583.

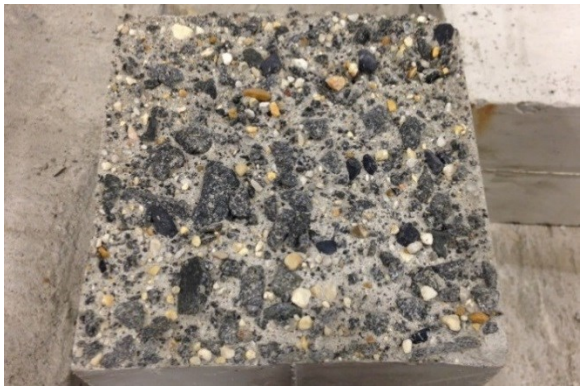

Figure 104. Photo. Representative photo of exposed aggregate interface on precast concrete.

Table 21. Constituents of ready-mix concrete used in bond tests.

Component	Weight / Cubic Yard	
	US Units	SI Units
Sand	1,018 lb	461.6 kg
No. 57 Stone	1,451 lb	658.2 kg
Cement (Type I/II)	407 lb	73.8 kg
Slag	163 lb	73.8 kg
Water	115 lb	51.9 kg
Air-Entrainer	2.25 oz	66.5 ml
Retarder	11.5 oz	340.1 ml
High Range Water Reducer	22.8 oz	672.7 ml

Table 22. Average 28 day mechanical properties for concrete used in bond tests.

Material Property	Average, ksi (MPa)	Standard Deviation, ksi (MPa)	Coefficient of Variation	Test Method
Compressive Strength	6.18 (42.6)	0.03 (0.18)	0.004	ASTM C39
Tensile Strength	0.559 (3.85)	0.05 (0.35)	0.091	ASTM C496
Modulus of Rupture	0.624 (4.29)	0.04 (0.28)	0.065	ASTM C78

Results

Flexural Beam Bond Tests

The peak flexural tension stress achieved by a bond test beam was determined using the equation shown in figure 105. All specimens tested failed in flexure within the constant moment region of the beam, and failure predominantly occurred within the precast concrete substrate. Figure 106 shows a representative photo of a bond test beam after failure. This photo illustrates that failure of the specimen occurred within the precast concrete; concrete is still bonded to UHPC after failure. Figure 107 presents the peak flexural tension stress achieved prior to failure. Each bar on the chart represents the average of three individual specimens. Error bars represent ± one standard deviation. A dashed line denotes the minimum modulus of rupture (MOR) of substrate concrete as determined by ASTM C78. This differs from that reflected in table 22 because the substrate concrete was over 70 days old when bond testing commenced. In each case, the peak flexural tension stress achieved by bond test beams was less than that of the baseline MOR result. Furthermore, the peak flexural tension stress prior to failure was not substantially affected by the age of UHPC.

$$f_{ft} = \frac{PL}{b\,h^2}$$

Figure 105. Equation. Peak flexural tensile stress as defined by ASTM C78.

Where

P = maximum applied load

L = simply-supported length of the beam

b = beam width

h = beam depth

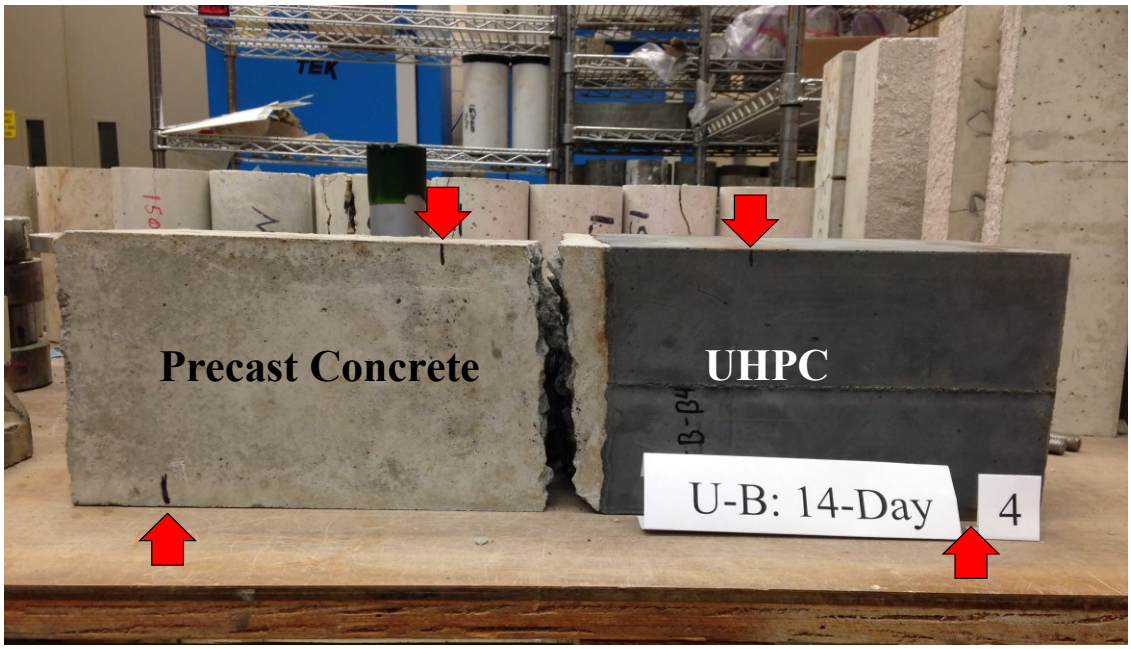

Figure 106. Photo. Representative photo from flexure beam bond tests after failure.

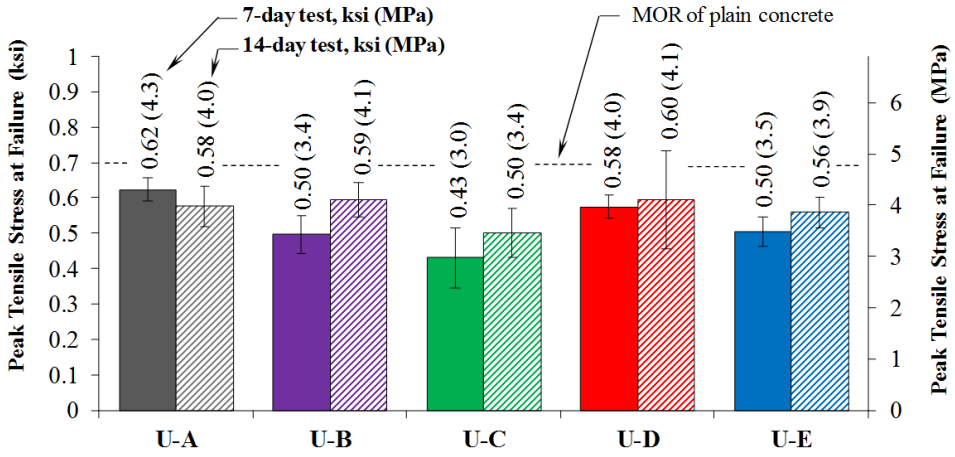

Figure 107. Graph. Results from flexural beam bond tests.

Direct Tension Pull-Off Bond Tests

As previously noted, the pull-off test specimen was formed by drilling a partial core perpendicular to the surface, and penetrating down to the concrete material, approximately 1 inch (25 mm) below the UHPC-concrete interface (as shown in figure 103). A tensile load is applied to a previously glued steel disc until failure occurs. The failure load and the failure mode were recorded and the nominal tensile stress was calculated. Specimens exhibited two primary failure modes which are shown in figure 108 and figure 109. If failure occurred at the UHPC-concrete interface (shown in figure 108), then the true bond strength could be assessed. If failure occurs in the concrete substrate (shown in figure 109), then the tensile strength of the concrete material could be assessed and the interface bond strength could be recognized to be higher than the value achieved. For the material

(either substrate concrete or UHPC) tensile tests, the partial core did not penetrate more than 1 inch (51 mm) into each material from the top surface.

Figure 108. Photo. Interface failure mode in direct tension pull-off tests.

Figure 109. Photo. Substrate failure mode in direct tension pull-off tests.

Figure 110 and figure 111 show the results obtained at 7 and 14 days of UHPC age, respectively. As observed in figure 110, the bond strength (interface failure) of most of the UHPCs is very similar to each other at 7 days, with values at about 400 psi (2.76 MPa), except for U-B that exhibits bond strengths of about 600 psi (4.14 MPa). Figure 111 shows that the 14-day bond strength does not increase with respect to that at 7 days. In fact, two of the UHPCs (U-C and U-E) show decreased bond strength at 14 days compared to 7 days. In regard to the tensile strength of the UHPC materials, all mixes range between 750 psi (5.2 MPa) and 1000 psi (6.9 MPa) at the ages tested. These values are considered to be the ultimate tensile strength.

Given the fact that bond is affected by several material parameters (e.g., rheology, fineness, tensile strength, etc.), some differences in the bond strength are expected, due to the differences in the materials' formulations. (Silfwerbrand and Beuhausen 2005) However, the UHPC materials selected in this study exhibit similar bond strengths at the ages tested, except for U-B which seems to perform slightly better. It is important to note that interface failure (bond strength) occurs at approximately the same stress level as the substrate failure, indicating that the bond strength of these materials might be mainly driven by the tensile strength of the concrete substrate used. A stronger concrete substrate would perhaps be more effective in evaluating the actual bond strength of these materials.

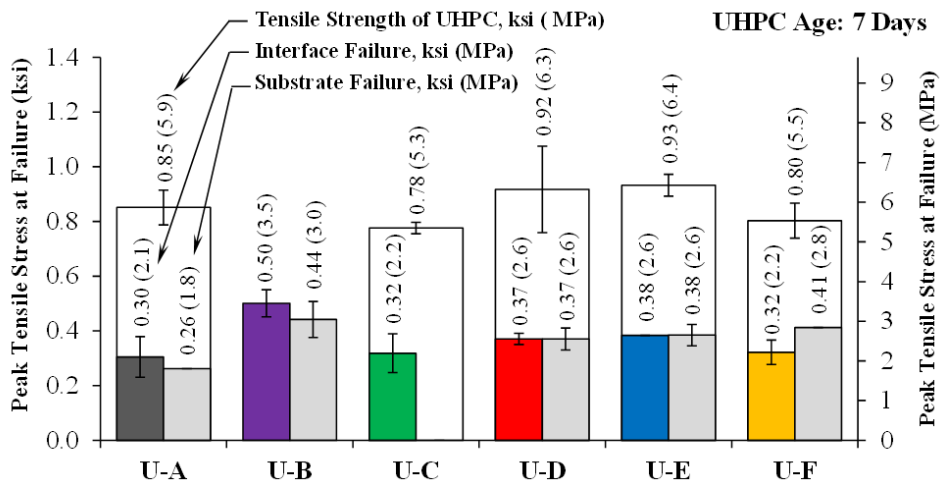

Figure 110. Graph. Results from 7-day direct tension pull-off testing.

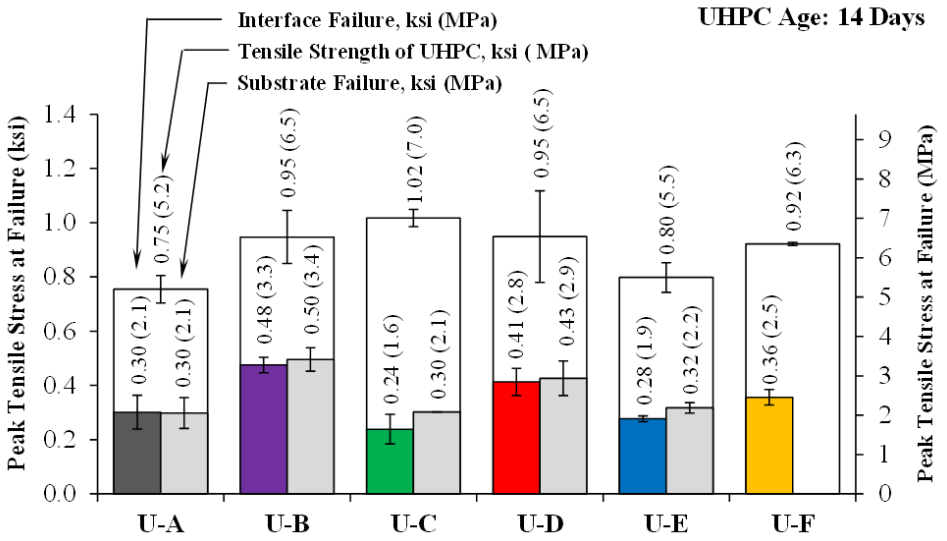

Figure 111. Graph. Results from 14-day direct tension pull-off testing.

CHAPTER 5. CREEP AND SHRINKAGE

INTRODUCTION

Creep and shrinkage of concrete results in time- and environmentally-dependent deformations over the service life of a structural element. These deformations, which can become excessive under certain circumstances, can result in cracking of concrete or excessive element deflections. Creep and shrinkage of concrete are complex mechanisms, and previous research has shown that there are a number of factors that influence the creep and shrinkage behavior of a given concrete mixture. (ACI Committee 209 2005) The tests and results presented in this chapter were intended to provide some initial knowledge as to the creep and shrinkage behavior of UHPC-class materials.

The first part of the chapter discusses creep (and the associated shrinkage) of UHPC. Creep is a time-dependent deformation induced by a sustained load. The structure-scale effects of creep include long-term element deformations as well as prestressing force losses in pre-tensioned concrete elements. There are numerous factors that influence the creep rate of concrete including age at loading, degree of hydration, pore water content, temperature, humidity, and many others. (Bazant and Wittmann 1982)

Creep of UHPC has been studied by numerous research groups. (Graybeal 2006a; Garas, Kurtis, and Kahn 2012; Victor Y. Garas, Kahn, and Kurtis 2009; Burkart and Muller 2008; Koh et al. 2011; Staquet and Espion 2004; Acker 2004; Flietstra 2011) In general, it is suggested that UHPC materials will undergo less creep than conventional concrete, due mainly to the higher strength development and modulus of elasticity. Some of these authors also recognize that creep performance may change if the material is cured in different conditions (e.g., steam-curing).

The second portion of this chapter focuses on evaluating autogenous and drying shrinkage of UHPC. Volume changes (primarily shrinkage) are accompanied by the loss of moisture from the capillary pores. In this regard, autogenous shrinkage is a deformation not caused by external influences such as moisture transfer or temperature changes. In other words, the material would be maintained in sealed and isothermal conditions. Autogenous shrinkage can then be thought of as an "internal drying" caused by the chemical shrinkage that occurs in the cement hydration reaction when cement is mixed with water. (Jensen and Hansen 2001; Le Chatelier 1900; R. G. L'Hermite 1960) This type of shrinkage is more common in low water-to-cement (*w/c*) ratio or low water-to-binder (*w/b*) ratio concretes and can be mitigated using additional water during external curing. On the other hand, deformations caused by drying shrinkage are a result of moisture transfer (i.e., moisture loss) from the capillary pores to the environment during the concrete hardened stage. If the environmental conditions are harsh (e.g., high temperature and low relative humidity), the hardened concrete will tend to dry faster, thus causing high drying shrinkage. Similarly, if the concrete is designed with a high w/c (that is, a larger pore size microstructure), high shrinkage will also be observed, since larger pores tend to dry faster than smaller pores. (Bissonnette, Pierre, and Pigeon 1999)

CREEP AND ASSOCIATED SHRINKAGE

Test Methods and Specimens Preparation

The creep testing was conducted according to ASTM C512 with the exception of maximum recommended load level; ASTM C512 recommends a maximum load level of $0.4f'_c$ where f'_c is measured at the initiation of sustained loading. (ASTM C512-15 2015, 512) Creep of UHPC was evaluated at two different sustained load levels. The target sustained loads were $0.4f'_c$ and $0.65f'_c$, which are herein referred to as "low-level" and "high-level" sustained load targets, respectively. The low-level target was selected in accordance with the maximum load recommended by ASTM C512. The high-level target was selected to be representative of the compressive stress limit at prestress transfer in the 2016 Interim Revisions to the AASHTO LRFD Bridge Design Specifications. (American Association of State Highway and Transportation Officials 2016) UHPC samples subjected to low-level sustained load were considered "mature" at the time of loading. That is, these samples had cured for 56+ days prior to testing and had compressive strengths greater than 17 ksi (117 MPa). UHPC samples subjected to high-level sustained load were considered "young" at the time of loading. That is, these samples had cured for 7 days or less prior to testing and had compressive strengths between 13 ksi (89.6 MPa) and 16.5 ksi (113 MPa). The design guidance provided in the *Design and Construction of Field-Cast UHPC Connections* suggests that UHPC should have a compressive strength of at least 14 ksi (96.5 MPa) prior to introducing structural loads. Thus, the $0.65f'_c$ sustained load target was applied to samples with compressive strengths in the vicinity of 14 ksi (96.5 MPa) to represent sustained stresses at prestressing force transfer. Each UHPC tested was dosed with 2-percent fiber by volume. Lastly, it should be noted that materials U-D and U-F were not tested, Instead, for U-D, data from a previous study conducted at TFHRC was used for comparison purposes. (B. A. Graybeal 2006a)

An individual test required four 4 inch by 8 inch (102 mm by 204 mm) and three 3 inch by 6 inch (76 mm by 152 mm) cylinders. Cylinders were cast using the methods described in Chapter 3, and the ends of all cylinders were ground to within 0.5 degree of parallel. After end preparation, cylinders were stored in a controlled environmental room where the relative humidity was 50 ± 5 percent and the temperature was 73.4 ± 3.6 °F (23 ± 2 °C). The 4 inch by 8 inch (102 mm by 204 mm) cylinders were instrumented with two detachable mechanical strain gauge (DEMEC) points with a nominal gauge length of 6 inches (152 mm) at three evenly spaced locations around the circumference (shown in figure 112). Two of the instrumented 4 inch by 8 inch (102 mm by 204 mm) cylinders were installed into the loading frames for creep testing, and remaining two cylinders were used as unloaded control specimens to measure simultaneous shrinkage. The ground ends the shrinkage specimens were sealed with epoxy to create the same volume-to-surface ratio as specimens installed in the creep frames; the epoxy coating was installed at initiation of creep testing. The 3 inch by 6 inch (76 mm by 152 mm) cylinders were used to test the compressive strength at the time of initial loading.

Creep testing was completed using four specially-design hydraulically actuated load frames (shown in figure 112). Unlike creep frames that employ springs, these frames are able to maintain sustained load for extended periods of time. The frames were located in an environmentally controlled room where the relative humidity was 50 ± 5 percent and the temperature was 73.4 ± 3.6 °F (23 ± 2 °C). Each frame contained two samples subjected to the low-level sustain load target and two subjected to the high-level sustained load target. Given that samples subjected to low- and

high-level target loads had different compressive strengths, a single frame could achieve the target sustained stresses using an applied load of 115 kips (511 kN). Additional half-height cylinders were placed at the bottom and top of the stacked cylinders to act as loading blocks.

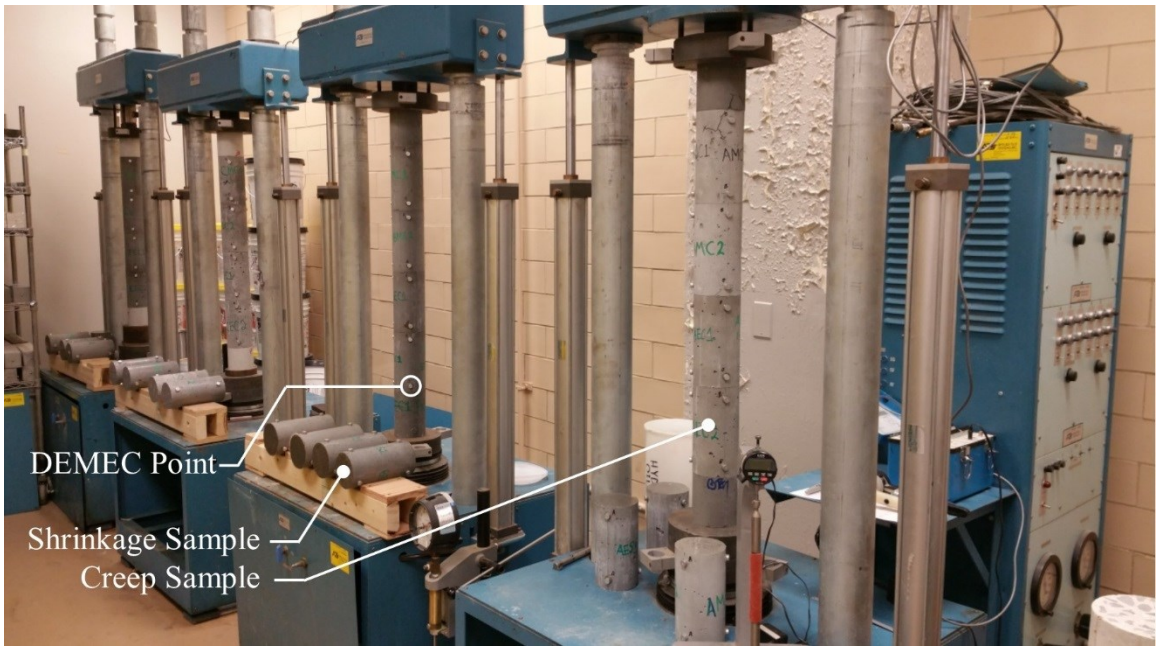

Figure 112. Photo. Creep cylinders in load frame and unloaded shrinkage cylinders.

Creep and shrinkage strains were determined using a micrometer (shown in figure 113). Prior to capturing measurements, the micrometer would calibrated using a 6-inch (152-mm) gauge length bars. Once the micrometer was positioned over the 6-inch (152-mm) gauge length the measurement would be zeroed. The change in deformation occurring in creep and shrinkage samples could then be measured across DEMEC points. For a single sample, the deformations recorded from the three DEMEC locations would be used to calculate the average strain. Measurements were taken immediately before and after loading, two to six hours after loading, then daily for one week, weekly for 13 weeks, and monthly thereafter. Measurements for shrinkage were taken simultaneously with those recorded for the loaded creep specimens.

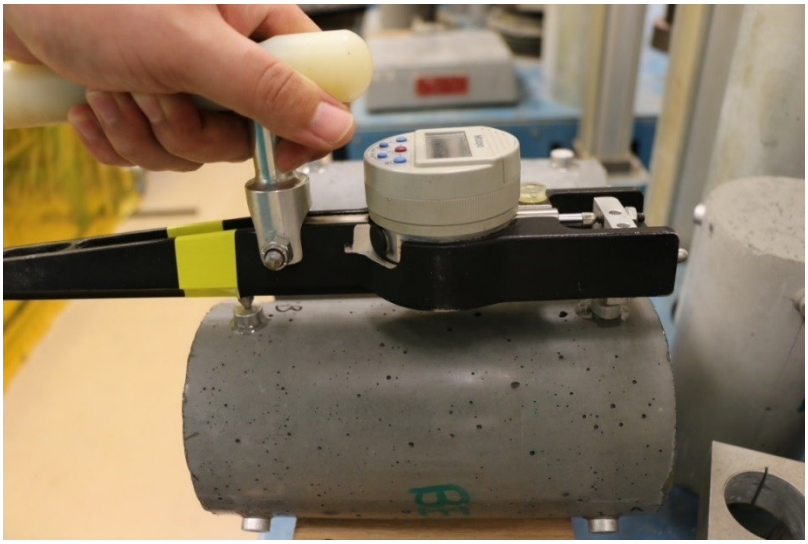

Figure 113. Photo. Measuring deformation along DEMEC points using a micrometer.

Results

A summary of results is presented in table 23 and table 24 for high- and low-level sustained loading, respectively. It should be noted that the achieved sustained stresses vary slightly from target values. For specimens tested under the high-level sustained load, achieved sustained stresses were between $0.58f'_c$ and $0.67f'_c$. For specimens tested under the low-level sustained load, achieved sustained stresses were between $0.37f'_c$ and $0.53f'_c$. The initial elastic strains reported in table 23 and table 24 were captured within 5 minutes of applying load to the specimens.

As noted by ACI Committee 209 – *Creep and Shrinkage of Concrete*, creep and shrinkage strains are typically assumed to be additive. Committee document 209.2R-08, Section 1.3.1 states:

> *Two nominally identical sets of specimens are made and subjected to the same curing and environment conditions. One set is not loaded and is used to determine shrinkage, while the other is generally loaded from 20 to 40-percent of the concrete compressive strength. Load induced strains are determined by subtracting the measured shrinkage strains on the non-loaded specimens from the strains measured on the loaded specimens. Therefore, it is assumed that the shrinkage and creep are independent of each other. (*ACI Committee 209 2009)

Thus, the creep strain, ε_{cp}, was calculated by subtracting the shrinkage strain, ε_{sh}, from the total load induced strain, ε_{total}. The long-term creep coefficient, C_u, was calculated by dividing the final creep strain by the initial elastic strain. The creep coefficients for samples tested in this study subjected to high-level sustained load ranged from 1.37 to 2.47. These creep coefficients were substantially higher that that reported by Graybeal 2006c. The testing conducted by Graybeal investigated the creep behavior of material U-D with the creep testing starting at 28-days after casting; at this time the UHPC had attained more than 90 percent of its full compressive strength. The long-term creep coefficient of material U-D was 0.78 when subjected to a curing environment and sustained applied stress similar to those employed in this study for high-level loading; this is reported in table 23. It is important to note, however, that the long-term creep coefficient reported

by Graybeal for U-D was after 372 days, and the samples tested in this study were subjected to longer periods of sustained load. The creep coefficients for samples tested in this study subjected to low-level sustained load ranged from 0.70 to 1.17. Typical creep coefficients for mature conventional concretes range between 1.5 and 3.0. (Meyers, Branson, and Schumann 1972)

Table 23. Summary of results for specimens subjected to high-level sustained loading.

UHPC	Compressive strength at the beginning of testing ksi (MPa)	Sustained Creep Stress		Initial Elastic Strain (με)	Final Creep Strain (με)	Long-Term Creep Coefficient, C_u
		ksi (MPa)	percent of compressive strength			
U-A†	15.4 (106)	9.15 (63)	59	1950	2672	1.37
U-B†	15.8 (109)	9.15 (63)	58	1947	2760	1.42
U-C‡	15.2 (105)	9.15 (63)	60	2436	3719	1.53
U-D*	16.5 (114)	9.15 (63)	67	2057	1600	0.78
U-E‡	13.8 (95)	9.15 (63)	66	2998	7402	2.47

† Long-term creep data reported after 458 days of sustained loading.

‡ Long-term creep data reported after 497 days of sustained loading.

* Data for UHPC with untreated curing taken from the study conducted by Graybeal 2006a. The material used in the previous study is an earlier formulation and may differ from the U-D presented in this report. Long-term creep data reported after 372 days of sustained loading.

Table 24. Summary of results for specimens subjected to low-level sustained loading.

UHPC	Compressive strength at the beginning of testing ksi (MPa)	Sustained Creep Stress		Initial Elastic Strain (με)	Final Creep Strain (με)	Long-Term Creep Coefficient, C_u
		ksi (MPa)	percent of compressive strength			
U-A	17.2 (119)	9.15 (63)	53	1441	1003	0.70
U-B	20.6 (142)	9.15 (63)	45	1622	1458	0.90
U-C	24.9 (172)	9.15 (63)	37	1432	1019	0.71
U-E	19.7 (136)	9.15 (63)	46	2076	2425	1.17

† Long-term creep data reported after 458 days of sustained loading

‡ Long-term creep data reported after 497 days of sustained loading

The creep (ε_{cp}) and shrinkage (ε_{sh}) strains measured throughout testing are shown in figure 114 to figure 117 for U-A, U-B, U-C, and U-E, respectively. The strains reported are average measurements from three DEMEC locations on two cylinders for each loading age. It can be observed that the creep of UHPC is significantly higher under the high-level sustained loading; however, this is not unexpected for a few reasons. First, the load level was higher. Second, samples subjected to this loading regime had been curing for no longer than seven days and thus had lower compressive strengths prior to the application of load. It was shown by L'Hermite (1960) that creep of concrete decreases as the age (or compressive strength) of concrete increases. Furthermore, as discussed by Acker, a majority of the creep and shrinkage takes place as the concrete is desiccating. (Acker 2004) Therefore, it is also expected that shrinkage strains were lower in the case were UHPC was mature prior to loading; this was the case with samples subjected to low-level loading.

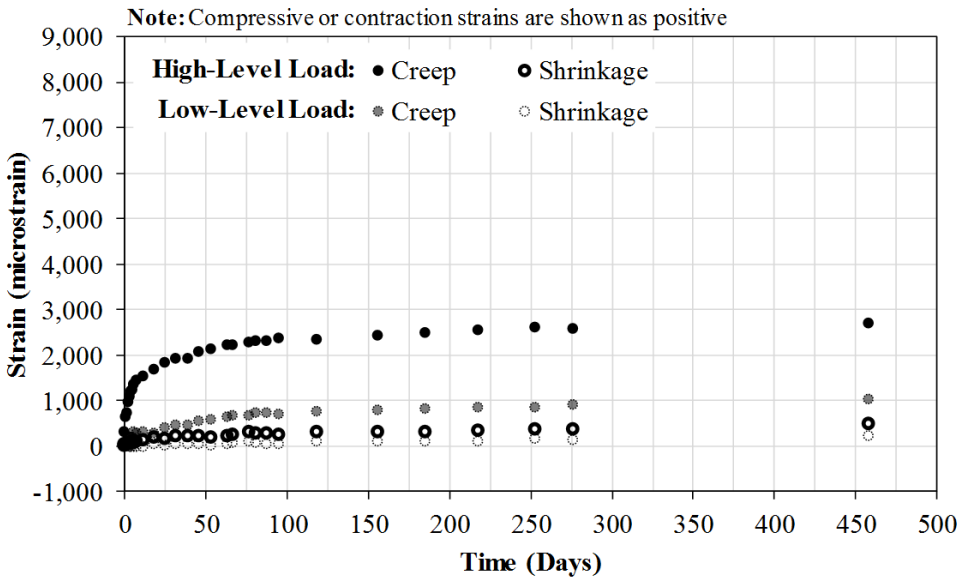

Figure 114. Graph. Creep and shrinkage of U-A.

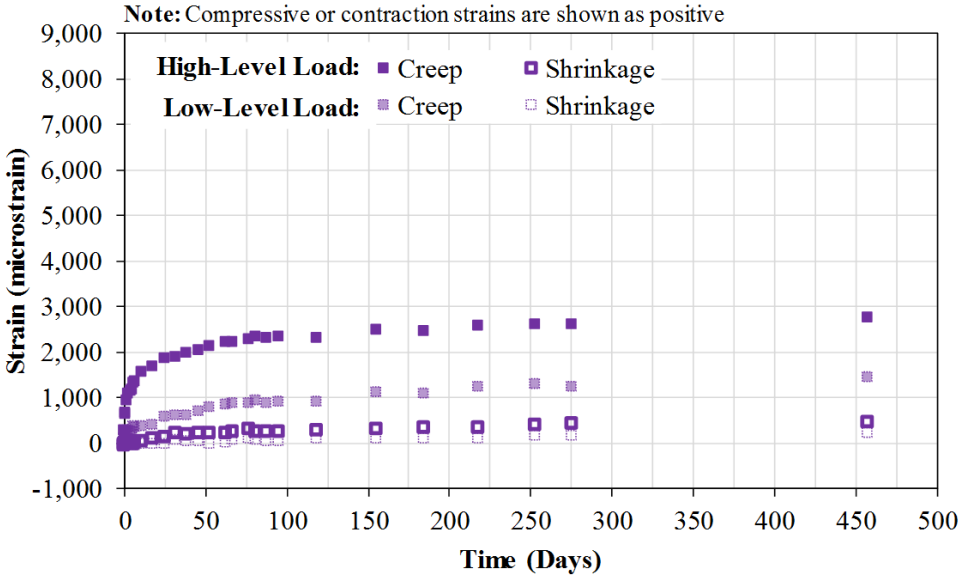

Figure 115. Graph. Creep and shrinkage of U-B.

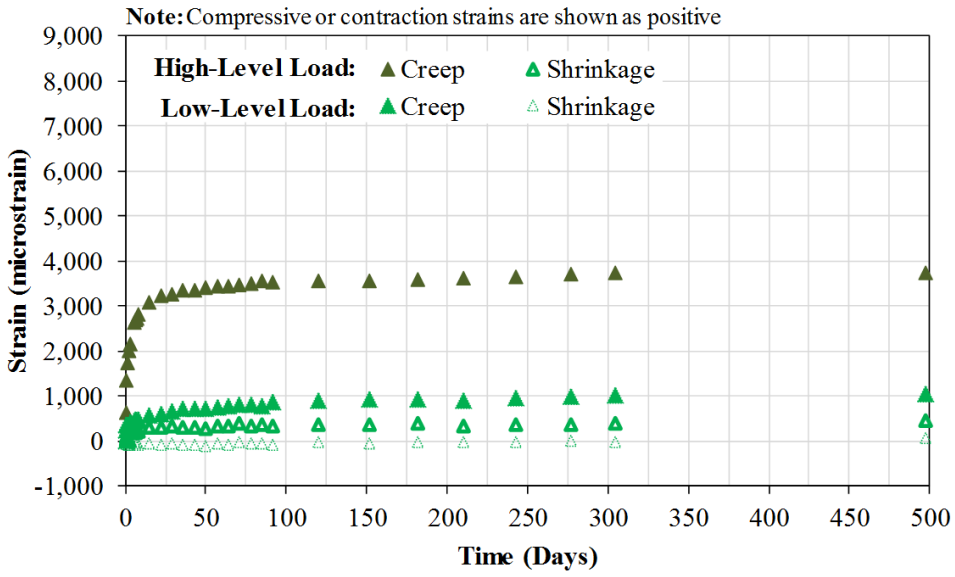

Figure 116. Graph. Creep and shrinkage of U-C.

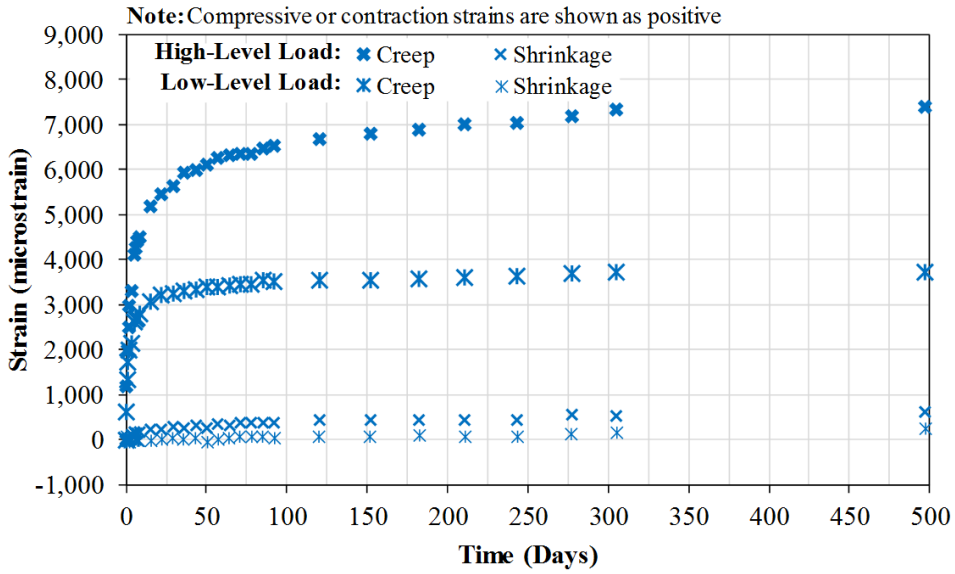

Figure 117. Graph. Creep and shrinkage of U-E.

For the purpose of comparison, measured creep strains were used to create a best-fit, continuous creep curves for each material under both high- and low-level loading. Previous research by Meyers, Branson, and Schumann (1972) discusses the origins of predicting creep and shrinkage behavior of conventional concretes. Building on work of earlier research, the equation shown in figure 118 was proposed to correlate the creep coefficient of concrete with time. This equation can be modified and presented in terms of creep strain as shown in figure 119. Here, the fit parameter ψ has been set equal to 0.6, as proposed in the work by Branson, Meyers, and Kripanarayanan (1970) and Branson and Christiason (1971). This equation was previously used by Graybeal (2006a) to create a best fit curve for the creep of UHPC-class materials.

$$C(t) = \frac{t^{\psi}}{d + t^{\psi}} C_u$$

Figure 118. Equation. Predictive equation for creep coefficient.

Where

$C(t)$ = Creep coefficient as a function of time t

t = Time in days after application of load

C_u = Ultimate creep coefficient

ψ, d = Fitting parameters

$$\varepsilon_{cp}(t) = \frac{t^{0.6}}{a + t^{0.6}} b$$

Figure 119. Equation. Modified version of the equation shown in figure 118 to predict creep strains at time *t*.

$\varepsilon_{cp}(t)$ = Creep strain as a function of time t

t = Time in days after application of load

a, b = Fitting parameters

The measured creep strains for specimens tested under high- and low-level sustained load are compared in figure 120 and figure 121, respectively. Each data series was best-fit using the equation shown in figure 119. Previous work has shown that compressive creep can be influenced by admixture, water, and cement contents. (Brooks 1989; Brooks 1999; ACI Committee 209 2005) Furthermore, aggregate type has also been shown to influence creep behavior. (Troxell, Raphael, and Davis 1958) Given that the volume fractions and types of cement (or cementitious materials) and inherit materials such as fine aggregates are not known, it is difficult to determine why a given UHPC material exhibited more creep than another. However, it is interesting to note that the materials with higher water and liquid admixture contents tended to exhibited more creep. For examples, material U-E employed the highest water content and also exhibited substantially more creep than the other UHPC-class materials. This is not necessarily causal, but could likely play a role in the distinctively higher creep exhibited.

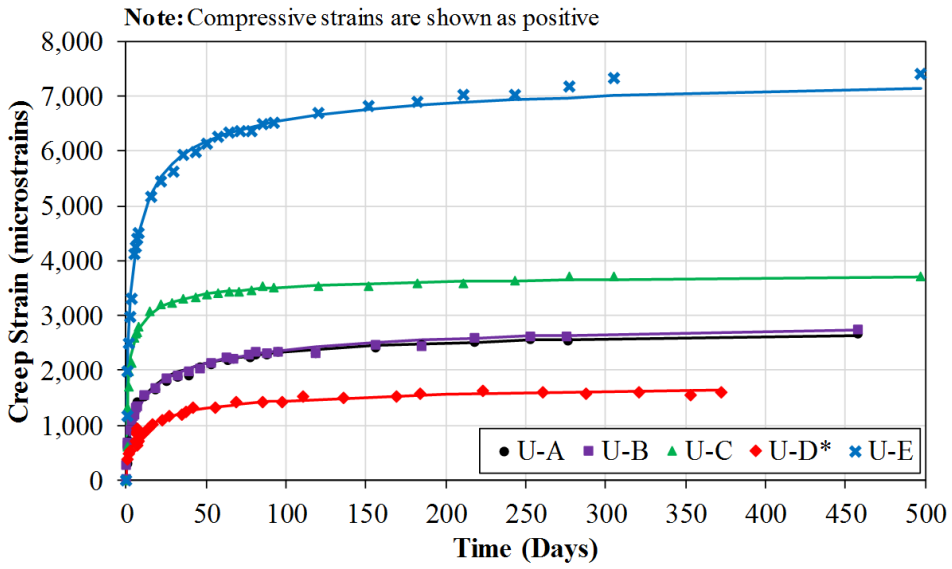

* Data for UHPC with untreated curing taken from the study conducted by Graybeal 2006a. The material used in the previous study is an earlier formulation and may differ from the U-D presented in this report.

Figure 120. Graph. Comparison of creep under sustained high-level load.

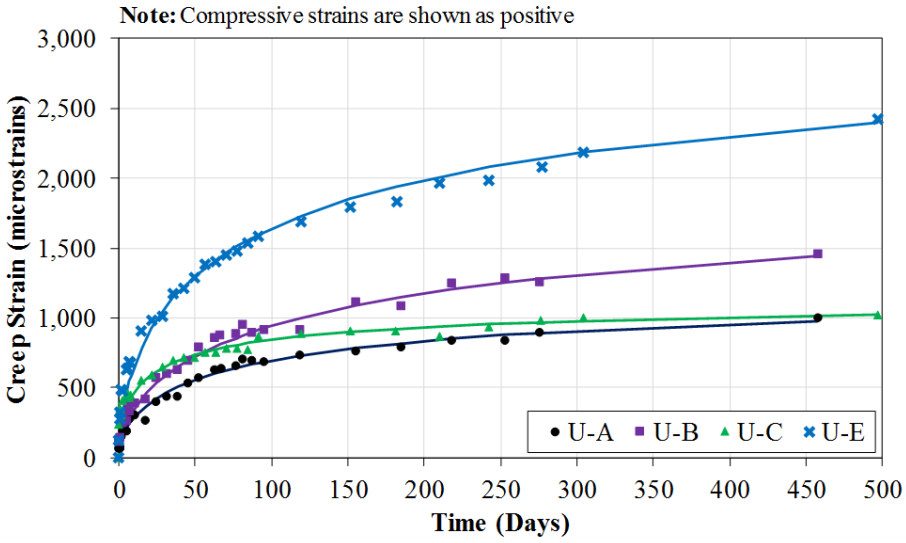

Figure 121. Graph. Comparison of creep under sustained low-level load.

AUTOGENOUS AND DRYING SHRINKAGE

Test Methods and Specimens Preparation

Autogenous (sealed) and drying deformations were assessed according to ASTM C157 using the modifications described in ASTM C1856. When evaluating shrinkage, it is recommended to measure both sealed and drying shrinkage. While the former would only consider the internal drying of the specimen (i.e., the hydration reaction consumes water), the latter is commonly referred to as "total" shrinkage because it would include both internal and external drying effects. To do so, three replicate prismatic specimens with dimensions of 3 by 3 by 11.25 inch (76 by 76 by 286 mm) were evaluated for each curing condition: sealed and drying (see figure 122). All the specimens were cured and tested in lab environmental conditions at 73.4 ± 3.6 ºF (23 ± 2 ºC) and 50 ± 5 percent relative humidity. However, for the autogenous shrinkage measurement, the six faces of three of the specimens were sealed with two layers of aluminum tape after removal from the molds at 24 hours. Length change measurements, as well as mass measurements, were taken every week for the first month and once a month for the next 6 months. Lastly, each UHPC tested was dosed with 2-percent fiber by volume.

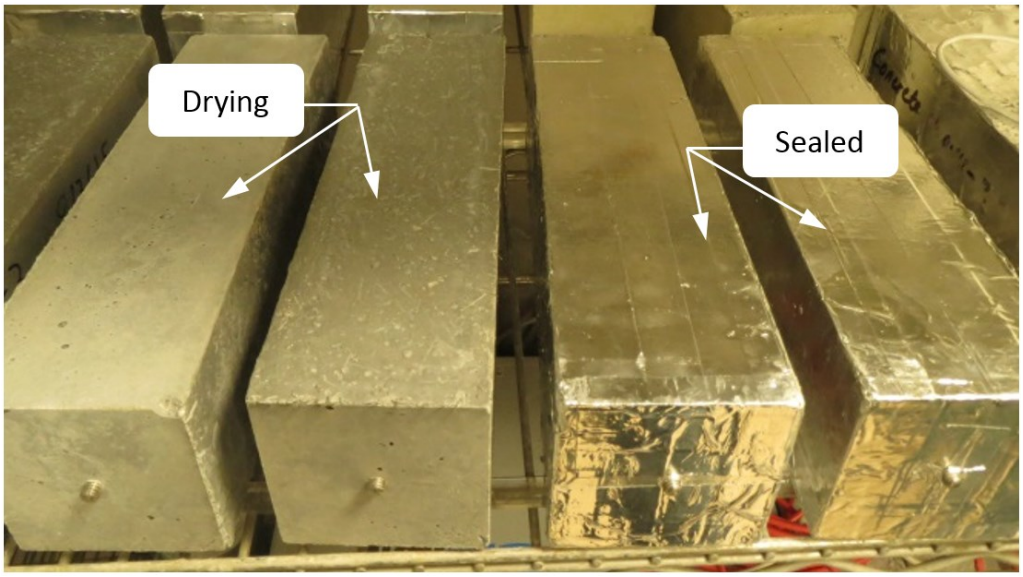

Figure 122. Photo. Sealed and drying ASTM C157 UHPC specimens.

Results

The shrinkage results in both sealed and drying curing conditions are presented in figure 123 and figure 124, respectively. As observed in figure 123, all UHPC materials undergo autogenous shrinkage throughout the duration of the test. In some cases (U-C and U-E) the amount of early autogenous shrinkage is high, reaching values above 400 με after only 7 days of hydration. At the end of the testing period, most of the UHPC materials exhibit autogenous shrinkage values above 500 με, except for U-D and U-F. These large values might result in high internal stresses in the material that can be reflected in the form of shrinkage cracking; however, it is also recognized that

the large amount of fibers in UHPC can bridge shrinkage cracks and help redistribute stresses. As for the drying deformations shown in figure 124, it is interesting to note that the shrinkage values are not particularly higher than those observed in sealed conditions (except of U-E which shows values about 400 με higher than those in sealed conditions). Typically drying shrinkage is about an order of magnitude larger than sealed shrinkage, at least in conventional concretes, due to the additional (external) drying effect which can be reflected in the mass loss of the specimens. In fact, mass loss has been observed in the UHPC materials investigated in this study (figure 125). However, this type of material seems to be less prone to develop drying shrinkage than conventional concretes. This may be mainly attributed to: 1) low water-to-binder ratio (i.e., low water content and low permeability); and 2) high fiber volume potentially generating internal restraint within the cementitious matrix.

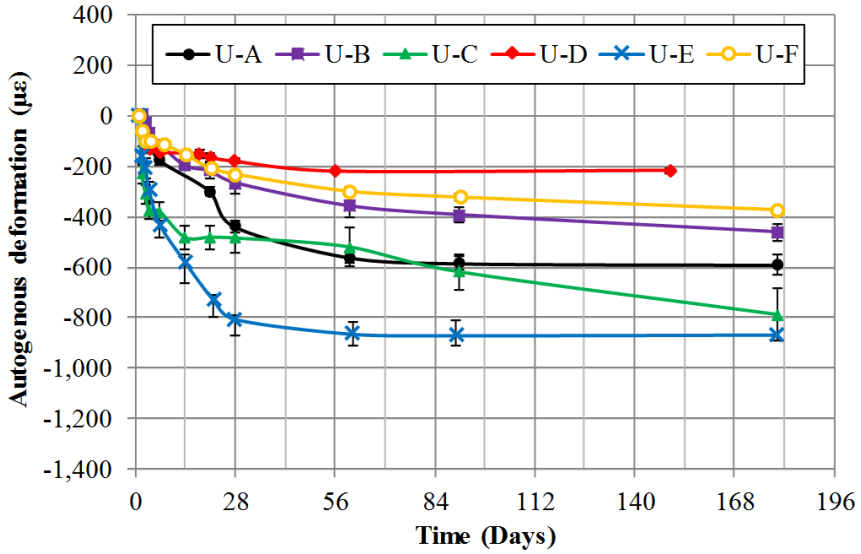

Figure 123. Graph. Autogenous (sealed) shrinkage as a function of time via ASTM C157.

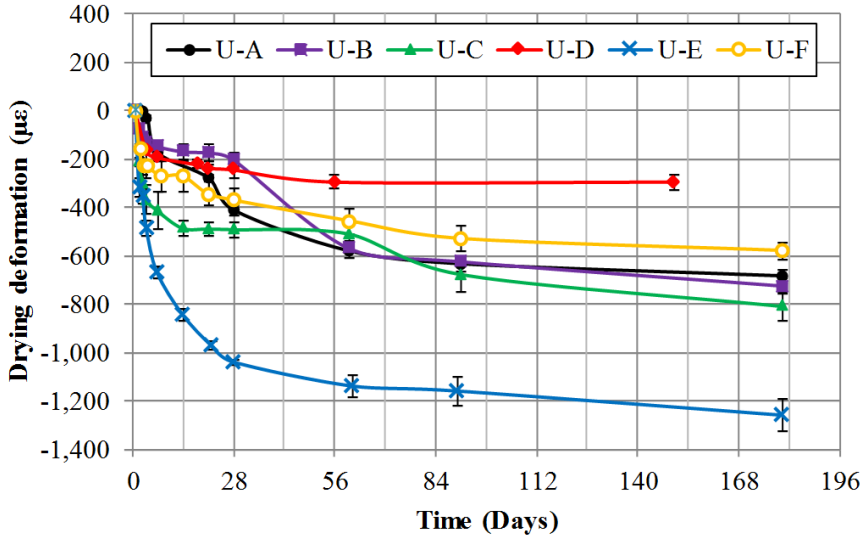

Figure 124. Graph. Drying shrinkage as a function of time via ASTM C157.

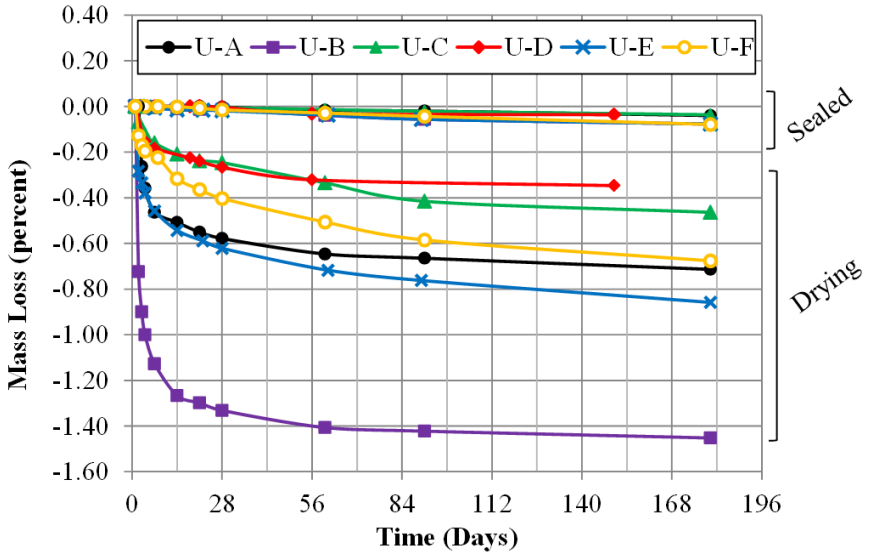

Figure 125. Graph. Mass loss of sealed and drying ASTM C157 specimens as a function of time.

Overall, these results demonstrate that the shrinkage of UHPC is commonly within the range associated with well-designed conventional concretes; however, the values can be somewhat higher for some products or mix designs. It must also be recognized that dimensional instability during the early age mechanical property development can cause distress in the material and can hinder the long-term performance of the constructed system. UHPCs commonly exhibit proportionally more autogenous shrinkage than conventional concretes, particularly at early ages (i.e., before 24 hours). The ASTM C1698 test method can capture these early age dimensional stability behaviors; however, the test can be difficult to complete for heavily fiber reinforced materials and thus the cementitious matrix without the fiber reinforcement may need to be assessed. (De la Varga and Graybeal 2016)

FRESH VOLUME DEFORMATIONS

Test Methods and Specimens Preparation

Fresh volume deformations are common in cementitious materials. Either expansions or contractions have been observed in numerous cases. While limited expansions are unlikely to compromise the integrity of the material as they would expose the material to a compression-type stress condition, contractions are more likely to result in early material degradation due to the comparatively lesser tensile strength of concretes. In this study, fresh volume deformations in terms of height change were assessed in accordance with a modified version of the ASTM C827 test method. The height change of a 3-inch (76-mm)-diameter by 6-inch (152-mm)-tall cylindrical specimen was measured using a non-contact laser placed above the specimen. The vertical distance from the laser to the indicator ball placed on the top surface of the specimen was measured, as shown in figure 126. The measured vertical distance corresponds to the increase or decrease in height (expansion or contraction) of the material laterally confined in the cylindrical mold from the time of molding to when the mixture becomes hard (i.e., final set). This approach has been compared with the original setup described in ASTM C827, and similar results are obtained. (Di Bella and Graybeal 2014) While some materials tend to show expansions before setting, due commonly to the presence of expansive additives (e.g., ettringite) or thermal stimulus, most cementitious materials tend to show contractions (i.e., height reductions) during their fresh stage. However, the height reduction measured in this test would include several parameters such as chemical and autogenous shrinkage, plastic shrinkage (due to drying of the specimen from the top surface), and some error given by the settlement of the ball on the top surface of the sample. Due to the presence of all these parameters, the measurements are primarily useful for comparative purposes, and not to independently evaluate a particular parameter (e.g., shrinkage, settlement, etc.). Lastly, each UHPC tested was dosed with 2-percent fiber by volume.

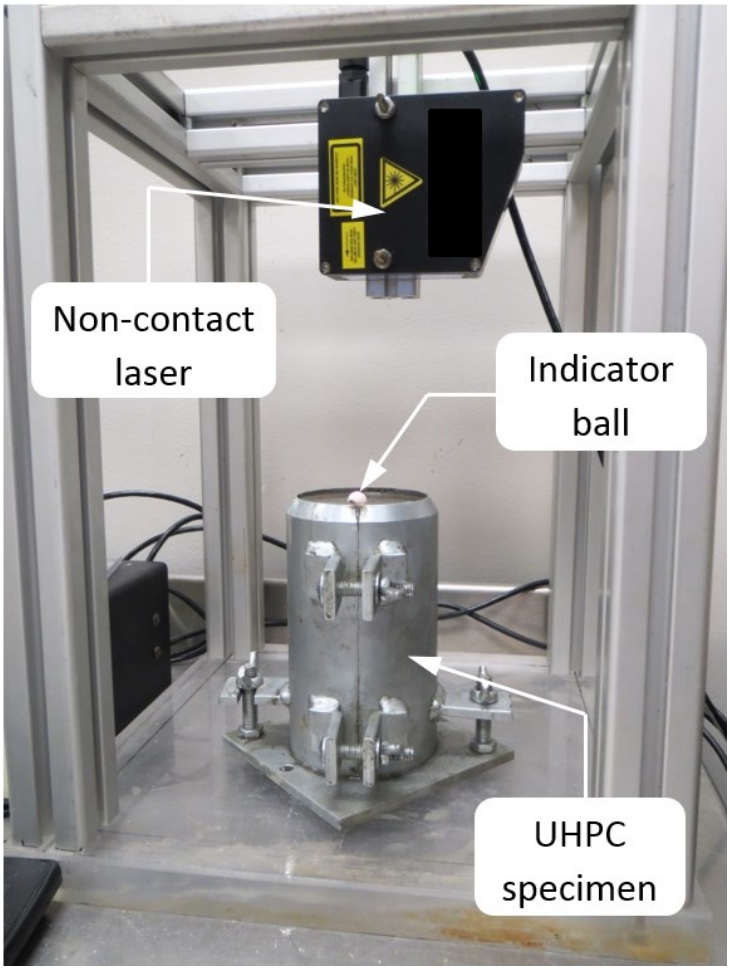

Figure 126. Photo. Height change in fresh UHPC specimens via a modified version of ASTM C827.

Results

Figure 127 shows the fresh volume deformations in terms of height change (i.e., expansion and contraction) of the UHPC materials used in this study. As observed, most of the UHPC materials undergo a height reduction of less than 1 percent, except for U-E which exceeds this value. In most cases, a fast decrease in height is observed over the first 2-3 hours. As already mentioned, the measured height reduction cannot be exclusively correlated to settlement or shrinkage since the height change measurement would include a variety of simultaneous effects such as chemical and autogenous shrinkage, surface settlement, and plastic shrinkage due to drying of the specimen from the top surface. An interesting result is observed for the U-F material, where pure expansion is observed throughout the test duration. This material is formulated specifically to be thixotropic, thus its fresh properties including fresh volume change are affected by the thixotropic behavior. The expansive behavior may be attributed to an expansive agent included in the proprietary U-F mix design.

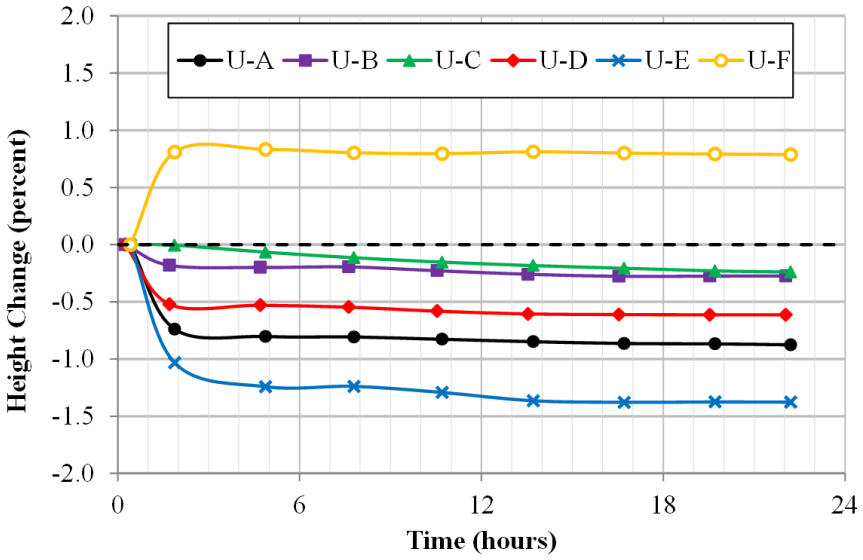

Figure 127. Graph. Height change of UHPC specimens as a function of time.

CREEP AND SHRINKAGE DISCUSSION

Creep is a deformation that increases over time and is caused by a sustained load. It is thought that the main mechanism of creep in UHPC involves the viscous strain in the calcium-silicate-hydrate (CSH) and that creep is more pronounced when it occurs as the UHPC is self-desiccating. (Acker 2004) The early-age UHPCs tested were still gaining strength and had not completely self-desiccated. This leads to an increase in measured creep compared to the mature age specimens. Although the early-age results show nearly twice the creep as the mature age, the structural effects could be mitigated during design. The early-age creep coefficients were within the range of conventional concrete. As long as an accurate representation of the creep is used in design, the long-term deflections or prestressing losses can be estimated. Alternatively, it is expected that an accelerated curing method would reduce the amount of creep as shown in previous research. (Graybeal 2006a)

In regard to the shrinkage results obtained, it is common that low *w/c* (or *w/b*) concretes such as UHPC are more prone to develop autogenous shrinkage. Additionally, UHPC materials are designed to have large contents of very fine and reactive cementitious materials, which increase the chemical shrinkage of the system, thereby increasing the autogenous shrinkage. The low water content in UHPC might also explain why the drying shrinkage observed is not particularly higher than the autogenous shrinkage, since no considerable (external) drying occurs. The higher the w/b of a cementitious system, the larger capillary pores will form in the cement matrix. Large pores dry faster than smaller pores, and this may explain why UHPC materials do not show considerable higher drying shrinkage with respect to their autogenous shrinkage. In any case, it is expected that the large amount of fiber reinforcement might help in mitigating most of the autogenous and/or drying shrinkage cracking.

The fresh height change results (expansion or contraction) presented in this chapter show some volume instability of these materials. The UHPC investigated in this study exhibit fresh contraction values ranging from 0.3 percent to just above 1 percent, in some cases, during the fresh stage of

the materials. This could be a direct consequence of the high (autogenous) shrinkage observed in these mixtures, although this test does not uniquely assess shrinkage, but a combination of other parameters including particle re-arrangement or settlement, for instance. From a practical perspective, if a freshly poured UHPC element is expected to exhibit height reduction, this could be counteracted by over-pouring the element. Therefore, these height reductions should be considered by designers and practitioners during both design and construction processes. A distinct case is that observed with the U-F material, which undergoes expansion throughout the test duration, contrary to the rest of the UHPC materials studied. As already mentioned, this material was designed to exhibit a thixotropic behavior. This may indeed explain the height change results, although a better understanding of the additive used in its formulation to make the material thixotropic might be needed to further explain the expansion observed.

CHAPTER 6. DURABILITY

INTRODUCTION

It is well accepted that a key factor in designing a UHPC mix is to improve the micro and macro properties of the mixture, thus affecting both the durability and mechanical performances. This chapter is focused on durability performance. The improvement in the micro properties is typically achieved by providing a dense particle packing. In UHPC, a higher proportion of cement and other cementitious materials (e.g., fly ash, microsilica) are used compared to normal or high strength concretes (NSC or HSC). Additionally, a low water-to-binder ratio (w/b) is used in the mixture design to enhance mechanical properties; hence, part of the unhydrated cementitious materials is replaced with inert micro particles such as silica flour. All these aspects will reduce the amount and size of total porosity of the material. Since durability of cementitious materials is directly related to the capability of the material to prevent the penetration of detrimental aggressors (e.g., chloride ions) by "refining" the microstructure, it is then expected that this type of material would exhibit enhanced durability compared to NSC and HSC.

Various researchers have studied the early-age properties of UHPC materials. (Shi et al. 2015; Wang et al. 2015; Schmidt and Fehling 2005; Wille and Boisvert-Cotulio 2015) Due to the increasing use of UHPC among state agencies and practitioners, it is crucial to provide a good understanding on how this material will perform during its service life, and whether the service life is significantly increased compared to that of NSC and HSC. Previous research has shown enhanced durability in terms of alkali-silica reaction (ASR) and delayed-ettringite formation (DEF). (Pfeifer et al. 2009) Others have investigated the resistance to chloride ions penetration. (B. Graybeal and Hartman 2003; Abbas, Soliman, and Nehdi 2015) Freeze-thaw, scaling, and abrasion resistance has also been the focus of other research studies. (Graybeal 2006a; Ahlborn et al. 2011) All these studies were performed on only one or two (commercially-available or locally produced) UHPC materials, and all concluded that the durability of this class of material is superior to that of NSC and HSC, due mainly to its "smaller" microstructure. This chapter presents a series of durability tests performed on five of the UHPC materials described in Chapter 2, allowing for a direct comparison of these commercially-available materials. The tests included measurements of the chloride ion penetrability, electrical surface resistivity, and freeze-thaw resistance, using ASTM test methods.

RAPID CHLORIDE ION PENETRATION

The ability of concrete to resist ingress of chloride ions can result in a significantly more durable concrete. The resistance to chloride ingress was evaluated according to ASTM C1202 using the modifications described in ASTM C1856. (ASTM C1202-12 2012; ASTM C1856/C1586-17 2017) The method determines the electrical conductance of concrete to provide a rapid indication of its resistance to the penetration of chloride ions. It does so by measuring the amount of electrical current that passes through a 2-inch (51-mm) thick slice of concrete over a 6-hour period. A 60-volt direct current is maintained across the ends of the specimen, one of which is immersed in a sodium chloride solution, whereas the other one is immersed in a sodium hydroxide solution. The total charge passed, in coulombs, is related to the resistance of the specimen to chloride ion penetration. Figure 128 shows the test method setup with a specimen being tested.

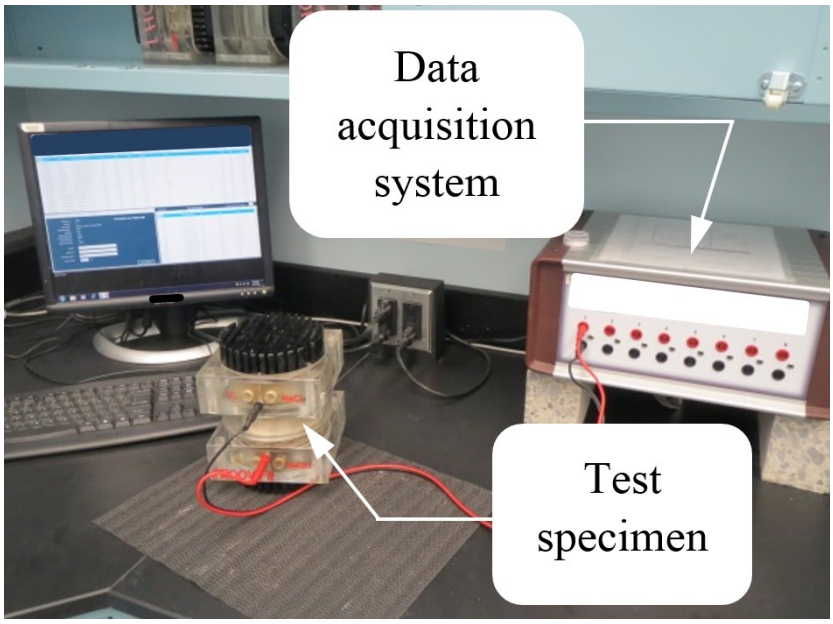

Figure 128. Photo. Setup for rapid chloride ion penetrability test.

The UHPCs were proportioned and mixed according to manufacturers' recommendations with the exception of fiber volume; each UHPC tested was dosed with 2-percent fiber by volume. The specimens consisted of 4-inch (102-mm) diameter by 8-inch (204-mm) height cylinders. The cylinders were demolded one day after mixing and maintained in a lime-saturated water bath at 73.4 ± 1.8 ºF (23 ± 1 ºC) for two curing periods of 28 and 56 days. After each curing time, the sides of the cylinders were coated with a two-part fast setting epoxy. Then, a 4-inch (102-mm) diameter by 2-inch (51-mm) height disc was cut from the central part of the cylinder. A disc from two different cylinders was used as RCPT test specimen. A final conditioning of the disc specimens is performed prior to the RCPT test execution, consisting of a vacuum-aired and vacuum-saturated curing for 3 and 18 hours, respectively.

Results of the tests are presented in table 25. It is observed that U-B exhibited much higher charge passed values than any other UHPC material tested. The high charge passed result would be typical in highly porous cementitious systems. However, although the total porosity of these materials was not measured, it is very unlikely that this type of material is characterized by having a highly porous cementitious matrix, due to the large amount of fine particles used in their design. Therefore, the only explanation to the large charge passed is that the fibers included in U-B created an electrically conductive path between the two ends of the specimen, making the test not valid for chloride penetration assessment. It is relevant to mention that U-B is formulated with two different fiber sizes, thus the contact between the fibers might be more likely to occur. The rest of the UHPC materials show much lower charge passed values even at early ages (i.e., 28 days), within ranges of "very low" or "negligible" chloride penetrability, according to ASTM C1202 qualitative indications. In all of them, the 56-day charge passed is lower than that at 28 days, which is indicative of the continuous hydration taking place in the system, further decreasing the total porosity.

Table 25. Rapid chloride ion penetrability results.

UHPC	Age (days)	Charge Passed (Coulombs)		Chloride Ion Penetrability[b]
		Average	Standard Deviation[a]	
U-A	28	302	112	Very Low
	56	53	16	Negligible
U-B	28	5100	159	High
	56	2501	284	Moderate
U-C	28	425	167	Very Low
	56	298	98	Very Low
U-D	28	789	10	Very Low
	56	495	45	Very Low
U-E	28	470	6	Very Low
	56	303	35	Very Low

[a]One standard deviation from the average of two samples.
[b]Qualitative indications according to ASTM C1202.

While the ASTM C1202 standard method raises awareness of using electrical testing for steel reinforced materials (e.g., fiber reinforced UHPC), the results obtained in this study show the possibility of using this test method for this type of materials, provided that no conductive path is created between the two ends of the specimens due to a possible contact of the steel fibers. Also, the standard deviation values obtained in this study are higher that what is described in the ASTM standard. Perhaps steel fiber reinforced materials provide more heterogeneity into the matrix, causing more variability in electrical parameters. This needs further investigation.

SURFACE RESISTIVITY

Another faster and non-destructive way of assessing the resistance to chloride ions penetration in concrete materials is by measuring the surface electrical resistivity. The surface resistivity tests conducted in this study were executed according to the AASHTO TP95 standard test method. (AASHTO TP 95 2014) The results obtained in this test have shown good correlation to those obtained from the RCPT test method. As applied in this study, the test consists of measuring the resistivity of 4-inch (102-mm) diameter by 8-inch (204-mm) height cylindrical specimens by using a 4-pin Wenner probe array. An alternating current (AC) potential difference is applied by the surface resistivity apparatus at the outer pins of the Wenner array generating a current flow in the concrete material. The resultant potential difference between the two inner pins is measured. This potential along with the current used are used to calculate the electrical resistivity of the material, which is automatically done by the apparatus. The resistivity is related to the resistance of the material to chloride ions penetration. Figure 129 shows the test method setup with a specimen being tested.

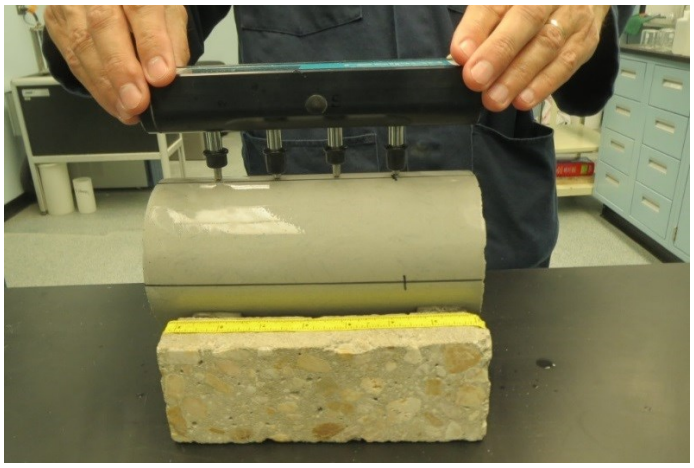

Figure 129. Photo. Setup for surface resistivity test.

The UHPC cylinder specimens were demolded one day after mixing and maintained in a lime-saturated water bath at 73.4 ± 1.8 ºF (23 ± 1 ºC). The specimens were taken out from the bath at different ages to measure the surface resistivity as a function of time. The resistivity was measured on the side of the specimen at four different locations, corresponding to 0, 90, 180 and 270-degree points of the top finished circular face of the cylinder. The resistivity results are shown in figure 130. As observed, electrical resistivity for all UHPCs except for U-B are within the ranges of "very low" to "negligible" chloride penetration at 28 and 56 days of age, according to the AASHTO standard qualitative indications. This shows agreement with the previously shown RCPT results. The U-B material shows much lower resistivity values than the other UHPCs (notice logarithmic scale on Y-axis), indicating that it exhibits less chloride penetration resistance. This may be due to the same reason explained for the U-B RCPT specimens, where possible fibers contact might have created an electrically conductive path within the specimen, making again the test not valid for chloride penetration assessment in this particular material.

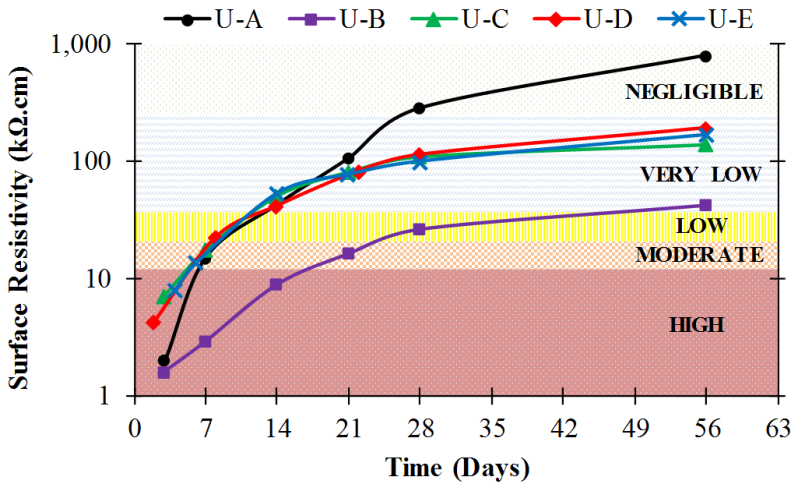

Figure 130. Graph. Electrical surface resistivity as a function of time.

FREEZE-THAW RESISTANCE

The resistance to freeze-thaw damage was assessed in accordance with ASTM C666 (Procedure A) using the modifications described in ASTM C1856. (ASTM C666-15 2015; ASTM C1856/C1586-17 2017) This tests consists of submerging 3- by 4- by 16-inch (76- by 102- by 406-mm) prismatic specimens in a water bath connected to an automated environmental chamber capable of producing six temperature cycles that range from 0 ºF (-18 ºC) to 40 ºF (4.4 ºC) over a 24-hour period, thus exposing the specimens to a fast freeze-thaw cycling environment (see figure 131). The aggressive environment created in this accelerated durability test helps determine if the concrete has a microstructure that can resist the thermal expansion and contraction effects of water. The concrete could achieve this resistance by either resisting the initial water penetration or by allowing the thermal expansion to occur within a voided microstructure. In the case of UHPC materials, the former effect is expected.

Figure 131. Photo. Environmental chamber for producing freeze-thaw cycles via ASTM C666 (Procedure A).

The UHPC mix designs followed the manufacturers' recommendations for each product. Three specimens were prepared for each of the materials. They were cured in a lime-saturated water bath at 73.4 ± 1.8 ºF (23 ± 1 ºC) for 2 weeks. After the curing period, they were submerged in a 39.92 °F (4.4 ºC) water bath for at least 2 hours to prepare them for the initial test measurement. A total of 600 freeze-thaw cycles, twice the number required by the ASTM standard, were conducted over the course of 4 months. Every 35-40 freeze-thaw cycles, the specimens were extracted from the chamber, and data collection was performed, which included mass determination and capture of the fundamental transverse frequency of each prism, the latter via ASTM C215. (ASTM C215 -

14 2014) An initial measurement of these parameters was taken prior to starting the freeze-thaw cycles. Figure 132 shows the setup used to measure the transverse frequency.

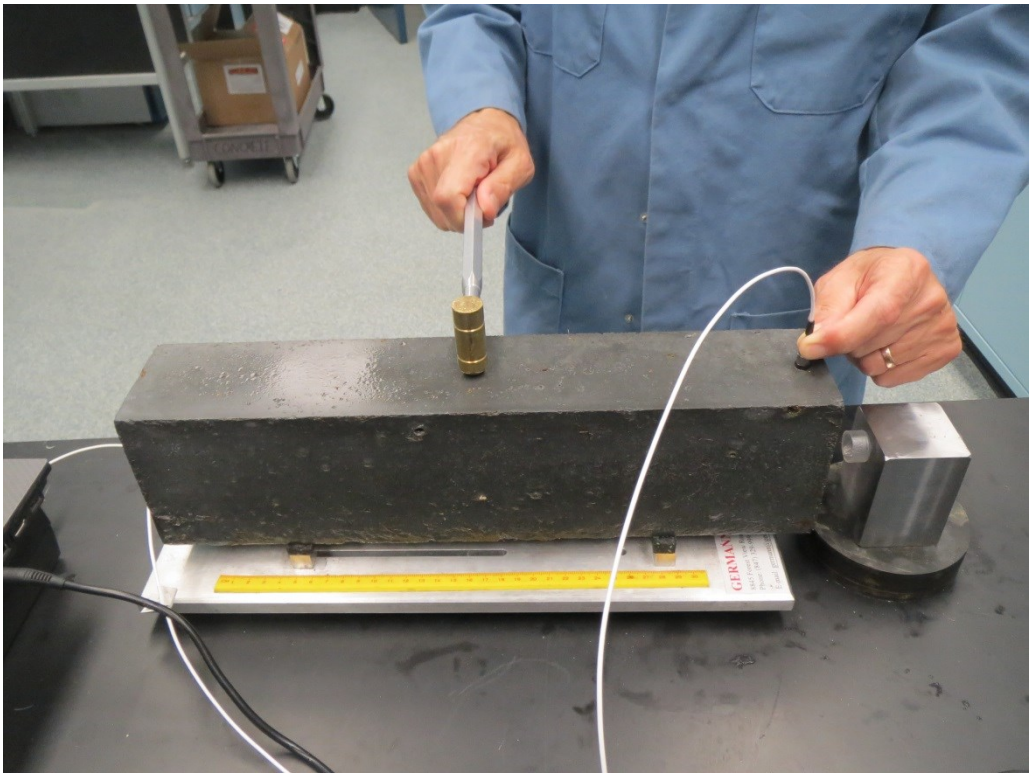

Figure 132. Photo. Resonant frequency testing of a freeze-thaw specimen.

The measured fundamental transverse frequency was used to calculate the relative dynamic modulus of elasticity (RDME), in percent, according to ASTM C666. The results obtained are presented in figure 133, where the dynamic modulus of elasticity is graphted against the number of freeze-thaw cycles conducted. This test method assumes that freeze-thaw cycling will cause the RDME to decrease as the concrete deteriorates because resonant frequency decreases if internal microcracking occurs. The results show very little change of RDME for any of the UHPC materials tested throughout the duration of the test. Typically, in a concrete material damaged by freeze-thaw cycles, one would expect to see the RDME dropping to values below 60 percent. This is then an indication of very little to no damage in the UHPC specimens, thus concluding that this type of materials exhibits very good freeze-thaw resistance.

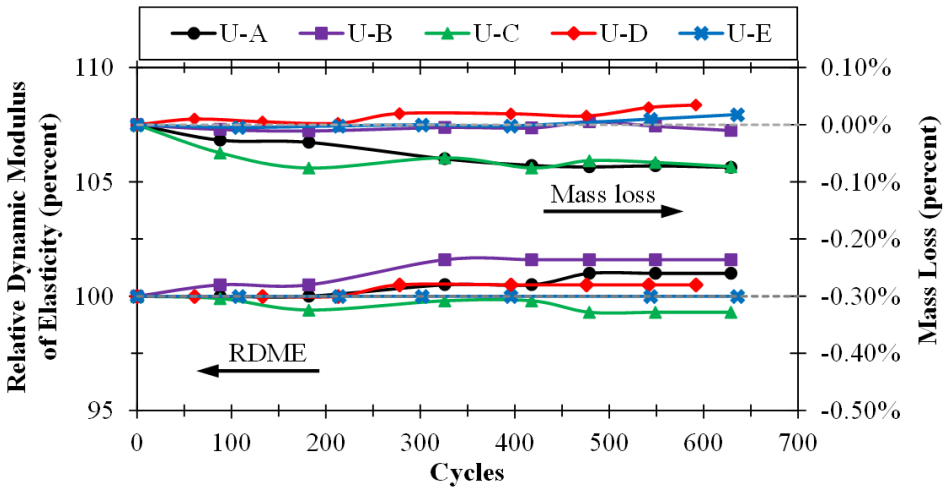

Figure 133. Graph. Relative dynamic modulus of elasticity as a function of number of freeze-thaw cycles.

Another evidence of the very low damage suffered by these specimens under freeze-thaw cycles is the negligible amount of mass loss reported in figure 133. Large values of mass loss would be indicative of specimen freeze-thaw damage. This damage typically initiates within the specimen, from water that percolated from the exterior, and expanded during a freezing phase, causing internal cracking. As observed in figure 133, none of the specimens lost more than 0.10 percent of their initial mass, indicative of the low freeze-thaw damage. This is also observed in figure 134, where a picture of a U-E specimen before and after the freeze-thaw cycles shows no evidence of damage.

A. Before testing.

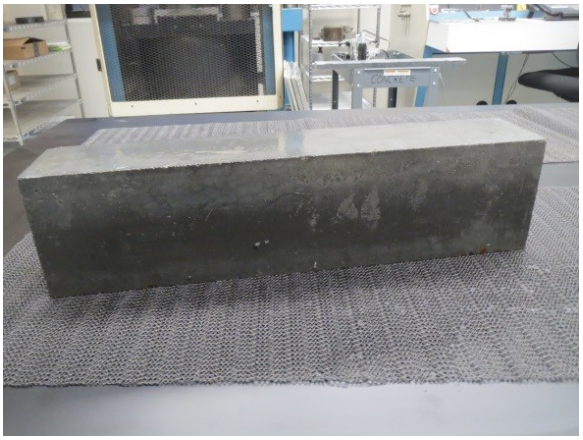

B. After 600 freeze-thaw cycles

Figure 134. Photo. Freeze-thaw specimens.

DURABILITY DISCUSSION

As already mentioned in the chapter introduction, UHPC materials are designed to exhibit exceptional durability performance by including high contents of cementitious materials and inert fillers in their mixture design, along with a low w/b. The durability results obtained in this study have shown an outstanding performance of the five UHPC materials investigated. The mechanism behind this performance seems to be the low penetrability of external (detrimental) aggressors into the UHPC material, regardless the external agent that may commonly penetrate and cause internal damage (e.g., chloride ions, water). The very dense microstructure along with the exceptional mechanical properties (i.e., high compressive and tensile strength) is crucial to prevent internal damage, thus ensuring good durability.

CHAPTER 7. STRUCTURAL PERFORMANCE

INTRODUCTION

As described in Chapter 1, UHPC has been commonly used in bridge construction to connect adjacent prefabricated bridge elements. The connections between elements most commonly employ interlaced reinforcing bars like that shown in figure 135. These connection regions are formed and filled with field-cast UHPC to create structural continuity. Once hardened, UHPC provides a load transfer mechanism between the two adjacent elements. That is, stress in the reinforcing bars in one prefabricated element is transferred to the surrounding UHPC which is subsequently transferred to the reinforcing bars in the adjacent element. In order to achieve the desired structural behavior reinforcing bars must be able to develop adequate stress levels which are typically above yield for ultimate limit state design.

Figure 135. Photo. Example of interlaced reinforcement in a UHPC connection.

This chapter investigates the structural performance of the different UHPC-class materials. Two series of tests were conditioned: UHPC-reinforcing bar bond tests and large-scale deck-level connections tests. The research presented in this chapter can also be found in the paper by Haber and Graybeal (2018).

UHPC-REINFORCING BAR BOND TESTS

This section presents the background, test parameters, and results from UHPC-reinforcing bar bond tests.

Objective

A series of tests were conducted to evaluate the bond between the different UHPC-class materials and deformed steel reinforcing bars. There were two primary goals of these tests:

1. Determine whether the different commercially available UHPC-class materials tested herein conform to the design guidance provided in FHWA TechNote entitled: *Design and Construction of Field-Cast UHPC Connections*. (Graybeal 2014a)

2. Investigate the influence of the fiber reinforcement content on the bond strength between UHPC and deformed steel bars.

The experimental approach used to achieve these two goals was previously employed by researchers at TFHRC. (Yuan and Graybeal 2014) A brief summary of this previous work and the design guidance contained in the TechNote by Graybeal (2014a) is presented herein to provide context.

Previous Research by Yuan and Graybeal (2014)

The research conducted by Yuan and Graybeal (2014, 2015) at TFHRC was the first to extensively examine the bond behavior of reinforcing bars embedded in UHPC subject to tensile loading. It should be noted that previous works in this area were conducted by Holschemacher et al. (2004, 2005), Fehling et al. (2012), and Swenty and Graybeal (2012). A brief review of the data gathered by Yuan and Graybeal (2014, 2015) is presented herein. This work provides a foundation for the tests that were conducted as a part of this research.

Summary of Test Variables and Set-up

The study conducted by Yuan and Graybeal considered a single UHPC-class material and a variety of structural characteristics. The UHPC formulation used in the research was commercially-available in the United States and was proprietary. The UHPC formulation contained a pre-mixed and prebagged power, water, a modified phosphonate plasticizer, a modified polycarboxylate high-range water-reducing admixture, a non-chloride accelerator, and high-strength steel microfiber reinforcement fibers. The steel fibers had a diameter of 0.008 inches (0.2 mm), a length of 0.5 inches (12.7 mm), and a tensile strength specified to be greater than 290 ksi (2000 MPa). Lastly, the formulation utilized a constant steel fiber reinforcement content of two percent by volume.

The primary parameters investigated included:

- The embedment length of reinforcing steel, l_d.
- Concrete side cover (clear cover), c_{so}.
- Clear bar spacing, $2c_{si}$.
- UHPC compressive strength, f'_c.
- Reinforcing bar type and size.

Throughout the study, in order to better assess the influence of a particular variable, each individual parameter was varied while others remained constant.

Bond was evaluated using a test set-up and specimen design developed to simulate the tension-tension lap splice configurations typically encountered in the aforementioned field-deployed connections; these tests are herein referred to as "pull-out" tests. The test set-up is shown in figure 136. UHPC strips were cast on top of a precast slab with a series of protruding No. 8 A615 Grade 60 (A615M Grade 420) bars which were centered on the strips. The dimensions of the strips varied based on the embedment length and concrete side cover used in the test. Each tested bar was positioned so it was embedded in the UHPC strip between two of the No. 8 bars. The pullout test was performed using a hydraulic jack putting both the reinforcing bar being tested and the No. 8 bars in tension. The slip displacement, which also includes the elongation of the reinforcing bars, is measured with three linear variable differential transducers (LVDT) along a loaded portion of the bar at about 2 inch (51 mm) above the top surface of the UHPC strip. A full discription of the test setup can be found in Yuan and Graybeal (2014, 2015). Figure 137 illustrates the test set-up and provides a visual definition of the aforementioned test variables. The summary of results provided in the following subsection only covers tests conducted with No. 5 test bars.

Table 26 lists the measured properties of No. 5 bars used in the study.

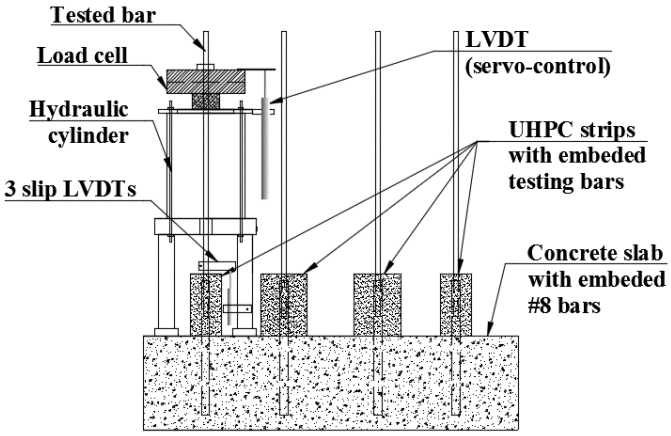

Figure 136. Illustration. Details of bond pull-out test set-up.

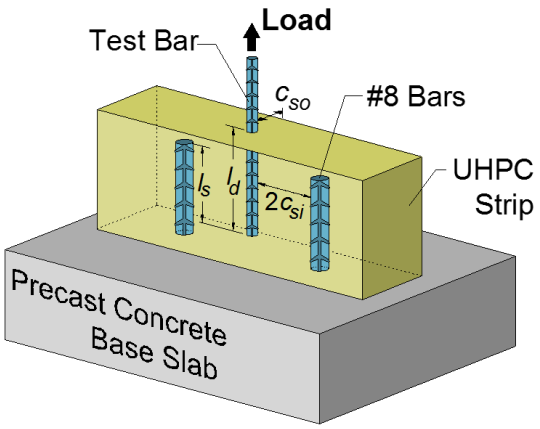

Figure 137. Illustration. Definition of bar spacing and embedment parameters.

Table 26. Properties of No. 5 reinforcing bars used in bond tests by Yuan and Graybeal 2014, 2015.

Bar type	Yield strength, ksi (MPa)	Tensile strength, ksi (MPa)	Mean rib height, in (mm)	Mean rib spacing, in (mm)	Relative rib area
Uncoated	75 (516)	118 (813)	0.034 (0.864)	0.402 (10.2)	0.085
Epoxy-Coated	68 (468)	108 (744)	0.034 (0.864)	0.408 (10.4)	0.083
ASTM A1035	126 (868)	167 (1151)	0.037 (0.939)	0.417 (10.6)	0.088

Summary of Key Findings

Figure 138 through figure 140 depict three of the key finds from the study by Yuan and Graybeal (2014, 2015). All three graphs depict the relationship between a given parameter and the peak reinforcing bar stress prior to bond failure. For each result, a set of parameters were kept constant. These parameters are noted in each respective figure or are explained in subsequent discussions.

Figure 138 depicts the relationship between the peak bar stress and the embedment length for the three different reinforcing bar types, uncoated (grade 60), epoxy-coated (grade 60) and high-strength (grade 120). In this graph, the side cover, bar spacing, and UHPC compressive strength were approximately constant. It can be observed that increasing the embedment length of a reinforcing bar increases the bar stress at bond failure and the relationship between the bar stress and the bonded length is nearly linear. This is similar to that observed in normal-strength concrete, but is not typically observed in high-strength concretes. (ACI Committee 408 2003; Azizinamini et al. 1993) Thus, the observed linear relationship between bond strength and embedment length implies that the behavior attributed to traditional high-strength concretes may not be present in UHPC, potentially due to the enhanced pre- and post-cracking tensile response of the UHPC.

Figure 139 depicts the relationship between the peak bar stress and the clear spacing between adjacent bars ($2c_{si}$) for two different values of clear cover (c_{so}); bar type (Gr. 120), embedment length, and compressive strength of UHPC were held constant. This graph indicates that bond strength tends to decrease as the clear distance between bars gets larger, which is not unexpected. The loaded bars must transfer stress through the UHPC to the adjacent bars in the concrete base slab. As the bars spacing gets large, stress transfer from the loaded bars to the adjacent bars becomes less effective and more load must be covered by UHPC alone. On the other hand, when the loaded bar is very close to the adjacent bars in the base slab load transfer also becomes less effective. This is likely due to reduced confinement of the bars by UHPC.

Figure 140 depicts the relationship between the peak bar stress and the clear cover between the loaded bars and the exterior of the UHPC strip. Here, bar type (Gr. 120), embedment length, and bars spacing were held constant, and the data is shown for two different compressive strengths of UHPC. Generally speaking, the data shown indicates that bond strength increases with increasing side cover.

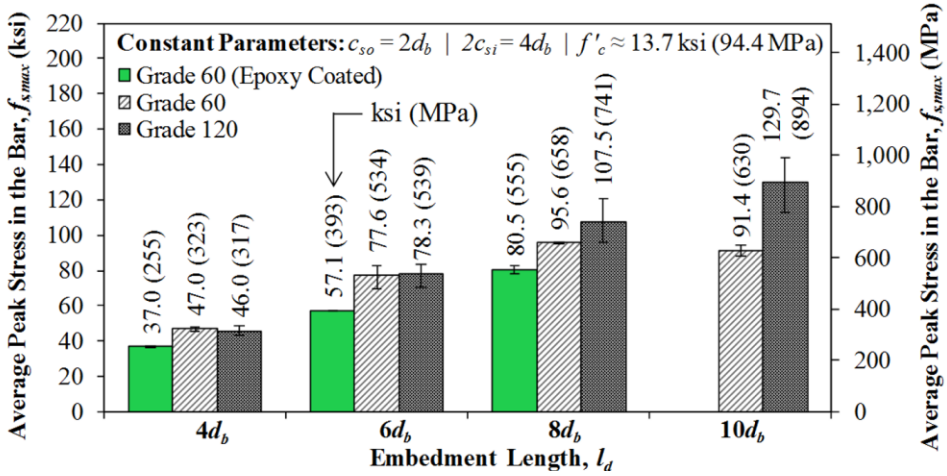

Figure 138. Graph. Relationship between bar embedment length and stress at failure.

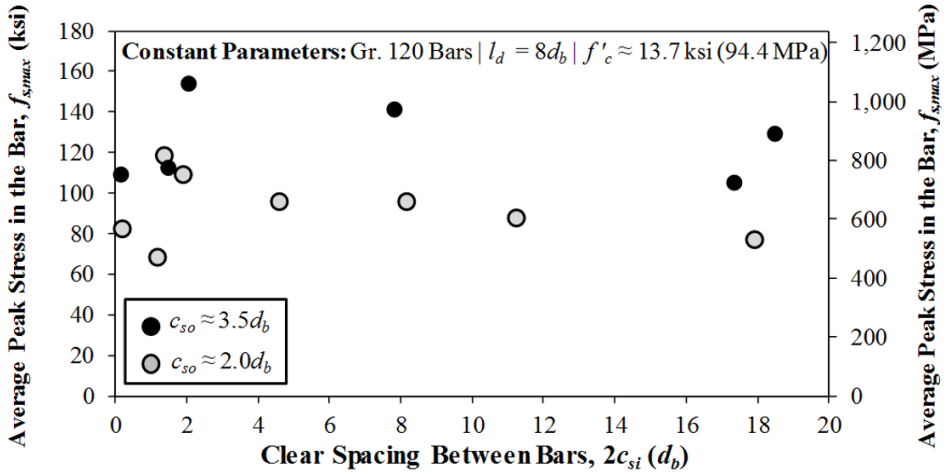

Figure 139. Graph. Relationship between bar clear spacing and stress at failure.

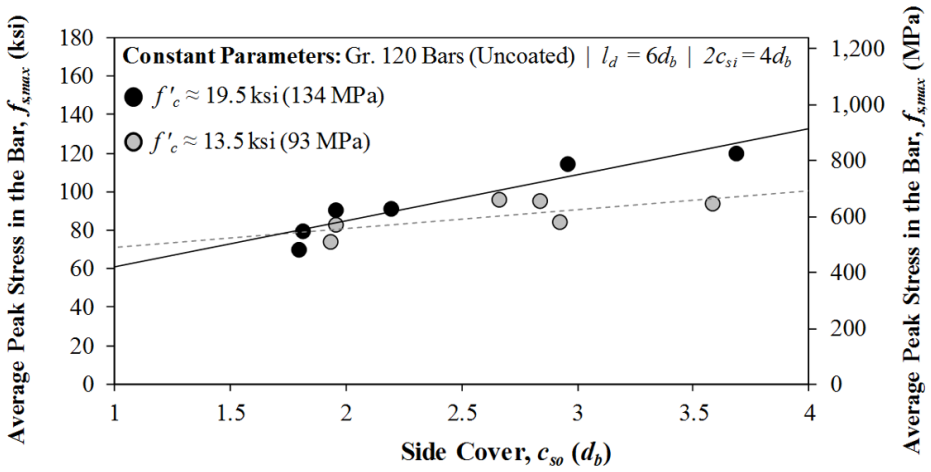

Figure 140. Graph. Relationship between side cover and stress at failure.

Summary of Design Guidance

Yuan and Graybeal synthesized the data collected and developed design guidance related to the embedment and splice lengths for bars embedded in UHPC. The final version of this guidance can be found in the FHWA TechNote entitled: *Design and Construction of Field-Cast UHPC Connections*. (B. A. Graybeal 2014a) The following items summarize the guidance published in this Technote:

Guidance Item 1: The minimum embedment length of deformed steel reinforcement, l_d, shall be taken as $8d_b$ for No. 8 bars and smaller with yield strength of the bar, f_y, less than or equal to 75 ksi (517 MPa) when the following conditions are met:

- Field-cast UHPC with 2-percent steel fiber reinforcement by volume and a compressive strength of at least 14 ksi (97 MPa).
- Side cover, c_{so}, greater than or equal to $3d_b$.

Guidance Item 2: The minimum embedment length of deformed steel reinforcement shall be taken as $10d_b$ for No. 8 bars and smaller when the following conditions are met:

- Field-cast UHPC with 2-percent steel fiber reinforcement by volume and a compressive strength of at least 14 ksi (97 MPa).
- Side cover, c_{so}, greater than or equal to $3d_b$.
- 75 ksi (517 MPa) $\leq f_y \leq$ 100 ksi (689 MPa).

Guidance Item 3: The minimum embedment length of deformed steel reinforcement shall be increased by $2d_b$ when the following conditions are met:

- $f_y \leq$ 100 ksi (689 MPa).

- $2d_b \leq$ minimum cover $< 3d_b$.

Guidance Item 4: For lap splices of straight lengths of deformed steel reinforcement, the lap-splice length, l_s, shall be at least 0.75 times the embedment length, $0.75l_d$.

Guidance Item 5: Clear spacing to the nearest lap-spliced bar should be less than or equal to l_s, but greater than 1.5 times the length (l_f) of the longest fiber reinforcement in the UHPC.

Testing Program

The test program had a limited yet focused scope. Bond was evaluated using the direct tension bond pull-out test detailed in figure 136 and figure 137. As previously noted, one of the primary goals was to determine whether the different commercially available UHPC-class materials would conform to the FHWA design guidance on embedment length. (Graybeal 2014a). Thus, the embedment length (l_d), lap splice length (l_s), clear bar spacing ($2c_{si}$), clear cover (c_{so}), and UHPC compressive strength (f'_c) were selected such that they conformed to the aforementioned design guidance; this group of parameters is subsequently referred to as the "embedment parameters." A summary of the embedment parameters used in this study is as follows:

- Embedment length: $l_d = 8d_b$ or $10d_b$.
- Lap splice length: $l_s \geq 0.75\ l_d$.
- Clear bar spacing: $1.5l_f \leq 2c_{si} \leq l_s$; where l_f is the maximum length of the fiber reinforcement.
- Clear cover: $2d_b \leq c_{so} \leq 3d_b$.
- UHPC compressive strength: 9 ksi (62 MPa) $\leq f'_c \leq$ 23 ksi (158 MPa).

Two different volumetric fiber volume fractions (V_f) were employed for tests focused on the conformance to FHWA embedment design guidance: 2.0 percent fiber by volume and the fiber volume fraction recommended by the UHPC manufacturer.

To study the effect of fiber volume fraction on bond strength, the UHPCs were dosed with different fiber volume fractions ranging between 1.0 percent and 4.5 percent. This series of tests employed the same set of embedment parameters stated above.

For each series of tests, the diameter of the embedded bar and the grade of the bar remained constant. Each test used US #5 (M16), ASTM A1035 Gr. 120 (Metric Gr. 830) bars. The material properties of these bars were shown in table 26.

Test Results

Figure 141 depicts the characteristic response of a deformed reinforcing bar embedded in UHPC in terms of the applied axial stress in the bar and slip of the bar from the UHPC. Herein, "slip" is defined as the combination of elongation of the embedded bar and the deformation caused by strain

penetration of the bar into UHPC. As previously noted, the deformation of the bar was measured using LVDTs. The length of bar contributing to bar elongation was approximately 1 inch (25 mm). As shown in figure 141, the stress-slip response of a deformed reinforcing bar embedded in UHPC is initially linear (approximately). As the load continues to increase, fine microcracks, not visible to the naked eye, begin to form and the stress-slip curve begins to soften. As the peak stress ($f_{s,max}$) is reached, localization of microcracks begins to occur which in turn allows the embedded bar to mobilize. Microcrack localization typically occurred in one of three distinct modes: sides splitting (figure 142); longitudinal splitting (figure 143); and cone-shaped block failure (figure 144). At this point bond begins to fail, resulting in loss of load resistance. Although the stress-slip behavior is examined for a few select parameter sets, the peak stress ($f_{s,max}$) prior to bond failure is the response parameter that drives the discussion of results.

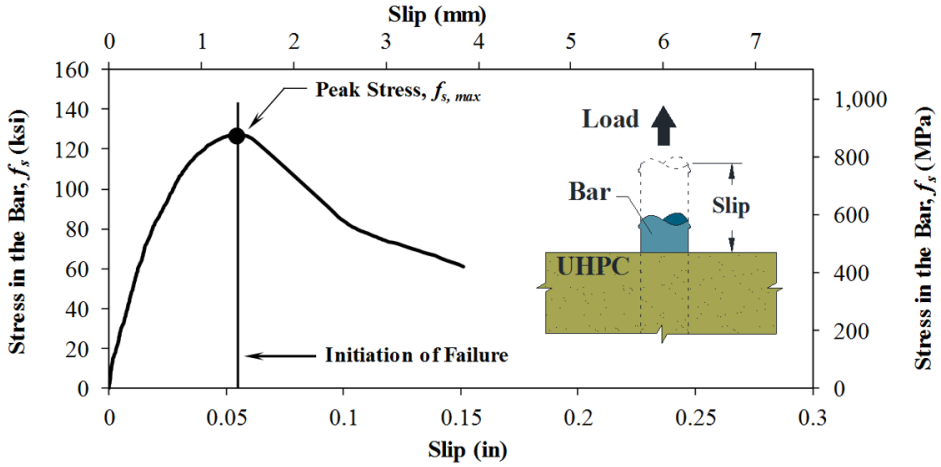

Figure 141. Illustration. Stress-slip behavior of bars embedded in UHPC.

Figure 142. Photo. Bond test failure due to side splitting.

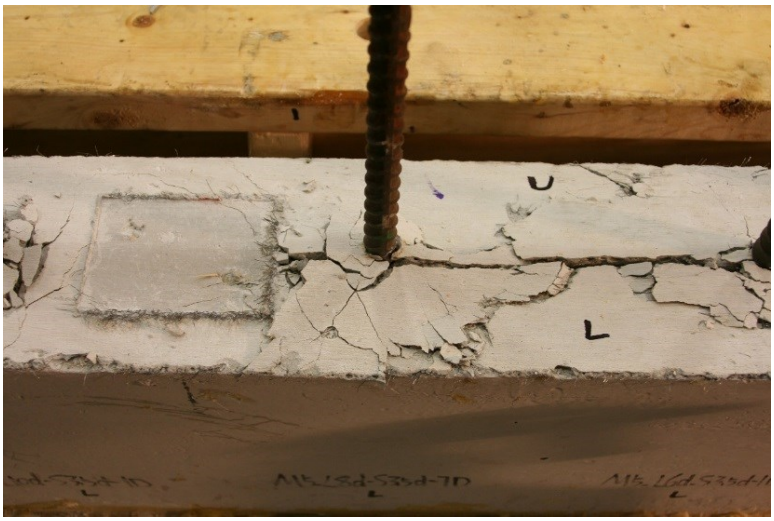

Figure 143. Photo. Bond test failure due to longitudinal splitting.

Figure 144. Photo. Bond test failure due to cone-shaped block fracture mode.

Table 27 summarizes the pull-out bond test results from different UHPCs when reinforced with 2.0 percent fiber by volume and employing an embedment length of $l_d = 8d_b$. Figure 145 compares the stress-slip behavior of five representative specimens from this series of tests; one for each UHPC. In order to provide an objective comparison, representative specimens were selected such that the peak stress was similar among the different UHPCs presented. In general, each UHPC exhibited the characteristic behavior shown in figure 141. It should be noted that although the peak stresses did not exhibit a significant amount of variance, the stress-slip behavior of individual specimens with like parameters could vary significantly. That is, the slip at which the peak stress occurred or the energy dissipated during loading (i.e., the area under the stress-slip curve). Figure 146 shows the average peak stress prior to bond failure for each UHPC-class material with 2.0 percent fiber by volume and $l_d = 8d_b$. *Guidance Item 1* noted that bars embedded $8d_b$ in UHPC

with 2.0 percent fiber and conforming to the aforenoted embedment parameters can develop a stress in the bar of 75 ksi (517 MPa); this recommendation is shown in figure 146. It can be observed that each UHPC far exceeds this recommendation.

Table 27. Pull-out results from the different UHPC mixtures with 2.0 percent fibers by volume and $l_d = 8d_b$.

Material	Peak Stress in the Bar, $f_{s,max}$ (ksi)			Compressive Strength of UHPC (ksi)	Average Embedment and Spacing Parameters (d_b)					Fiber Volume (percent)	Samples Tested
	Average	Max	Min	f'_c	c_{so}	$2c_{si}$	l_d	l_s	l_s / l_d		
U-A	116.0	126.4	93.7	16	3.1	7.7	8.2	6.6	0.80	2.0	4
U-B	136.5	145.3	127.3	16.3	3.0	4.8	7.9	6.3	0.80	2.0	4
U-C	125.6	134.6	117.6	13.6	2.8	4.9	8.1	6.5	0.80	2.0	4
U-D	133.1	138.2	125.6	13.8	2.8	4.9	8.3	6.7	0.81	2.0	4
U-E	109.5	115.7	100.5	13.3	3.1	4.9	8.0	6.4	0.80	2.0	5

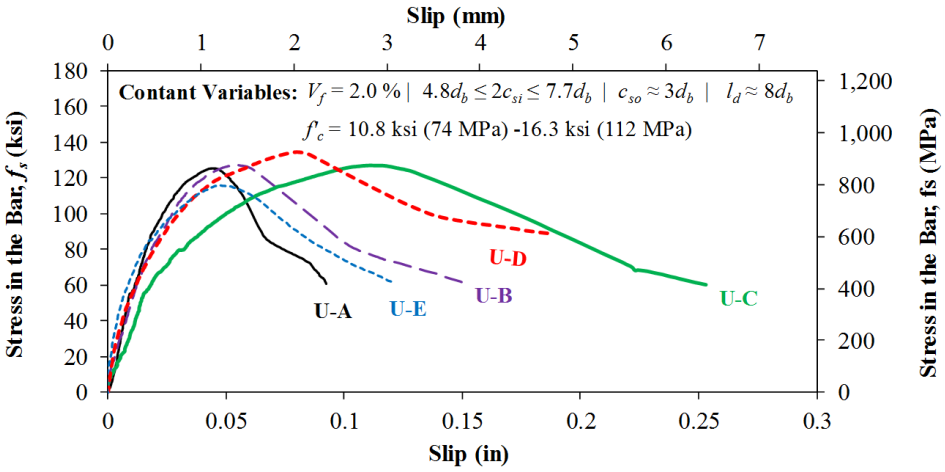

Figure 145. Graph. Stress-slip behavior the different UHPC mixtures with 2.0 percent fibers by volume.

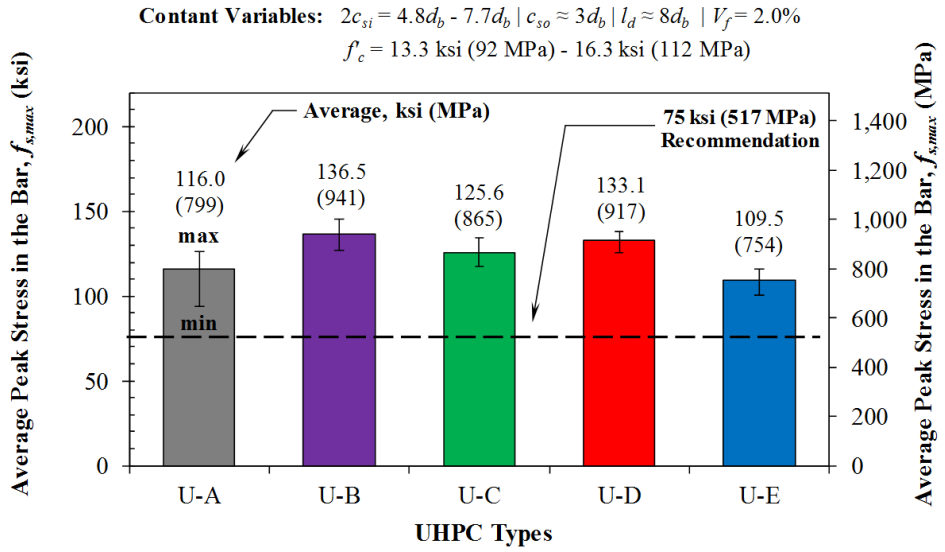

Figure 146. Graph. Average peak stress achieved from the different UHPC mixtures with 2.0 percent fibers by volume and $l_d = 8d_b$.

Table 28 summarizes the pull-out bond test results from different UHPCs when reinforced with the manufacturer-recommended volumetric fiber content and employing an embedment length of $l_d = 8d_b$; note, some of the data listed in table 27 is repeated in table 28. Specifically, U-A (V_f = 3.0 percent) and U-C (V_f = 4.5 percent) had higher manufacturer-recommended volumetric fiber contents than the other three UHPCs. The increased fiber volume fractions in U-A and U-C resulted in slightly higher bond strengths. When the fiber volume fraction in U-A was increased from 2.0 percent to 3.0 percent, the peak stress in the bar prior to failure increased 6 percent, and when the fiber volume fraction in U-C was increased from 2.0 percent to 4.5 percent, the peak stress in the bar prior to failure increased 17 percent. Lastly, it can be observed that each UHPC exceeds the 75 ksi (517 MPa) recommendation when the manufacturer-recommended fiber volume fraction is used. It should be kept in mind that these materials were designed for structural

engineering applications, and therefore the volumetric fiber contents have been proportioned specifically for such application.

Table 28. Pull-out results from the different UHPC mixtures with the manufacturer-recommended volumetric fiber content and $l_d = 8d_b$.

Material	Peak Stress in the Bar, $f_{s,max}$ (ksi)			Compressive Strength of UHPC (ksi)	Average Embedment and Spacing Parameters (d_b)					Fiber Volume (percent)	Samples Tested
	Average	Max	Min	f'_c	c_{so}	$2c_{si}$	l_d	l_s	l_s / l_d		
U-A	123.8	128.5	121.4	15.2	3.1	4.6	8.1	6.5	0.80	3.0	3
U-B	136.5	145.3	127.3	16.3	3.0	4.8	7.9	6.3	0.80	2.0	4
U-C	147.2	157.5	131.3	10.8	2.9	4.9	8.0	6.4	0.80	4.5	6
U-D	133.1	138.2	125.6	13.8	2.8	4.9	8.3	6.7	0.81	2.0	4
U-E	109.5	115.7	100.5	13.3	3.1	4.9	8.0	6.4	0.80	2.0	5

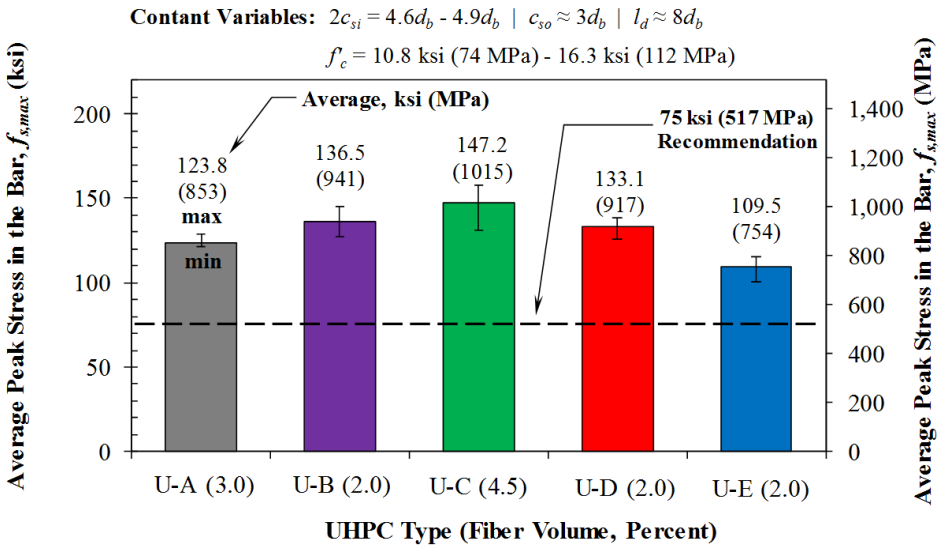

Figure 147. Graph. Average peak stress achieved from the different UHPC mixtures with the manufacturer-recommended volumetric fiber content and $l_d = 8d_b$.

Table 29 summarizes the pull-out bond test results and figure 148 compares the average peak stress prior to bond failure from different UHPCs when reinforced with the manufacturer-recommended volumetric fiber content and employing an embedment length of $l_d = 10d_b$. With the exception of U-C, increasing the embedment length results in higher peak stresses in the bar prior to bond failure. The benefit of an additional $2d_b$ of embedment length might not have been apparent in U-C due to such a high fiber volume fraction. As will be subsequently shown, increasing fiber content does not always enhance performance. That is, there is a point of diminishing return, which could explain why U-C does not exhibit enhanced performance as the embedment length increases.

Guidance Item 2 noted that bars embedded $10d_b$ in UHPC with 2.0 percent fiber and conforming to the aforenoted embedment parameters can develop a stress in the bar of 100 ksi (517 MPa); this recommendation is shown in figure 148. It can be observed that the bond strength of each UHPC far exceeds this recommendation.

Table 29. Pull-out results from the different UHPC mixtures with the manufacturer-recommended volumetric fiber content and $l_d = 10d_b$.

Material	Peak Stress in the Bar, $f_{s,max}$ (ksi)			Compressive Strength of UHPC (ksi)	Average Embedment and Spacing Parameters (d_b)					Fiber Volume (percent)	Samples Tested
	Average	Max	Min	f'_c	c_{so}	$2c_{si}$	l_d	l_s	l_s / l_d		
U-A	149.9	162.5	132.1	15.2	3.0	4.4	9.9	8.3	0.84	3.0	3
U-B	145.6	164.0	130.2	16.3	2.9	4.5	10.0	8.4	0.84	2.0	4
U-C	144.8	162.3	133.5	10.8	2.8	4.4	9.9	8.3	0.84	4.5	4
U-D	140.5	140.5	140.5	13.9	2.9	4.8	9.8	8.4	0.86	2.0	1
U-E	124.6	133.9	115.2	13.3	3.0	4.4	10.2	8.6	0.84	2.0	2

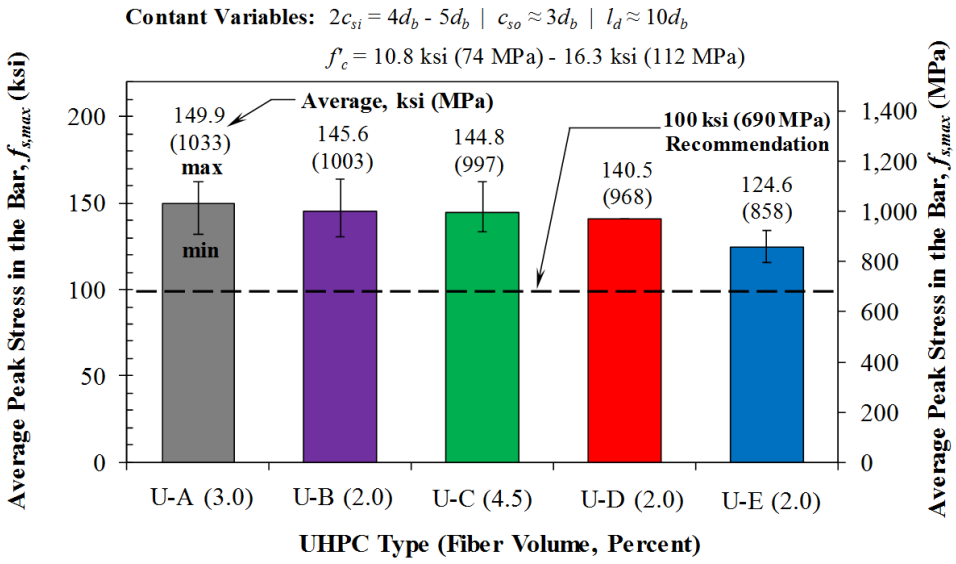

Figure 148. Graph. Average peak stress achieved from the different UHPC mixtures with the manufacturer-recommended volumetric fiber content and $l_d = 10d_b$.

The following discussion pertains to the investigation of UHPC fiber volume fraction. Figure 149 shows a set of representative photos of rebar bond test specimens after failure and the corresponding failure mechanisms for different fiber volume fractions. In general, specimens employing lower fiber volume fractions exhibited localized splitting cracks that formed and propagated along the length of the UHPC strip. This indicates that the tensile strength of UHPC was overcome by radial stresses introduced by the loaded test bar, which caused UHPC cracking and subsequent mobilization of the test bar. Splitting cracks at failure became finer as fiber

volume fractions were increased. This can be observed by comparing figure 149-A and -B. A cone-like failure mechanism began to control specimen behavior when fiber volume fractions were increased beyond 4-percent (figure 149-C). This indicates that additional fiber reinforcement enhances the confinement of the bar, preventing splitting failure. It should be noted that reducing the clear side cover, even with higher fiber volume fraction, could result in splitting failure. Lastly, there was not apparent difference in failure mode among the different UHPC-class materials when the fiber volume fraction was held constant.

A. Wide splitting cracks: U-D with V_f = 1.5 percent

B. Thin splitting cracks: U-D with V_f = 2.5 percent

C. Cone failure: U-C with V_f = 4.5 percent

Figure 149. Photos. Rebar bond tests after failure for different fiber volume fractions.

Figure 150 compares the stress-slip behavior of material U-D with the different fiber volume fractions. Each curve is a representative specimen for a given fiber volume fraction, and was selected such that the peak stress was approximately equally the average response from a given specimen group. Furthermore, the stress in the bar was normalized by the square root of the compressive strength of UHPC; this is common in concrete design and has been used in previous studies on UHPC-reinforcing bar bond. (Marchand et al. 2016) In general, each U-D mixture with varied V_f exhibited the characteristic stress-slip response. It was observed that increasing fiber content tended to increase the peak stress prior to bond failure and post-peak energy dissipation capacity. The initial slope of the stress-slip curve and the slope of the post-peak curve were unaffected by varied fiber content.

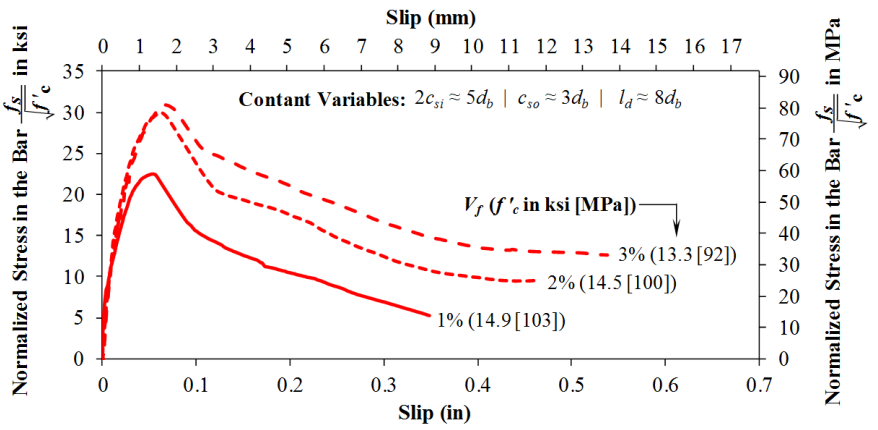

Figure 150. Graph. Stress-slip behavior of U-D with different volumetric fiber contents.

Figure 151 and figure 152 depict the relationship between the normalized peak bar stress and the fiber volume fraction for the two different embedment lengths; $l_d = 8d_b$ and $l_d = 10d_b$, respectively. Each data point represents a single, unaveraged data point. A linear regression analysis was performed on the data. The graph shows the best-fit line, goodness of fit, and the 95-percent confidence and predication intervals. The goal was not to develop a predictive model, but to show overarching trends with particular level of certainty. Both data sets indicate that there is an increasing relationship between the fiber volume fraction and the bond capacity between reinforcing bars and UHPC. Previous research by Yoo et al. (2014) showed that there was very little increase in bond strength as the fiber volume fraction was increased; a fiber content increase from 1-percent to 4-percent resulted in only a 4.5-percent increase in bond strength with the embedment length was $2d_b$. However, the study by Yoo et al. (2014) employed a modified version of the RILEM bond test which generated a different stress state than the test used herein and may have thus affected results. (RILEM TC 1983) The result shown in Fig. 8 indicates that increasing V_f results in enhanced confinement of the embedded bars when subjected to direct tension which increases bond strength. These results would also indicate that connections employing UHPCs with fiber volume fractions less that V_f = 2-percent may result in reduced ductility at the ultimate limit state; note, this assumes that the cover and spacing requires from Graybeal (2014a) are followed. For example, tests by Lee and Lee (2015) showed that $10d_b$ lap splices embedded in UHPCs with V_f < 1.5-percent exhibited lap splice failure under monotonic loading.

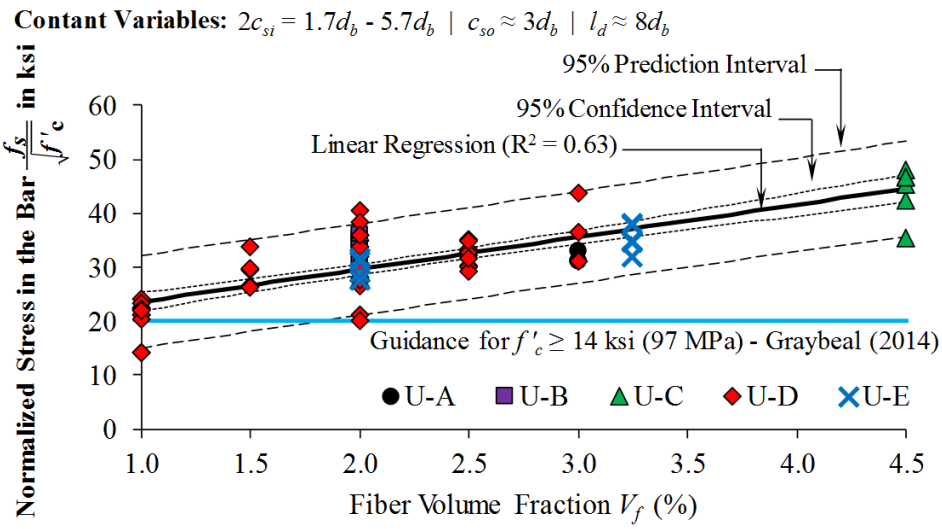

Figure 151. Graph. Relationship between peak bar stress and fiber content for $l_d = 8d_b$.

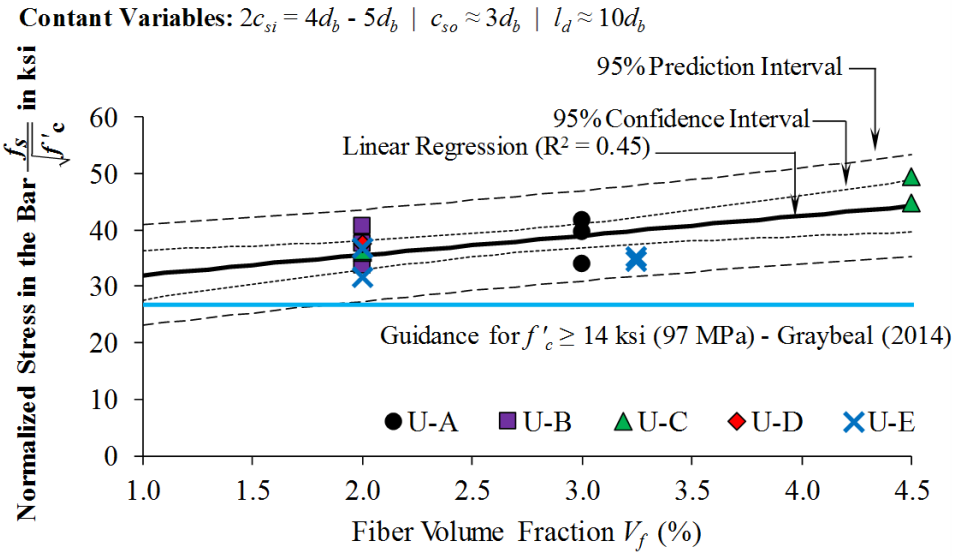

Figure 152. Graph. Relationship between peak bar stress and fiber content for $l_d = 10d_b$.

PREFABRICATED BRIDGE DECK CONNECTION TESTS

This section presents the performance of the different UHPC-class materials in deck-level connections between adjacent prefabricated bridge deck elements. The performance of deck-level connections was evaluated using large-scale precast deck panel specimens. Specimens were subjected to three different loading protocols to assess behavior under different levels of cyclic and monotonic loading. Focal areas of the investigation included interface bond between UHPC and precast concrete, cracking behavior under cyclic loading, response under long-term cyclic

loading, and monotonic ultimate loading behavior. five deck panel connections specimens were designed, constructed, and tested.

Background

The performance of prefabricated bridge systems is highly dependent on the design and detailing of connections between elements. Structural continuity between elements is commonly created using field-cast grout cast over interlaced reinforcing bars. Ideally, these connection grouts are self-consolidating, have high early strength, good dimensional stability, and bond well to precast concrete. Traditionally, connections grouted using conventional non-shrink cementitious grouts (NSG). Recently, UHPC has been identified as an alternative to conventional grouts because the fresh and hardened properties of UHPC-class materials better align with the desired properties mentioned above.

Currently, the most popular application of UHPC in U.S. bridge construction is for connections between prefabricated bridge deck elements. Previous studies have demonstrated the structural performance of prefabricated bridge decks with UHPC connections is similar to that of conventional cast-in-place construction (Graybeal 2014b; Haber, De la Varga, and Graybeal 2016). Furthermore, the advanced properties of UHPC allows for simple reinforcement details within the connection region. Using conventional non-shrink grouts, the flexural reinforcement within the connection region typically requires hooked or U-shaped bars to meet development length requirements (Li et al. 2010). Furthermore, additional reinforcing bars are typically required to resist secondary forces such as temperature and shrinkage loads; these bars are usually referred to as “lacer” bars. Such details increase congestion within connection region and can result in poor constructability. Using UHPC, there is typically no need for hooked flexural reinforcement or lacer bars, thus greatly simplifying the detailing and increasing the constructability.

Specimen Design and Details

Deck panel connection specimen geometric and reinforcement details are shown in figure 153. Specimens were designed to be representative of prefabricated bridge deck systems currently being employed in the field. Specifically, the deck panel thickness was similar to what would be typically found on a pre-decked superstructure element such as a prestressed deck bulb tee (DBT) girder. Each specimen was composed of two individual, precast concrete panel elements. Individual panel elements had a series of protruding reinforcing bar dowels that would be interlaced during specimen construction (figure 154-a) to form a 5.5-in (140-mm) non-contact lap splice length, and a connection width of 6 in. (152 mm). Lap splice details were designed according to the publication *Design and Construction of Field-Cast UHPC Connections* (B. A. Graybeal 2014a).

The design and expected flexural behaviors of deck panel specimens were calculated using the working stress / strength method and the moment-curvature analysis methods, respectively. The strength method is commonly used in the design of non-prestressed, flexure concrete elements, and provides a conservative estimate of the flexural capacity of the member. On the other hand, the moment-curvature analysis method is less conservative but provides a more accurate representation of the expected behavior. Moment-curvature analysis was conducted using a computer code written in a commercially available scientific computing platform. For moment-curvature analysis, the stress-strain behavior of concrete was described using the model presented

by Hognestad, Hanson, and McHenry (1955), and the stress-strain behavior of the reinforcing steel was described using the model presented by Mander (1983). Table 30 lists the cracking, yield and ultimate moments for deck panel specimen calculated using the working stress and moment-curvature methods; the moments shown in this table where determined assuming a concrete strength of 6 ksi (41.3 MPa).

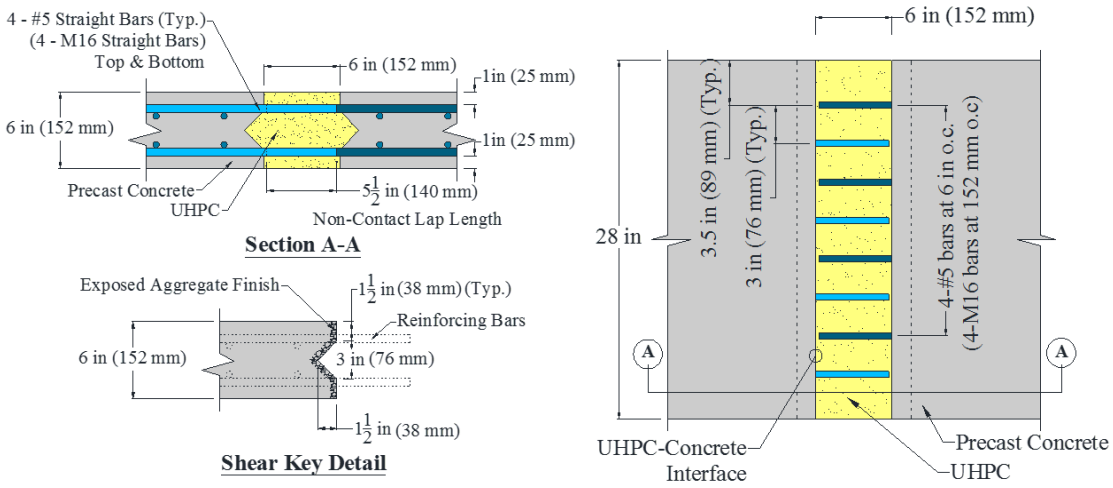

Figure 153. Illustration. Pertinent details of deck-level connection test specimens.

Table 30. Cracking, yield and ultimate moments calculated using working stress and moment-curvature methods.

	Working Stress (Strength) Method		Moment-Curvature Method	
	kip-in	(kN-m)	kip-in	(kN-m)
Cracking Moment, M_{cr}	98.8	(11.2)	98.8	(11.2)
Yield Moment, M_y	313.7	(35.4)	313.8	(35.4)
Ultimate Moment, M_u	324.5	(36.6)	380	(42.9)

The construction of deck panels and connection grouting was completed in the Structural Testing Laboratory at TFHRC. Deck panel concrete was the same as displayed in table 21. Once cast, panels were allowed to cure in the laboratory for at least 24 hours prior to being removed from formwork. Once removed, panels were stored indoors until being prepped for constructing deck-level connections. Individual precast concrete panel elements employed an exposed aggregate finish on the portion of the deck intended to interface with UHPC within the connection region. The exposed aggregate finish was created using an in-form, paint-on retarder which was described in detail in Chapter 4.

Deck panel specimens were constructed by placing two precast deck panels together such that the protruding rebar dowels interlaced between panels as shown in figure 154-a; the seam shown is referred to as the "connection region." The connection region was blocked off and sealed on the lower and side faces prior to grouting (shown in figure 154-b). Each UHPC was mixing according

to the procedures discussed in Chapter 3, and was placed using a bucket or wheelbarrow as shown in figure 154-b. UHPC was allowed to cure for seven days under controlled laboratory conditions prior to removal of forms. Prior to installing instrumentation, the tension surface of UHPC and the concrete adjacent to the concrete-UHPC interface was ground smooth using a hand grinder (figure 154-c). This not only allowed for installation of instrumentation but also facilitated visual identification of interface cracking.

During the fabrication procedures, deck concrete and UHPC compression cylinders were cast. The compressive strength of concrete was determined using 4 x 8 in (102 x 204 mm) cylinders, which were cast during the construction of individual deck panel elements. The compressive strength of UHPC was determined using 3 x 6 in (75 x 150 mm) cylinders, which were fabricated during connection casting. Lastly, a set of companion interface bond specimens were also fabricated for each deck panel specimen. Each set of companion specimens consisted of three flexural bond samples and a direct tension pull-off slab. These specimens were fabricated according to the details provided in Chapter 4.

A. Connection prepared for casting UHPC.

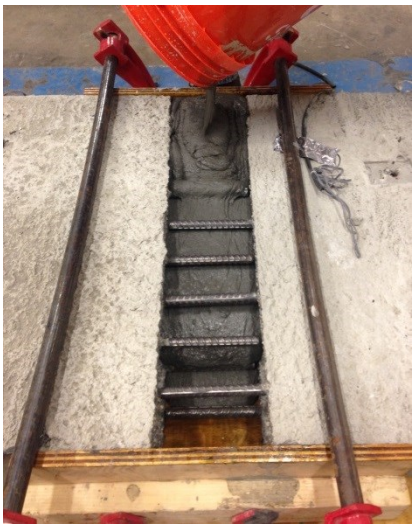

B. Casting UHPC.

C. Prepared interface tension surface.

Figure 154. Photos. Specimen construction and preparation for testing.

Instrumentation and Test Set-Up

The instrumentation plan is shown in figure 155 along with the loading configuration. Deck panel specimens were instrumented with ten LVDTs and two foil-backed electrical resistance strain gauges. As shown in figure 155, each interface location was instrumented with four LVDTs to capture curvature over the interface and within adjacent precast concrete deck panel. Two vertical LVDTs, mounted on a load spreader beam, were used to capture the vertical deflection of the specimen at mid-span. Strain gauges were installed on a single tension reinforcing bar within each individual precast panel element.

Deck panels were tested in four-point bending using a 110-kip (490 kN) servo-controlled hydraulic actuator. The tension face of the panel was positioned upward to facilitate inspection during testing. The connection region was located within the constant moment region between supports spaced at 36 in (914 mm) on center. The actuator load was transferred to the deck panel using a spreader beam with load points at 90 in (2.3 m) on center. During testing, displacement and load measurements were captured form the actuator. Furthermore, specimens were periodically inspected during testing using a crack mircoscope. Prior to initial application of load, each specimen was inspected for cracks that may have been caused by shrinkage or handling.

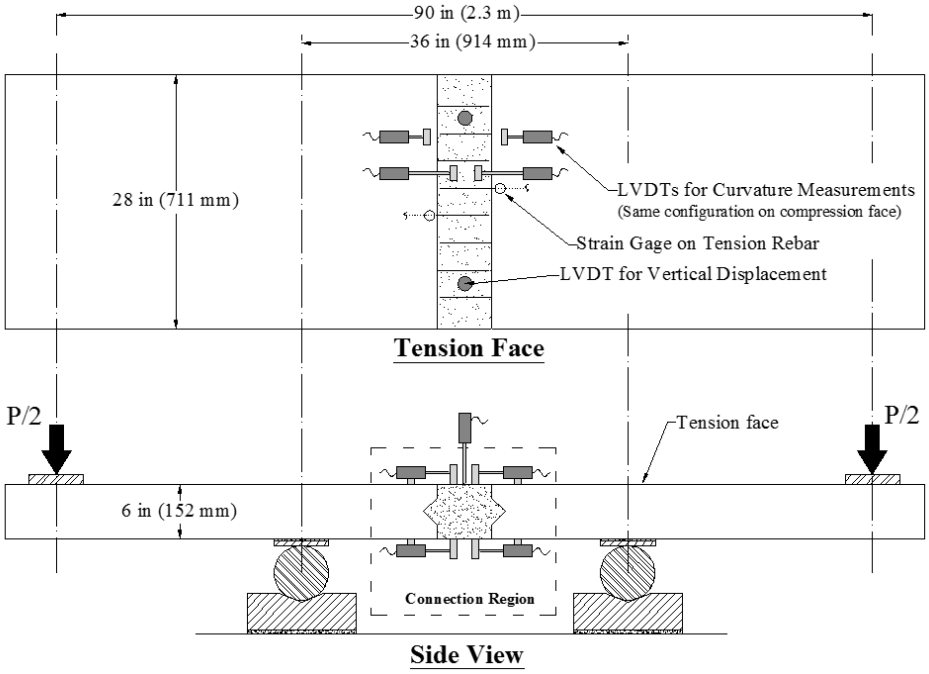

Figure 155. Illustration. Instrumentation and loading configuration.

Loading Protocols

Specimens were subjected to three different loading protocols. Loading protocols included pre-cracking cyclic loading, post-cracking cyclic loading, and monotonic ultimate loading, which were applied in succession. If a specimen failed, which was defined as an abrupt loss of load carrying capacity during one of the loading protocols, then subsequent loading was not pursued.

Pre-Cracking Cyclic Loading

The primary goals of the pre-cracking cyclic loading procedure were to investigate the performance of the UHPC-to-concrete interface at the component-level scale and to investigate the cracking resistance of the connection region. The cyclic crack loading protocol is shown in figure 156. The cracking moment, M_{cr}, was calculated using the equation shown in figure 157, which is based on provisions specified in section 5.7.3.3.2 of the AASHTO LRFD Bridge Design Specifications (AASHTO, 2014). M_{cr} was determined to be 98.8 kip-in (11.2 kN-m). The required actuator force to produce M_{cr} was 6.2 kip (27.6 kN) which took into account the moment due to specimen self-weight and loading fixtures such as bearing plates. Load was applied at a frequency

of 3 Hz, and was cycled between 10 percent of M_{cr} and an upper load target which varied with the number of applied cycles. Five thousand cycles were applied for each upper load target which ranged from 30 percent to 120 percent of M_{cr}. An additional 50,000 cycles were applied at the 120 percent of M_{cr} target.

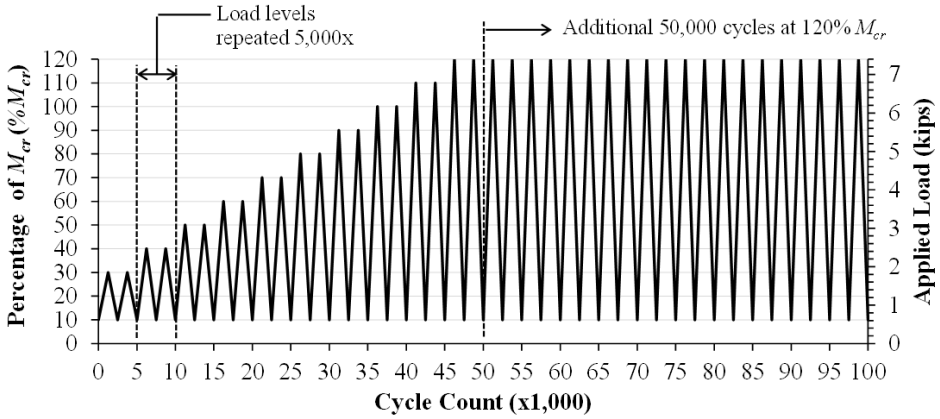

Figure 156. Graph. Cyclic crack loading protocol (1 kip = 4.448 kN).

$$M_{cr} = f_r \frac{I_g}{y_t}$$

Figure 157. Equation. Cracking moment as defined by AASHTO (2014).

Where

f_r = modulus of rupture of concrete defined by the equation shown in figure 158

I_g = gross moment of inertia of the deck cross-section

y_t = distance between the neutral axis of bending and the extreme tension fiber of the deck cross-section

$$f_r = 0.24\sqrt{f'_c} \text{ (in ksi)}$$

Figure 158. Equation. Modulus of rupture for normal-weight concrete (AASTHO, 2014).

Where

f'_c = specified 28-day compressive strength of concrete; deck panel concrete was specified to have compressive strength of 6 ksi (41.3 MPa) after 28-days.

Post-Cracking Cyclic Loading

The post-cracking cyclic loading protocol is shown in figure 159. This protocol had two different loading ranges: a low-level range, and a high-level range which is referred to as "overloading."

The primary goal of the low-level range was to subject the connection region to the maximum stress range without inducing fatigue fracture of the steel reinforcing bars. The load limits for the low-level cycles were determined using the constant amplitude fatigue threshold expression defined by AASHTO (2014) which is shown in figure 160. A minimum load target of approximately 11 percent of calculated yield moment (M_y) was selected, which was used to determine f_{min}. The upper load target for the low-level ranged was subsequently selected to be 47 percent of yield moment M_y. This resulted in a calculated stress range of 21.2 ksi (146 MPa) in the tension steel. The overload cycles employed the same minimum load target as the low-level cycles but included an increased upper load target. The upper load target for the over cycles was selected to be approximately 75 percent of M_y. Specimens were subjected to an initial set of 20,000 low-level cycles, and an initial 1,000 overload cycles. Thereafter, 99,000 low-level cycles where applied followed by 1,000 overload cycles. These two cycle sets were repeated 20 times. At the conclusion of the loading protocol, specimens would have endured a total of 2 million low-level cycles and 20,000 overload cycles.

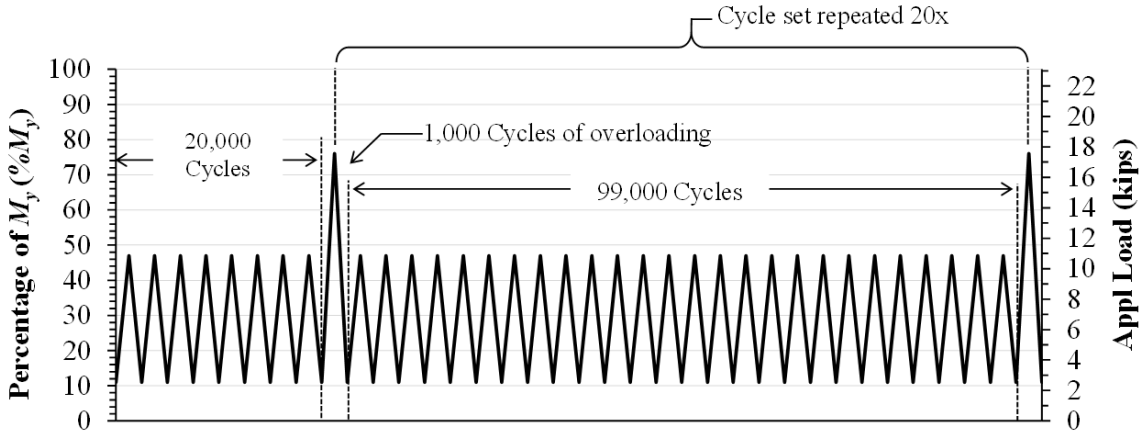

Figure 159. Graph. Post-cracking cyclic loading protocol.

$$(\Delta F)_{TH} = 24 - 20 f_{s,min} / f_y \text{ (in ksi)}$$

Figure 160. Equation. Constant amplitude fatigue threshold defined by AAHSTO (2014).

Where

$f_{s,min}$ = minimum tensile stress in reinforcing steel

f_y = yield strength of reinforcing steel

Monotonic Ultimate Loading

Specimens that survived the fatigue loading protocol were subsequently subjected to monotonic loading until failure. Load was applied in displacement-control in 0.05 inch/min (1.28 mm/min) increments until failure.

Results

Pre-Cracking Cyclic Loading

Performance of connections under pre-cracking cyclic loading was evaluated by visual inspection, global stiffness degradation due to cracking, and measured strains in the steel reinforcing bars.

Specimens were visually inspected for cracks after each set of 5,000 cycles. Of specific interest was when the first crack occurred at the connection interface or in the vicinity of the connection interface within the precast concrete deck panel. Table 31 lists the load levels when cracking was first observed at the interface and within the precast concrete; the stress associated with the given moment is also listed assuming an uncracked section. The only specimen that exhibited first flexural cracking at the connection interface employed U-C. This specimen exhibited interface bond failure during the 60 percent of M_{cr} load cycles. The other specimens did not exhibit interface bond failure. In these specimens, first cracking occurred near the interface in precast concrete. Although interface cracking was not visually observed in four out of five specimens this does not guarantee some degree of cracking was not present.

Table 31 also reports results from interface bond tests conducted on the same day at the pre-cracking cyclic loading protocol. These tests employed concrete and UHPC from the same batches of material used to construct the deck panel specimens and grout connections. Results indicate that the stress at first cracking within the connection specimen is bounded by the results from the interface bond tests. That is, in all cases, the peak tensile stress from flexural beam bond testing tends to be larger than the stress at first cracking in the deck panel specimens. While, the peak tensile stress from the direction tension pull-off test tends to be lower.

Figure 161 depicts the measured flexural stiffness of each specimen as a function of both cycle number and maximum load applied (percent M_{cr}) during a given cycle group; the horizontal axis at the top of the graph indicates the peak load target for a given set of 5,000 cycles. The two dashed lines shown in figure 161 represent the expected (theoretical) response of the deck panel specimens assuming uncracked and fully-cracked sections. The uncracked section response line was determined using the gross moment of inertia, I_g, of the deck panel specimen, and the fully-cracked section response line was calculated using the cracked moment of inertia, I_{cr}, determined using a transformed section.

The initial stiffness of each specimen was approximately equal to that calculated using the gross moment of inertia I_g which is shown as the upper dashed line in the graph. The flexural stiffness of the specimens begins to decrease once cracking begins to occur. Regardless of when and where first cracking occurs, the flexural behavior of specimens was ultimately governed by crack formation with the precast concrete deck panel elements. At the conclusion of the loading protocol, the flexural stiffness of the specimens was approximately the same, and bounded by the theoretical stiffness calculated using the gross (I_g) and cracked (I_{cr}) moments of inertia.

Figure 162 depicts the change in measured rebar strain near the connection interface as a function of cycle number. The change in rebar strain, as shown in figure 163, is defined as the difference between the maximum and minimum strain recorded for a given cycle. The graph also displays the calculated (expected) response of an elastic, uncracked section. For specimens grouted with U-C and U-E, it was apparent that cracking at or near the concrete-UHPC interface may have

occurred prior to what was determined by visual inspection; the measured response for these two specimens tends to deviate from the expected response prior to the observed crack marker.

Representative photos of specimens U-A, -B, -C, -D, and -E at the conclusion of the pre-cracking cyclic loading protocol are provided in figure 164 through figure 168, respectively. Each specimen exhibited well-distributed flexural cracks in the precast panels. There was no observed damage within the UHPC connections; observations were made both visually and with a crack microscope.

Table 31. Results from pre-cracking cyclic loading and associated interface bond tests.

ID	Deck Panel Test						Interface Bond Tests ††			
	Interface Cracking			Deck Cracking Near Interface			Peak Tensile Stress from Flexural Bond Testing*, ksi (MPa)		Peak Tensile Stress from Direct Tension Pull-Off Test**, ksi (MPa)	
	percent M_{cr}	Tensile Stress, ksi (MPa)		percent M_{cr}	Tensile Stress, ksi (MPa)					
U-A		†		90	0.507	(3.49)	0.598	(4.12)	0.339	(2.34)
U-B		†		100	0.563	(3.88)	0.607	(4.18)	0.482	(3.32)
U-C	60	0.338	(2.33)	110	0.619	(4.27)	0.491	(3.38)	0.217	(1.50)
U-D		†		110	0.619	(4.27)	0.684	(4.71)	0.417	(2.87)
U-E		†		80	0.450	(3.10)	0.538	(3.71)	0.371	(2.56)

† Interface bond failure did not occur in these specimens

†† Interface bond test were completed on the same day as cracking cycles

* Results are the average of three specimens, all of which failed in concrete.

** Results are the average of two to four specimens, all of which failed at the interface.

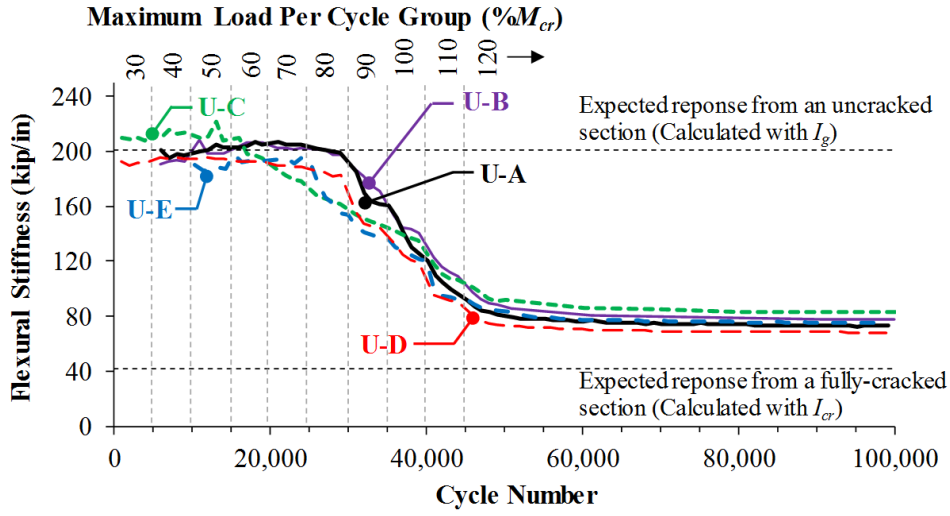

Figure 161. Graph. Stiffness degradation during pre-cracking cyclic loading.

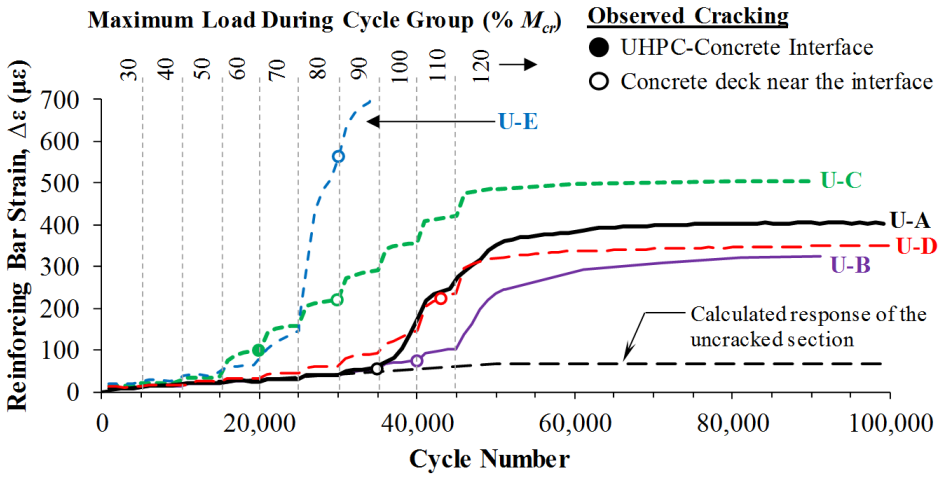

Figure 162. Graph. Reinforcing bar strains during pre-cracking cyclic loading.

$$\Delta\varepsilon = \varepsilon_{t,max} - \varepsilon_{t,min}$$

Figure 163. Equation. Change in tensile strain.

Where

$\varepsilon_{t,max}$ = measured strain at peak load for a given cycle

$\varepsilon_{t,min}$ = measured strain at minimum load for a given cycle

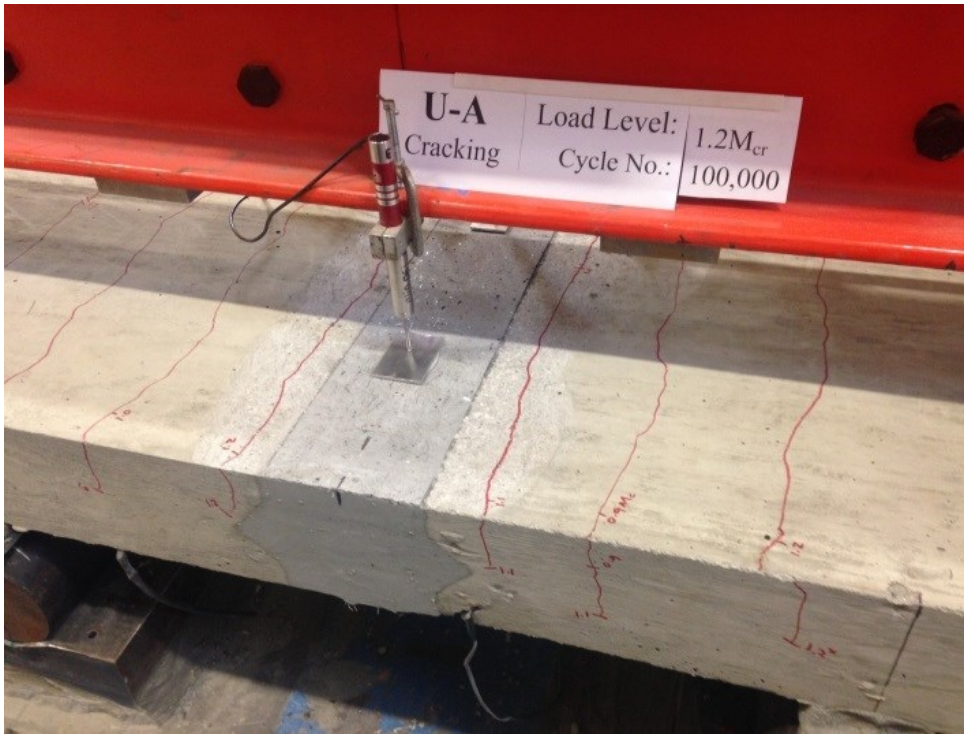

Figure 164. Photo. Observed cracking in specimen U-A after pre-cracking cyclic loading.

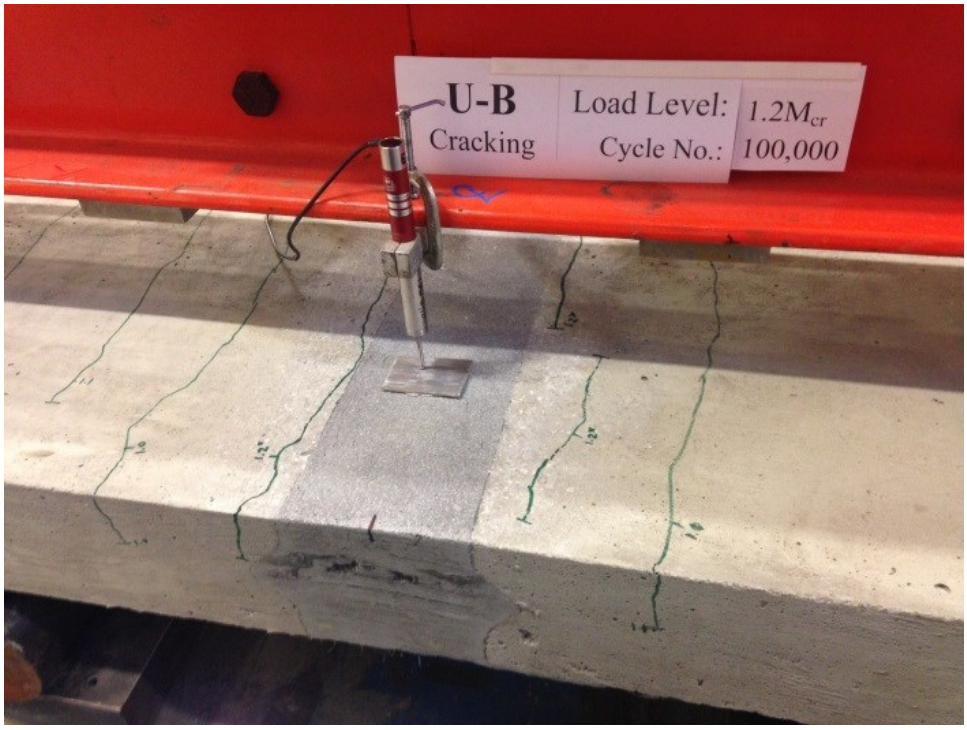

Figure 165. Photo. Observed cracking in specimen U-B after pre-cracking cyclic loading.

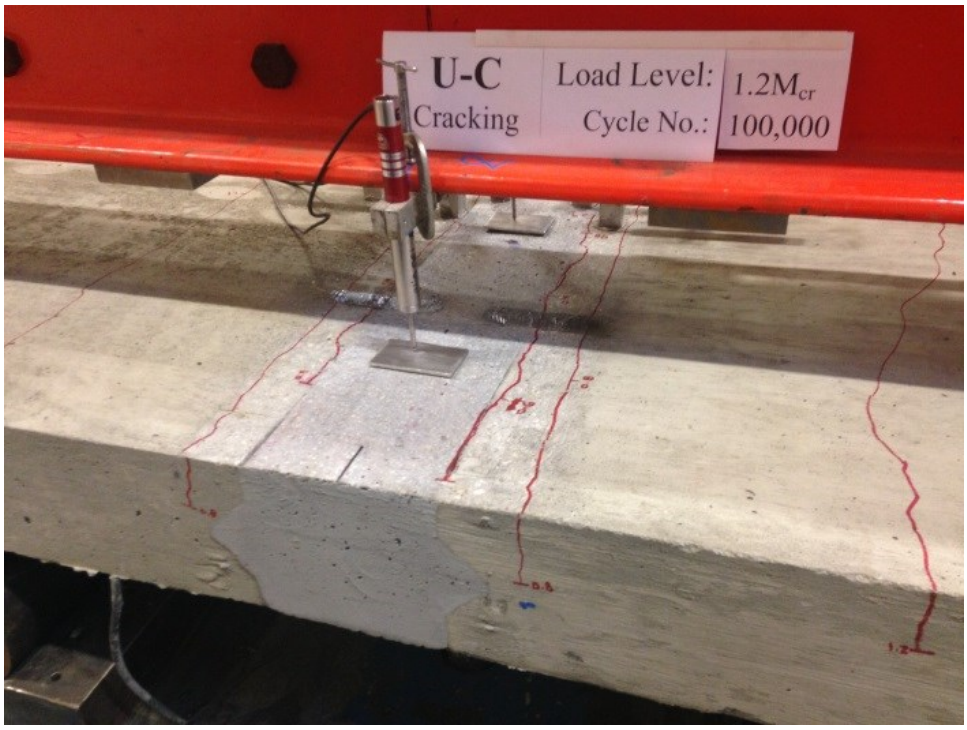

Figure 166. Photo. Observed cracking in specimen U-C after pre-cracking cyclic loading.

Figure 167. Photo. Observed cracking in specimen U-D after pre-cracking cyclic loading.

Figure 168. Photo. Observed cracking in specimen U-E after pre-cracking cyclic loading.

Post-Cracking Cyclic Loading

Performance of connections under post-cracking cyclic loading was evaluated by visual inspection, global stiffness degradation due to cracking, and measured curvatures occurring at the concrete-UHPC interface. The primary goal of the post-cracking cyclic loading protocol was to subject the connection region to the maximum stress range without inducing fatigue fracture of the steel reinforcing bars. Table 32 reports the average reinforcing bar stress ranges along with the calculated stress ranges. The stress ranges were determined from strain measurements, and were comparable to the calculated ranges determined using the moment-curvature method. Each specimen completed the post-cracking cyclic loading protocol without failure.

Figure 169 shows the relationship between flexural stiffness degradation and number of load cycles. The data presented in this graph only reflects measurements taken during the low-level cycles. As noted previously, a set of 20,000 low-level cycles was applied prior to the first set of overload cycles. During these first 20,000 cycles, there was very little stiffness degradation. A sizable drop in stiffness can be observed immediately after the 20,000 cycle mark, which is a result of the first set of overload cycles. The abrupt stiffness loss was a result of newly formed cracks and propagation of existing cracks. New cracks primarily formed within the precast concrete deck sections. Comparatively speaking, all five specimens exhibited very little stiffness loss in the cycles following the first overload set.

Figure 170 depicts the change in interface curvature ($\Delta\phi$) as a function of cyclic number; $\Delta\phi$ is defined by the expression shown in figure 171. A dashed horizontal line shown in figure 170 represents the expected response as determined by moment-curvature analysis. During the first 20,000 cycles, there was very change in $\Delta\phi$. Similar to the data shown figure 169, $\Delta\phi$ increases

after the application of the first set of overload cycles, which is to be expected. Thereafter, $\Delta\phi$ remains stable which indicates good bond between the UHPC and the embedded reinforcing bars. If poor bond existed, $\Delta\phi$ would increase with relative slip between the reinforcing bars and UHPC.

Representative photos of specimens U-A, -B, -C, -D, and -E at the conclusion of the post-cracking fatigue loading protocol are provided in figure 172 through figure 176, respectively. Each specimen exhibited similar, uniformly-distributed crack patterns within the precast concrete deck panel sections. Visual inspection of the UHPC connection grouts revealed no damage apparent to the naked eye. A crack microscope was used to further inspect the UHPC in the connection region and revealed that a few fine microcracks were present in each of the specimens. However, crack widths ere extremely small, less than 0.001 in. (0.025 mm).

Table 32. Average reinforcing bar stress ranges (Δf_s) during fatigue cycles.

ID	Low-Level Cycles ksi, (MPa)		Overload Cycles ksi, (MPa)	
	Test	Calculated	Test	Calculated
U-A	20.5 (141)		37.8 (260)	
U-B	17.4 (120)		32.5 (224)	
U-C	20.1 (139)	21.3 (147) *	36.3 (250)	38.5 (265) *
U-D	17.9 (123)		32.5 (224)	
U-E	21.1 (145)		38.6 (266)	

*Calculated with moment-curvature analysis using specified material properties

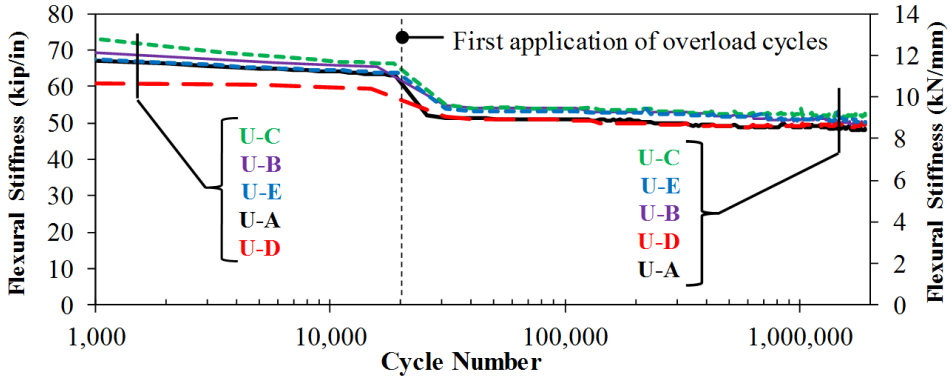

Figure 169. Graph. Flexural stiffness as a function of cycle number; data recorded during overload cycles not shown.

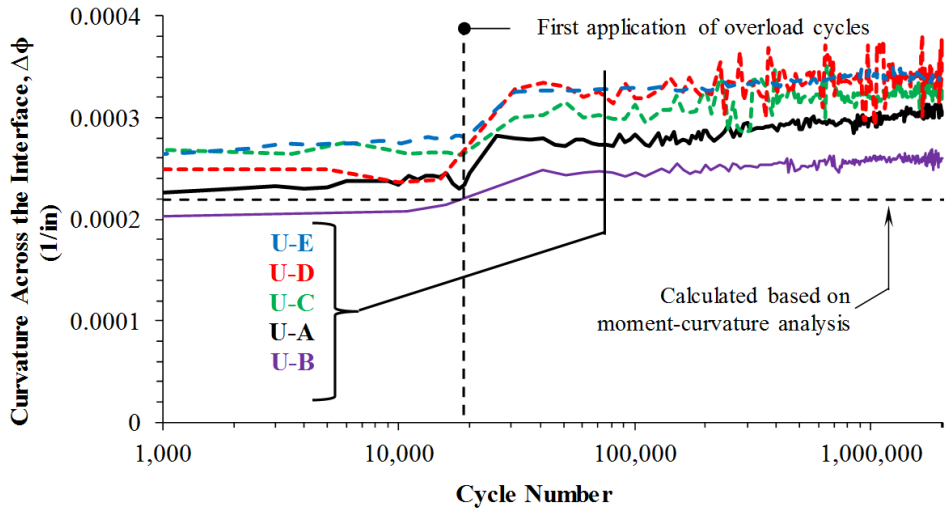

Figure 170. Graph. Interface curvature as a function of cycle number; data recorded during overload cycles not shown.

$$\Delta\phi = \phi_{max} - \phi_{min}$$

Figure 171. Equation. Change in interface curvature, $\Delta\phi$.

Where

ϕ_{max} = measured curvature at peak load for a given cycle

ϕ_{min} = measured curvature at minimum load for a given cycle

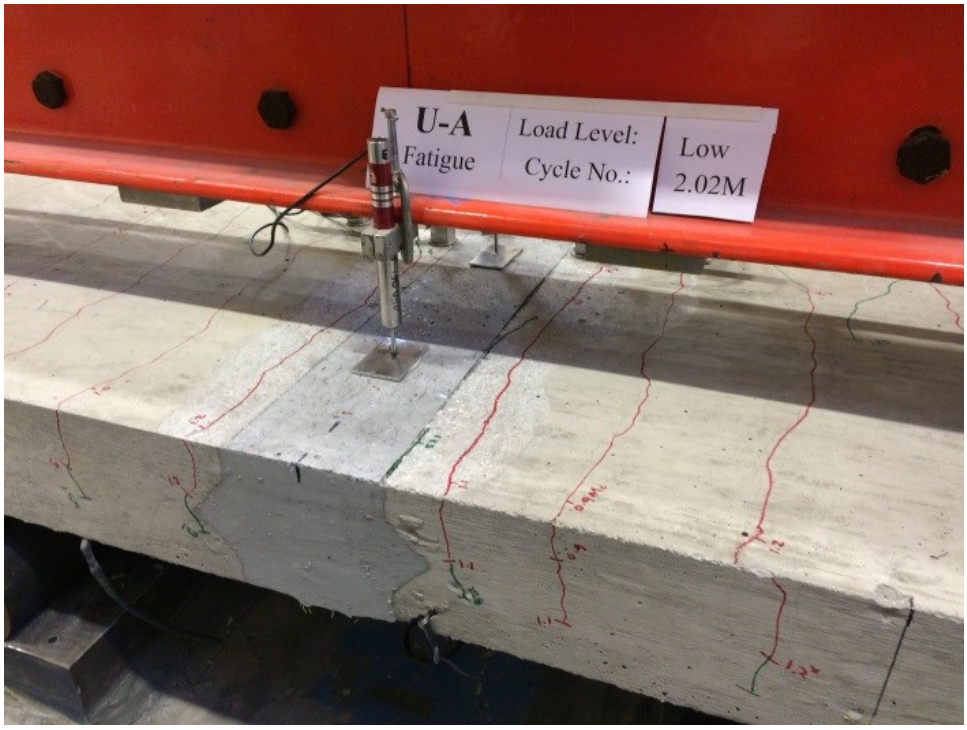

Figure 172. Photo. Observed cracking in specimen U-A after fatigue loading.

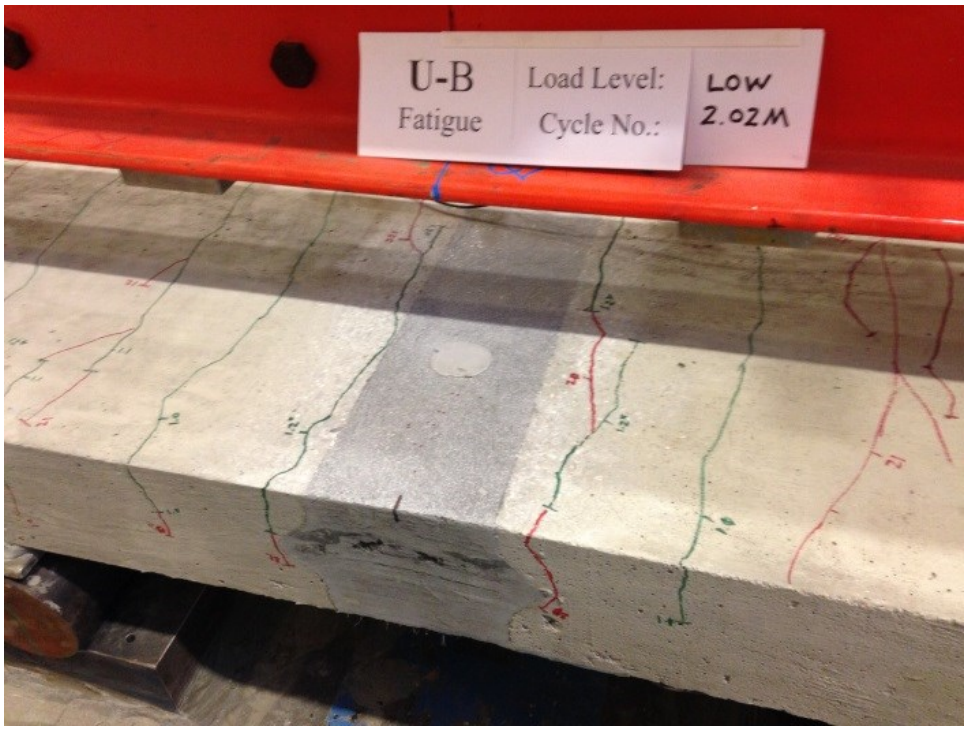

Figure 173. Photo. Observed cracking in specimen U-B after fatigue loading.

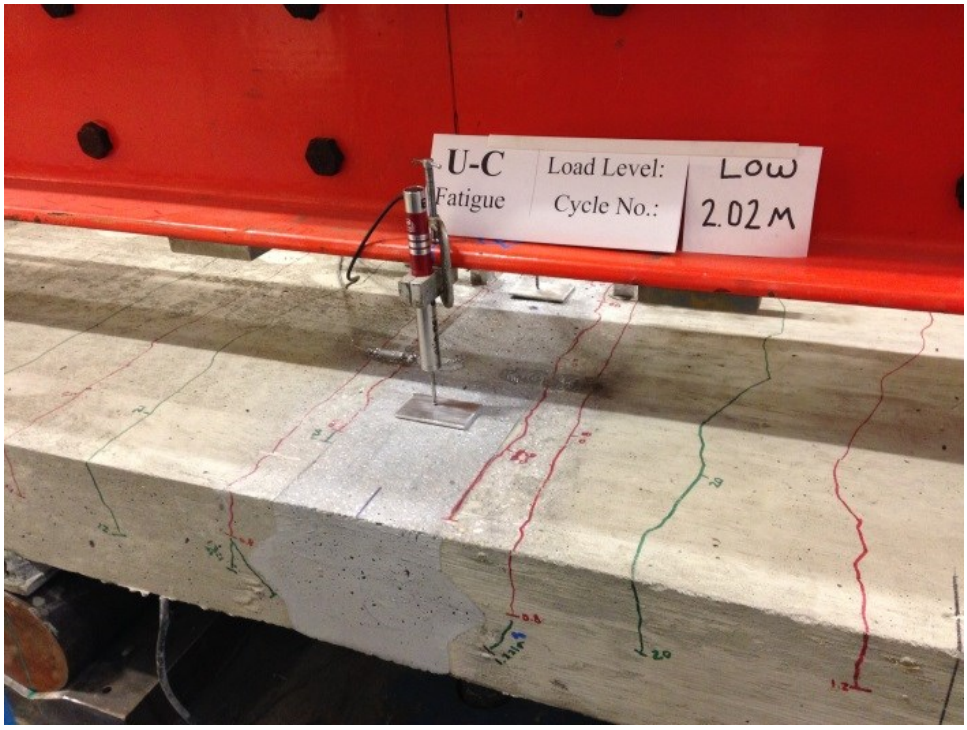

Figure 174. Photo. Observed cracking in specimen U-C after fatigue loading.

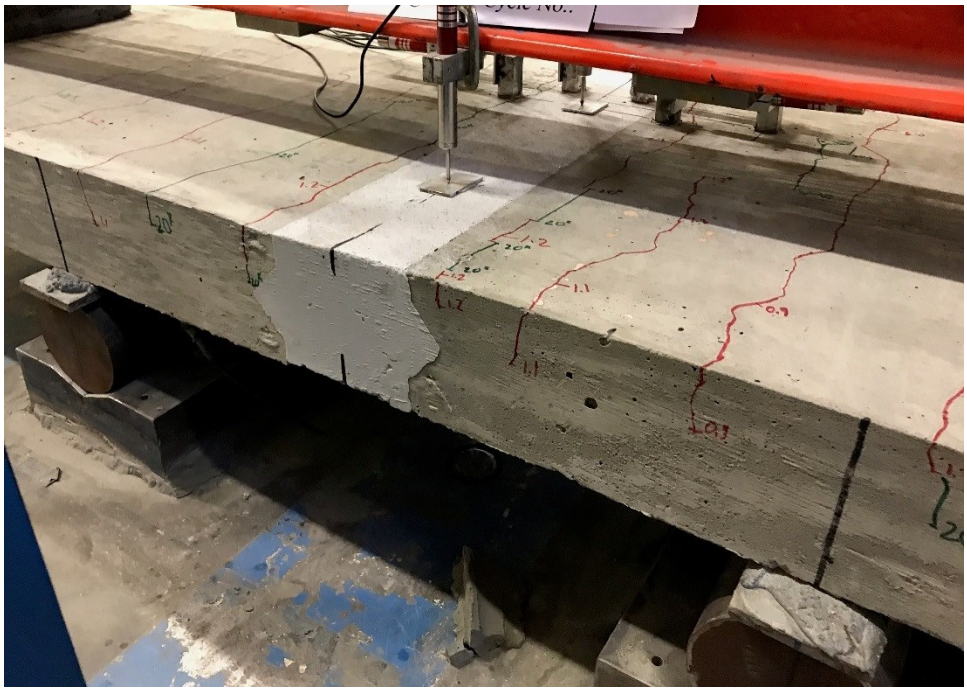

Figure 175. Photo. Observed cracking in specimen U-D after fatigue loading.

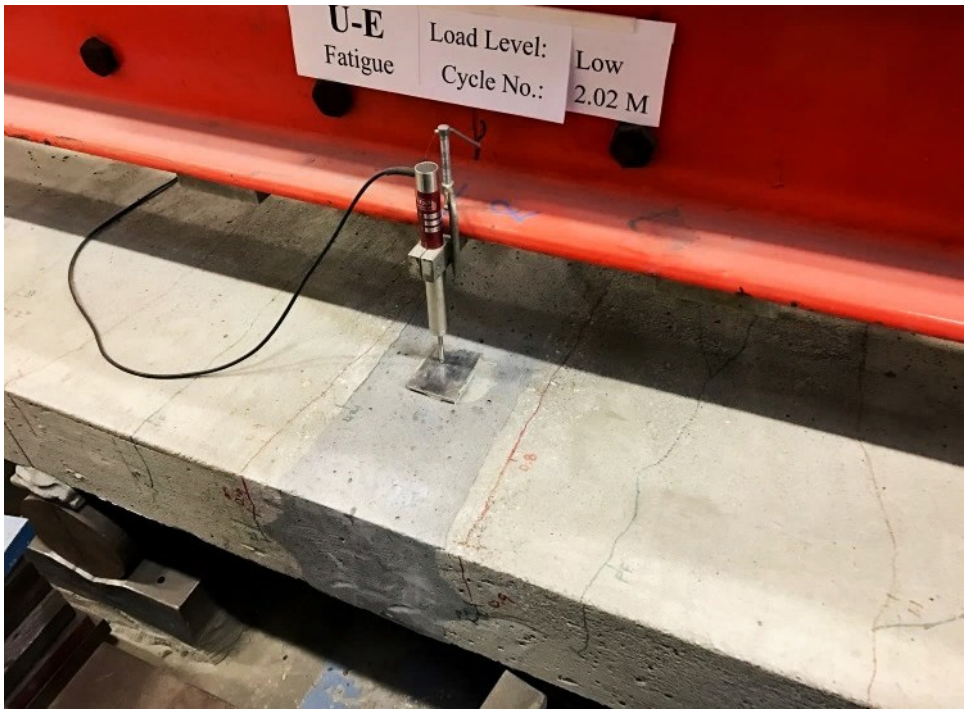

Figure 176. Photo. Observed cracking in specimen U-E after fatigue loading.

Ultimate Loading

The measured compressive strength of UHPC and deck concrete at the time of ultimate testing are listed in table 33. Tabulated results from ultimate loading are presented in table 34 and table 35, and the force-displacement relationships for each specimen are shown in figure 177. Each curve was truncated at the point of peak load for comparison purposes. It can be observed that each specimen exhibits approximately the same initial stiffness, yield point, and have similar ultimate strength and ultimate displacement. The displacement ductilities (ultimate displacement / yield displacement) for specimens U-A, U-B, U-C, U-D, and U-E were 4.24, 3.67, 5.06, 3.68, and 4.43, respectively. Each specimen failed as a result of concrete crushing. At failure, the stress in reinforcing steel were estimated to be between 70 ksi (482 MPa) and 82 ksi (564 MPa). For each specimen, the measured flexural strength at failure exceeded that calculated by the strength method, which is used by AASHTO, and the moment-curvature analysis method as shown in figure 177. Figure 178 shows the load-curvature relationships measured over the two interface locations; north and south correspond to the left- and right-hand interface locations depicted in figure 155. For reference, a set of markers indicate the calculated (expected) response from moment-curvature analysis. At both interface locations, the specimens exhibit behavior similar to one another and show good agreement to the expected response. This indicates that very little bond-slip deformation is occurring at these interface locations, which indicate good bond between the reinforcing steel and UHPC.

Representative photos of specimens U-A, -B, -C, -D, and -E at the conclusion of the ultimate loading protocol are provided in figure 180 through figure 184, respectively. Each specimen exhibited many flexural cracks along with some wide, localized cracking at support locations. In all cases, concrete crushing occurred on the underside of the precast concrete panel elements near

the support locations. For the most part, there was little to no apparent damage to the UHPC materials. Specimens grouted with U-A and U-B did exhibit some visible hairline cracks in UHPC at the conclusions of the tests, but these cracking were fine and did not have any apparent influence on the ultimate behavior of these specimens.

Table 33. Measured compressive strength of UHPC and deck concrete on the day of ultimate loading.

ID	Compressive Strength, ksi (MPa)			
	UHPC		Deck Concrete	
U-A	25.3	(174)	6.25	(43.1)
U-B	23.6	(163)	6.15	(42.4)
U-C	21.5	(148)	6.33	(43.6)
U-D	27.5	(189)	6.23	(42.9)
U-E	21.5	(148)	6.12	(42.2)

Table 34. Key response parameters from ultimate loading.

ID	Load at Yielding, kip (kN)				Displacement at Yield, Δ_y in (mm)		Peak Applied Load, kip (kN)				Displacement at Peak Load, Δ_u in (mm)		Ductility Index, Δ_u / Δ_y
	Test		Calculated*				Test		Calculated*				
U-A	23.8	(106)	24.3	(108)	0.518	(13.2)	32.3	(144)	29.9	(133)	2.20	(55.8)	4.24
U-B	26.7	(119)	24.3	(108)	0.509	(12.9)	31.9	(142)	29.8	(133)	1.87	(47.5)	3.67
U-C	24.0	(107)	24.4	(109)	0.405	(10.3)	33.3	(148)	30.1	(134)	2.05	(52.1)	5.06
U-D	25.5	(114)	24.3	(108)	0.483	(12.3)	32.2	(143)	29.9	(133)	1.78	(45.1)	3.68
U-E	22.1	(98)	24.3	(108)	0.403	(10.2)	32.4	(144)	29.7	(132)	1.78	(45.3)	4.43

* Calculated using moment-curvature analysis and measured properties of concrete and reinforcing steel

Table 35. Reinforcing bar strains, stress, and interface curvature at ultimate.

ID	Reinforcing Bar Strain			Reinforcing Bar Stress**, ksi (MPa)						Interface Curvature, 1/in		
	North Side	South Side	Calc. *	North Side		South Side		Calc. *		North Side	South Side	Calc. *
U-A	0.0132	0.0154	0.0134	69	(476)	72	(493)	69.4	(478)	0.0047	-	0.0036
U-B	0.0141	0.0154	0.0133	70	(483)	72	(493)	69.3	(477)	0.0036	0.0031	0.0036
U-C	0.0194	0.0195	0.0137	76	(521)	76	(522)	69.6	(480)	0.0039	0.0035	0.0037
U-D	0.0174	0.0158	0.0134	74	(508)	72.0	(496)	69	(477)	0.0044	0.0027	0.0036
U-E	0.0257	0.0192	0.0134	82	(563)	75	(520)	69	(477)	0.0040	0.0036	0.0036

* Calculated using measured properties of concrete and reinforcing steel

** Estimated from measured strains

1 in = 25.4 mm

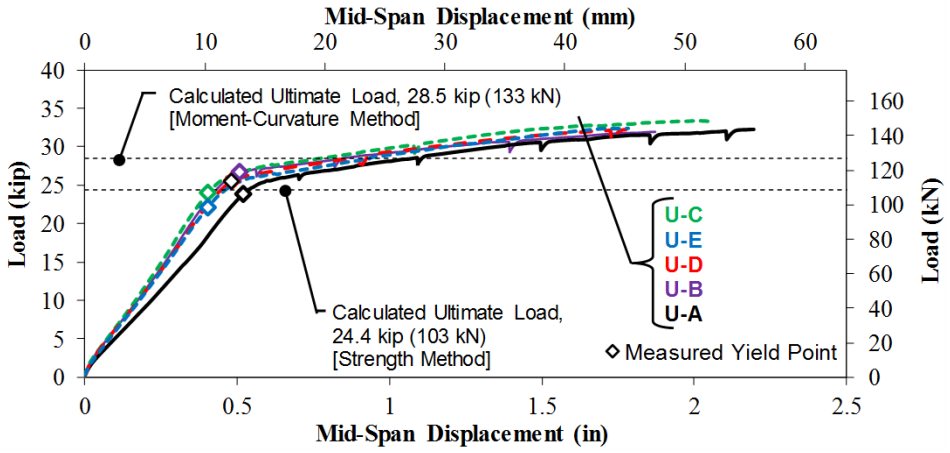

Figure 177. Graph. Force-displacement relationships during ultimate loading.

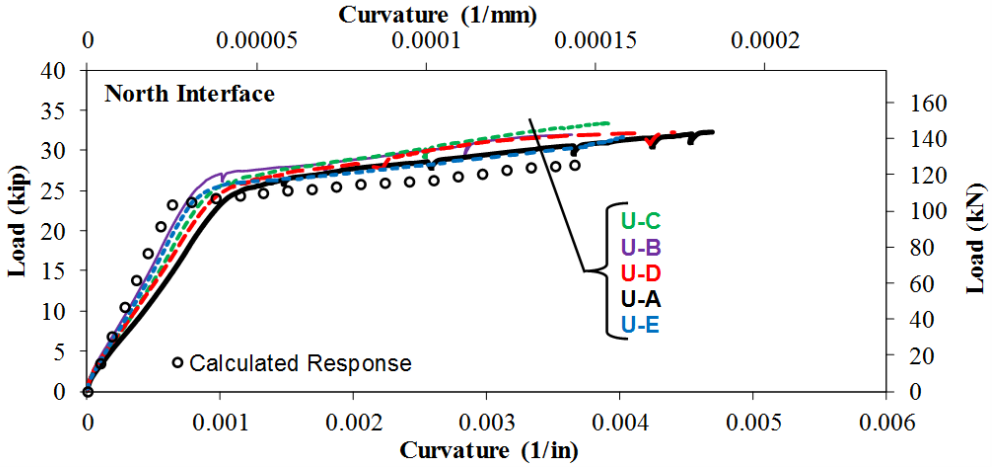

Figure 178. Graph. Load versus curvature relationships during ultimate loading - north interface.

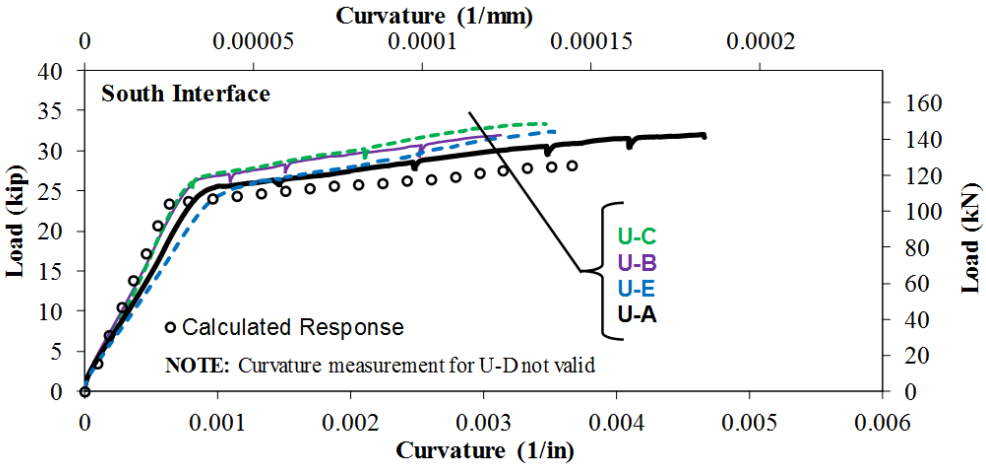

Figure 179. Graph. Load versus curvature relationships during ultimate loading - south interface.

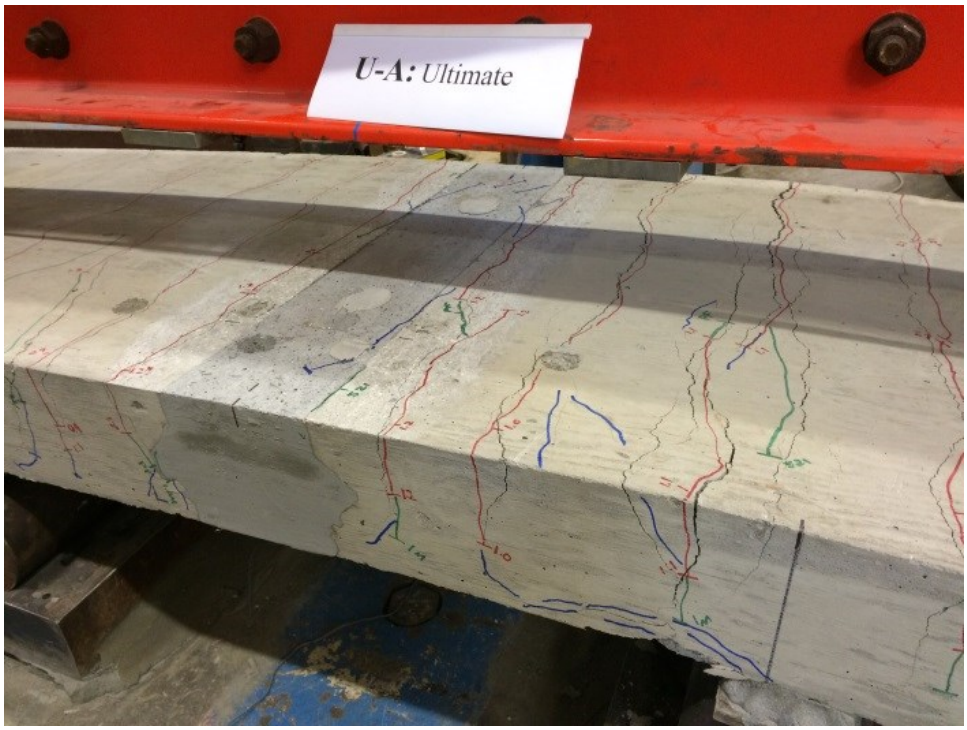

Figure 180. Photo. Specimen U-A after ultimate loading.

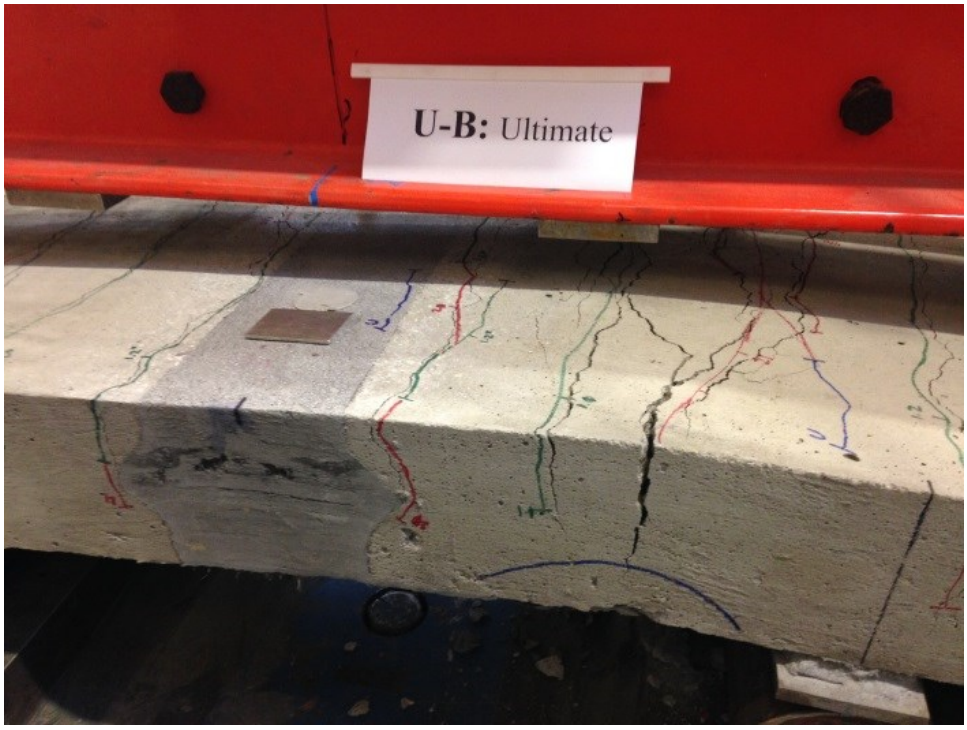

Figure 181. Photo. Specimen U-B after ultimate loading.

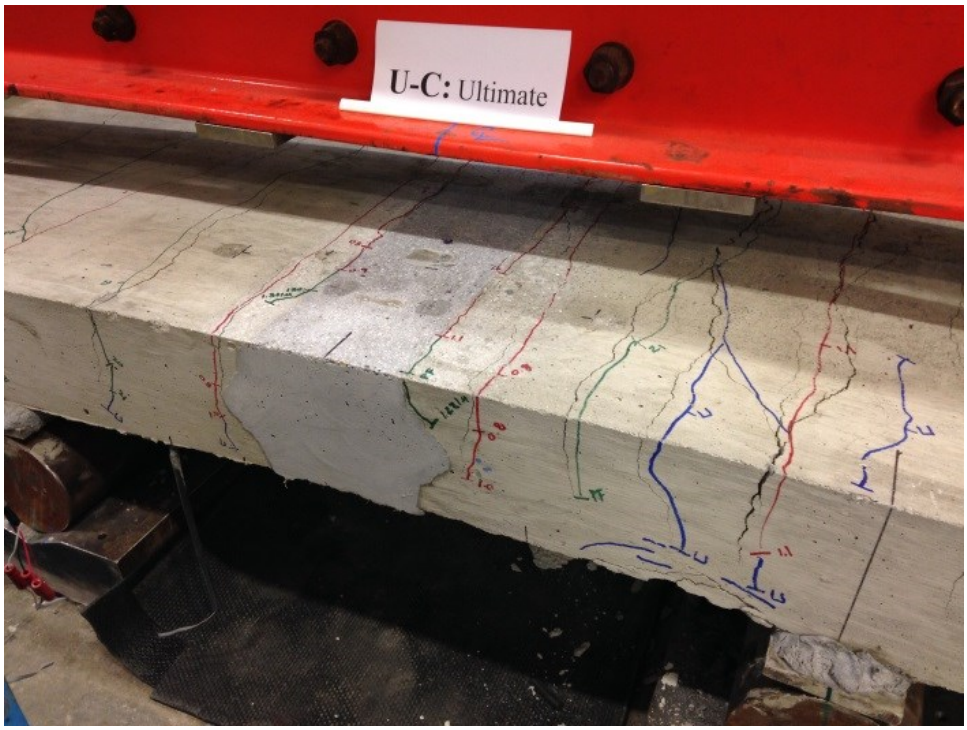

Figure 182. Photo. Specimen U-C after ultimate loading.

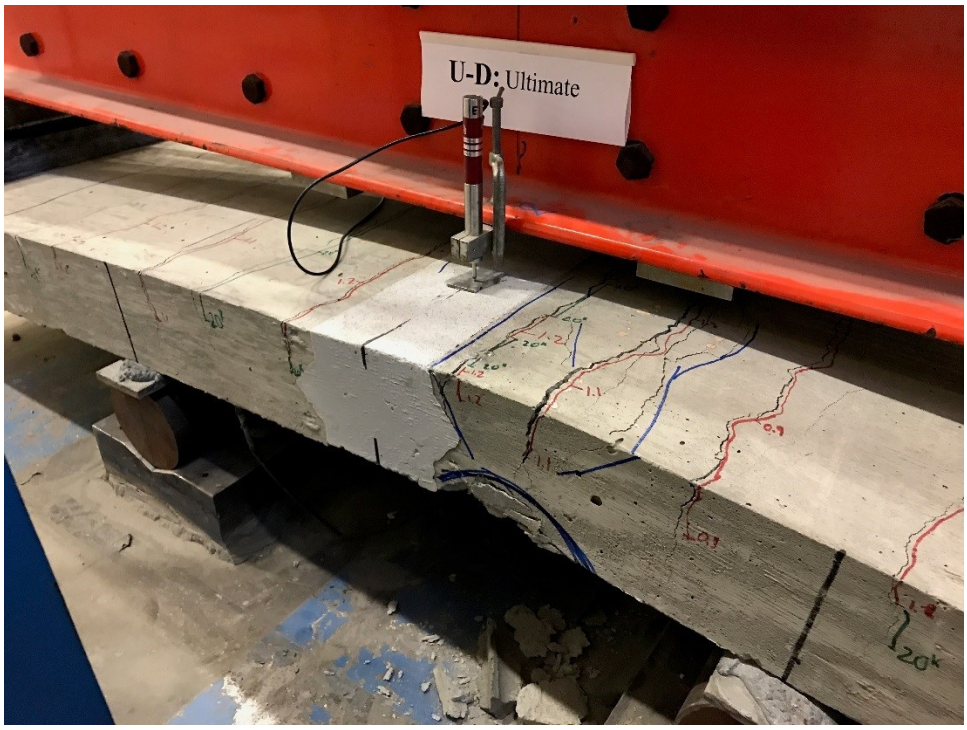

Figure 183. Photo. Specimen U-D after ultimate loading.

Figure 184. Photo. Specimen U-E after ultimate loading.

Discussion

Generally speaking, all five UHPC-class materials exhibited good performance in deck panel connection tests. The only difference among the five materials was observed during the pre-cracking cyclic loading protocol. During this protocol, specimens employing materials U-C and U-E exhibited responses that might indicate premature interface failure. In the case of U-C, interface failure was observed well before deck cracking was expected. In general, these results were consistent with the companion interface bond test results. The post-cracking and ultimate loading behaviors of each specimen were consistent, and correlated well with the expected behavior.

CHAPTER 8. SUMMARY AND CONCLUSIONS

REPORT OVERVIEW

This report presented a comprehensive experimental study focused on characterizing the properties and behavior of different material being marketed as "UHPC." The primary point of emphasis was placed on properties relevant to the bridge engineering research and design communities. Tests conducted at the material-level focused on mechanical and durability properties, and tests at the component-level focused on bond to reinforcing bars and performance of UHPC in precast bridge deck connections.

SUMMARY, KEY OBSERVATIONS AND CONCLUSIONS

The key observations and conclusions are presented in the following sections, and have been broken down, for the most part, by chapter. Each section briefly reviews the objectives and scope prior to providing key observations and conclusions.

Setting Time and Flow

Chapter 3 discussed batching, mixing, placement and curing of the UHPC materials. The flow of each UHPC was measured prior to placement according ASTM C1437 using the modifications described in ASTM C1856. The initial and final setting times for the UHPC materials were measured according to ASTM C403. The following key observations were made or the following conclusions can be drawn:

- The UHPCs were found to have initial setting times as short as 4 hours but could be greater than 9 hours, and finial setting times were found to be between 7 hours and 24 hours.

- The workability of the materials, which was measured using the flow table test, was found to vary significantly. Static flow measurements ranged between 4 inches and 10 inches, and dynamic flow measurement ranged between 7 inches and 10 inches. These differences are attributed to fine aggregate content, fiber geometry, and water and admixture contents.

Compressive Behavior

Chapter 4 discussed the compressive strength gain, compressive stress-stain behavior, Poisson ratio, and compressive elastic modulus. The materials were tested according to ASTM test methods typically used for conventional concrete or cementitious materials. It should be noted that material U-F was not a part of the compressive behavior investigation. The following key observations were made or the following conclusions can be drawn:

- The UHPCs achieved compressive strengths above 14 ksi (96.5 MPa) within 7 days without steam or heat treatments during curing. With the exception of material U-E, the UHPCs exhibited compressive strengths between 20 ksi (137 MPa) and 25 ksi (172 MPa) after longer periods of curing. On the other hand, material U-E tended to have compressive strength just below 20 ksi (137 MPa) after longer curing durations.

- The UHPCs exhibited similar pre-peak compressive stress-strain relationships. At early ages, the materials exhibited substantial non-linearity in the compressive stress-strain curve. As compressive strength increased, the level of non-linearity in the stress-strain curve was reduced. A simple, pre-peak stress-strain model was presented and validated using experimental results.

- The UHPCs exhibited similar axial compressive strains and circumferential strains at failure. At peak compressive strength, average axial compressive strains were between 0.003 and 0.005, and circumferential strains were between 0.001 and 0.002.

- The UHPCs exhibited comparable compressive elastic moduli and Poisson ratios. A best-fit curve was established as a function of $\sqrt{f'_c}$ and was compared with a previously published equation of similar form. It was found that these expressions were similar, and therefore the compressive elastic moduli for all five UHPCs were comparable with previous reported findings. The Poisson's ratios for the five materials were between 0.14 and 0.17.

Tensile Behavior

Chapter 4 discussed the direct and indirect (splitting) tension behavior of UHPC. Direct tension behavior was assessed using the direct tension test method developed at the FHWA TFHRC, and the indirect tension behavior was assessed using a modified version of ASTM C496. It should be noted that material U-F was not a part of the tensile behavior investigation. The following key observations were made or the following conclusions can be drawn:

- Direct tension testing showed that the uniaxial stress-strain response of UHPC has three distinct phases: elastic phase, multi-cracking phase, and localized deformation phase. The elastic phase represents the global elastic straining of the material before the first discrete crack is formed. The second phase describes the formation of simultaneous cracks, during which the specimen accumulates strains in the uncracked matrix between cracks and within the crack-bridging fiber segments. The third phase characterizes the behavior of UHPC when the deformation localizes into a single crack.

- To determine the first cracking strength for use in material models for the design of UHPC members, an objective method, based on a strain offset approach, was proposed and calibrated for all five commercially-available UHPC materials tested herein. The method involves drawing linear line, having a slope equal to the elastic modulus, at an offset strain of 0.02 percent on the individual uniaxial stress-strain graph. The first cracking stress and strain corresponds to the intersection of the line with the stress-strain curve.

- The UHPC materials examined in this study showed a pseudo stress plateau (nearly constant stress as strain increases after cracking) or strain hardening (increasing stress as new cracks form) characteristic responses. Increasing the fiber fraction in the matrix improved the overall resistance against tensile load by increasing the cracking stress, ultimate strength, and in a number of cases, changing the material response from pseudo-stress to strain hardening.

- Indirect tension testing revealed that each UHPC, regardless of fiber volume fraction, exhibited the same apparent first cracking strength, which was approximately 1.0 ksi (6.9 MPa). Each UHPC exhibited post-cracking loading-carrying capacity. The peak splitting tensile stress was always found to significantly greater than the apparent first cracking strength, but there was little apparent correlation between fiber volume fraction and the peak splitting tensile strength.

Bond Strength to Precast Concrete

Chapter 4 discussed the bond strength of the different UHPCs to precast concrete. Bond strength was assessed using a flexural beam bond test based on ASTM C78, and using the direct tension pull-off bond test which was performed according to ASTM C1583. The following key observations were made or the following conclusions can be drawn:

- The UHPCs (U-A through U-E) exhibited good bond strength with precast concrete in flexural beam bond tests. That is, each specimen failed by tensile rupture of the precast concrete. However, the tensile stress in concrete at failure was lower than the modulus of rupture of the control specimen, a plain concrete beam.

- The UHPC materials tested in this portion of the investigation (U-A through U-F) exhibited similar direct tensile bond strengths at the ages of 7 and 14 days, except for U-B which seemed to perform slightly better than the rest of the UHPC materials. However, failure of the bonded interface occurred at approximately the same stress level as the substrate failure, indicating that the bond strength of these materials might have been mainly driven by the tensile strength of the concrete substrate.

Creep and Shrinkage

Chapter 5 investigated the creep and shrinkage behavior of the different UHPC-class materials. The experimental phase presented in this chapter focused on evaluating the creep and shrinkage properties of six commercially-available UHPC materials. The materials were tested according to ASTM test methods typically used for conventional concrete or cementitious materials. The following conclusions can be drawn:

- The creep and shrinkage were measured for U-A, U-B, U-C, and U-E at two different loading ages. The early age specimens underwent about twice as much creep as the mature age specimens. The creep coefficients for the early-age specimens were within the typical range of conventional concrete while the mature age creep coefficients were lower. U-E for both early and mature ages underwent significantly more creep than U-A, U-B, and U-C.

- Within the first few days after casting, UHPC materials tend to exhibit more autogenous shrinkage than is commonly observed in conventional concrete. However, even under unsealed, drying conditions they do not exhibit a significant amount of drying shrinkage as is commonly observed in concrete. While the high autogenous shrinkage is explained by the low w/b and high cementitious contents in UHPC mixture designs, the low w/b may also result in low drying shrinkage due to a lack of free water and a low permeability. It is

also conjectured that the presence of large amount of fibers may be able to help redistribute shrinkage strains and mitigate shrinkage cracking.

- Aside from material U-F which displayed expansion, all UHPCs showed height reduction during the fresh stage of the materials. This height reduction might be indicative of a portion of the autogenous shrinkage observed in these materials; however other parameters such as particle settlement are simultaneously measured, and they must also be considered in the results interpretation.

Durability

The experimental phase assessing durability properties of the five commercially-available UHPC materials focused on their resistance to chloride ions penetration and freeze-thaw damage. The materials were tested using ASTM standardized test methods. The following key observation were made or the following conclusions can be drawn:

- The resistance to chloride penetration was evaluated using both RCPT (charge passed) and surface resistivity test methods. The U-B material showed unexpected results (i.e., very large charge passed and very low surface resistivity values) which seems to be due to the fact that the fibers included in this material tend to touch each other, thus creating an electrical conductive path within the material, and making these test methods invalid for evaluation purposes. Results for the other UHPC materials show charge passed values below 1000 coulombs, and surface resistivity values above 100 kΩ.cm after only 28 days of age. Using the qualitative indications described in both standards, these values fall into the categories of "very low" and "negligible" chloride penetrations. This is mainly attributed to the very dense microstructure achieved through the use of large contents of cementitious materials and other fillers (e.g., silica flour), that prevent the penetration of external and detrimental aggressors (e.g., chloride ions) into the material.

- All the UHPCs tested in the study display enhanced durability in terms of freeze-thaw resistance. There is practically no change in the RDME values throughout the test duration, which lasted for about 600 freeze-thaw cycles (the ASTM standard calls for 300 cycles for conventional concretes). A drop in the RDME to values below 60 percent would be indicative of specimen damage (internal or external). RDME values were maintained above 98 percent in all UHPC materials throughout the testing. Also, minimal mass loss was observed throughout the testing. It is concluded that neither internal nor external damage occurred in the UHPC materials.

Bond to Reinforcing Bars

The first part of Chapter 7 presented a series of tests that were conducted to evaluate the bond between the different UHPC-class materials and deformed steel reinforcing bars. There were two primary goals of these tests. First, to determine whether the different UHPC-class materials tested herein conformed to the design guidance provided in FHWA TechNote entitled: *Design and Construction of Field-Cast UHPC Connections*. (B. A. Graybeal 2014a) Second, to investigate the influence of the fiber reinforcement content on the bond strength between UHPC and deformed steel bars. It should be noted that material U-F was not a part of the reinforcing bar bond

investigation. The following key observation were made or the following conclusions can be drawn:

- Findings suggest that the bond strengths between the reinforcing bars and the UHPC -class materials tested in this study were similar to those from previous research conducted at TFHRC by Yuan and Graybeal (2014). Furthermore, results also suggest that the guidance in the *Design and Construction of Field-Cast UHPC Connections* Technote is applicable to the UHPCs tested herein; this holds for both a 2 percent fiber volume factor and the fiber volume recommend by the material supplier.

- The bond strength of reinforcing bars embedded in UHPC were influenced by the fiber volume fraction of UHPC. That is, the bond strength increased as the volume of fibers increased. It was determined that fiber volume fractions less than 2-percent may have adverse effects on the system-level behavior of prefabricated elements employing UHPC connections. That is, UHPCs with fiber volume fractions less than 2-percent may not be able to develop sufficient stress in embedded bars prior to lap splice failure which would cause reduced ductility.

Performance in Deck-Level Connections

The second part of Chapter 7 investigated the performance of the different UHPC-class materials in deck-level connections between adjacent prefabricated bridge deck elements. The performance of deck-level connections was evaluated using large-scale precast deck panel specimens. Specimens were subjected to three different loading protocols to assess behavior under different levels of cyclic and monotonic loading. Focal areas of the investigation included interface bond between UHPC and precast concrete, cracking behavior under cyclic loading, response under long-term cyclic loading, and monotonic ultimate loading behavior. It should be noted that material U-F was not a part of the deck-level connections investigation. The following key observation were made or the following conclusions can be drawn:

- Generally speaking, all UHPC-class materials exhibited good performance in deck panel connection tests. In each test, the UHPC connection region exhibited little to damage.

- Differences among the five materials tested were observed during the pre-cracking cyclic loading protocol. During this protocol, specimens employing materials U-C and U-E exhibited responses that might indicate premature interface failure. In the case of U-C, interface failure was observed well before deck cracking was expected.

- Stiffness degradation observed during the two cyclic loading protocols was primarily controlled by the cracking in precast concrete deck panels. During pre-cracking cyclic loading, the observed stiffness of specimens was bounded from above by the expected (calculated) response of an uncracked section, and bounded from below by the expected (calculated) response of a fully-cracked section. During post-cracking fatigue loading, observed stiffnesses and interface curvatures were similar to the expected response.

- The ultimate loading response of each specimen was consistent, ductile, and failure was a result of concrete crushing. Furthermore, the behavior of each specimen correlated well

with the expected behavior determined using moment-curvature analysis. Prior to concrete crushing, the maximum stresses in the tension steel reinforcement were between 72 ksi (496 MPa) and 76 ksi (524 MPa).

REFERENCES

AASHTO TP 95. 2014. *Standard Method of Test for Surface Resistivity Indication of Concrete's Ability to Resist Chloride Ion Penetration*. American Association of State Highway and Transportation Officials.

Abbas, S., A. M. Soliman, and M. L. Nehdi. 2015. "Exploring Mechanical and Durability Properties of Ultra-High Performance Concrete Incorporating Various Steel Fiber Lengths and Dosages." *Construction and Building Materials* 75: 429–441. doi:10.1016/j.conbuildmat.2014.11.017.

ACI Committee 209. 2005. *Report on Factors Affecting Shrinkage and Creep of Hardened Concrete*. Farmington Hills, MI.

ACI Committee 209. 2009. *Prediction of Creep, Shrinkage, and Temperature Effects in Concrete Structures*. Farmington Hills, MI.

ACI Committee 408. 2003. "Bond and Development of Straight Reinforcing Bars in Tension." 408R–03. Farmington Hills, MI.

Acker, P. 2004. "Why Does Ultrahigh-Performance Concrete (UHPC) Exhibit Such a Low Shrinkage and Such Low Creep?" In *Autogenous Deformation of Concrete*, edited by O.M. Jensen, D. P. Bentz, and P. Lura, 141–54. American Concrete Institute.

Ahlborn, T. M., E. J. Peuse, and D. L. Misson. 2008. "Ultra-High-Performance-Concrete for Michigan Bridges Material Performance – Phase I." RC-1525. Michigan Technological University.

Ahlborn, T.M, D.K. Harris, D.L. Misson, and E.J. Peuse. 2011. "Strength and Durability Characterization of Ultra-High Performance Concrete Under Variable Curing Conditions." *Transportation Research Record* 22 (51): 68–75.

American Association of State Highway and Transportation Officials. 2014. *LRFD Bridge Design Specifications*. 7th Edition. Washington, D.C. 7th ed. Washington DC.

———. 2016. *AASHTO LRFD Bridge Design Specifications*. Interim Revisions.

ASTM C39 / C39M-16b. 2016. *Standard Test Method for Compressive Strength of Cylindrical Concrete Specimens*. West Conshohocken, PA: ASTM International.

ASTM C78 / C78M-16. 2016. *Standard Test Method for Flexural Strength of Concrete (Using Simple Beam with Third-Point Loading)*. West Conshohocken, PA: ASTM International.

ASTM C157-08. 2008. *Standard Test Method for Length Change of Hardened Hydraulic-Cement Mortar and Concrete*. West Conshohocken, PA: ASTM International.

ASTM C215 - 14. 2014. *Standard Test Method for Fundamental Transverse, Longitudinal, and Torsional Resonant Frequencies of Concrete Specimens*. West Conshohocken, PA: ASTM International. doi:10.1520/C0215-14.

ASTM C403 / C403M-08. 2008. *Standard Test Method for Time of Setting of Concrete Mixtures by Penetration Resistance*. West Conshohocken, PA: ASTM International.

ASTM C469 / C469M-14. 2014. *Standard Test Method for Static Modulus of Elasticity and Poisson's Ratio of Concrete in Compression*. West Conshohocken, PA: ASTM International.

ASTM C496 / C496M-11. 2004. *Standard Test Method for Splitting Tensile Strength of Cylindrical Concrete Specimens*. West Conshohocken, PA: ASTM International.

ASTM C512-15. 2015. *Standard Test Method for Creep of Concrete in Compression*. West Conshohocken, PA: ASTM International.

ASTM C666-15. 2015. *Standard Test Method for Resistance of Concrete to Rapid Freezing and Thawing*. West Conshohocken, PA: ASTM International.
ASTM C827-16. 2016. *Standard Test Method for Change in Height at Early Ages of Cylindrical Specimens of Cementitious Mixtures*. West Conshohocken, PA: ASTM International.
ASTM C1202-12. 2012. *Standard Test Method for Electrical Indication of Concrete's Ability to Resist Chloride Ion Penetration.* West Conshohocken, PA: ASTM International.
ASTM C1437-15. 2015. *Standard Test Method for Flow of Hydraulic Cement Mortar*. West Conshohocken, PA: ASTM International.
ASTM C1583 / C1583M-13. 2013. *Standard Test Method for Tensile Strength of Concrete Surfaces and the Bond Strength or Tensile Strength of Concrete Repair and Overlay Materials by Direct Tension (Pull-off Method)*. West Conshohocken, PA: ASTM International.
ASTM C1856/C1586-17. 2017. *Standard Practice for Fabricating and Testing Specimens of Ultra-High Performance Concrete*. West Conshohocken, PA: ASTM International.
Azizinamini, A, M. Stark, J. J. Toller, and S. K. Ghosh. 1993. "Bond Performance of Reinforcing Bars Embedded in High-Strength Concrete." *ACI Structural Journal* 90 (5): 554–61.
Bazant, Z. P., and F. H. Wittmann. 1982. "Creep and Shrinkage Concrete Structures." Edited by Z.P. Bazant and F.H. Wittmann.
Bissonnette, B., P. Pierre, and M. Pigeon. 1999. "Influence of Key Parameters on Drying Shrinkage of Cementitious Materials." *Cement and Concrete Research* 29 (10): 1655–62. doi:10.1016/S0008-8846(99)00156-8.
Blais, P. Y., and M. Couture. 1999. "Precast, Prestressed Pedestrian Bridge—World's First Reactive Powder Concrete Structure." *PCI Journal* 44 (5): 60–71.
Branson, D. E., B. L. Meyers, and K. M. Kripanarayanan. 1970. "Loss of Prestress, Camber, and Deflection of Noncomposite and Composite Structures Using Different Weight Concretes." Final Report No. 70-6.
Brooks, J. J. 1989. "Influence of Mix Proportions, Plasticizers and Superplasticizers on Creep and Drying Shrinkage of Concrete." *Magazine of Concrete Research* 41 (148): 145–53. doi:10.1680/macr.1989.41.148.145.
Brooks, J. J., 1999. "How Admixtures Affect Shrinkage and Creep." *Concrete International* 21 (4).
Brühwiler, E., M. Bastien-Masse, H. Mühlberg, B. Houriet, B. Fleury, S, Cuennet, P. Schär, F. Boudry, and M. Maurer. 2015. "Strengthening the Chillon Viaducts Deck Slabs with Reinforced UHPFRC." In *IABSE Conference Proceedings*. Geneva, Switzerland.
Brühwiler, E., and E. Denarié. 2013. "Rehabilitation and Strengthening of Concrete Structures Using Ultra-High Performance Fibre Reinforced Concrete." *Structural Engineering International* 23 (4): 450–457. doi:10.2749/101686613X13627347100437.
Branson D. E., and M. L. Christiason. 1971. "Time Dependent Concrete Properties Related To Design-Strength and Elastic Properties, Creep, and Shrinkage." *Special Publication* 27 (January). doi:10.14359/17187.
Burkart, I., and H. S. Muller. 2008. "Creep and Shrinkage Characteristics of Ultra High Strength Concrete (UHPC)." In *Second International Symposium on Ultra High Performance Concrete*. Kassel, Germany: Kassel University.

De la Varga, I., Z. B. Haber, and B. A. Graybeal. 2016. “Performance of Grouted Connections for Prefabricated Bridge Elements-Part I: Material-Level Investigation on Shrinkage and Bond.” In *PCI National Bridge Conference Proceedings*. Nashville, TN.

De la Varga, I., and B. A. Graybeal. 2016. “Dimensional Stability of Grout-Type Materials Used as Connections between Prefabricated Concrete Elements.” FHWA-HRT-16-008.

Di Bella, C., and B. Graybeal. 2014. “Volume Stability and Cracking Potential of Prebagged, Cement-Based Nonshrink Grouts for Field-Cast Connections.” *Transportation Research Record: Journal of the Transportation Research Board* . 2441 (December). Transportation Research Board of the National Academies: 6–12.

FHWA. 2017a. *Ultra-High Performance Concrete - Deployments*. Accessed August 23. https://www.fhwa.dot.gov/research/resources/uhpc/bridges.cfm.

———. 2017b. *Ultra-High Performance Concrete Interactive Web Map*. Accessed August 23. http://usdot.maps.arcgis.com/apps/webappviewer/index.html?id=41929767ce164eba934d70883d775582.

Flietstra, J. C. 2011. “Creep and Shrinkage Behavior of Ultra High-Performance Concrete under Compressive Loading with Varying Curing Regimes.” Michigan Technological University.

Garas, V. Y., L. F. Kahn, and K. E. Kurtis. 2009. “Short-Term Tensile Creep and Shrinkage of Ultra-High Performance Concrete.” *Cement and Concrete Composites* 31 (3): 147–52. doi:10.1016/j.cemconcomp.2009.01.002.

Garas, V.Y., K. E. Kurtis, and L. F. Kahn. 2012. “Creep of UHPC in Tension and Compression: Effect of Thermal Treatment.” *Cement and Concrete Composites* 34 (4): 493–502. doi:10.1016/j.cemconcomp.2011.12.002.

Graybeal, B., and J. Hartman. 2003. “Strength And Durability Of Ultra-High Performance Concrete.” In *Concrete Bridge Conference*.

Graybeal, B. A. 2006a. “Material Property Characterization of Ultra-High Performance Concrete, FHWA-HRT-06-103.” *FHWA-HRT-06-103*. Washington DC.

———. 2006b. “Practical Means for Determination of the Tensile Behavior of Ultra-High Performaonce Concrete.” *Journal of ASTM International* 3 (8): 100387. doi:10.1520/JAI100387.

———. 2006c. “Material Property Characterization of Ultra-High Performance Concrete.” FHWA-HRT-06-103.

———. 2007. “Compressive Behavior of Ultra-High-Performance Fiber-Reinforced Concrete.” *ACI Materials Journal* 104 (2): 146–52.

———. 2009a. “Structural Behavior of a 2nd Generation Ultra-High Performance Concrete Pi-Girder.” FHWA-HRT-10-026.

———. 2009b. “Structural Behavior of a Prototype Ultra-High Performance Concrete Pi-Girder.” FHWA-HRT-10-027.

———. 2014a. “Design and Construction of Field-Cast UHPC Connections.” FHWA-HRT-14-084 FHWA-HRT-14-084.

———. 2014b. “Ultra-High-Performance Concrete Connections for Precast Concrete Bridge Decks.” *PCI Journal* Fall: 48–62.

———. 2014c. “Compression Testing of Ultra-High-Performance Concrete.” *Advances in Civil Engineering Materials*, November, 20140027. doi:10.1520/ACEM20140027.

Graybeal, B. A., and F. Baby. 2013. “Development of Direct Tension Test Method for Ultra-High- Performance Fiber-Reinforced Concrete.” *ACI Materials Journal* 110 (2): 177–86.

Graybeal, B. A., and B. Stone. 2012. “Compression Response of a Rapid-Strengthening Ultra-High Performance Concrete Formulation.” FHWA-HRT-12-065.
Habel, K., E. Denarié, and E. Brühwiler. 2007. “Experimental Investigation of Composite Ultra-High-Performance Fiber-Reinforced Concrete and Conventional Concrete Members.” *ACI Structural Journal* 104 (1): 93–101.
Haber, Z. B., I. De la Varga, and B. A. Graybeal. 2016. “Performance of Grouted Connections for Prefabricated Bridge Elements-Part II: Component-Level Investigation on Bond and Cracking.” In *PCI National Bridge Conference Proceedings*. Nashville, TN.
Haber, Z. B., J. F. Munoz, and B. A. Graybeal. 2017. “Field Testing of an Ultra-High Performance Concrete Overlay.” FHWA-HRT-17–096.
Haber, Z. B. and B. A. Graybeal. 2018. “Lap-Spliced Rebar Connections with UHPC Closures.” *ASCE Journal of Bridge Engineering*, In Press.
Hognestad, E., N. W. Hanson, and D. McHenry. 1955. “Concrete Stress Distribution in Ultimate Strength Design.” *Journal of the American Concrete Institute* 27 (4): 455–79.
Jensen, O. M., and P. F. Hansen. 2001. “Autogenous Deformation and RH-Change in Perspective.” *Cement and Concrete Research* 31 (12): 1859–65. doi:10.1016/S0008-8846(01)00501-4.
Keierlebar, B., D. Bierwagen, T. Wipf, and A. Abu-Hawash. 2010. “FHWA, Iowa Optimize Pi Girder.” *Aspire* Winter Issue. 24-26.
Koh, K., G. Ryu, S. Kang, J. Park, and S. Kim. 2011. “Shrinkage Properties of Ultra-High Performance Concrete (UHPC).” *Advanced Science Letters* 4 (3): 948–52. doi:10.1166/asl.2011.1505.
Le Chatelier, H. 1900. “Sur Les Changements de Volume Qui Accompagnent Le Durcissement Des Ciments.” Bulletin Société de l’Encouragement pour l’Industrie Nationale. Paris, France.
Lee, J. K., and S. H. Lee. 2015. “Flexural Behavior of UHPFRC Moment Connection for Precast Concrete Decks.” *ACI Structural Journal* 112 (4). doi:10.14359/51687657.
L’Hermite, R. 1960. *What Do We Know about Plastic Deformation and Creep of Concrete?* Waterways Experiment Station. https://books.google.com/books?id=JaBhHQAACAAJ.
L’Hermite, R. G. 1960. “Volume Changes of Concrete.” In *4th International Symposium on the Chemistry of Cement*. Washington DC.
Li, L., Z. (John) Ma, M. E. Griffey, and R. G. Oesterle. 2010. “Improved Longitudinal Joint Details in Decked Bulb Tees for Accelerated Bridge Construction: Concept Development.” *Journal of Bridge Engineering* 15 (3): 327–36. doi:10.1061/(ASCE)BE.1943-5592.0000067.
Ma, J., and M. Orgass. 2004. “Comparative Investigations on Ultra-High Performance Concrete with and without Coarse Aggregates.” In *International Symposium on Ultra High Performance Concrete (UHPC)*. Kassel, Germany.
Mander, J. 1983. “Seismic Design of Bridge Piers.” Dissertation, Christchurch, New Zealand: University of Canterbury.
Marchand, P., F. Baby, A. Khadour, T. Battesti, P. Rivillon, M.c Quiertant, H. H. Nguyen, et al. 2016. “Bond Behaviour of Reinforcing Bars in UHPFRC: Experimental Investigation.” *Materials and Structures* 49 (5): 1979–95. doi:10.1617/s11527-015-0628-0.
Massicotte, B., M. A. Dagenais, and J. F. Garneau. 2014. “Bridge Pier Seismic Strengthening Using UHPFRC Cover.” In *9th International Conference on Short and Medium Span Bridges*, 15. Calgary, Canada.

Meyers, B. L., D. E. Branson, and C. G. Schumann. 1972. “Prediction of Creep and Shrinkage Behavior for Design from Short Term Tests.” *PCI Journal* May-June: 29–45.
Nanni, A. 1988. “Splitting-Tension Test for Fiber Reinforced Concrete.” *ACI Materials Journal* 85 (4): 229–33.
Noshiravani, T., and E. Bruhwiler. 2013. “Experimental Investigation on Reinforced Ultra-High-Performance Fiber-Reinforced Concrete Composite Beams Subjected to Combined Bending and Shear.” *ACI Materials Journal* 110 (2): 251–61.
Pfeifer, C, B. Möeser, C. Giebson, and J. Stark. 2009. “Durability of Ultra-High-Performance Concrete.” In *ACI Special Publication*, 261:1–16.
RILEM TC. 1983. “RILEM Recommendations for the Testing and Use of Constructions Materials. RC 6 Bond Test for Reinforcement Steel. 2. Pull-out Test.”
Schmidt, M., and E. Fehling. 2005. “Ultra-High-Performance Concrete: Research, Development and Application in Europe.” In *Seventh International Symposium on the Utilization of High Strength/High-Performance Concrete*, 51–78.
Shi, C., Z. Wu, J Xiao, D. Wang, Z. Huang, and Z. Fang. 2015. “A Review on Ultra High Performance Concrete: Part I. Raw Materials and Mixture Design.” *Construction and Building Materials* 101. Elsevier Ltd: 741–51. doi:10.1016/j.conbuildmat.2015.10.088.
Silfwerbrand, J., and H. Beuhausen. 2005. “Bonded Concrete Overlays–bond Strength Issues.” In *International Conference on Concrete Repair, Rehabilitation and Retrofitting*, 19–21. Cape Town.
Staquet, S., and B. Espion. 2004. “Early Age Autogenous Shrinkage of UHPC Incorporating Very Fine Fly Ash or Metakaolin in Replacement of Silica Fume.” In *International Symposium on Ultra High Performance Concrete*, 587–99. Kassel, Germany.
Steinberg, E. P., A. A. Semendary, and K. A. Walsh. 2016. “Implementing Ultra High Performance Concrete (UHPC) with Dowel Bars in Longitudinal Joints (Shear Key) in an Adjacent Box Beam Bridge.” In *Proceedings of the International Symposium on Ultra High Performance Concrete*. Des Moines, IA.
Troxell, G. E., J. M. Raphael, and R.E. Davis. 1958. “Long-Term Creep and Shrinkage Tests of Plain and Reinforced Concrete.” *Proceedings of ASTM* 58: 1101–20.
Vande Voort, T., A. Suleiman, and S. Sritharan. 2008. “Design and Performance Verification of Ultra-High Performance Concrete Piles for Deep Foundations.” IHRB Project TR-558.
Wang, D., C. Shi, Z. Wu, J. Xiao, Z. Huang, and Z. Fang. 2015. “A Review on Ultra High Performance Concrete: Part II. Hydration, Microstructure and Properties.” *Construction and Building Materials* 96. Elsevier Ltd: 368–77. doi:10.1016/j.conbuildmat.2015.08.095.
Wille, K., and C. Boisvert-Cotulio. 2015. “Material Efficiency in the Design of Ultra-High Performance Concrete.” *Construction and Building Materials* 86: 33–43. doi:10.1016/j.conbuildmat.2015.03.087.
Yoo, D. Y., H. O. Shin, J. M. Yang, and Y. S. Yoon. 2014. “Material and Bond Properties of Ultra High Performance Fiber Reinforced Concrete with Micro Steel Fibers.” *Composites Part B: Engineering* 58 (March): 122–33. doi:10.1016/j.compositesb.2013.10.081.
Yuan, J., and B. A. Graybeal. 2015. “Bond of Reinforcement in Ultra-High-Performance Concrete.” *ACI Structural Journal* 112 (6). doi:10.14359/51687912.
———. 2016. “Full-Scale Testing of Shear Key Details for Precast Concrete Box-Beam Bridges.” *Journal of Bridge Engineering* 21 (September): 04016043. doi:10.1061/(ASCE)BE.1943-5592.0000906.

Yuan, J., and B. A. Graybeal. 2014. “Bond Behavior of Reinforcing Steel in Ultra-High Performance Concrete.” FHWA-HRT-14-090.
Zhang, G., B. A. Graybeal, and L. Chen. 2013. “Development of a Family of Ultra-High Performance Concrete Pi-Girders.” FHWA-HRT-14-027.
Zmetra, K. M. 2015. “Repair of Corrosion Damaged Steel Bridge Girder Ends by Encasement in Ultra-High Strength Concrete.” Dissertation, Storrs, Connecticut: University of Connecticut.

This page was intentionally left blank

Publication FHWA-HRT-18 036
HRDI-40/3-18(WEB)EHIF